

## INFORMATION TO USERS

This manuscript has been reproduced from the microfilm master. UMI films the text directly from the original or copy submitted. Thus, some thesis and dissertation copies are in typewriter face, while others may be from any type of computer printer.

**The quality of this reproduction is dependent upon the quality of the copy submitted.** Broken or indistinct print, colored or poor quality illustrations and photographs, print bleedthrough, substandard margins, and improper alignment can adversely affect reproduction.

In the unlikely event that the author did not send UMI a complete manuscript and there are missing pages, these will be noted. Also, if unauthorized copyright material had to be removed, a note will indicate the deletion.

Oversize materials (e.g., maps, drawings, charts) are reproduced by sectioning the original, beginning at the upper left-hand corner and continuing from left to right in equal sections with small overlaps. Each original is also photographed in one exposure and is included in reduced form at the back of the book.

Photographs included in the original manuscript have been reproduced xerographically in this copy. Higher quality 6" x 9" black and white photographic prints are available for any photographs or illustrations appearing in this copy for an additional charge. Contact UMI directly to order.

# UMI

A Bell & Howell Information Company  
300 North Zeeb Road, Ann Arbor, MI 48106-1346 USA  
313/761-4700 800/521-0600



HYDROTHERMAL HISTORY OF THE LONG VALLEY CALDERA,  
CALIFORNIA:  
LIFE AFTER COLLAPSE

A  
DISSERTATION

Presented to the Faculty  
of the University of Alaska Fairbanks  
in Partial Fulfillment of the Requirements  
for the Degree of  
DOCTOR OF PHILOSOPHY

By  
Vicki Sue McConnell, B.S.

Fairbanks, Alaska  
December 1995

**UMI Number: 9608767**

---

**UMI Microform 9608767**

**Copyright 1995, by UMI Company. All rights reserved.**

**This microform edition is protected against unauthorized  
copying under Title 17, United States Code.**

---

**UMI**

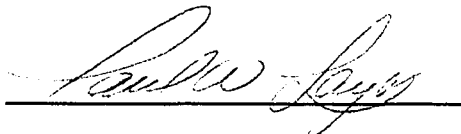
**300 North Zeeb Road  
Ann Arbor, MI 48103**

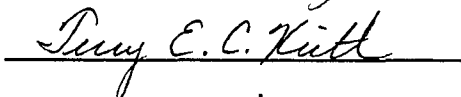
HYDROTHERMAL HISTORY OF THE LONG VALLEY CALDERA,  
CALIFORNIA:  
LIFE AFTER COLLAPSE

By

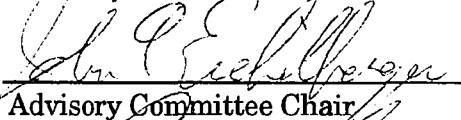
Vicki Sue McConnell

RECOMMENDED:

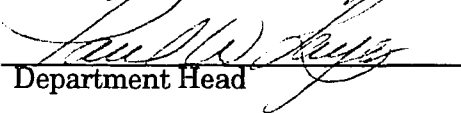
  
\_\_\_\_\_

  
\_\_\_\_\_

  
\_\_\_\_\_

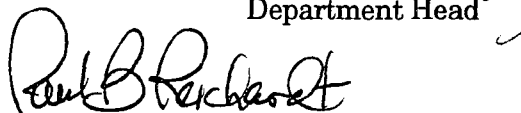
  
\_\_\_\_\_

Advisory Committee Chair

  
\_\_\_\_\_

Department Head

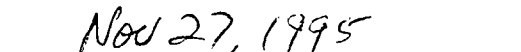
APPROVED:

  
\_\_\_\_\_

Dean, School of Natural Sciences

  
\_\_\_\_\_

Dean of the Graduate School

  
\_\_\_\_\_

Date

## ABSTRACT

Drilling of the Long Valley Exploratory Well (LVEW) on the resurgent dome in the 760 ka Long Valley Caldera opened a window to view the geologic history of the central caldera. Stratigraphic relationships indicate piston/cylinder (Valles-type) collapse for this caldera, and a resurgent structure intimately linked to post-caldera-collapse rhyolitic intrusions. Samples recovered from this and other wells proximal to the resurgent dome were characterized through isotope microanalytical techniques, petrographic and microprobe study, and analysis of fluid inclusions within alteration minerals. This work revealed the complexity of primary magmatic and secondary hydrothermal activity involved in the formation of a resurgent dome.

Measurements of the  $\delta^{18}\text{O}$  composition of silicate components forming the intracaldera lithologies display disequilibrium within samples as a result of variable exchange with hydrothermal fluids. A maximum calculated temperature of  $350^\circ\text{C}$  at 1800 m depth in LVEW indicates paleohydrothermal temperatures exceeded the known present-day hydrothermal conditions by more than  $100^\circ\text{C}$ . Contouring of  $\delta^{18}\text{O}$  values from wells on a line crossing the caldera define a pattern of convective flow with upwelling beneath the resurgent dome. Although surface volcanism at the LVEW site ended about 650 ka, laser probe  $^{40}\text{Ar}/^{39}\text{Ar}$  microanalysis of samples from sill-like intrusions into the intracaldera ignimbrite reveals intrusive events at ~650 ka, ~450 ka,

and ~350 ka. Sanidine phenocrysts from the Bishop Tuff at 1772 and 1792 m depths and whole rock samples of the Mesozoic metavolcanic basement rocks at 1957 m depth record times of disturbance by hydrothermal pulses at ~530 ka and ~350 ka.

Repeated emplacement of intrusions into the centrally located caldera ignimbrite was a primary process of resurgence. In turn, the feeders for the intrusions and the intrusions themselves supplied heat for resurgent-dome-centered hydrothermal flow. After approximately 300 ka, all activity shut off in the central caldera only to resume at ~40 ka in response to renewed Holocene volcanic activity in the West Moat. Geophysical evidence of recent intrusive activity beneath the resurgent dome indicates this shallow magma emplacement mechanism is not totally extinct in the central caldera. Most likely a new cycle of volcanism and hydrothermal circulation is underway as the caldera matures.

## TABLE OF CONTENTS

LIST OF FIGURES.....	vii
LIST OF TABLES.....	viii
ACKNOWLEDGEMENTS.....	ix
I.1 INTRODUCTION.....	1
I.2 REFERENCES.....	4
II.1 RHYOLITE INTRUSIONS IN THE INTRACALDERA BISHOP TUFF, LONG VALLEY CALDERA, CALIFORNIA.....	5
II.2 ABSTRACT.....	5
II.3 INTRODUCTION.....	7
II.3.1 <i>Geologic setting</i> .....	8
II.4 METHODS.....	11
II.4.1 <i>Sampling</i> .....	11
II.4.2 <i>Analytical techniques</i> .....	13
II.5 DISCUSSION OF RESULTS.....	15
II.5.1 <i>Petrology of Long Valley Exploratory Well and the resurgent dome</i> .....	15
II.5.2 <i>Relationship of Intrusions to Early Rhyolite volcanism</i> .....	20
II.5.3 <i>Chemical Alteration</i> .....	22
II.5.4 <i>Chemical Mass Balance</i> .....	23
II.5.5 <i>Oxygen Isotopes</i> .....	26
II.5.6 <i><sup>40</sup>Ar/<sup>39</sup>Ar Age Determinations</i> .....	29
II.6 DISCUSSION AND CONCLUSIONS.....	30
II.7 ACKNOWLEDGEMENTS.....	33
II.8 REFERENCES.....	51
III.1 OXYGEN ISOTOPE COMPOSITIONS OF INTRACALDERA ROCKS: HYDROTHERMAL HISTORY OF THE LONG VALLEY CALDERA, CALIFORNIA.....	58
III.2 ABSTRACT.....	58
III.3 INTRODUCTION.....	60
III.3.1 <i>Geologic Setting</i> .....	63
III.3.2 <i>Hydrothermal History</i> .....	65
III.3.3 <i>Previous oxygen isotope studies</i> .....	67
III.4 SAMPLE SELECTION AND PREPARATION.....	69
III.5 DATA COLLECTION, STANDARDIZATION, AND ANALYTICAL PRECISION.....	71
III.6 RESULTS.....	74
III.6.1 <i>Long Valley Exploratory Well (LVEW)</i> .....	74
III.6.2 <i>LV13-26</i> .....	79
III.6.3 <i>Other wells</i> .....	80
III.7 DISCUSSION.....	82
III.7.1 <i>Did the intracaldera volcanic rocks reach equilibrium exchange with the hydrothermal water?</i> .....	82
III.7.2 <i>What was the temperature range of the hydrothermal fluid?</i> .....	85
III.7.3 <i>What was the path of the hydrothermal flux?</i> .....	90
III.7.4 <i>Where was the source of the heat and when was it present?</i> .....	92
III.8 SUMMARY.....	93
III.9 ACKNOWLEDGEMENTS.....	95
III.10 REFERENCES.....	117



<b>IV.1 AGE CORRELATIONS IN INTRACALDERA ROCKS FROM LONG VALLEY CALDERA, CALIFORNIA: IMPLICATIONS OF INTRUSION, RESURGENCE, AND HYDROTHERMAL PULSES .....</b>	<b>124</b>
IV.2 ABSTRACT.....	124
IV.3 INTRODUCTION.....	126
IV.4 SAMPLING AND ANALYSES.....	127
IV.4.1 For $^{40}\text{Ar}/^{39}\text{Ar}$ .....	128
IV.4.2 For $^{87}\text{Sr}/^{86}\text{Sr}$ .....	129
IV.4.3 For Fluid Inclusion Analysis .....	130
IV.5 DISCUSSION OF RESULTS.....	130
IV.5.1 Laser probe vs. bulk step heating techniques for $^{40}\text{Ar}/^{39}\text{Ar}$ dating of altered rocks..	130
IV.5.2 $^{40}\text{Ar}/^{39}\text{Ar}$ age determinations of samples and Sr and O isotopes .....	132
IV.5.3 Fluid inclusion study and Sr isotopes in calcite.....	138
IV.6 CONCLUSIONS.....	141
IV.7 ACKNOWLEDGEMENTS.....	144
IV.8 REFERENCES .....	155
<b>V.1 CONCLUSIONS.....</b>	<b>159</b>
V.1.2 REFERENCES.....	162
<b>APPENDIX I. STRATIGRAPHY DIAGRAMS FOR LVEW.....</b>	<b>164</b>
<b>APPENDIX II. FELDSPAR PHENOCRYST COMPOSITIONS IN INTRACALDERA BISHOP TUFF .....</b>	<b>171</b>
<b>APPENDIX III. COMPARISON OF TECHNIQUES FOR WHOLE-ROCK <math>\delta^{18}\text{O}</math> ANALYSIS .....</b>	<b>203</b>
AIII.1 CONVENTIONAL VS. LASER ANALYSIS OF WHOLE ROCK AND PUMICE SAMPLES .....	207
AIII.2 WATER MEASUREMENTS OF SAMPLES.....	209
<b>APPENDIX IV. <math>^{40}\text{Ar}/^{39}\text{Ar}</math> DATA FROM LASER PROBE ANALYSIS.....</b>	<b>217</b>
<b>APPENDIX V. Sr ISOTOPE MEASUREMENTS AND RELATED TRACE ELEMENT CONCENTRATIONS.....</b>	<b>236</b>

## LIST OF FIGURES

Figure II.1 Sketch map of Long Valley Caldera and resurgent dome.....	35
Figure II.2 Stratigraphy of the Long Valley Exploratory Well.....	36
Figure II.3A Photograph of boxed core with intrusion into the Bishop Tuff. ....	37
Figure II.3B Photomicrograph of Bishop Tuff at 914 m.....	38
Figure II.3C Photomicrograph of an Early Rhyolite intrusion at 1263 m.....	38
Figure II.4A Comparison of Ba/Sr ratios in intracaldera rhyolite rocks. ....	39
Figure II.4B Spider diagram for major, trace, and rare earth elements.....	40
Figure II.5 Major oxide and $\delta^{18}\text{O}$ values in the <i>shallow</i> Early Rhyolite intrusion. ....	41
Figure II.6 Isocon diagrams for alteration assemblages.....	42
Figure II.7 Measured and calculated $\delta^{18}\text{O}_{\text{WT}}$ values.....	43
Figure III.1 Generalized geologic map of Long Valley Caldera. ....	97
Figure III.2 Major stratigraphic units in LVEW with alteration mineralogy. ....	98
Figure III.3a Oxygen isotope compositions of silicate components in LVEW lithologies.....	99
Figure III.3b Profiles of paleogeothermal gradients in LVEW.....	100
Figure III.4a Oxygen isotope compositions of silicate components in LV13-26.....	101
Figure III.4b Profile of paleogeothermal gradient in LV13-26.....	102
Figure III.5a Oxygen isotope compositions of silicate components in LV13-21.....	103
Figure III.5b Profile of paleogeothermal gradient in LV13-21.....	104
Figure III.6 Oxygen isotope compositions of silicate components in remaining wells.....	105
Figure III.7 Interpretative cross-section of Long Valley Caldera with oxygen isotope isopleths.....	106
Figure IV.1 Ages determined by bulk step heating and laser probe.....	146
Figure IV.2 Comparison of multiple age series of Early Rhyolite samples.....	147
Figure IV.3 Location of dated samples in LVEW.....	148
Figure IV.4 Age spectra for laser probe analysis of Paleozoic metasediments.....	149
Figure IV.5 Salinity vs. Temperature of Homogenization (Th).....	150
Figure IV.6 Temperature of homogenization of fluid inclusion plotted to depth in LVEW. ....	151
Figure AI.1 Detailed Stratigraphy of LVEW.....	164
Figure AI.2 Core sampling locations in LVEW.....	169
Figure AI.3 Cored section of <i>Shallow</i> Early Rhyolite intrusion. ....	170
Figure AIII.1 Comparison of analytical techniques using whole-rock samples.....	212
Figure AIII.2a Comparison of conventional extraction analysis.....	213
Figure AIII.2b Comparison of laser-probe and reaction vessel extraction analysis.....	214
Figure AIII.3 Total water content of volcanic rocks versus oxygen isotope differences.....	215

## LIST OF TABLES

Table II.1 Major and trace element chemistry of Early Rhyolite samples.....	44
Table II.2 $^{40}\text{Ar}/^{39}\text{Ar}$ ages for whole rock samples dated in 1992.....	50
Table III.1 Oxygen isotope values of silicate components in intracaldera lithologies.....	108
Table III.2 Fluid inclusion temperatures and equilibrium $\delta^{18}\text{O}(\text{H}_2\text{O})$ calculations .....	114
Table III.3 Chronology of central caldera volcanic and hydrothermal activity.....	115
Table IV.1 Isotopic values of selected samples. ....	152
Table IV.2 Fluid inclusion values and $^{87}\text{Sr}/^{86}\text{Sr}$ compositions.....	154
Table AII.1 Feldspar compositions: electron microprobe analyses .....	171
Table AIII.1 Comparative data from conventional and laser-probe extraction methods....	216
Table AIV.1 $^{40}\text{Ar}/^{39}\text{Ar}$ age data.....	217
Table AV.1 Sr isotope values for intracaldera rocks and extrusive equivalents.....	236
Table AV.2 Sr isotope concentration in alteration calcite in LVEW.....	237

## ACKNOWLEDGEMENTS

It is not possible to accomplish this type of task alone; neither scientific research nor humans exist in a vacuum. I have had much professional support both as funding and as collaboration. Primary funding for geologic work came from the Department of Energy Office of Basic Energy Science and the Geothermal Department of Sandia National Laboratories, Albuquerque, New Mexico. This part of the work was closely monitored by my advisor, Dr. John C. Eichelberger, and geochemical analysis and collaboration were conducted with Dr. Charles Shearer, University of New Mexico. Additional funding by the Office of Basic Energy Science of a proposal written by Dr. John W. Valley, University of Wisconsin allowed me to pursue the oxygen isotope study under the auspices of Dr. Valley at the University of Wisconsin. The strontium isotope study, conducted at the University of Berkeley's Center for Isotope Geochemistry, was funded by an American Western Universities Thesis Parts Fellowship. I thank Dr. Harold Wollenberg and Dr. Don DePaolo for sponsoring my endeavors there. Finally, I have the University of Alaska Fairbanks and the Geophysical Institute to thank for support in the forms of teaching and research assistantships during the final throes of completion.

I take this opportunity to publicly acknowledge the excellent graduate students I have encountered along the way at all the institutes mentioned above, their interest, provocative conversations, and good humor made many a day shine. Thanks is also extended to my advisory committee, Dr. Mary J. Keskinen, Terry E.C. Keith, and Dr. Paul W. Layer, a fine group of scientists

and wonderful friends. To my mentor and friend, Dr. John C. Eichelberger, who talked me into this and guided me throughout, I am eternally grateful.

On a personal note, I have been blessed with friends and family whose belief in me is much of the time stronger than my belief in myself. Thank you all, forever.

“Out of chaos comes order, sorta”



Oct. 4, 1995

Graduate School  
305 Signer's Hall  
PO Box 757560.  
University of Alaska Fairbanks  
Fairbanks, AK 99775-7560

To whom it may concern,

I, the undersigned, do grant Vicki S. McConnell permission to include the co-authored journal article as part of her dissertation undertaken to fulfill partial requirements for a Ph.D. in Geology at the University of Alaska Fairbanks. The references of said articles are:

McConnell, V.S., C.K. Shearer, J.C. Eichelberger, M.J. Keskinen, P.W. Layer, and J.J. Papike, 1995. Rhyolite intrusions in the intracaldera Bishop Tuff, Long Valley Caldera, California, *J. Volcanol. Geotherm. Res.*, (in press).

McConnell, V.S., J.W. Valley, and J.C. Eichelberger, 1995. Oxygen isotope compositions of intracaldera rocks reveal the hydrothermal history of the Long Valley Caldera, California, prepared for submission in *J. Volcanol. Geotherm. Res.*

Mary J. Keskinen  
Co-author's signature

10.6.95

Date

Geophysical Institute, University of Alaska  
Fairbanks, Alaska 99775-0800

PHONE: 907-474-7558    TELEX: 354140 GEOPH INST FBK  
FAX: 907-474-7290    TELEMAIL: GEOPH.INST.FBK

Established by Act of Congress, dedicated to the maintenance of geophysical research concerning the Arctic regions.



Oct. 4, 1995

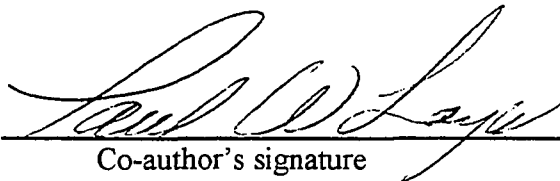
Graduate School  
305 Signer's Hall  
PO Box 757560.  
University of Alaska Fairbanks  
Fairbanks, AK 99775-7560

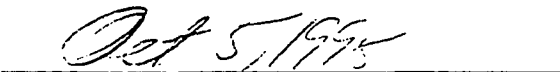
To whom it may concern,

I, the undersigned, do grant Vicki S. McConnell permission to include the co-authored journal article as part of her dissertation undertaken to fulfill partial requirements for a Ph.D. in Geology at the University of Alaska Fairbanks. The references of said articles are:

McConnell, V.S., C.K. Shearer, J.C. Eichelberger, M.J. Keskinen, P.W. Layer, and J.J. Papike, 1995. Rhyolite intrusions in the intracaldera Bishop Tuff, Long Valley Caldera, California, *J. Volcanol. Geotherm. Res.*, (in press).

McConnell, V.S., J.W. Valley, and J.C. Eichelberger, 1995. Oxygen isotope compositions of intracaldera rocks reveal the hydrothermal history of the Long Valley Caldera, California, prepared for submission in *J. Volcanol. Geotherm. Res.*

  
Co-author's signature

  
Date

Geophysical Institute, University of Alaska  
Fairbanks, Alaska 99775-0800

PHONE: 907-474-7558    TELEX: 354140 GEOPH INST FBK  
FAX: 907-474-7290    TELEMAIL: GEOPH.INST.FBK

Established by Act of Congress, dedicated to the maintenance of geophysical research concerning the Arctic regions.



Oct. 4, 1995

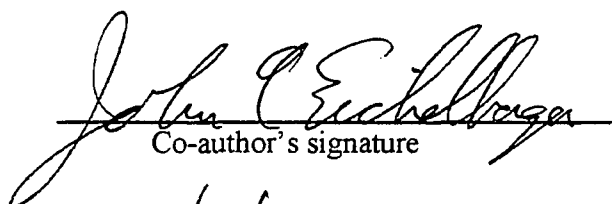
Graduate School  
305 Signer's Hall  
PO Box 757560.  
University of Alaska Fairbanks  
Fairbanks, AK 99775-7560

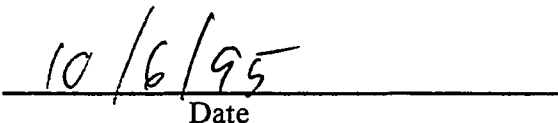
To whom it may concern,

I, the undersigned, do grant Vicki S. McConnell permission to include the co-authored journal article as part of her dissertation undertaken to fulfill partial requirements for a Ph.D. in Geology at the University of Alaska Fairbanks. The references of said articles are:

McConnell, V.S., C.K. Shearer, J.C. Eichelberger, M.J. Keskinen, P.W. Layer, and J.J. Papike, 1995. Rhyolite intrusions in the intracaldera Bishop Tuff, Long Valley Caldera, California, *J. Volcanol. Geotherm. Res.*, (in press).

McConnell, V.S., J.W. Valley, and J.C. Eichelberger, 1995. Oxygen isotope compositions of intracaldera rocks reveal the hydrothermal history of the Long Valley Caldera, California, prepared for submission in *J. Volcanol. Geotherm. Res.*

  
Co-author's signature

  
Date

Geophysical Institute, University of Alaska  
Fairbanks, Alaska 99775-0800

PHONE: 907-474-7558    TELEX: 354140 GEOPH INST FBK  
FAX: 907-474-7290    TELEMAIL: GEOPH.INST.FBK

Established by Act of Congress, dedicated to the maintenance of geophysical research concerning the Arctic regions.





Oct. 4, 1995

Graduate School  
305 Signer's Hall  
PO Box 757560.  
University of Alaska Fairbanks  
Fairbanks, AK 99775-7560

To whom it may concern,

I, the undersigned, do grant Vicki S. McConnell permission to include the co-authored journal article as part of her dissertation undertaken to fulfill partial requirements for a Ph.D. in Geology at the University of Alaska Fairbanks. The references of said articles are:

McConnell, V.S., C.K. Shearer, J.C. Eichelberger, M.J. Keskinen, P.W. Layer, and J.J. Papike, 1995. Rhyolite intrusions in the intracaldera Bishop Tuff, Long Valley Caldera, California, *J. Volcanol. Geotherm. Res.*, (in press).

McConnell, V.S., J.W. Valley, and J.C. Eichelberger, 1995. Oxygen isotope compositions of intracaldera rocks reveal the hydrothermal history of the Long Valley Caldera, California, prepared for submission in *J. Volcanol. Geotherm. Res.*

Co-author's signature

Date

Geophysical Institute, University of Alaska  
Fairbanks, Alaska 99775-0800

PHONE: 907-474-7558    TELEX: 354140 GEOPH INST FBK  
FAX: 907-474-7290    TELEMAIL: GEOPH.INST.FBK

Established by Act of Congress, dedicated to the maintenance of geophysical research concerning the Arctic regions.



Oct. 4, 1995

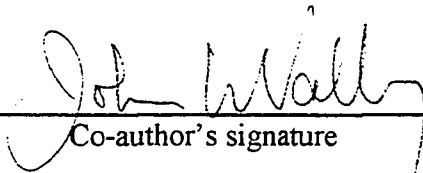
Graduate School  
305 Signer's Hall  
PO Box 757560.  
University of Alaska Fairbanks  
Fairbanks, AK 99775-7560

To whom it may concern,

I, the undersigned, do grant Vicki S. McConnell permission to include the co-authored journal article as part of her dissertation undertaken to fulfill partial requirements for a Ph.D. in Geology at the University of Alaska Fairbanks. The references of said articles are:

McConnell, V.S., C.K. Shearer, J.C. Eichelberger, M.J. Keskinen, P.W. Layer, and J.J. Papike, 1995. Rhyolite intrusions in the intracaldera Bishop Tuff, Long Valley Caldera, California, *J. Volcanol. Geotherm. Res.*, (in press).

McConnell, V.S., J.W. Valley, and J.C. Eichelberger, 1995. Oxygen isotope compositions of intracaldera rocks reveal the hydrothermal history of the Long Valley Caldera, California, prepared for submission in *J. Volcanol. Geotherm. Res.*

  
\_\_\_\_\_  
Co-author's signature

  
\_\_\_\_\_  
Date

Geophysical Institute, University of Alaska  
Fairbanks, Alaska 99775-0800

PHONE: 907-474-7558    TELEX: 354140 GEOPH INST FBK  
FAX: 907-474-7290    TELEMAIL: GEOPH.INST.FBK

Established by Act of Congress, dedicated to the maintenance of geophysical research concerning the Arctic regions.



Oct. 4, 1995

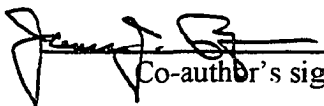
Graduate School  
305 Signer's Hall  
PO Box 757560.  
University of Alaska Fairbanks  
Fairbanks, AK 99775-7560

To whom it may concern,

I, the undersigned, do grant Vicki S. McConnell permission to include the co-authored journal article as part of her dissertation undertaken to fulfill partial requirements for a Ph.D. in Geology at the University of Alaska Fairbanks. The references of said articles are:

McConnell, V.S., C.K. Shearer, J.C. Eichelberger, M.J. Keskinen, P.W. Layer, and J.J. Papike, 1995. Rhyolite intrusions in the intracaldera Bishop Tuff, Long Valley Caldera, California, *J. Volcanol. Geotherm. Res.*, (in press).

McConnell, V.S., J.W. Valley, and J.C. Eichelberger, 1995. Oxygen isotope compositions of intracaldera rocks reveal the hydrothermal history of the Long Valley Caldera, California, prepared for submission in *J. Volcanol. Geotherm. Res.*

 JAMES J. PAPIKE  
Co-author's signature

OCTOBER 10, 1995

Date

Geophysical Institute, University of Alaska  
Fairbanks, Alaska 99775-0800

PHONE: 907-474-7558    TELEX: 354140 GEOPH INST FBK  
FAX: 907-474-7290    TELEMAIL: GEOPH.INST.FBK

Established by Act of Congress, dedicated to the maintenance of geophysical research concerning the Arctic regions.

## I.1 INTRODUCTION

Our understanding of the mechanisms that control the behavior of truly colossal, silicic volcanic centers, such as the Quaternary Long Valley Caldera in east-central California, is limited by the information we can unravel from the buried and frequently altered intracaldera rocks. It is not possible to simultaneously study the plutonic roots of these systems, which require millions of years of erosion to expose, and the caldera, which represents the volcanic surface expression of the system. Thus, crucial information regarding the link between parent magmatic systems and resulting volcanic and hydrothermal activity is lost and must be inferred from study of older systems alone. Yet, eruptions that form calderas represent one of a limited category of catastrophic geologic events that have shaped the earth's surface (Lipman, 1984). Their impact on human endeavors continues through hydrothermal activity, ore deposition, and post-collapse volcanic hazards. It behooves us to develop a better understanding of the history of these systems with an eye to present and future episodes of intrusive and volcanic activity.

Drilling of scientific and exploratory wells in the 760 ka Long Valley Caldera opened a window to view the geologic history of the central caldera while the intracaldera rocks record only the syn- and post-collapse story. A detailed geochemical site characterization conducted on the recovered samples from the well employed isotope microanalytical techniques, a petrographic and microprobe study, and analysis of fluid inclusions within alteration quartz. This work revealed the complex, causal link between episodic primary

magmatic events and secondary hydrothermal activity that is incorporated during post-caldera-collapse resurgence.

This dissertation is divided into three main chapters, each comprised of a journal article manuscript, and is preceded by this explanatory introduction and concluded by a discussion section. The progression of the journal article chapters records the chronology of the study. Thus some interpretations in Chapter II are not repeated exactly in later chapters as more data were compiled and my understanding of the problem increased. In addition, the dissertation emphasizes the work conducted using laser probe techniques for isotope analyses on the altered rocks. While this work was crucial to my interpretations, it is also important to recognize both the usefulness and restrictions of this analytical tool. Appendix III is a discussion of the results of a comparative study between conventional and laser probe extraction techniques for oxygen isotopes.

Chapter II deals primarily with whole-rock geochemistry, including  $\delta^{18}\text{O}$  and  $^{40}\text{Ar}/^{39}\text{Ar}$  age determinations, of samples recovered from LVEW. Included is the work to characterize the primary and alteration mineralization found in the recovered core and cuttings from the resurgent dome wells used in this study. Appendix I displays the stratigraphic diagrams compiled from study of LVEW geophysical and geologic logs, and Appendix II is a compilation of the microprobe analyses conducted on feldspar phenocrysts in the Bishop Tuff. The whole rock analyses showed the resurgent dome area had certainly been exposed to a more vigorous hydrothermal pulse in the past. Moreover, the

sill-like intrusions into the intracaldera Bishop Tuff displayed chemical and petrographic correlation to post-caldera-collapse Early Rhyolite. Yet, the calculated geothermal gradient of  $\sim 70^{\circ}\text{C}/\text{km}$  for the Bishop Tuff was insufficient for near-surface intrusions and the dates determined from whole-rock samples of the intrusions were anomalous for known post-caldera-collapse extrusive events. This work set the direction for the microanalyses that followed.

Chapter III describes the laser-probe/mass spectrometer microanalysis of silicate components from intracaldera lithologies. This work was undertaken with the aim of more precisely characterizing the hydrothermal alteration and quantifying any disequilibrium in the water/rock oxygen isotope exchange of the intracaldera rocks in response to paleohydrothermal systems. Determination of silicate component disequilibria allowed accurate calculation of the dominant temperature regime of the paleohydrothermal fluids from wells across the caldera. Contouring of  $\delta^{18}\text{O}$  isotopes across the resurgent dome revealed the effects of free convective circulation that operated in the central caldera area in the past.

Chapter IV introduces  $^{40}\text{Ar}/^{39}\text{Ar}$  microanalyses of the same materials in order to place age constraints on the evolution of intrusion, resurgence, and hydrothermal pulses. Modal analysis of the distribution of dates determined for the Early Rhyolite samples in LVEW are interpreted as indicating times of post-caldera-collapse intrusive events. Dates determined from intracaldera lithologies with well constrained ages, such as the Bishop Tuff and the

Mesozoic metavolcanic rocks, are interpreted as indicating times of post-caldera-collapse hydrothermal activity. The correlation of the times of intrusion to hydrothermal activity leads to the conclusion that there is a causal link between the events. Appendix IV records the geochronological data used for the interpretations. In addition, the results of measuring the  $^{87}\text{Sr}/^{86}\text{Sr}$  ratios of alteration calcite and host rocks throughout the caldera and analyses of fluid inclusions in hydrothermal vein quartz and calcite are discussed. This work was undertaken to determine the composition and path of the paleohydrothermal fluids. Appendix V is a compilation of the data collected from the strontium isotope study.

## I.2 REFERENCES

- Lipman, P.W., 1984. The roots of ash flow calderas in Western North America: windows into the tops of granitic batholiths. *J. Geophys. Res.*,89:B10:8801-8841.

## **II.1 Rhyolite intrusions in the intracaldera Bishop Tuff, Long Valley Caldera, California<sup>1</sup>**

### II.2 ABSTRACT

Drilling of the Long Valley Exploratory Well on the resurgent dome in the Long Valley Caldera revealed >300 m cumulative thickness of granophyric intrusions within the 1180 m thick, 760 ka intracaldera Bishop Tuff. The intrusions are aphyric to sparsely plagioclase-phyric, high-silica, high-barium, and low-strontium rhyolites. They resemble the lavas of the Early Rhyolite, the first phase of post-caldera volcanism. A mean  $^{40}\text{Ar}/^{39}\text{Ar}$  age of  $590 \pm 17$  ka from a part of a shallow intrusion is coeval with Early Rhyolite volcanism. A second mean age of  $454 \pm 17$  ka from the same intrusion may reflect either younger Early Rhyolite activity with no external equivalent or hydrothermal resetting of the argon system.

Hydrothermal alteration of the intrusions is characterized by introduction of quartz, calcite and pyrite and formation of illite/smectite. High  $\text{CO}_2$  content of fluids apparently inhibited zeolite formation. Alteration varies locally within intrusions and intrusive groups and does not vary systematically with depth.

Oxygen shows consistent depletion of the  $^{18}\text{O}$  isotope from an initial

---

<sup>1</sup> Rhyolite intrusions in the intracaldera Bishop Tuff, Long Valley Caldera, California by V.S. McConnell, C.K. Shearer, J.C. Eichelberger, M.J. Keskinen, P.W. Layer, J.J. Papike in *J. Volcanol. Geotherm. Res.*, v. 67, pp. 41-60, 1995.



magmatic composition of +6.0 to +8.5‰ to values ranging from +1.4 to -0.4‰. The constant oxygen isotope depletion most likely reflects alteration of intrusions due to local emplacement-induced hydrothermal circulation rather than a caldera-scale hydrothermal system. In contrast,  $^{18}\text{O}$  depletion of the host Bishop Tuff increases regularly with depth (except at an intrusive contact). A pre-Early Rhyolite geothermal gradient of approximately 70°C/km was inferred. This is substantially higher than the current gradient but substantially lower than expected for the case of a conductive regime over a shallow residual magma chamber. Either the intrusions were fed from a deep chamber, or a cool hydrologic recharge regime was established early in caldera history.

The age, thickness, and suspected lateral extent of these shallow intrusions are such that emplacement of the intrusions, rather than inflation of a shallow chamber, is responsible for resurgence of the central Long Valley Caldera. Similar intrusions occur in another well on the resurgent dome (LV13-21) but not in wells located off the dome.

### II.3 INTRODUCTION

The Long Valley Caldera, located in east-central California (Figure II.1), has been the locus of numerous studies to understand the relationship between a large crustal magma chamber and its associated hydrothermal circulation (Muffler and Williams, 1976; Blackwell, 1985; Shevenell et al., 1987; Suemnicht and Varga, 1988; Sorey et al., 1991; Flexer, 1991). This interest intensified in the early 1980's when seismic activity began increasing in the south moat of the caldera and in the high Sierra to the south. At the same time renewed inflation in the central caldera uplifted the resurgent dome by >0.5 m, and lateral extension across it of up to 3-5 microstrain/yr was observed (Hill et al., 1985). Workers interpret this activity as indicating injection of 0.15-0.20 km<sup>3</sup> of magma at a depth of <10 km beneath the dome (Savage and Clark, 1982; Hill et al., 1985; Rundle and Hill, 1988). A deep drill hole located on the resurgent dome provides a test of this interpretation as well as an opportunity to sample through the intracaldera fill and perhaps the crystallized carapace of the magma chamber. The Long Valley Exploratory Well (LVEW) was designed to open a window into the central intracaldera region (Long Valley Science Panel, 1991). Drilling proceeded in two phases and intersected post-collapse Early Rhyolite and intracaldera Bishop Tuff, and bottomed in precaldera metamorphic rocks. The metamorphic rocks are correlated to the hornfels of the Mt. Morrison roof pendant of the Sierran batholith (Rinehart and Ross, 1964). Cuttings, core, and downhole geophysical

logging data were made available for this current study. At a total depth of 2.3 km, the well is short of its 6-km design depth but nevertheless within new territory in the central caldera. The well is relatively cool, with a bottom hole temperature of 103°C and a geothermal gradient of approximately 50°C/km (Sass et al., 1991).

In addition to the three main lithologies, we identified numerous rhyolite intrusions into the Bishop Tuff. These intrusions are important, previously unrecognized units of significance to the structural and thermal history of the Long Valley Caldera. Furthermore, to the extent the original magmatic composition can be established, the intrusions identified from wells on the resurgent dome will offer important clues to fluid transport within the central caldera regime.

### *II.3.1 Geologic setting*

Volcanism in Long Valley began 3-4 Ma and culminated approximately 760 ka in the eruption of the Bishop Tuff. This eruption promoted the collapse of the Long Valley Caldera along arcuate fractures formed in response to magma upwelling (Bailey et al., 1976; Izett and Obradovich, 1991). Initial explosive Plinian ash eruptions are thought to have issued from a single vent along the south-central caldera ring fracture (Figure II.1; Hildreth and Mahood, 1986), distributing up to 300 km<sup>3</sup> of ash from the eastern Pacific Ocean to the Great Plains of Nebraska. Proximal ash deposits were rapidly buried beneath subsequent voluminous ash flows that formed the Bishop Tuff. Eruptions from

multiple vents along the ring fractures spread two lobes of pyroclastic flows of approximately 100 - 200 km<sup>3</sup> in total volume. Syn-eruptive subsidence also allowed the Bishop ash flows to fill the caldera to a depth of as much as 1500 m. As much as two-thirds of the Bishop Tuff flows are thought to have ponded over the 2-3 km deep collapsed roof of the magma chamber (Bailey et al., 1976). This intracaldera Bishop Tuff was buried by post-caldera lavas, tuff, and sediments. The elevation of the buried Bishop Tuff surfaces within the caldera is substantially lower than the elevation of the top of the outflow sheets, implying some post-eruptive collapse of the caldera (Bailey et al., 1976; Eichelberger and McConnell, 1990). Data from wells in the caldera have clarified the geometry of the intracaldera pyroclastic deposits (Suemnicht and Varga, 1988). Comparison of the thickness of this unit across the caldera reveals a wedge-shaped block that thickens from west to east by as much as 1000 m. Variable top and bottom contacts of intracaldera Bishop Tuff imply much pre-emplacment relief and post-caldera faulting. We re-evaluated the total volume of the intracaldera tuff by using measured thicknesses and a simple geometric model with a wedge-shaped taper for the Bishop Tuff. We calculate an estimate of 340 km<sup>3</sup> for the volume of the intracaldera Bishop Tuff. Thus, the total volume for the Bishop Tuff in outflow sheets and intracaldera units approaches 600 km<sup>3</sup>, and the entire eruptive sequence has a volume of 840 km<sup>3</sup>. This converts to approximately 600 km<sup>3</sup> of a dense rock equivalent and is very similar to estimates for the eruptive volume based on geologic mapping of outcrops by R.L. Smith and R.A. Bailey (Bailey et al., 1976).

Intermittent post-caldera-collapse igneous activity formed a 10-km-diameter, 500-m-high resurgent dome and covered the caldera floor with rhyolitic lavas and tuffs. Two major episodes of rhyolitic volcanic activity occurred. The 730 to 600 ka aphyric to sparsely porphyritic Early Rhyolite is considered coeval with resurgence. Early Rhyolite on the resurgent dome flowed radially away from a central uplift and is tilted radially outward by as much as 30° (Bailey et al., 1976). This structure coupled with the observation that the dome formed an island in the now drained caldera lake is interpreted as resulting from positive central uplift and not collapse in the moat (Bailey et al., 1976). Early Rhyolite volcanism was followed by the 500 to 100 ka phenocryst-rich Moat Rhyolite flows (Bailey et al., 1976; Bailey, 1989).

Volcanism from 200 to 60 ka in the west moat spilled basaltic lava that ponded to a depth of 250 m (Bailey, 1989). Associated intermittent low-silica rhyolites and dacites erupted from local vents in the west moat and also formed the Mammoth Mountain cumulo volcano along the southwest caldera rim (Bailey, 1989). Felsic volcanic activity resumed in the Long Valley area between 40 and 38 ka with the emplacement of the Mono Craters north of the caldera (Bailey, 1989). This continued with the emplacement of the 0.65-0.55 ka Inyo chain rhyolite domes and craters that intersect the caldera in the northwest moat (Miller, 1985).

Bailey et al. (1976) and Sorey (1985) suggest that the caldera hydrothermal system has been active intermittently for at least the past 300 ka. Sorey et al. (1991) reported  $^{230}\text{Th}/^{234}\text{U}$  isotopic ages determined for hot-

spring deposits. These support a hypothesis of two periods of hot-water discharge within the caldera, with one peaking approximately 300 ka and the other beginning about 40 ka and continuing through the present. They postulated the present-day hydrothermal system has its heat source deep below the caldera's west moat where the most recent volcanic activity has occurred. In Well 44-16 in the west moat (Figure II.1), maximum downhole temperatures of 214°C at a depth of 1000 m in Bishop Tuff and 190°C at a depth of 1490 m in Tertiary pre-caldera andesite were measured (Suemnicht, 1987). It is inferred that volcanic fill in the caldera provides a lateral flow zone for geothermal fluids from the west moat to the surface on or near the resurgent dome (Shevenell et al., 1987; Sorey et al., 1991). Recent interpretations of oxygen isotopic data for intracaldera volcanics by Smith and Suemnicht (1991) suggest that hydrothermal activity beneath the resurgent dome occurred as early as 500 ka and was driven by post-caldera rhyolitic intrusions into the resurgent dome. We suggest that both resurgence and hydrothermal alteration in the central Long Valley Caldera are due to emplacement of post-caldera intrusions.

## II.4 METHODS

### *II.4.1 Sampling*

Well cuttings, limited intervals of spot and continuous core, and 26 sidewall cores compose the sample suite provided by Long Valley Exploratory

Well. In addition, outcrop samples from pre- to post-caldera-collapse volcanic rocks and metamorphic basement rocks were collected for comparison. Roy A. Bailey of the U.S.G.S. provided sample splits and oxide and trace element data (See Table II.1) of Early Rhyolite obsidians from his outcrop sample suite. He also provided information on the petrographic and geochemical nature of the post-caldera-collapse rhyolite units of the Long Valley Caldera. Other wells discussed in this paper were reviewed and logged by Vicki S. McConnell at the US DOE Core Repository in Grand Junction, Colorado.

Thin sections were made at intervals throughout the total depth of Long Valley Exploratory Well and at intervals of interest in other resurgent dome wells. A smaller suite of intrusive and Bishop Tuff samples from core and cuttings from Long Valley Exploratory Well were chosen for more detailed geochemical studies. This in-depth study focused on samples from a *shallow* (766-811 m), an *intermediate* (1189-1295 m) and a *deep* (1509-1548 m) intrusion and from intervening Bishop Tuff. The *shallow* intrusion was continuously cored from 780-811 m and this interval is sampled in detail.

Well cuttings were first rinsed of drilling mud contamination, dried in a low-temperature (<90°C) drying oven, and then hand-picked for analysis. Because the cuttings were collected over intervals of 10 ft.-20 ft., the vertical error in determining sample depth locations and contacts could be as great as 20 ft. In addition, some lithologic contamination occurs in cuttings samples from sloughing in the well. Care was taken to reduce the error associated with such contamination by a detailed study of the cuttings and well logs prior to choosing representative samples.

#### *II.4.2 Analytical techniques*

Major and minor element analyses of the intrusion samples were conducted at the University of New Mexico using a Rigaku 364m X-ray fluorescence spectrometer (XRF). Samples were prepared for XRF by fusing one gram of sample, 9 grams of lithium tetraborate, and 0.1 gram of ammonium nitrate in a Pt-Au crucible at 1000°C for 15 minutes. The fused sample was then poured into a Pt-Au mold.

Trace element analyses were performed using several different analytical techniques. These include the INAA at the Oregon State University; atomic absorption (AA) at Battelle National Laboratory, Richland, Washington and the South Dakota School of Mines and Technology; and inductively coupled plasma-mass spectrometry (VG PQ2 ICP-MS) at Battelle National Laboratory and the University of New Mexico.

Mineral phases, igneous textures, and the presence of clay minerals were initially determined petrographically and subsequently verified by X-ray diffractometry (XRD) at University of Alaska Fairbanks. Whole-rock samples were disaggregated by mortar and pestle, then sieved. The <200  $\mu\text{m}$  fraction was prepared as bulk, randomly oriented samples on glass slides. Samples were run on a Rigaku diffractometer, with Ni-filtered CuK $\alpha$  radiation, at 30 kV. Bulk sample scans were run over a range of 70 to 3° 2 $\theta$  using a scan rate of 1° 2 $\theta$ /min.



The 250 to 150  $\mu\text{m}$  size fraction from the whole-rock splits was used for oxygen isotope analyses. The samples were analyzed at Geochron Laboratories Division of Krueger Enterprises by the standard  $\text{BrF}_5$  technique. Data are reported as  $\delta^{18}\text{O}$  relative to SMOW. Analytical precision for  $\delta$ -values is about  $\pm 0.1\text{‰}$ .

$^{40}\text{Ar}/^{39}\text{Ar}$  dating was done on whole rock samples from the intrusions, on a sample of obsidian from a surface exposure of Early Rhyolite, and on sanidine mineral separates of relatively unaltered Bishop Tuff. Step heating analyses were done using a resistance-heating furnace connected on-line to a computer-controlled Nuclide 6-60-SGA mass spectrometer located at the Geophysical Institute, University of Alaska Fairbanks. For whole-rock samples, a 1.0 to 0.5 mm size fraction was rinsed with deionized water, fines and organics removed by ultrasonic disaggregation and decanting, and placed in a drying oven at  $<90^\circ\text{C}$  overnight. Samples and standards were irradiated for 2 MWh at the McMaster Nuclear Reactor, Hamilton, Ontario. Analyses are reported relative to the Bern 4B biotite standard with an age of 17.25 Ma. Ages were calculated using the constants of Steiger and Jäger (1977), and uncertainties are reported as  $\pm 1\sigma$ .

## II.5 DISCUSSION OF RESULTS

### *II.5.1 Petrology of Long Valley Exploratory Well and the resurgent dome*

Stratigraphic contacts in the Long Valley Exploratory Well were determined from core samples when possible. For non-cored intervals of the well, contacts were inferred from changes in apparent abundance of lithologies and interpretation of standard e-logs and televiewer logs. The lithology of the resurgent dome and the central intracaldera fill consists of three primary units: Early Rhyolite flows and tuffs (Qer/Qef), intracaldera Bishop Tuff (Qbt), and metamorphic basement rocks (Figure I.2).

The top 622 m of the well consists of post-caldera-collapse Early Rhyolite units. They are dense, microlite-rich obsidian and flow-banded lithoidal rhyolite and thick tuffs. The tuffs consist of fresh, vesicular pumice and vitric, welded tuffs which contain pyroxene and plagioclase phenocrysts. Vesicles in pumice lapilli vary from rounded, to flattened and elongate. The welded tuffs are lithic-poor and rarely devitrified. Vents for the tuffs have not been identified. The obsidian and rhyolite, however, have been correlated with microlite-rich obsidian and flow-banded rhyolite flows from a vent located <1 km to the east of the Long Valley Exploratory Well drill site. The rocks from this vent were designated by Bailey (1974 and pers. comm., 1992) as part of the pyroxene-bearing Early Rhyolite subunit. The Early Rhyolite in Long Valley Exploratory Well and in the next nearest well, LV13-21, is not intensely hydrothermally altered. This is in contrast to the altered condition of the Early

Rhyolite in the wells along the east and west flanks of the resurgent dome graben (Figure II.1).

Crystal-rich, welded, and devitrified Bishop Tuff underlies the Early Rhyolite units in the well. The intracaldera Bishop Tuff varies from gray to white and is densely welded throughout its 1178 m thickness. Some relict pumice is present as fiamme. The phenocrysts consist of dipyrmidal quartz up to 4 mm in diameter and quartz fragments, sanidine, plagioclase, biotite, titanomagnetite, ilmenite, zircon, and apatite in order of decreasing abundance. The sanidine is generally subhedral and ranges from 1-3 mm in diameter. Euhedral plagioclase varies from 0.1 mm to 2 mm in diameter and in abundance. Plagioclase becomes almost entirely replaced by calcite below 1000 m depth. Biotite phenocrysts are small, <1 mm, frequently altered to white mica, chlorite, and pyrite and rarely appear below 1340 m. Titanomagnetite and ilmenite are usually altered to rutile. Connolly et al. (1991) and this paper report the presence of rare allanite phenocrysts in the Bishop Tuff in Phase I core (622-839 m). Hildreth (1979) reported allanite to be more abundant in the lower temperature, early-erupted Bishop Tuff. This would suggest thick, early deposition of the intracaldera tuff, though absence of late Bishop Tuff would be difficult to explain. If late Bishop Tuff is absent, then most syn-eruptive collapse of the caldera block occurred soon after the change from Plinian to Pelean eruptions. Primary pyroclastic textures throughout the entire thickness of tuff are obscured by intense post-emplacement crystallization and devitrification dominated by spherulitic and axiolitic structures. This texture has, in turn, been overprinted by a secondary mosaic

of anhedral quartz, calcite, and authigenic clays. Disseminated, euhedral pyrite occurs throughout the matrix, and fractures in the tuff are filled with quartz, calcite, and pyrite.

The well intersects highly chloritized and altered metavolcanic rock at 1891 m. This unit is correlated to Mesozoic metavolcanics of the Mt. Morrison roof pendant of the Sierran batholith and marks the contact between intracaldera collapse units and pre-caldera basement rocks. Below 2025 m the basement rock changes to banded hornfels with minor interbedded metaquartzite and marble. The types of hornfels range from silicic to pelitic with minor calcic layers but are dominated by very fine-grained silicic, graphitic hornfels. We determine these rocks to represent Paleozoic metasediments of the Mt. Morrison roof pendant. The entire basement sequence is highly fractured, and several generations of fracturing can be delineated by changes in fracture orientation, fracture fill, and cross-cutting and offset of the primary banding. Most fractures contain varying ratios of quartz, calcite, and pyrite. Disseminated euhedral to anhedral pyrite is common to all units. Altered and metamorphosed igneous intrusions of yet-to-be-determined age have been identified in the hornfels.

A remarkable well-indurated epiclastic breccia 90 m thick occurs between the intracaldera tuff and the metavolcanic basement rock. This crudely graded and bedded breccia is poorly sorted, consisting of angular clasts as large as 7 cm of basement metasediments and unidentified volcanic rock in a matrix of very fine-grained clastic material and calcite. The unit is of undetermined age and origin. Its occurrence has neither been recognized in

lithic fragments in the Bishop Tuff outflow sheets (W. Hildreth. pers. comm. and G. Mahood. pers. comm., 1991) nor in the intracaldera tuff. We do not consider this unit to be part of the metamorphic basement. A similar unit was identified in core from well LV68-28, located 4.2 km southeast of Long Valley Exploratory Well. In that well the unit sharply contacts the basal ashfall of the Early Rhyolite and the top of the Bishop Tuff. Although these units cannot be correlated, they may represent a similar origin and depositional environment. Most likely such units are the result of local debris-flow deposits mobilized by caldera wall slumping and collapse.

A final important lithology is the main topic of this study. It consists of several discrete intervals of aphyric- to sparsely-porphyrific and aphanitic rhyolite intrusions into the Bishop Tuff. The individual units are horizontal in cored intervals and recognized by the brecciated and occasionally glassy nature of their contacts with Bishop Tuff (Figure II.3A). They are more difficult to recognize in cuttings and must be distinguished by their coarser granophyric texture, paucity of phenocrysts, and, in shallower intrusions, the presence of glass cuttings. All intrusions have secondary quartz and calcite in the matrix and filling elongate vesicles, as well as calcite and clay minerals replacing feldspar phenocrysts (Figure II.3C).

The intrusions vary in logged interval thickness from less than 1 m to 100 m with a cumulative thickness of 330 m, or 28% of the intracaldera tuff interval assuming horizontal contacts. Structurally, this thickness could account for the majority of the dome resurgence if all the units are subhorizontal and laterally extensive. Similar aphyric and aphanitic rocks

were identified in thin sections of the Bishop Tuff interval of LV13-21 (Figure II.1). They occur in cuttings from depth intervals of 701 and 732 m. In this well, the fine-grained rock cuttings also contain clasts of fresh, microlite-rich obsidian. However, identification of the intrusions from cuttings alone is difficult and determination of the exact geometry of the unit(s) in the subsurface is not possible.

Seven other wells were petrographically logged as part of this study; LV34-29, LV48-29, LV28-29, LV35-28, LV46-28, LV68-28 and LV13-26 and the well logs from the Clay Pit, M1, and Republic 66-29 wells were reviewed (Figure II.1). Six of the wells are located along the east and west flanks of the resurgent dome graben and are generally shallow in total depth (<1000 m) with only two, LV48-29 and LV68-28, reaching the Bishop Tuff. These two wells continue into the Bishop Tuff only a maximum of 20 m and do not intersect any intrusions within that thickness. On the other hand, the Clay Pit well, located approximately 5 km to the northeast of the Long Valley Exploratory Well, bottomed in a hypabyssal intrusion correlated with the biotite- and hornblende-rich Moat Rhyolite flows (Suemnicht, 1987; Smith and Suemnicht, 1991). A nearby off-dome well, LV13-26, cores 914 m of the Bishop Tuff and does not intersect intrusions within that thickness nor are intrusive intervals described in the well logs of M1 or Republic 66-29.

### *II.5.2 Relationship of Intrusions to Early Rhyolite volcanism*

Initial work on the petrology of the intrusive units indicated that they consisted of phenocryst-poor, granophyric rocks more similar to the post-collapse Early Rhyolite than to the phenocryst-rich and devitrified Bishop Tuff that they intruded (McConnell et al., 1991). Figure 3B and 3C illustrate the textural differences between the rhyolite intrusions and the intracaldera Bishop Tuff. Fresh, microlite-rich obsidian occurs in Long Valley Exploratory Well at the contacts of the shallower intrusions with Bishop Tuff, and is also observed in the well cuttings of LV13-21. Both rocks closely resemble outcrop samples of Early Rhyolite obsidian.

Chemical comparisons of Ba to Sr between the least altered samples of the *shallow* rhyolite intrusion and extrusive rhyolite units found in the Long Valley Caldera are made on Table II.1 and in Figure II.4A. The Early Rhyolite from the resurgent dome (Bailey, per. comm., 1992), the west moat South Inyo Crater (Eichelberger et al., 1988), and most of the intrusive units sampled by Long Valley Exploratory Well have Ba concentrations of  $\geq 1000$  ppm. Other extrusive lithologies have concentrations less than 1000 ppm, e.g., the Bishop Tuff with a maximum whole rock Ba concentration of 465 ppm (Hildreth, 1979) and Inyo Dome rhyolites with a mean Ba concentration of less than 820 ppm (Vogel et al., 1987). Comparisons in Figure II.4B between the extrusive Early Rhyolite and the least altered intrusive rhyolite for major, trace, and REE elements further indicate that these units are equivalent. In addition, the samples from the early and late Bishop Tuff outflow sheets have

been plotted for the same elements in Figure II.4B, illustrating considerable difference in composition between the intrusive unit and the Bishop Tuff.

There is some variation in composition among the Early Rhyolite units. Barium concentrations in the least altered samples of the intrusive units (~1200 ppm) more closely resemble those of the Early Rhyolite from beneath the west moat (~1200 ppm) than the Early Rhyolite from the resurgent dome (~1000 ppm). This is unexpected because of the proximity of the drill site to an Early Rhyolite vent on the resurgent dome. Deviation of the intrusive rhyolite from its "extrusive equivalent" on the resurgent dome could be attributed to either hydrothermal alteration or magmatic processes. The concentration of Ba observed in altered rhyolite intrusions resulted in either no change or a negative change in concentration. Thus we attribute the measured concentrations in the least altered samples to represent magmatic values.

It is possible to explain the deviation in the Early Rhyolite field, exemplified by the Ba/Sr diagram of Figure II.4A, by separation of on the order of 10% of near-liquidus plagioclase, pyroxene, and/or biotite (vector diagram, Figure II.4A). However, such fractionation is not wholly consistent with all elemental concentrations. For example, derivation of Long Valley Exploratory Well intrusions from Early Rhyolite by extraction of pyroxene would produce an enrichment in REE that is not observed in the compositions listed Table II.1 or Figure II.4B. The Early Rhyolite units appear to represent several batches of slightly different rhyolitic magmas unrelated by shallow fractional crystallization processes.



### II.5.3 Chemical Alteration

Intrusions have variations in both primary and secondary mineralogy. In the 43-m-thick *shallow* intrusion between 784 and 811 m, textures change from a dense, aphanitic rock with abundant plagioclase microlaths (<0.2 mm) and k-feldspar at 784 m to a moderate gray, friable, and argillized rock lacking plagioclase microlaths by 801 m. Sparse plagioclase phenocrysts are replaced by calcite crystals with depth. Clays were identified as mixed-layer illite/smectite based on the location of broad 10Å peaks and broad peaks in the 4-5Å range measured by XRD.

The amount of alteration within an intrusion appears to be related to the thickness of the intrusion. For example, in Figure II.5, the bulk major element composition of the *shallow* intrusion from 780 to 811 m is compared to three <1 m thick intrusions at depths of about 812 m, 822 m, and 829 m. Assuming all are hypabyssal equivalents of the Early Rhyolite flows, then the thinner units are relatively depleted in SiO<sub>2</sub> and Na<sub>2</sub>O and enriched in Al<sub>2</sub>O<sub>3</sub> and K<sub>2</sub>O. The thinner units have been hydrated and approach a clay composition. In contrast, in the thicker *shallow* unit, SiO<sub>2</sub> and Al<sub>2</sub>O<sub>3</sub> values have retained near magmatic values for the entire width of the intrusion. Within the thicker intrusion, K<sub>2</sub>O/Na<sub>2</sub>O ratios vary from ~2-10, with high ratios reflecting internal zones of brecciation and clay alteration. It is possible that this interval was intruded more than once. CaO remains relatively constant although the value is depleted from the surface equivalents.

The *intermediate* and *deep* intrusions follow similar patterns of compositional variation. H<sub>2</sub>O contents are elevated (>1wt.%) relative to surface outcrops of Early Rhyolite (<1wt.%) and CaO and Na<sub>2</sub>O show no consistent variation across the intrusions. There is no evidence of plagioclase microlaths although XRD indicates groundmass plagioclase is present in samples from the *deep* intrusion. Rare phenocrysts are now replaced by massive quartz with radiating extinction. K<sub>2</sub>O concentration remains equivalent to surface values in both intrusions. Illite and/or illite/smectite are present in all samples, although the clay fraction does not increase with depth.

Disseminated euhedral pyrite is pervasive in the intrusions and in the Bishop Tuff. Small vesicles in the intrusive rocks are lined with quartz and filled with either clay or calcite.

No zeolites have yet been identified in the Long Valley Exploratory Well intrusive units. Since these rhyolitic composition units are of a suitable bulk composition for zeolite growth at low temperatures (as in Yellowstone, Bargar and Beeson, 1981, or at Newberry Volcano, Keith and Bargar, 1988) it is probably high mole fraction CO<sub>2</sub> in the fluid phase that has inhibited zeolite stability (Kerrick, 1974). The dominance of calcite in the alteration assemblages also supports this interpretation.

#### *II.5.4 Chemical Mass Balance*

Chemical losses and gains resulting from alteration of the intrusive rhyolite were estimated using the isocon method of Grant (1986). This method is a graphical application of Gresens' (1967) analysis of chemical mass

balance. An advantage of this method when studying porous samples such as volcanic rocks and fractured core is measured rock densities are not required. In these graphical analyses, the concentrations of specific major and trace elements in the relatively unaltered rhyolite (Sample S1, Table 1= $C^O$ ) are plotted against those in the altered rock ( $C^A_i$ ). If there is no detectable alteration, the data points define a line with a slope of 1, representing constant mass. In most cases, a linear array is defined by some combination of the  $Al_2O_3$ ,  $TiO_2$ , REE, Hf, Ta, Th, and Zr components. These elements are commonly considered to be relatively immobile during alteration of volcanic rocks (Leshner et al., 1986; Sturchio et al., 1986).

There are four commonly observed mineralogical alteration assemblages in the rhyolite intrusions (Figure II.6). They are: (A) alkali-depletion alteration assemblage typified by a sample at a depth of 803 m in the *shallow* intrusion, (B) clay alteration assemblage from a <1 m-thick intrusion at 822 m, (C) sulfide alteration assemblage from a fracture zone in the *shallow* intrusion, and (D) calcite alteration assemblage from a deeper intrusion at 1445 m containing plagioclase phenocrysts. The slope of best-fit isocons,  $C^A_i/C^O$ , is used to assess possible changes in rock mass that occurred during alteration and is designated as mass original/mass altered ( $M^O/M^A$ ). Isocon slopes for assemblages A and D deviate very little from a value of 1. This indicates that rock mass was essentially conserved during alteration processes. The isocon slope for the clay alteration assemblage corresponds to a mass decrease of 50%. The isocon slope for the pyrite alteration assemblage corresponds to a mass increase of approximately 10%.

Based on isocon diagrams, gains and losses for major and minor elements may be established for each type of alteration. For the alkali-depletion alteration assemblage, Sr, Ba,  $K_2O$ , and  $Na_2O$  are depleted and As and Mo are enriched. XRD data of a sample of the intrusion at 802 m indicate the breakdown of the feldspars and crystallization of illite clays. In the clay alteration assemblage, feldspar breakdown and alkali loss are more pronounced than in the alkali-depletion assemblage. As illustrated in Figure II.6B, this type of alteration results in the loss of  $Na_2O$ , Sr, CaO, Ba,  $SiO_2$ , and  $K_2O$  and gain of Zn, Sb, As, and Mg. XRD data indicate the quartz fraction to be relatively small in this sample, potassium feldspar is only sparingly present, and plagioclase is absent. An abundant clay fraction of interlayered illite/smectite and smectite is present. Sulfide alteration results in enrichments in Zn, FeO, As, Mo, S, and Cu and slight depletions in  $K_2O$  and Sr (Figure II.6C). This alteration is a result of pyrite mineralization in fine, hairline fractures and minimal transport of the feldspar component of the rock. The last style of alteration is a result of calcite replacing both feldspar phenocrysts and the fine grained matrix in the rhyolite intrusion. This results in substantial enrichment of CaO in the rhyolite with virtually no change in the concentration of the other feldspar-related oxides such as  $SiO_2$ ,  $Na_2O$ ,  $K_2O$ , and  $Al_2O_3$ .

### II.5.5 Oxygen Isotopes

A fresh Early Rhyolite obsidian sample has a  $\delta^{18}\text{O}_{\text{WR}}$  value of +8.2‰ (Figure II.7). This is on the high end of the range of measured values on fresh, vitreous Early Rhyolite obsidian (+6.7 to +8.4‰) as reported by Smith and Suemnicht (1991). Samples from the *shallow*, *intermediate*, and *deep* intrusions have lower values ranging from +1.4 to -0.4‰ (Figure II.7). Two relatively low  $\delta^{18}\text{O}_{\text{WR}}$  values of +0.3 and +0.4‰ are reported by Smith and Suemnicht (1991) for fresh, frothy Early Rhyolite pumice. These low values were interpreted to be primary and related to the increased oxygen isotope diffusivity of rhyolitic glass at elevated temperatures (Smith et al., 1988). The values reported here for the Early Rhyolite intrusions are not believed to reflect primary  $^{18}\text{O}$  values.

The measured  $\delta^{18}\text{O}_{\text{WR}}$  values for the intracaldera Bishop Tuff range from +4.1 to 0.0‰ (Figure II.7). This is low compared to values of +6.1‰ and +8.7‰ measured on two fresh outflow sheet samples by Smith and Suemnicht (1991) and a range of values of +5.9 to +10.3‰ by Halliday et al. (1984) from the Bishop Tuff outflow sheets. It is likely that the wide range in measured values for the outflow Bishop Tuff reflects  $^{18}\text{O}$ -enrichment during weathering or low-temperature hydrothermal alteration (Stuckless and O'Neil, 1973). Measurements made on sanidines in the Bishop Tuff have a value of +7.0±0.2‰ (Halliday et al., 1984) and better reflect a magmatic  $^{18}\text{O}$  value. The

$\delta^{18}\text{O}_{\text{WR}}$  for Bishop Tuff includes oxygen in the abundant quartz phenocryst fraction which is not readily available for ionic exchange during post-emplacement devitrification and hydrothermal activity. The measured values from LVEW were recalculated assuming 15% of the volume of the whole rock to be quartz with an  $^{18}\text{O}$  value of 8.2‰ (Taylor, 1968, p.6). These recalculated values (+3.4 to -1.2‰) (Figure II.7) are used in the model calculations. Both the intracaldera Bishop Tuff and the intrusions are very depleted in  $^{18}\text{O}$  relative to their surface equivalents.

A  $\delta^{18}\text{O}_{\text{WR}}$  profile was calculated using the measured values of the geothermal gradient (50°C/km) of the well after the model of O'Neil and Taylor (1967). Whole rock oxygen isotope behavior is assumed to be approximated by that of alkali feldspars. The oxygen isotope composition of the Long Valley Exploratory Well fluid has not been determined as appropriate fluid samples are not available. Therefore, the value of -14.3‰ (White et al., 1990) measured at the RDO-8 well (See Figure II.1) was used. It is assumed that the hydrothermal fluids in the caldera have a uniform oxygen isotope composition and that the rocks have totally equilibrated at high water/rock ratios with the circulating fluid (Smith and Suemnicht, 1991). The results are displayed in Figure II.7. Measured values for both the intrusive rocks (solid squares) and the Bishop Tuff (open squares) are considerably depleted in  $^{18}\text{O}$  relative to the calculated values (solid and open triangles) for the rather cool temperature regime presently in the well. This would indicate that the temperature of circulating fluids was much higher in the past throughout the intracaldera fill

at this location. The 100°C/km geothermal gradient that was projected for the intracaldera fill on the basis of recent injection of magma to a depth of 6-8 km (Sass et al.,1991) was used to calculate a second profile (solid and open diamonds). Its location is also displaced relative to the measured values of the Early Rhyolite intrusive rocks and Bishop Tuff but, this case, toward higher temperatures.

Measured  $\delta^{18}\text{O}_{\text{wt}}$  values show the intrusive rocks experienced conditions almost isothermal with depth; the equilibration temperature for each of the intrusions is similar and the temperature range was much higher than present-day temperatures in the well. On the other hand, Bishop Tuff  $^{18}\text{O}$  values continue to deplete with depth in a fashion similar to but less extreme than the projected shallow magma profile, suggesting an increase in alteration and paleotemperature with depth. The one exception is the value for the shallowest sample which was taken immediately below the contact zone with the thick *shallow* intrusion and most likely has been perturbed by the intrusion. All other Bishop Tuff samples were chosen from areas determined to be free of intrusions. The  $^{18}\text{O}$  values for the Bishop Tuff appear to be approaching the calculated values for the higher geothermal gradient. Assuming that the measured values are linear with depth and the shallowest sample is dropped from consideration, a paleogeothermal gradient may be back-calculated from the previously determined model. This calculation yields a past geothermal gradient of approximately 70°C/km in the Bishop Tuff.

### II.5.6 $^{40}\text{Ar}/^{39}\text{Ar}$ Age Determinations

$^{40}\text{Ar}/^{39}\text{Ar}$  ages were determined for Early Rhyolite, Early Rhyolite intrusions, and Bishop Tuff from the Long Valley Exploratory Well. A plateau age of  $675 \pm 9$  ka (Table 2) obtained from an extrusive Early Rhyolite obsidian sample is identical to the age for the Early Rhyolite of  $680 \pm 29$  ka determined by K-Ar techniques and reported as Sample 3 in Mankinen et al. (1986). Plateau ages of  $789 \pm 21$  ka and  $759 \pm 15$  ka (two sample average of  $769 \pm 15$  ka, Table 2) were determined for the intracaldera Bishop Tuff from a depth of 820 m. These match well with the age of  $762 \pm 12$  ka determined on sanidine separates from Bishop Tuff outflow sheet samples by the single-crystal laser technique (Izett and Obradovich, 1991). This implies that the top of the Bishop Tuff (<800 m depth) in the well has not had post-emplacement hydrothermal activity  $>300^\circ\text{C}$  that would have reset the primary crystallization age of the sanidines (Layer et al., 1992). This is consistent with the  $\delta^{18}\text{O}$  results from sanidines. Ages determined from samples at depths of 784 and 802 m of the *shallow* 43 m thick intrusion display two very different plateau ages based on replicate analyses of  $454 \pm 17$  ka and  $590 \pm 17$  ka, respectively (Table 2). The older age supports the interpretation that the intrusions are part of the Early Rhyolite unit. The younger age may be attributed to continuing Early Rhyolite intrusive activity beneath the resurgent dome that has no extrusive equivalent or may be associated with resetting of the Ar-isotopic clock by localized hot circulating fluids. Either



process could also explain the change in the petrologic characteristics through this intrusion.

## II.6 DISCUSSION AND CONCLUSIONS

Within the intracaldera Bishop Tuff unit in the Long Valley Exploratory Well, the presence of several discrete aphyric and aphanitic hypabyssal rhyolite intrusions has been recognized. The importance of these intrusions lies in their relationship to the large caldera system, because calderas are presumed to result from the close approach of magma bodies to the surface (e.g., Lipman, 1984). Development of batholithic-sized bodies is implicated both in piston-like collapse and in high-amplitude, centralized resurgence. It is, of course, also implicated in the sudden and voluminous release of highly fractionated melts. This association of calderas with large magma bodies has been directly shown in dissected systems, and has been suggested for Long Valley on the basis of geophysical evidence and by analogy to other systems. The center of the resurgent dome, where current uplift is occurring, is the logical place to look for past or present shallow magma.

Long Valley Exploratory Well has to date provided two important observations relative to the existence of magma under the caldera. First, it is clear that at this central location the main subjacent pluton has not yet penetrated upward into the down-dropped volcanic pile, as is the case in many resurgent cauldrons. The failed roof of the magma chamber remains relatively intact. Second, however, the intracaldera tuff contains an impressive apparent thickness of early post-caldera intrusions. The importance of these

intrusions in caldera history depends upon geometry which cannot be well-resolved by a limited number of drill holes. The Long Valley Exploratory Well could have wandered down the contact of a single near-vertical intrusion and its apophyses, in which case the intrusion is probably not volumetrically important. The repeated intersections of the intrusion would be a coincidence, and the absence of a vent at the surface here surprising, especially given that the intrusion encountered appears to have been emplaced toward the close of Early Rhyolite activity. Also surprising is that these intersections only occurred within the Bishop Tuff, not within the basement.

On the other hand, the intrusions could be a series of sills of Early Rhyolite magma that preferentially spread out within the Bishop Tuff horizon. This view is supported but not confirmed by the finding of similar material in a neighboring well. Furthermore, the presence of hypabyssal Moat Rhyolite at the bottom of Clay Pit well could evoke the model of a near-surface laccolith and sills consisting of post-collapse rhyolites (Johnson, 1970; Jackson and Pollard, 1988). If they are sills, then their 330-m-cumulative thickness is impressive, though still short of the surface accumulation of Early Rhyolite at the site of >620 m. Such activity is not surprising for the resurgent dome of Long Valley Caldera, as its location is a result of tectonic control along pre-caldera faults (Bailey et al., 1976). Few wells drilled in the caldera have pierced the total thickness of the Bishop Tuff (44-16, M1, Long Valley Exploratory Well, Clay Pit) and the geometry of these contacts indicate a thinning of the Bishop Tuff to the west.

Clearly, Early Rhyolite ranks second only to the Bishop Tuff eruption among the magmatic events in the caldera's development. If we conservatively take the average thickness of Early Rhyolite to be 500 m (Suemnicht and Varga, 1988) within the area of the main ring fracture of 200 km<sup>2</sup>, then the erupted volume is 100 km<sup>3</sup> of lavas and tuffs. Early Rhyolite magmatism could be responsible for both post-Bishop Tuff collapse and resurgence. The eruption of 100 km<sup>3</sup> of magma could explain why the top of the Bishop Tuff in the west and east moats is down about 700 m relative to the top of the proximal portion of the southeast outflow sheet. Indeed, thick Early Rhyolite extends well west of the Bishop Tuff in the subsurface, as if the caldera broadened to the west after Bishop Tuff emplacement. Three hundred meters of Early Rhyolite sills centered beneath the resurgent dome would explain resurgence in Early Rhyolite time. Such a mechanism seems more in accord with the absence of a steep paleogeotherm, as implied by oxygen isotope data for the tuff, than one requiring a huge inflating pluton. The repeatedly intruded shallow sills gradually uplifted the center of the caldera and with it their own surface equivalents, and briefly drove local hydrothermal systems within the caldera fill. Alteration was confined mainly to the intrusions, and was characterized by clay mineralization as well as post-emplacement deposition of quartz, calcite, and pyrite in the crystalline matrix and calcite replacing sparse phenocrysts.

Long Valley Exploratory Well has provided a new glimpse into the intrusive root of Long Valley Caldera, but an important problem has yet to be solved. Where is the magma chamber that produced the caldera? Are the

crystalline remnants of the Bishop Tuff chamber within future reach of Long Valley Exploratory Well? Is it possible these remnants were supplanted by later magma through mechanical (stoping) or magmatic (fractionation) means, or is the shallow magma model incorrect at Long Valley? Ultimately, understanding voluminous silicic magmatism will require one or more deep holes from the surface well into the central pluton of a young, well-preserved system such as Long Valley Caldera.

## II.7 ACKNOWLEDGEMENTS

We would like to thank Roy Bailey, USGS and Gene Suemnicht, Unocal for sharing their interest and insight into the Long Valley Caldera and Jim Dunn, John Finger, Ron Jacobson, and Robert Meyers of the Geothermal division of Sandia National Laboratories Albuquerque, NM for able management of the LVEW project.

Geochemical analyses were conducted by Dr. Monte Smith at Battelle National Labs, John Hustler at University of New Mexico, and the INAA-facility at Oregon State University.

Also thanks to Jeff Drake at the Geochronology Lab for invaluable assistance with geochronology sample preparation and data collection, Jim Burton for assistance with graphics, and to Don Triplehorn, University of Alaska, Fairbanks, and Jim Krumhansl, Sandia National Labs, for insights on clay XRD.

C. K. Shearer and J. J. Papike acknowledge support for this research from DOE Grant DE-FG04-90ER14149 and the Institute of Meteoritics.

University of Alaska research was funded by Sandia National Labs as part of a program under the Division of Geothermal Energy of U.S. Department of Energy.

This manuscript was improved by the editorial comments of R. Bailey, T. E.C. Keith, G. Heiken, J. Hulen, D. Neilson, and G. Suemnicht.

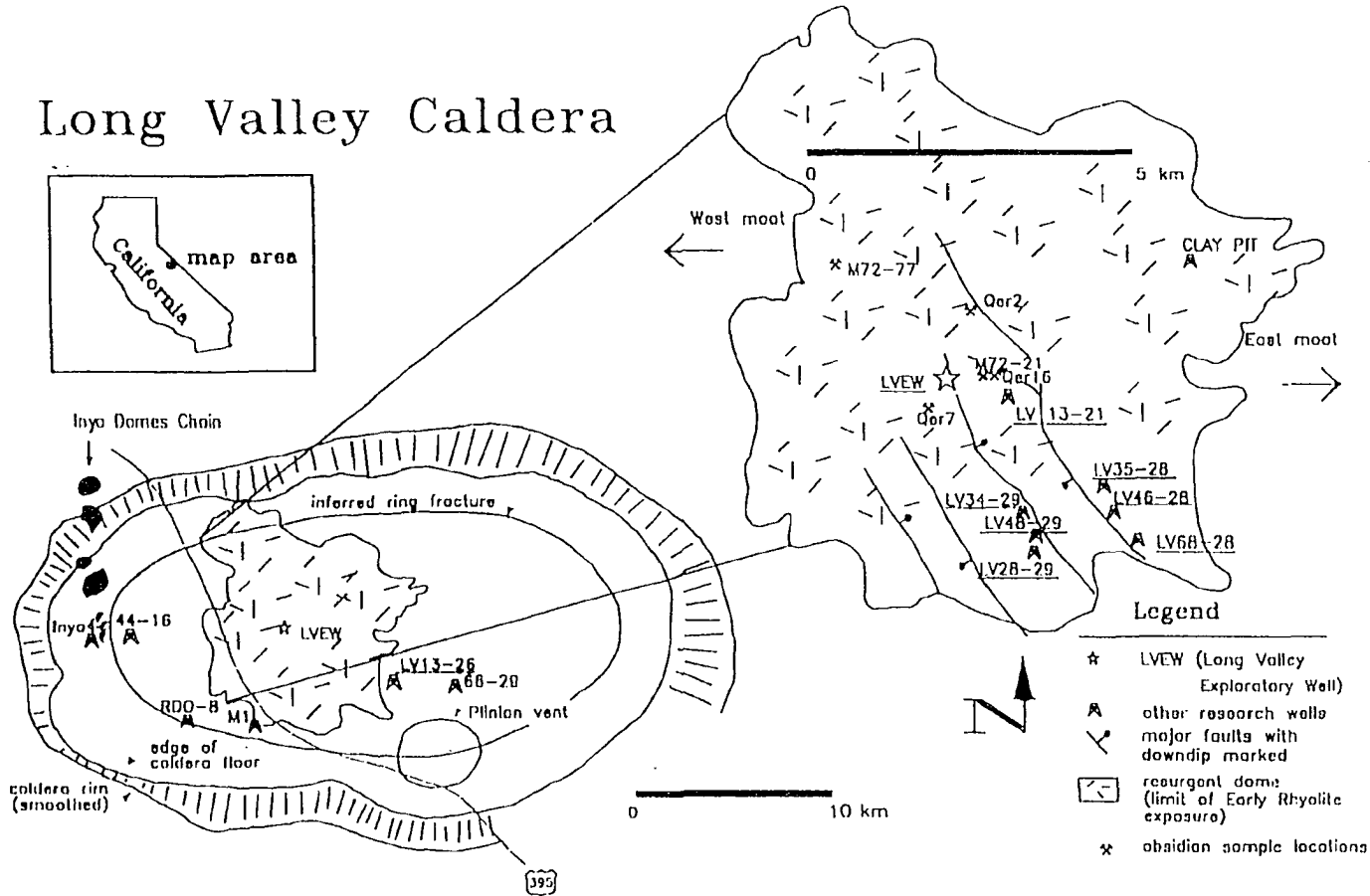


Figure II.1 Sketch map of Long Valley Caldera and resurgent dome. Map shows locations of the wells and surface samples referenced in text. Underlined wells were relogged for this study. Hydrothermal fluid sample referenced in oxygen isotope modeling was taken from well RDO-8. Major faults on resurgent dome are mapped and downthrown side marked with bar and ball.

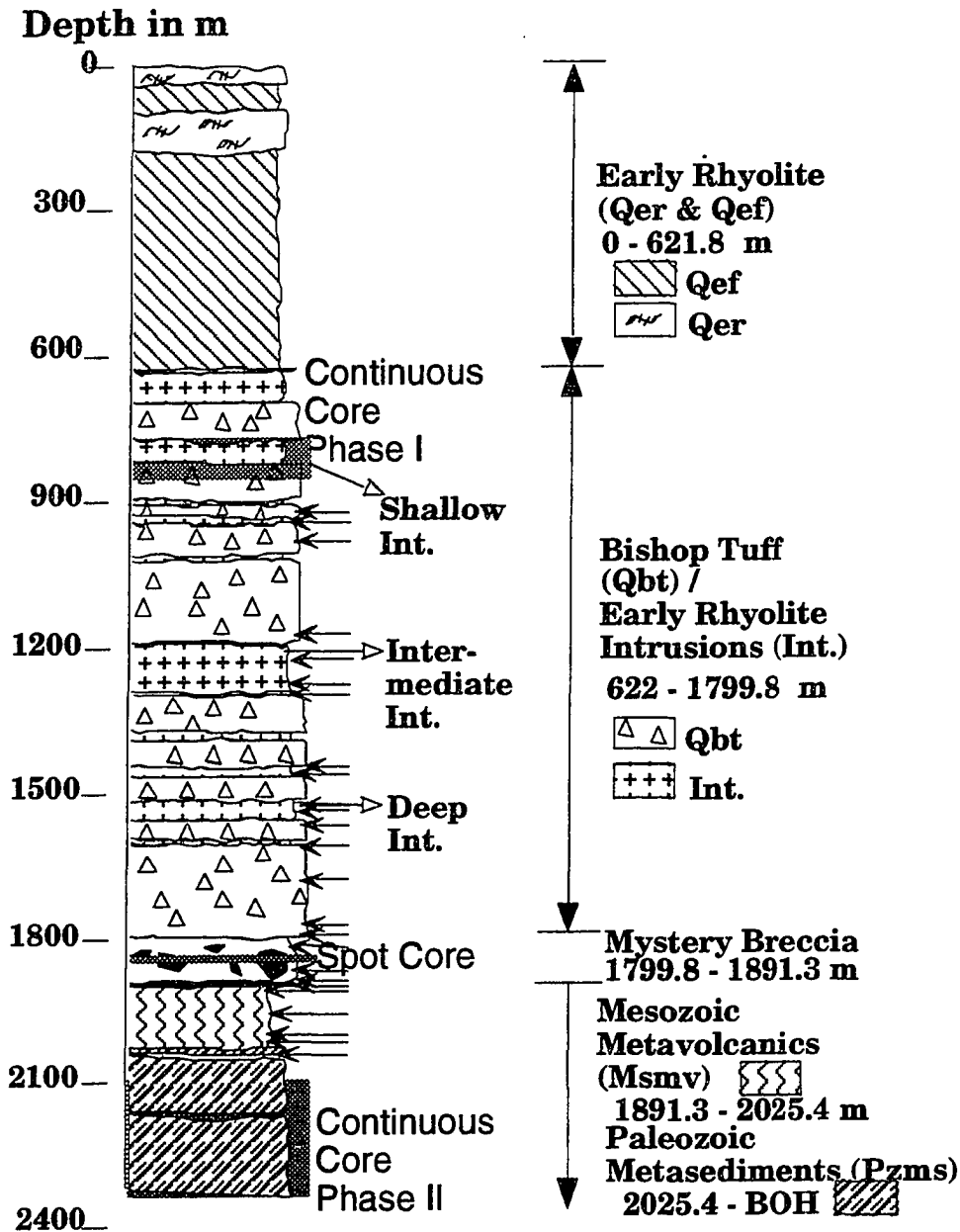


Figure II.2 Stratigraphy of the Long Valley Exploratory Well. Lithology determined by well logging of core and cuttings, downhole geophysical logs, and petrography. The three Early Rhyolite intrusions used for this study are designated as *shallow*, *intermediate*, and *deep*. Location of cored intervals in the well are indicated, continuously cored sequence recovered at the end of each phase of drilling, intermittent continuously cored sequence (Spot core), 26 sidewall cores designated by arrows.

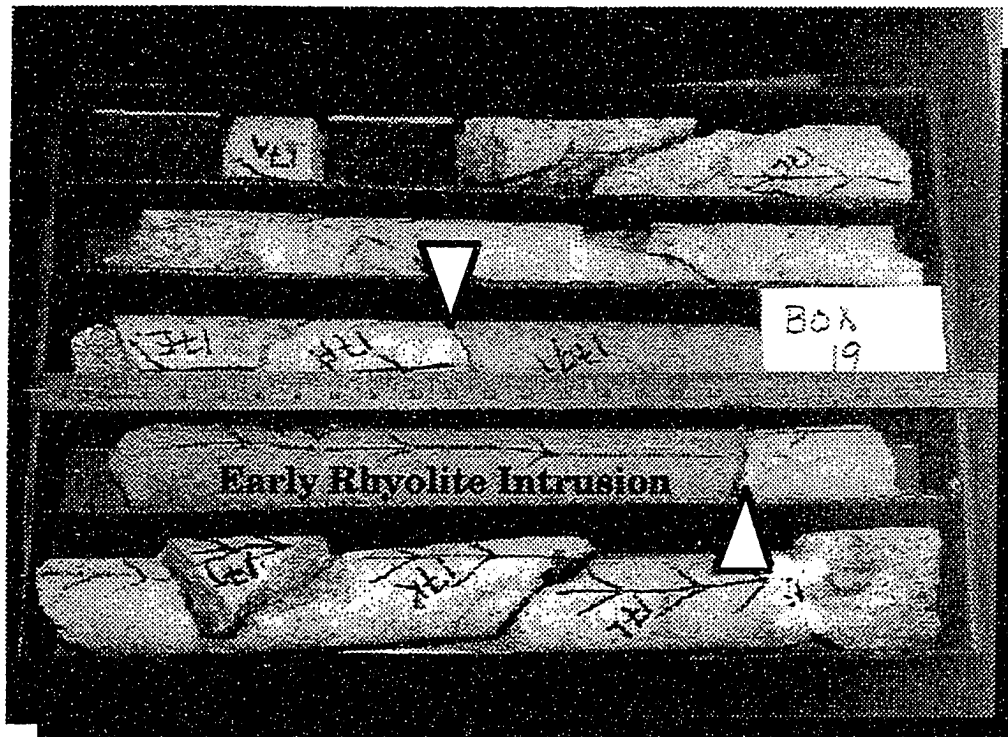


Figure II.3A Photograph of boxed core with intrusion into the Bishop Tuff. This intrusion shows a sharp contact at 828.5 m (upper V) and a sheared bottom contact (lower V) with the Bishop Tuff at 829.3 m. The intrusion is subhorizontal to the Bishop Tuff.



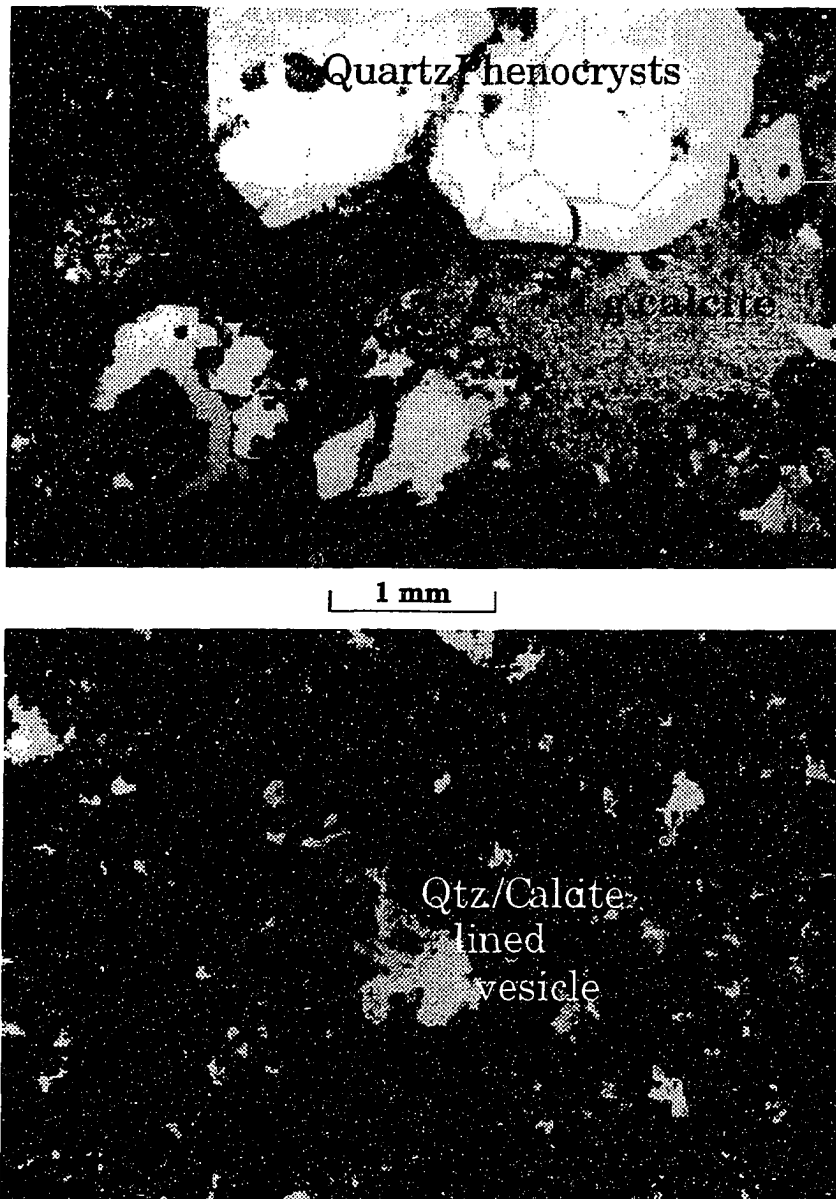


Figure II.3B Photomicrograph of Bishop Tuff at 914 m. Note the euhedral quartz phenocrysts, devitrified flow-texture matrix, and the quartz and calcite overprinting.

Figure II.3C Photomicrograph of an Early Rhyolite intrusion at 1263 m. The scale is the same as 3B. Note the very fine grained aphanitic matrix texture, absence of phenocrysts, and quartz and calcite lined vesicles. The intervals identified as intrusions lack any evidence of the distinctive euhedral quartz phenocrysts ubiquitous to the Bishop Tuff.

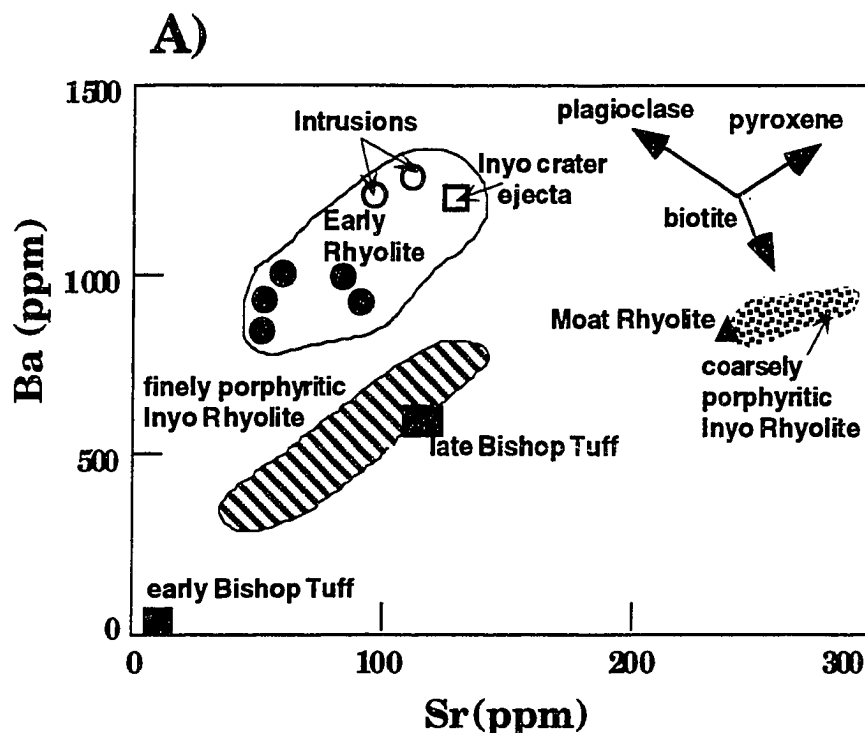


Figure II.4A Comparison of Ba/Sr ratios in intracaldera rhyolite rocks. Lithologies included in comparison: intrusion samples from Table II.1 (open circles), Early Rhyolite samples from Table II.1 (closed circles)<sup>1</sup>, Early Rhyolite ejecta from South Inyo Crater (open square)<sup>2</sup>, Moat Rhyolite from Deer Mt. (solid triangle)<sup>1</sup>, coarsely porphyritic Inyo Rhyolite (stippled field)<sup>3</sup>, finely porphyritic Inyo Rhyolite (striped field)<sup>3</sup>, early Bishop Tuff (solid square)<sup>4</sup>, and late Bishop Tuff (solid square)<sup>4</sup>.

<sup>1</sup>(Sampson and Cameron, 1987 and R. Bailey, pers. comm., 1992); <sup>2</sup>Eichelberger et al., 1988); <sup>3</sup>(Vogel et al., 1987); <sup>4</sup>(Hildreth, 1979).

Vector diagram, upper right-hand corner, shows the expected enrichment or depletion of Ba and Sr if approximately 10 wt. % of plagioclase, pyroxene, or biotite were crystallized from Early Rhyolite magma. Although the vector for crystallization of pyroxene corresponds to the trend of the Early Rhyolites, trace element concentrations do not match fractionation projections.

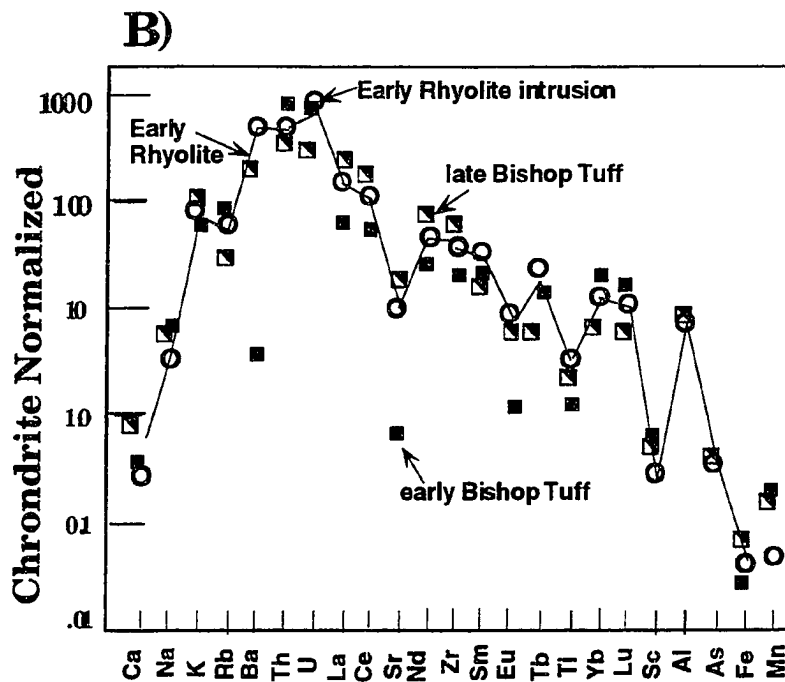


Figure II.4B Spider diagram for major, trace, and rare earth elements. Diagram shows the excellent fit between the least altered intrusion from the drill core (open circles) and Early Rhyolite from the resurgent dome (solid line). Early Bishop Tuff and late Bishop Tuff outflow sheet samples are plotted as half filled and solid squares. Chemistry of the least altered of the Early Rhyolite intrusions sampled by drilling compared to extrusive rhyolite lithologies from Long Valley Caldera.

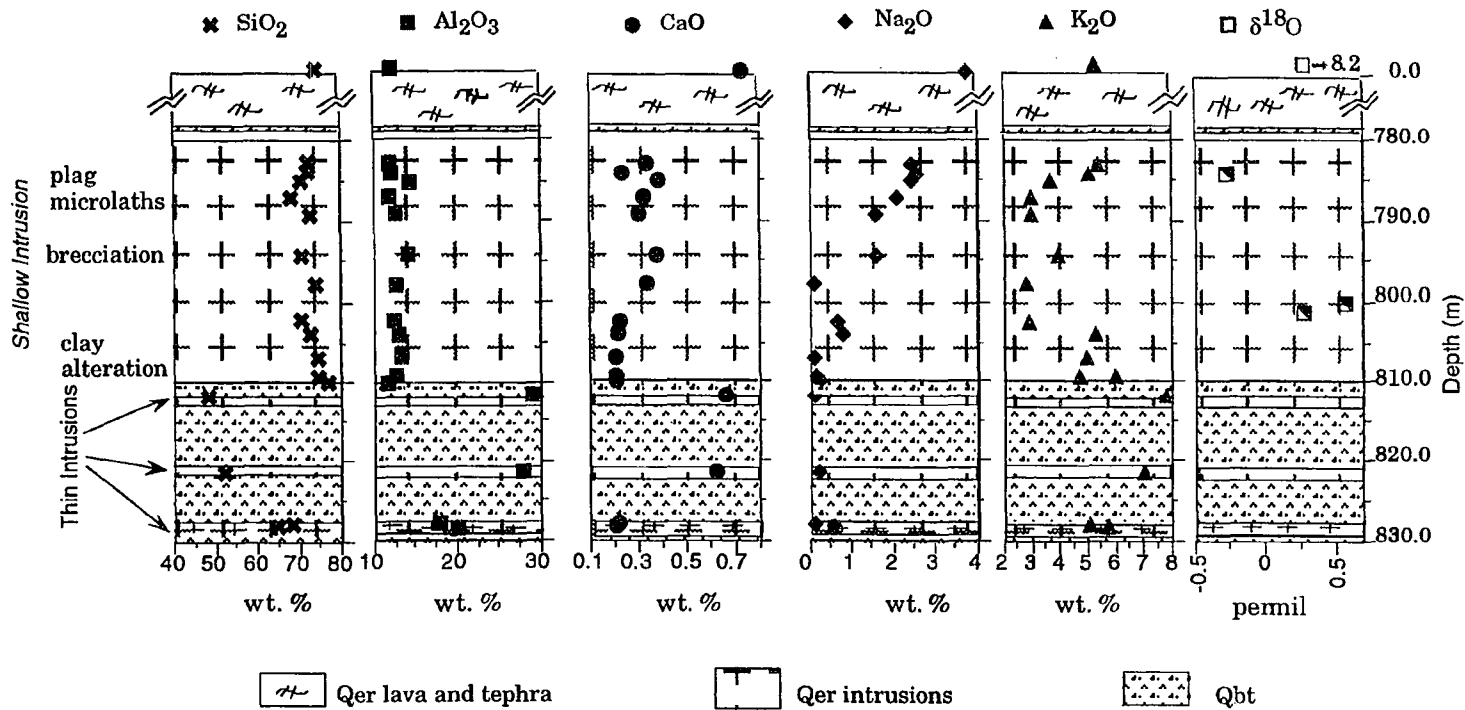


Figure II.5 Major oxide and  $\delta^{18}\text{O}$  values in the *shallow* Early Rhyolite intrusion. Three thin intrusions from Long Valley Exploratory Well are also plotted on a simplified stratigraphy diagram. Early Rhyolite designated "Qer", Early Rhyolite intrusions designated "Qer intrusions", and Bishop Tuff designated "Qbt". *Shallow* intrusion (768-811 m) shows only the cored section (784-811 m) that has been sampled in detail. Data taken from Table II.1, samples S1-Int. to S16-Int. Thin intrusions appear to show the effect of hydrothermal alteration (decrease in SiO<sub>2</sub> and Na<sub>2</sub>O and increase in Al<sub>2</sub>O<sub>3</sub> and CaO) more keenly than the thicker *shallow* intrusion.

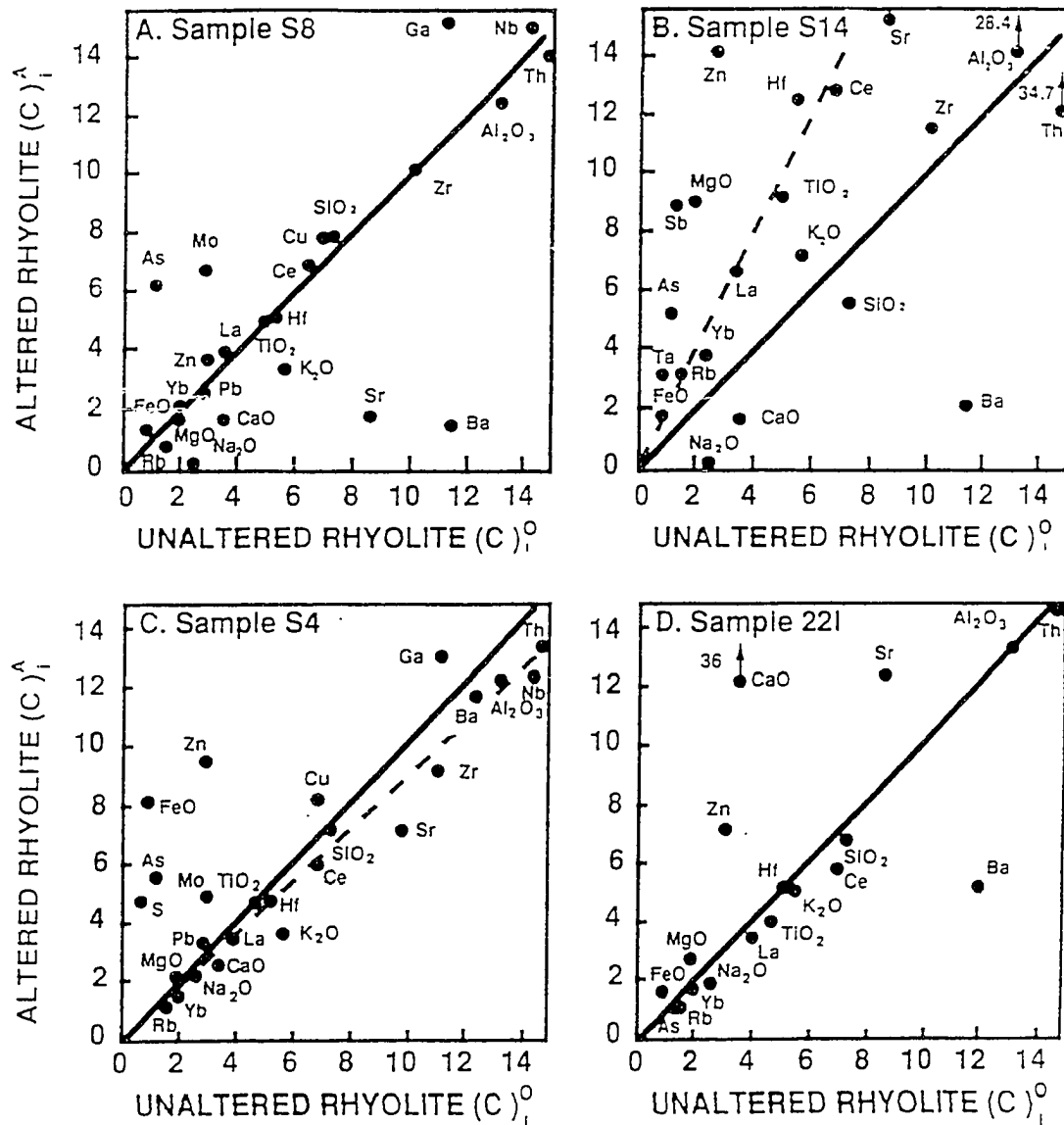


Figure II.6 Isocon diagrams for alteration assemblages. Four alteration assemblages observed in the intrusions from Long Valley Exploratory Well after Grant (1986). The plotted points represent variation in concentration between altered and unaltered samples (no variation would define a line with a slope of 1). Dashed lines represent the best fit line through elements least affected by hydrothermal fluid. Major oxides are plotted as wt.% and elements plotted as ppm.

A. Alkali-depletion alteration assemblage (*shallow* intrusion at about 803 m, sample S8-Int.), B. Clay alteration assemblage (0.3 m thick intrusion at about 822 m, sample S14-Int.), C. Pyrite alteration assemblage (*shallow* intrusion at about 788 m, sample S4-Int.), D. Calcite alteration assemblage (intrusion at about 1445 m, sample 221- Int.).

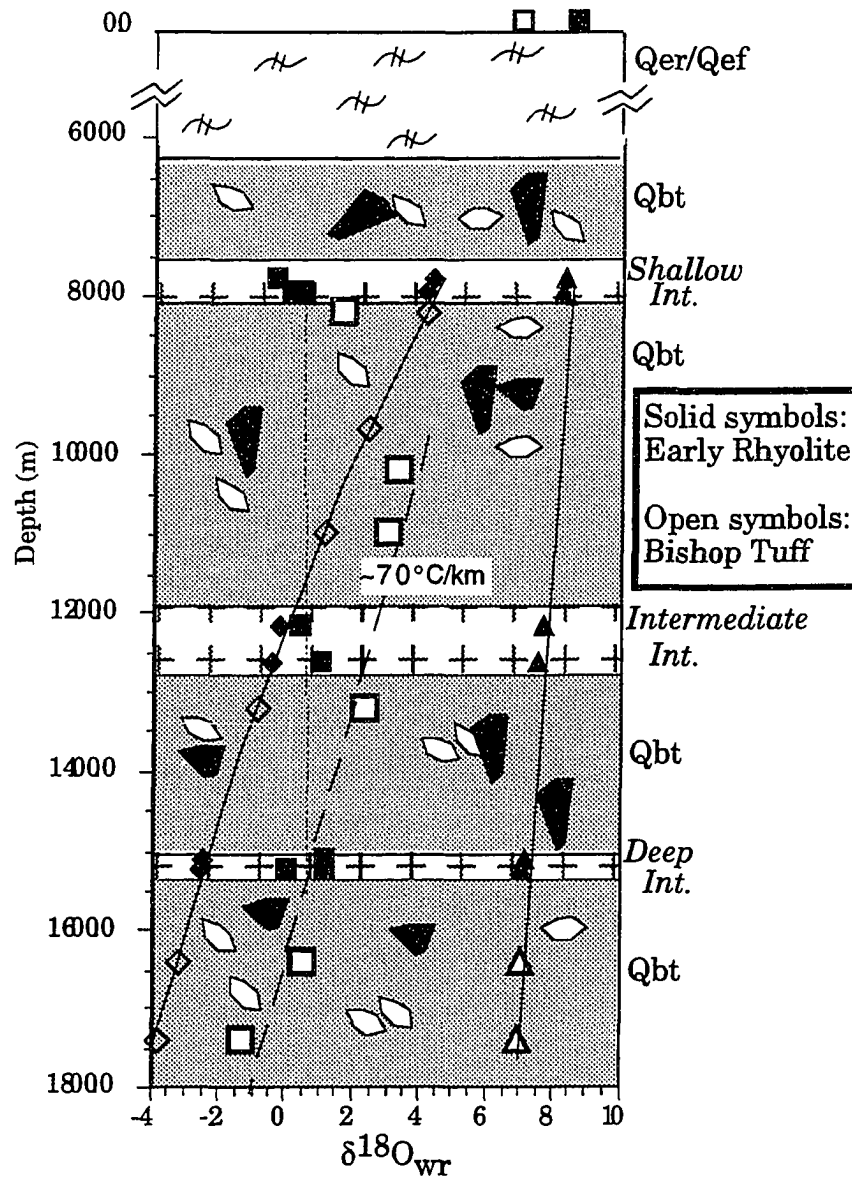


Figure II.7 Measured and calculated  $\delta^{18}\text{O}_{\text{WR}}$  values. Plot shows values for *shallow*, *intermediate*, and *deep* Early Rhyolite intrusions and intervening Bishop Tuff (Qbt). The corresponding magmatic values are shown at "0.0" depth. Solid squares and dotted line define a nearly isothermal trend for the intrusions, open squares and dashed line define depletion-with-depth trend for Bishop Tuff. Not all intrusions are shown on this generalized stratigraphy. Triangles define values expected if the rocks had equilibrated at the present geothermal gradient of  $50^\circ\text{C}/\text{km}$ . Diamonds define values expected for water/rock equilibrium at a geothermal gradient of  $100^\circ\text{C}/\text{km}$ .

Table II.1 Major and trace element chemistry of Early Rhyolite samples.  
Chemical analyses of Early Rhyolite obsidian samples (Qer<sub>1</sub> and Qer<sub>2</sub>) from surface, and intrusion samples (Int.) from Long Valley Exploratory Well.

n.a. = not analyzed, n.d. = not detected \*Data kindly provided by R. A. Bailey (1992)  
Major oxides and volatiles (wt. %)

Sample	M72-21(CS)	M72-77(CS)	Qer-2	Qer-7	Qer-16	M72-21(RB)*
Depth (m)	0.0 (Qer <sub>1</sub> )	0.0 (Qer <sub>2</sub> )	0.0 (Qer <sub>2</sub> )	0.0 (Qer <sub>1</sub> )	0.0 (Qer <sub>1</sub> )	0.0 (Qer <sub>1</sub> )
SiO <sub>2</sub>	74.36	74.42	73.91	74.69	74.54	74.97
TiO <sub>2</sub>	.16	.16	.19	.16	.16	.15
Al <sub>2</sub> O <sub>3</sub>	13.68	13.77	13.69	13.82	13.60	13.62
FeO	1.05	1.06	1.08	1.10	1.10	1.23
MnO	.03	.03	.03	.03	.03	.04
MgO	.17	.18	.25	.22	.19	.14
CaO	.75	.72	.84	.76	.73	.84
Na <sub>2</sub> O	3.77	3.74	3.56	3.72	3.87	3.87
K <sub>2</sub> O	5.21	5.21	5.23	5.19	5.22	5.17
P <sub>2</sub> O <sub>5</sub>	.07	.06	.07	.06	.06	n.a.
S	n.a.	n.a.	n.a.	n.a.	n.a.	n.a.
H <sub>2</sub> O(-)	<.01	.03	<.01	<.01	<.01	.04
volatiles	.37	.13	.20	.13	.18	.35
<b>Trace Elements (ppm)</b>						
As	8.2	8.5	8.2	7.9	8.4	n.a.
Ba	845	897	710	805	804	1001
Co	.61	.55	.85	.56	.70	0.6
Cs	5.1	5.1	5.2	5.0	5.1	4.7
Cu	n.a.	n.a.	n.a.	n.a.	n.a.	1.0
Ga	n.a.	n.a.	n.a.	n.a.	n.a.	n.a.
Hf	5.16	4.97	5.15	4.97	5.25	4.9
Hg	n.d.	n.d.	n.d.	n.d.	n.d.	n.a.
Mo	n.a.	n.a.	n.a.	n.a.	n.a.	<7
Pb	n.a.	n.a.	n.a.	n.a.	n.a.	n.a.
Rb	129	127	131	132	129	143
Sb	1.2	1.1	1.1	1.1	1.2	1.0
Sc	2.1	2.0	2.1	2.0	2.1	2.08
Se	1.9	1.8	2.1	1.7	1.5	n.a.
Sr	45	89	120	45	54	60
Ta	1.26	1.23	1.18	1.22	1.16	1.37
Th	15.8	15.6	15.5	15.3	15.5	16.0
U	5.6	5.6	4.9	5.6	5.8	5.5
W	.9	.80	n.a.	1.5	1.5	n.a.
Zn	29	30	30	31	31	34
Zr	n.a.	n.a.	n.a.	n.a.	n.a.	223
La	35.1	35.2	35.4	35.8	35.8	43
Ce	59.7	59.0	56.4	58.7	57.4	68
Nd	17.4	18.9	16.7	18.5	15.5	24
Sm	3.32	3.24	3.33	3.30	3.33	3.6
Eu	.39	.39	.44	.36	.39	.40
Tb	.41	.41	.39	.41	.40	.41
Yb	1.87	1.82	1.87	1.69	1.79	1.8
Lu	.30	.30	.28	.25	.25	.28

Table II.1 (continued) Major oxides and volatiles (wt.%)

Sample	M72-77(RB)*	S1-Int.	S2-Int.	S3-Int.	S4-Int.	S5-Int.
Depth (m)	0.0 (Qer <sub>2</sub> )	783.4	784.4	785.9	787.8	790.0
SiO <sub>2</sub>	75.00	73.32	72.96	71.19	69.18	73.74
TiO <sub>2</sub>	.14	.24	.22	.24	.23	.20
Al <sub>2</sub> O <sub>3</sub>	13.31	13.17	13.17	14.95	12.11	12.82
FeO	1.22	.80	.79	1.20	7.30	1.22
MnO	.04	.01	.01	.02	.02	.02
MgO	.15	.20	.14	.22	.21	.22
CaO	.92	.35	.26	.30	.26	.28
Na <sub>2</sub> O	3.93	2.56	2.69	2.52	2.21	1.63
K <sub>2</sub> O	5.04	5.50	5.20	3.82	3.13	3.13
P <sub>2</sub> O <sub>5</sub>	n.a.	n.d.	n.d.	.25	.64	.16
S	n.a.	.43	.38	.40	4.74	.51
H <sub>2</sub> O(-)	.36	n.a.	n.a.	n.a.	n.a.	n.a.
volatiles	.21	1.50	1.60	2.70	7.90	3.00
<b>Trace Elements (ppm)</b>						
As	n.a.	14.7	14.7	21.5	67.3	24.1
Ba	1000	1241	1116	1089	1012	683
Co	0.7	.65	.74	.98	.78	.80
Cs	4.9	2.9	3.4	6.2	4.3	6.4
Cu	<2	6.9	6.5	5.3	8.2	5.6
Ga	n.a.	11	12	17	13	15
Hf	4.6	5.3	5.2	6.2	4.4	5.3
Hg	n.a.	n.d.	n.d.	.02	n.d.	n.d.
Mo	<4	3	4	4	6	4
Pb	n.a.	29	26	27	33	27
Rb	130	134	124	119	124	119
Sb	1.0	1.7	1.5	1.4	2.5	2.2
Sc	2.11	1.5	1.5	2.1	1.8	1.9
Se	n.a.	2.0	1.8	2.4	1.6	1.8
Sr	80	85	81	98	70	80
Ta	1.29	1.3	1.3	1.5	1.1	1.3
Th	15.0	14.7	15.2	18.1	13.2	15.5
U	5.3	7.4	7.6	8.2	6.1	9.2
W	n.a.	2.6	n.d.	1.9	1.7	n.d.
Zn	30	10	14	24	32	14
Zr	213	150	167	153	155	173
La	37	40.9	40.6	47.2	33.7	41.5
Ce	65	68.2	66.4	77.1	58.6	66.9
Nd	19	23.7	26.8	19.6	26.4	32.1
Sm	3.4	4.58	4.59	5.25	3.60	4.78
Eu	.37	.46	.49	.58	.42	.46
Tb	.40	.82	.51	.57	.36	.50
Yb	1.7	2.09	1.84	2.03	1.44	1.95
Lu	.25	.27	.29	.32	.22	.25



Table II.1 (continued) Major oxides and volatiles (wt.%)

Sample	S6-Int.	S7-Int.	S8-Int.	S9-Int.	S10-Int.	S11-Int.
Depth (m)	794.8	798.9	803.3	804.9	807.6	809.8
SiO <sub>2</sub>	71.51	74.37	77.52	73.83	75.11	75.14
TiO <sub>2</sub>	.25	.18	.19	.25	.23	.23
Al <sub>2</sub> O <sub>3</sub>	14.60	12.46	12.46	13.17	13.17	12.82
FeO	1.42	2.93	1.13	1.04	1.29	1.31
MnO	.02	.02	.01	.02	.01	.02
MgO	.29	.34	.17	.08	.07	.11
CaO	.37	.34	.16	.21	.20	.20
Na <sub>2</sub> O	1.68	.22	.22	.88	.22	.26
K <sub>2</sub> O	4.05	2.98	3.06	5.43	5.12	4.82
P <sub>2</sub> O <sub>5</sub>	.21	.28	.18	n.d.	.13	.14
S	.62	1.78	.75	.59	.83	.72
H <sub>2</sub> O(-)	n.a.	n.a.	n.a.	n.a.	n.a.	n.a.
volatiles	3.40	4.80	3.40	2.60	3.00	3.00
<b>Trace Elements (ppm)</b>						
As	22.2	63.0	66.9	30.9	58.5	74.4
Ba	968	229	138	1208	980	1101
Co	.95	.75	.95	1.0	.72	n.d.
Cs	7.0	7.9	7.9	4.8	5.8	n.a.
Cu	5.3	5.3	7.8	5.6	6.3	5.5
Ga	16	14	15	13	13	13
Hf	5.6	4.8	4.8	5.4	5.4	n.a.
Hg	n.d.	n.d.	n.d.	n.d.	n.d.	n.d.
Mo	5	2	7	5	12	6
Pb	29	32	25	24	28	27
Rb	163	85	76	125	124	140
Sb	2.8	9.3	8.7	7.1	10.1	<9
Sc	2.2	1.7	1.6	2.1	2.0	n.a.
Se	2.7	2.0	2.1	2.2	2.5	2.5
Sr	70	83	17	37	75	73
Ta	1.4	1.2	1.3	1.3	1.4	n.a.
Th	16.8	14.6	14.0	16.1	16.5	n.a.
U	6.1	4.4	4.7	5.0	5.2	<5.0
W	n.d.	n.d.	n.d.	n.d.	n.d.	n.d.
Zn	41	14	15	16	16	33
Zr	163	167	130	124	138	138
La	41.8	35.5	38.0	40.5	40.8	35
Ce	71.5	60.7	63.9	70.0	72.0	74
Nd	19.8	17.5	16.1	14.2	18.0	16.0
Sm	4.68	3.74	4.02	4.42	4.41	4.0
Eu	.54	.44	.47	.52	.55	.50
Tb	.52	.48	.77	.56	.51	.46
Yb	1.79	1.46	1.95	1.69	1.82	1.45
Lu	.29	.22	.25	.23	1.99	1.60

Table II.1 (continued) Major oxides and volatiles (wt.%)

Sample	S12-Int.	S13-Int.	S14-Int.	S15-Int.	S16-Int.	22B-Int.
Depth (m)	810.7	812.7	821.9	828.7	829.0	926.6
SiO <sub>2</sub>	77.01	49.20	52.59	69.36	65.62	73.85
TiO <sub>2</sub>	.21	.44	.43	.28	.35	.18
Al <sub>2</sub> O <sub>3</sub>	12.46	29.56	28.40	18.45	20.55	13.75
FeO	.85	2.21	1.91	1.68	1.94	.58
MnO	.02	.06	.03	.03	.04	.03
MgO	.16	1.45	.92	.49	.45	.16
CaO	.19	.68	.67	.23	.21	1.12
Na <sub>2</sub> O	.31	.22	.32	.23	.69	2.22
K <sub>2</sub> O	6.04	7.87	7.15	5.20	5.89	5.30
P <sub>2</sub> O <sub>5</sub>	n.d.	.06	.06	.07	.07	.07
S	.28	n.a.	n.a.	n.a.	n.a.	n.a.
H <sub>2</sub> O(-)	n.a.	1.65	2.15	.34	.37	.26
volatiles	2.20	6.93	5.51	3.60	3.65	1.95
<b>Trace Elements (ppm)</b>						
As	32	.49	308	218	67.5	17.8
Ba	1222	174	250	161	145	772
Co	n.d.	1.38	1.4	1.3	1.3	2.4
Cs	n.a.	14.7	14.8	6.7	8.2	4.2
Cu	4.7	n.a.	n.a.	n.a.	n.a.	n.a.
Ga	12	n.a.	n.a.	n.a.	n.a.	n.a.
Hf	n.a.	11.6	12.6	8.0	9.3	5.3
Hg	n.d.	n.d.	n.d.	n.d.	n.d.	n.d.
Mo	6	n.a.	n.a.	n.a.	n.a.	n.a.
Pb	22	n.a.	n.a.	n.a.	n.a.	n.a.
Rb	179	295	282	199	215	130
Sb	<9	14.0	9.9	13.5	7.1	3.8
Sc	n.a.	6.2	5.2	3.4	3.9	2.2
Se	2.2	4.2	5.4	6.9	4.0	1.7
Sr	75	67	161	118	n.d.	125
Ta	n.a.	2.6	3.0	3.7	2.6	1.2
Th	n.a.	32.8	34.7	23.6	26.0	16.5
U	<5.0	11.6	5.2	8.2	9.5	5.2
W	n.d.	n.d.	n.d.	2.4	1.4	14.1
Zn	28	76	47	33	52	30
Zr	193	n.a.	164	166	n.a.	n.a.
La	42	44.4	73.7	58.5	64.8	36.0
Ce	74	80.7	130.7	104.3	104	60.6
Nd	19	24.2	35.5	31.1	31	19.7
Sm	4.5	4.5	6.36	5.92	6.05	3.51
Eu	.58	.90	.89	.77	.81	.44
Tb	.52	.66	.69	.38	.70	.32
Yb	1.85	3.42	3.15	2.89	3.10	2.02
Lu	2.03	.54	.40	.39	.44	.32

Table II.1 (continued) Major oxides and volatiles (wt.%)

Sample	22E-Int.	22F-Int.	22I-Int.	22J-Int.	22K-Int.
Depth (m)	1222.2	1263.4	1444.8	1515.0	1530
SiO <sub>2</sub>	73.06	72.46	69.64	75.81	73.99
TiO <sub>2</sub>	.19	.20	.20	.21	.20
Al <sub>2</sub> O <sub>3</sub>	14.18	13.91	13.60	13.70	13.63
FeO	1.04	1.42	1.36	.87	.84
MnO	.08	.05	.08	.01	.02
MgO	.18	.19	.27	.19	.14
CaO	1.44	1.53	3.57	.16	.36
Na <sub>2</sub> O	.74	1.83	1.90	1.36	2.99
K <sub>2</sub> O	5.25	5.06	4.41	4.91	5.61
P <sub>2</sub> O <sub>5</sub>	.07	.07	.08	.08	.07
S	n.a.	n.a.	n.a.	n.a.	n.a.
H <sub>2</sub> O(-)	.22	.14	.14	.20	.07
volatiles	3.02	2.52	4.10	2.05	1.43
<b>Trace Elements (ppm)</b>					
As	52.9	14.6	11.6	132	53.3
Ba	1000	955	520	976	1080
Co	1.5	2.5	12.9	2.6	6.0
Cs	6.6	5.8	5.7	3.3	2.1
Cu	n.a.	n.a.	n.a.	n.a.	n.a.
Ga	n.a.	n.a.	n.a.	n.a.	n.a.
Hf	5.3	5.3	5.3	5.2	5.1
Hg	n.d.	n.d.	n.d.	n.d.	n.d.
Mo	n.a.	n.a.	n.a.	n.a.	n.a.
Pb	n.a.	n.a.	n.a.	n.a.	n.a.
Rb	115	119	107	117	126
Sb	4.3	2.6	2.9	2.8	2.8
Sc	2.4	2.5	2.3	2.1	2.0
Se	1.9	2.0	1.8	2.3	1.8
Sr	67	103	123	n.d.	119
Ta	1.3	1.3	1.3	1.2	1.23
Th	16.2	16.1	16.0	15.7	15.5
U	6.0	5.7	3.8	4.7	5.4
W	1.5	4.2	55.7	6.2	n.d.
Zn	32	26	24	24	22
Zr	n.a.	n.a.	n.a.	n.a.	n.a.
La	36.5	35.0	34.1	38.4	35.0
Ce	60.5	60.1	58.5	66.0	60.3
Nd	19.2	18.5	18.5	19.5	18.9
Sm	3.52	3.39	3.29	3.44	3.24
Eu	.49	.50	.48	.45	.43
Tb	.42	.39	.40	.38	.37
Yb	1.92	1.82	1.82	1.83	1.80
Lu	.31	.29	.29	.30	.29

Table II.1 (continued) Major oxides and volatiles (wt.%)

Sample	58-I-c3*
Depth (m)	2199.7
SiO <sub>2</sub>	39.69
TiO <sub>2</sub>	1.01
Al <sub>2</sub> O <sub>3</sub>	16.12
FeO	11.73
MnO	0.26
MgO	4.69
CaO	8.38
Na <sub>2</sub> O	0.21
K <sub>2</sub> O	4.25
P <sub>2</sub> O <sub>5</sub>	0.28
S	3.69
H <sub>2</sub> O(-)	0.09
volatiles	0.02
<b>Trace Elements (ppm)</b>	
As	n.a.
Ba	n.a.
Co	n.a.
Cs	n.a.
Cu	n.a.
Ga	n.a.
Hf	n.a.
Hg	n.a.
Mo	n.a.
Pb	n.a.
Rb	n.a.
Sb	n.a.
Sc	n.a.
Se	n.a.
Sr	n.a.
Ta	n.a.
Th	n.a.
U	n.a.
W	n.a.
Zn	n.a.
Zr	n.a.
La	n.a.
Ce	n.a.
Nd	n.a.
Sm	n.a.
Eu	n.a.
Tb	n.a.
Yb	n.a.
Lu	n.a.

\*58-I-c3 is from Paleozoic metasedimentary basement rocks. Fe is Fe<sub>2</sub>O<sub>3</sub> and S is SO<sub>3</sub>.

Table II.2  $^{40}\text{Ar}/^{39}\text{Ar}$  ages for whole rock samples dated in 1992.

Sample ID	Depth (m)	Mass (g)	# of Splits	Integrated Age (ka)	% $^{40}\text{Ar}$ Atmos.	K <sub>2</sub> O (wt.%)	CaO (wt.%)	Plateau Age(ka)	% $^{39}\text{Ar}$ in Plateau
Qer Obsidian	0.0	2.6589	12	684±11	53	5.53	0.75	675±9	99
2B1-Qer Intrusive	784.4	1.1347	8	426±28	94	4.95	0.21	473±20	89
2B1-Qer Intrusive	784.4	1.0008	8	478±21	94	4.43	0.19	439±18	71
<b>weighted mean age=</b>								<b>454±17</b>	
LVF2628-Intrusive	802.0	0.7751	8	707±49	96	3.18	0.11	626±38	90
LVF2628-Intrusive	802.0	1.0823	7	767±39	96	3.12	0.09	577±34	43
LVF2628-Intrusive	802.0	1.0001	8	694±30	95	3.13	0.15	582±24	77
<b>weighted mean age=</b>								<b>590±17</b>	
Qbt Sanidine	820.0	0.1046	1	845±40	88	10.31	0.13	none	
Qbt Sanidine	820.0	0.6861	8	993±17	78	10.51	0.17	789±21	41
Qbt Sanidine	820.0	0.6497	8	795±17	83	11.07	0.18	759±15	81
<b>weighted mean age=</b>								<b>769±15</b>	

Notes:

All samples run with Bern 4B biotite standard (17.25 Ma) and ages calculated using constants of Steiger and Jäger, 1977.

K<sub>2</sub>O and CaO concentrations are approximate. Uncertainties in ages are quoted at the 1σ level.

Table II.2  $^{40}\text{Ar}/^{39}\text{Ar}$  ages for whole rock samples dated in 1992.

## II.8 REFERENCES

- Bailey, R.A., 1974. Preliminary geologic map and cross sections of the Casa Diablo geothermal area, Long Valley Caldera, Mono County, California. USGS Open File Report, 1-2.
- Bailey, R.A., Dalrymple, G.B., and Lanphere, M.A., 1976. Volcanism, structure, and geochronology of the Long Valley Caldera, Mono County, California. *J. Geophys. Res.*, 81(5):725-744.
- Bailey, R.A., 1989. Geologic map of Long Valley Caldera, Mono- Inyo volcanic chain, and vicinity, Eastern California. USGS Miscellaneous Investigations Series Map I-1933.
- Bargar, K.E. and Beeson, M.H., 1981. Hydrothermal alteration in research drill hole Y-2, Lower Geyser Basin, Yellowstone National Park, Wyoming. *Amer. Mineral.*, 66:473-490.
- Blackwell, D.D., 1985. A transient model of the geothermal system of the Long Valley Caldera, California. *J. Geophys. Res.*, 90:11,229-11,241.
- Connolly, J.R., Shearer, C.K., and Papike, J.J., 1991. Petrography of Bishop Tuff in Phase I core from the LVF51-20 drill hole: a small window into a hydrothermal system in a resurgent caldera, Long Valley, California. *Eos, Trans. Am. Geophys. Union*, 72(44):505.
- Eichelberger, J.C., Vogel, T.A., Younker, L.W., Miller, C.D., Heiken, G.H., and Wohletz, K.H., 1988. Structure and stratigraphy beneath a young

phreatic vent: South Inyo Crater, Long Valley Caldera, California. *J. Geophys. Res.*, 93:13,208-13220.

Eichelberger, J.C. and McConnell, V.S. 1990. Initial stratigraphic results from the Magma Energy Exploratory Well, Long Valley Caldera, California. *Eos, Trans. Am. Geophys. Union*, 71:6, 260.

Flexer, S., 1991. Hydrothermal alteration and past and present thermal regimes in the western moat of Long Valley caldera. *J. Volcanol. Geotherm. Res.*, 48:303-319.

Grant, J.A., 1986. The isocon diagram-a simple solution to Gresens' equation for metasomatic alteration. *Economic Geology*, 81: 1976-1982.

Gresens, R.I., 1967. Compositional-volume relationships of metasomatism. *Chemical Geology*, 2:42-65.

Halliday, A.N., Fallick, A.E., Hutchinson, J. and Hildreth, W., 1984. A Nd, Sr and O isotopic investigation into the causes of chemical and isotopic zonation in the Bishop Tuff, California. *Earth Planet. Sci. Lett.*, 68: 379-374.

Hildreth, W. 1979. The Bishop Tuff: evidence for the origin of compositional zoning in silicic magma chambers. In: C.E. Chapin and W.E. Elston (Editors), *Ash Flow Tuffs*. *Geol. Soc. Am. Special Paper* 180:43-75.

Hildreth, W., and Mahood, G.A., 1986. Ring fracture eruption of the Bishop Tuff. *Geol. Soc. Am. Bulletin*, 97:396-403.

- Hill, D.P., Bailey, R.A., and Ryall, A.S., 1985. Active tectonic and magmatic processes beneath Long Valley caldera. eastern California: an overview: *J. Geophys. Res.*, 90: B13:111-120.
- Izett, G.A., and Obradovich, J.D., 1991. Dating of the Matuyama-Brunhes Boundary based on  $^{40}\text{Ar}/^{39}\text{Ar}$  ages of the Bishop Tuff and Cerro San Luis Rhyolite. *Geolog. Soc. Am. Bulletin*, 23(5):A106.
- Jackson, M.D. and Pollard, D.D., 1988. The laccolith-stock controversy: New results from the southern Henry Mountains, Utah, *Geolog. Soc. Am. Bulletin*, 100:117-139.
- Johnson, A.M, 1970. *Physical Processes in Geology*, Freeman, Cooper, and Co., San Francisco, CA, 577 pp.
- Keith, T.E.C and Bargar, B.E., 1988. Petrology and hydrothermal mineralogy of U.S. Geological Survey Newberry 2 drill core from Newberry Caldera, Oregon. *J. Geophys. Res.*, 93:10,174-10,190.
- Kerrick, D.M., 1974. Review of metamorphic mixed volatile ( $\text{H}_2\text{O}-\text{CO}_2$ ) equilibria, *Am. Mineral.*, 59:729-762.
- Layer, P.W., McConnell, V.S., and Eichelberger, J.C., 1992. New age constraints on magmatic and hydrothermal activity in central Long Valley Caldera, California. *Eos, Trans. Am. Geophys. Union*, 73(14):345.



- Leshner, C.M., Gibson, H.L., and Campbell, I.H., 1986. Composition-volume changes during hydrothermal alteration of andesite at Buttercup Hill, Noranda District, Quebec. *Geochemica et cosmochemica Acta*, 50: 2693-2705.
- Lipman, P.W., 1984. The roots of ash flow calderas in Western North America: windows into the tops of granitic batholiths. *J. Geophys. Res.*, 89:B10:8801-8841.
- Long Valley Science Panel, 1991. Investigation of active volcanic processes in Long Valley Caldera via deep continental drilling. U.S. DOE, UCRL-PROP-108826, 1-31.
- Mankinen, E.A., Gromme, C.S., Dalrymple, G.B., Lanphere, M.A., and Bailey, R.A., 1986. Paleomagnetism and K-Ar ages of volcanic rocks from Long Valley caldera, California. *J. Geophys. Res.*, 91:633-652.
- McConnell, V.S., Eichelberger, J.C., and Keskinen, M.J., 1991. Phase II of the Long Valley Exploratory Well, Long Valley Caldera, California: early geologic results. *Eos, Trans. Am. Geophys. Union*, 72(44):550.
- Miller, C.D., 1985. Holocene eruptions at the Inyo volcanic chain, California: implications for possible eruptions in Long Valley. *Geology*, 13:14-17.
- Muffler, L.J.P. and Williams, D.L., 1976. Geothermal investigations of the U. S. Geological Survey in Long Valley, California, *J. Geophys. Res.*, 81:721-724.

- O'Neil, J.R. and Taylor, H.P., Jr., 1967. The oxygen isotope and cation exchange chemistry of feldspars. *Am. Mineral.*, 52: 1414-1437.
- Rinehart, C.D. and Ross, D.C., 1964. Geology and mineral deposits of the Mount Morrison Quadrangle Sierra Nevada, California. U.S. Geol. Surv. Prof. Paper, 385:7-30.
- Rundle, J.B., and Hill, D.P., 1988. The geophysics of a restless caldera--Long Valley, California. *Ann. Rev. Earth Planet, Science*, 16:251-271.
- Sampson, D.E. and Cameron, K.L., 1987. The geochemistry of the Inyo Volcanic Chain: multiple magma systems in the Long Valley Region, Eastern California. *J. Geophys. Res.*, 92:B10, 10,403-10,421.
- Sass, J.H., Jacobson, R., and Sorey, M.L., 1991. Implications of thermal observations in the Long Valley Exploratory Well. *Eos, Trans. Am. Geophys. Union*, 72(44):504.
- Savage, J.C. and Clark, M.M., 1982. Magmatic resurgence in Long Valley Caldera, California; possible cause of the 1980 Mammoth Lakes earthquakes, *Science*, 217:531-533.
- Shevenell, L., Goff, F., Grigsby, C.O., Janik, C.J., Trujillo, P.E. and Counce, D., 1987. Chemical and isotopic characteristics of thermal fluids in the Long Valley Caldera lateral flow system, California. *Trans. Geotherm. Resour. Council*, 11: 195-201.

- Smith, B.M. and Suemnicht, G.A., 1991. Oxygen isotope evidence for past and present hydrothermal regimes of Long Valley caldera, California. *J. Volcanol. Geotherm. Res.*, 48:319-339.
- Smith, B.M., Gunderson, R.P., and Suemnicht, G.A., 1988. Oxygen isotope evidence for magma-groundwater interactions in early, post-collapse rhyolites from the Long Valley Caldera. *Geol. Soc. Am. Abstr. Programs*, A114.
- Sorey, M.L., 1985. Evolution and present state of the hydrothermal system in Long Valley caldera. *J. Geophys. Res.*, 90:11,219-11,228.
- Sorey, M.L., Suemnicht, G.A., Sturchio, N.C., and Nordquist, G.A., 1991. New evidence on the hydrothermal system in Long Valley Caldera, California, from wells, fluid sampling, electrical geophysics, and age determinations of hot-spring deposits. *J. Volcanol. Geotherm. Res.*, 48:229-263.
- Steiger, R.H. and Jäger, E., 1977. Subcommittee on geochronology: Convention of the use of decay constraints in geo- and cosmochemistry. *Earth and Planetary Science Letters*, 36:359-362.
- Sturchio, N.C., Muehlenbachs, K.,<sup>89</sup> and Seitz, M.G., 1986. Element redistribution during hydrothermal alteration of rhyolite in an active geothermal system: Yellowstone drill core Y-7 and Y-8. *Geochimica et Cosmochimica Acta*, 50: 1619-1631.
- Stuckless, J.S. and O'Neil, J.R., 1983. Petrogenesis of the Superstition-Superior volcanic area as inferred from strontium- and oxygen-isotope studies. *Geol. Soc. Am. Bull.*, 84: 1987-1998.

- Suemnicht, G., 1987. Results of deep drilling in the western moat of Long Valley, California. *Eos, Trans. Am. Geophys. Union*, 68 (40): 785, 798.
- Suemnicht, G.A. and Varga, R.J., 1988. Basement structure and implications for hydrothermal circulation patterns in the western moat of Long Valley caldera, California. *J. Geophys. Res.*, 93 (B11): 191-207.
- Taylor, H.P., 1968. The oxygen isotope geochemistry of igneous rocks. *Contr. Mineral. and Petrol.*, 19: 1-71.
- Vogel, T.A., Younker, L.W., and Schuraytz, B.C., 1987. Constraints on magma ascent, emplacement, and eruption: geochemical and geological data from drill-core samples at Obsidian Dome, Inyo Chain, California. *Geology*, 15:405-408.
- White, A.F., Peterson, M., Wollenberg, H., and Flexer, S., 1990. Sources and fractionation processes influencing the distribution of D,  $^{18}\text{O}$ , and  $^{13}\text{C}$  in the Long Valley hydrothermal system, California, USA. *Appl. Geochem.*, 5:571-585.

### **III.1 Oxygen isotope compositions of intracaldera rocks: hydrothermal history of the Long Valley Caldera, California<sup>2</sup>**

#### **III.2. ABSTRACT**

The Bishop Tuff and associated rocks filling Long Valley Caldera, California represent a case where thick and relatively uniform geologic units of known initial compositions have been subjected to a strong geothermal fluid flux within an enclosed basin. Oxygen isotopic compositions within individual components of this "flux plate" are used to characterize a magmatically-driven paleohydrothermal system. Oxygen isotope ratios of silicate components analyzed with a laser-probe/mass-spectrometer system clearly illustrate the isotopic heterogeneity in the felsic volcanic rocks resulting from moderately high-temperature hydrothermal alteration. This hydrothermal activity is linked to periods of post-caldera-collapse volcanism and resurgence in the central caldera.

In general, <sup>18</sup>O depletion in the Bishop Tuff resulting from exchange with hydrothermal fluids proceeds as pumice > matrix > sanidine > quartz due to progressive resistance to alteration. Samples from the Long Valley Exploratory Well (LVEW) centered on the resurgent dome show downward increasing exchange and disequilibrium over the well's 2000-m depth. A flanking well shows the opposite pattern over 1300 m depth. Oxygen isotope isopleths along a west-east vertical cross-section of the caldera reveals convective circulation upwards and outwards from the central resurgent dome.

---

<sup>2</sup> Oxygen isotope compositions of intracaldera rocks: hydrothermal history of the Long Valley Caldera, California by V.S. McConnell, J.W. Valley, and J.C. Eichelberger for submittal to J. Volcanol. Geotherm. Res., 1996.

A paleotemperature maximum of  $\sim 350^{\circ}\text{C}$  in LVEW and a geothermal gradient of  $\sim 130^{\circ}\text{C}/\text{km}$  are deduced from feldspar/water oxygen isotope fractionation equation using pumice and sanidine. This is consistent with the degree of alteration and the secondary mineralogy. Present-day temperature maximum in the well is  $\sim 100^{\circ}\text{C}$ , and the geothermal gradient is  $50^{\circ}\text{C}/\text{km}$ .

Fossil hydrothermal water, trapped in fluid inclusions in hydrothermal vein quartz hosted by intracaldera rocks, has a calculated oxygen isotope composition of  $-10.2\text{‰}$  based on chemistry and trapping temperature. This is  $4\text{‰}$  heavier than the average value for the present-day hydrothermal water and consistent with higher temperatures and water/rock ratios.

Intrusive activity was initiated in the resurgent dome area soon after caldera collapse (760 ka), but migrated toward the western margin of the caldera, the locus of Holocene volcanism. Thus, the central hydrothermal system matured and waned as the heat sources from intrusions shifted westward. Geophysical evidence of renewed intrusive activity located beneath the resurgent dome may presage a future renewal of the cycle of hydrothermal activity in the central caldera region. Although the hydrothermal activity is complex and transitory, this history is normal for a large, relatively active caldera system such as Long Valley Caldera.

### III.3 INTRODUCTION

The episodic nature of development of silicic calderas and associated hydrothermal systems was established through geologic field work (e.g., Smith and Bailey, 1968; Smith and Shaw, 1975; Lipman, 1984) and geochemical studies of active hydrothermal systems (e.g., Blackwell, 1985; Gardner et al., 1986; Sturchio et al., 1990). Cyclic behavior of hydrothermal systems is evident from the occurrence of fossil fumarolic and hot spring deposits and secondary mineralization not in chemical equilibrium with the present-day geothermal gradient and/or hydrothermal flux. What is not well understood is the causal and space-time relationship between the inferred source of heat, that is, the magma chamber responsible for the volcanic activity, and the hydrothermal activity (Criss and Taylor, 1986). Quaternary systems, like the Long Valley Caldera in east-central California, provide ideal locations for study of fundamental processes of caldera development (Smith and Bailey, 1968; Hildreth, 1981; and Lipman, 1984). Recently, Long Valley has come under close scrutiny related to practical concerns such as geothermal energy potential and volcanic hazards (Rundle and Hill, 1988; LVEW Science Panel, 1991).

This study provides a view of the fossil hydrothermal activity in a relatively young caldera system. By analyzing well samples, a caldera not yet eroded to expose the roots of the system and consequently degraded by near-surface alteration can be studied. The heating of a hydrothermal system is in turn the record of cooling of a shallow magma body. How long magma bodies persist in the mid to upper crust is information fundamental to

understanding the evolution of silicic igneous rocks and, more practically, the relationship of silicic volcanism to geothermal resources.

In the last 30 years, exploratory and scientific drilling into the Long Valley intracaldera has opened a window to its internal structure. In this study, we emphasize the centrally located resurgent dome (Figure III.1) concentrating on understanding the relationship between post-caldera-collapse intrusions, resurgence, and hydrothermal activity. The primary sources of material were the core and cuttings from the Long Valley Exploratory Well (LVEW), located near the summit of the 500-m-high resurgent dome. Drilled in 1989 and 1991 to a total depth of 2.3 km, LVEW penetrated post- and syn-caldera-collapse volcanic rocks, bottoming 400 m into the Mesozoic metavolcanic and Paleozoic metasedimentary rocks that form the basement of the central caldera (Figure III.2). Samples from several earlier exploratory wells on or near the resurgent dome were used to complete the sample suite and increase spatial coverage (Figure III.1)

Alteration minerals identified by petrologic examination and X-ray diffraction consist of ubiquitous quartz, pyrite, calcite, mixed illite/smectite clays becoming more illite-rich with depth, sericitic mica, and the appearance of chlorite and epidote with depth (McConnell et al., 1995). In the Bishop Tuff, plagioclase phenocrysts are generally albitized and/or replaced by a patchwork of calcite and clay or sericitic mica. Pumice clasts display both high-temperature spherulitic crystallization to quartz and feldspar and moderate-temperature hydrothermal overprints of clay and potassium feldspar.



The utility of light stable isotope analyses of hydrothermal minerals and host rocks to characterize volcanic hydrothermal areas has been well established. Oxygen isotope geochemistry has been used at such areas as Ohaki-Broadlands Geothermal Field, New Zealand (Eslinger and Savin, 1973); Valles Caldera, New Mexico (Goff et al., 1985); and Newberry Crater, Oregon (Carothers et al., 1987) to infer fluid temperatures, water/rock ratios, and physical conditions of mineral deposition. Isotope geothermometric calculations require the assumption that alteration components of the volcanic rocks precipitated in isotopic equilibrium with coeval hydrothermal fluids, a condition not easily proven due to the size and dispersion of the alteration minerals. These calculations are generally made by measuring a representative portion of the heterogeneous volcanic host rock, and by assuming that isotopic exchange between the pre-existing rock and the hydrothermal fluid has reached equilibrium and that kinetic isotopic exchange was not a strong influence. The assumption of isotopic equilibrium tacitly requires that minerals and rock are isotopically homogeneous, an assumption that is seldom tested. Whole-rock oxygen isotope geothermometry of intracaldera Bishop Tuff samples from LVEW indicates the rocks were subjected to alteration by fluids with a *minimum* geothermal gradient of 70°C/km (McConnell et al., 1995). The present-day geothermal gradient of 50°C/km beneath the resurgent dome is insufficient to have caused the degree of alteration observed in the intracaldera rocks (McConnell, 1993).

The whole-rock oxygen isotope studies (Smith and Suemnicht, 1991; McConnell et al., 1995) leave several questions unanswered. In particular, how reliable is the paleogeothermal gradient calculated from  $\delta^{18}\text{O}$  values for bulk

whole-rock samples of Bishop Tuff? What is the areal extent of the paleohydrothermal system within the resurgent dome? Can a heat source be identified based on spatial distribution of the isotopic values? Furthermore, McConnell et al. (1995) established a link between sill-like rhyolite intrusions within the Bishop Tuff beneath the resurgent dome and resurgence in the caldera. Is there a chronological link between the occurrence of intrusive activity and hydrothermal events?

Recent work has shown the importance of isotope microanalysis for investigating crystallization and fluid/rock interaction in non-equilibrium metamorphic regimes and plutonic rocks (Valley and Graham, 1991, 1993, 1996; Kohn et al., 1993; Eiler et al., 1995). In this study, a laser-probe/mass-spectrometer provides spatial resolution of 0.5 mm necessary to measure the oxygen isotope ratios in microsamples of primary and alteration silicate phases in volcanic and metamorphic rocks. This has allowed us to evaluate the heterogeneity of isotopic exchange during hydrothermal alteration, to determine the most representative portion of the rock for further interpretations, and to interpret the spatial alteration pattern around the resurgent dome.

### *III.3.1 Geologic Setting*

Previous investigators have described the volcanic history of the Long Valley area, both preceding and following caldera development (e.g., Gilbert et al., 1968; Smith and Bailey, 1968; Hildreth, 1979; Huber, 1981; Metz and Mahood, 1985; Miller, 1985; Chaudet, 1986; Mankinen et al., 1986; Eichelberger et al., 1988), which is briefly summarized here. The Long Valley

Caldera represents culmination of volcanic activity that began with extensive mafic eruptions approximately 3.6 Ma in a graben situated east of the High Sierran front and west of the westernmost extension of the Basin and Range Province (Huber, 1981). Progressively more silicic eruptive activity proceeded from 3.0 Ma through the 2.1-0.8 Ma Glass Mountain rhyolite complex, and is viewed as evidence of magmatic accumulation and differentiation in the crust which formed a large shallow, zoned magma chamber (Bailey et al., 1976; Hildreth, 1979; Bailey, 1989). Inflation of this chamber formed arcuate fractures along which the chamber roof eventually failed, resulted in catastrophic Plinian and pyroclastic eruptions from multiple circumferential vents at 760 ka (Bailey et al., 1976; Izett and Obradovich, 1991; McConnell et al., 1995). Over a period of less than two years (Hildreth, 1977; Snow and Yund, 1988) these eruptions distributed ashfall deposits and voluminous ash flows of Bishop Tuff coeval with hinged piston-cylinder collapse that formed the 17x30 km-wide caldera. Syn-eruptive subsidence permitted Bishop Tuff ash flows to partially backfill the caldera to depths of as much as 1500 m. An estimated total volume of 600 km<sup>3</sup> of rhyolitic magma (i.e., dense rock equivalent) formed pyroclastic outflow sheets, intracaldera ignimbrite, and proximal and distal ash deposits (Bailey et al., 1976; McConnell et al., 1995). The intracaldera Bishop Tuff lies at a lower elevation than its correlative outflow and was completely buried by later lavas, tuffs, and sediments, implying some further post-eruptive subsidence of the caldera (Bailey et al., 1976; Eichelberger and McConnell, 1990; McConnell et al., 1995). Two major episodes of rhyolitic volcanic activity within the caldera occurred after caldera collapse; 730 to 600 ka aphyric to sparsely porphyritic Early Rhyolite,

considered coeval with resurgence, and the 500 to 100 ka phenocryst-rich Moat Rhyolite flows (Bailey et al., 1976; Bailey, 1989).

Basaltic lava ponded in the west moat to a depth of 250 m from 200 to 60 ka (Bailey, 1989; Eichelberger et al., 1988; Vogel et al., 1994), also erupting from vents southwest of the caldera to form Devil's Postpile. Low-silica rhyolites and associated dacites erupted intermittently from local vents in the west moat and also formed the Mammoth Mountain cumulo-volcano along the southwest caldera rim (Bailey et al., 1976). Silicic volcanic activity resumed in the Long Valley area between 40 and 38 ka with the onset of formation of the Mono Craters rhyolite dome, flows, and craters north of the caldera (Bailey, 1989). This activity continued virtually to the present emplacement of the 0.65-0.55 ka Inyo chain of rhyolite domes and craters that intersect the caldera's west moat (Figure III.1; Miller, 1985; Eichelberger et al., 1988).

### *III.3.2 Hydrothermal History*

Sorey et al. (1991) lists Th/U age determinations for hot-spring deposits indicating two periods of peak caldera-related hydrothermal activity occurring at approximately 300 ka and 40 ka, with a hiatus in activity between 200 ka and 40 ka. The timing of the most recent hydrothermal flux appears to correspond to reactivation of silicic volcanism in the Long Valley area (Bailey, 1989). Although the highest temperatures (202-214°C) occur in intracaldera volcanic fill at depths of 335 m and from 900 to 1100 m in the west moat, the roots of the hydrothermal system have not been located (Sorey et al., 1991). Hydrothermal waters from the present-day system vent primarily as

fumaroles on the south side of the resurgent dome and as hot springs along its west and south flanks. Cooler, more dilute warm springs occur in the east moat. Comparison of the strontium and carbon isotope ratios of Long Valley Caldera thermal waters and of rocks from across the caldera has been interpreted to indicate deep circulation of meteoric water in the silicic and calcareous Paleozoic metasedimentary basement rocks (Goff et al., 1991). Compositional gradients in Cl and B in thermal waters and oxygen isotope ratios in alteration minerals corroborate the model of a west-to-east lateral plume being chemically and thermally diluted by cold meteoric water (Goff et al., 1991; Sorey et al., 1991; White and Peterson, 1991). Possibly the thermal upwelling of deeply circulating meteoric water is heated by recent intrusions originating beneath Mammoth Mtn. (Figure III.1) and/or the Inyo chain and flows laterally eastward through the less radiogenic intracaldera volcanic rocks. Alternatively, recharge may be associated with an area of low-resistivity extending into the Paleozoic basement rocks identified by two-dimensional magnetotelluric models (Sorey et al., 1991). This U-shaped region tracks the inferred projection of the Laurel-Convict fault (Figure III.1) within the caldera adjacent to the western resurgent dome. In this case, flow would travel both to the west and east (Sorey et al., 1991).

More difficult to interpret is the activity of paleohydrothermal system(s) and identification of a heat source or sources. Bailey et al. (1976) inferred that at least one ancient hydrothermal system located in the central caldera region peaked approximately 300 ka. His inference is based on Th/U age determinations of argillaceous zones along the flanks of the resurgent dome which yielded a date of 310-210 ka (Sorey et al., 1991) and mapping of

hydrothermal alteration in lacustrine deposits southeast of the resurgent dome. In addition, the extent of hydrothermal alteration in the intracaldera volcanic fill beneath the resurgent dome requires higher temperatures than the present-day 50°C/km gradient measured in LVEW (Sass et al., 1991; Smith and Suemnicht, 1991; McConnell et al., 1995).

### *III.3.3 Previous oxygen isotope studies*

Halliday et al. (1984) reported the first oxygen isotope measurements of the Bishop Tuff, conducted on silicate components from outflow sheet samples. Whole-rock pumice blocks and sanidine separates, measured using externally heated Ni reaction vessels (Clayton and Mayeda, 1963), yielded  $\delta^{18}\text{O}$  values of 5.9-10.3‰ and 6.7-7.9‰, respectively. Disequilibrium between phases was attributed to post-eruptive interaction with meteoric water. They argued that an oxygen isotope value derived from pristine sanidine samples of  $7.0 \pm 0.2$ ‰ represents the best estimate of the composition of the parent magma.

Smith and Suemnicht (1991) extended the whole-rock oxygen isotope study to include intracaldera volcanic and basement rocks retrieved from wells within the caldera and metasedimentary outcrop samples of the Mt. Morrison roof pendant. Analyses of hand-picked core and drill cuttings samples were made using Ni reaction vessels with the goal of acquiring a sense of the timing of alteration in the intracaldera rocks, considered the pathways for transportation of hydrothermal fluids. Measured oxygen isotope values were plotted on depth profiles for the wells and compared to oxygen isotope values calculated using the present-day temperature gradients from the wells and assuming water/rock exchange for the silicic rocks to be fully equilibrated and

equal to water/potassium feldspar exchange. They assumed the water exchanging with the silicic rocks to be of the same chemical and isotopic composition as present-day thermal waters in the caldera and used the measured value from Well RDO-8 ( $\delta^{18}\text{O} = -14.3\text{‰}$ ) for the calculations. Most significant is the observation that the intracaldera rocks in the west moat are uniformly higher in  $\delta^{18}\text{O}$  composition relative to the calculated isotopic value for the temperature profile. They interpret this as indicating a relatively young hydrothermal system exists in the west moat where rocks have not fully equilibrated isotopically with the low  $\delta^{18}\text{O}$  circulating fluid. Only in the Clay Pit well (CP-1 in Figure III.1) on the resurgent dome is there evidence of isotopic depletion in the rock, in this case the Bishop Tuff, that far exceeds the calculated value. This is regarded as evidence of a fossil hydrothermal system that circulated fluids in the central caldera at temperatures in excess of the present-day system.

McConnell et al. (1995) reported the results of conventional oxygen isotope analysis on whole-rock samples of intracaldera volcanic rocks from the LVEW. Whole-rock samples of the Bishop Tuff display a trend of decreasing  $\delta^{18}\text{O}$  with depth from 1.7 to -1.2‰. Moreover, all values are lowered in  $\delta^{18}\text{O}$  relative to outflow sheet equivalents of 7.0‰. This trend is best explained by increasing temperature and/or the extent of fluid/rock exchange with depth and is corroborated by increasing hydrothermal alteration of the Bishop Tuff (McConnell et al., 1995). Figure III.2 shows the primary stratigraphy and alteration mineralogy of LVEW. Three aphyric Early Rhyolite intrusions into the Bishop Tuff are similarly lowered in  $\delta^{18}\text{O}$  relative to extrusive equivalents.

However, unlike the tuff, the trend of lower values in these intrusions appears independent of depth in the well, with values ranging from 1.4 to -0.3‰.

#### III.4 SAMPLE SELECTION AND PREPARATION

The sample suite for the present investigation consists of drill core and cuttings from all lithologic units identified in LVEW, cuttings from volcanic rocks in LV13-21, core samples of Early Rhyolite and Bishop Tuff from LV13-26, and core samples of Bishop Tuff from SF38-32, LV48-29, and LV66-28 (Figures III.1&III.2). Surface samples of Early Rhyolite, Bishop Tuff, and Paleozoic metasediments (Figure III.1) were also selected for comparative analysis and processed by the same procedures as the well samples. Individual samples were prepared for analysis in a manner appropriate to their composition and the sample type. All analyses were performed on discrete pieces removed from the whole-rock samples, thus avoiding contamination by depth and edge effects reported when lasing *in situ* samples (Elsenheimer and Valley, 1992). For example, the cryptocrystalline Early Rhyolite intrusions found in the Bishop Tuff in LVEW were generally prepared as tiny whole-rock chips of ~2 mg. After microscopic inspection, chips were hand-picked from thin sliced wafers (500-900 μm thick) in areas determined to be free of hydrothermal microveining or the rare phenocrysts. Oxygen isotope composition of extrusive Early Rhyolite was measured on aphyric obsidian chips or fresh, glassy tephra cuttings. Chips of fine-grained siliceous or graphitic hornfels, quartzite, and pelite were also hand-picked from thin wafers to exclude porphyroblasts or alteration mineralogy. The lithic- and crystal-rich Bishop Tuff samples were separated into pumice, matrix or altered



rock, quartz phenocrysts, and sanidine phenocrysts and prepared accordingly. Individual pumice or fiamme clasts and glassy or altered matrix were dry-drilled with either a 0.25 mm tungsten carbide or 3 mm diamond bit in areas determined to be relatively free of lithics, phenocrysts, or hydrothermal veining. The dry powders were collected and weighed for analysis. Individual phenocrysts of quartz or sanidine up to 3 mm in diameter were hand-picked from thin wafers or separated from cuttings and immersed in a 1.5 N HCl bath for 2 minutes to eliminate any calcite contamination. Quartz phenocrysts in the Bishop Tuff are generally distinctive subhedral crystals or crystal shards with little macroscopic evidence of resorption or disequilibrium growth. Most phenocrysts contain devitrified melt inclusions that were unavoidable when hand-picking samples. Phenocrysts of primary oligoclase are generally albitized and/or replaced by hydrothermal calcite, rendering them unfit for analysis. Sanidine phenocrysts were generally less altered and more abundant than plagioclase phenocrysts. Where hydrothermal alteration is intense, the sanidine phenocrysts display some increase in K/Na ratio at crystal edges. In addition, they generally become cloudy and skeletal, and contain clay or calcite inclusions. Phenocrysts chosen for analyses were not cleaned in HF to eliminate hydrothermal clay contamination or melt inclusions due to their fragile nature. This decision probably led to some of the spread in the quartz phenocryst data which will be discussed later in the article. Fracture-filling quartz (in core samples) was hand-separated and cleaned in HCl to eliminate calcite.

Sanidine phenocrysts were placed in the sample holder as-plucked from the sample matrix. Quartz phenocrysts were lightly crushed in an  $\text{Al}_2\text{O}_3$  mortar to ensure complete fusing during lasing.

### III.5 DATA COLLECTION, STANDARDIZATION, AND ANALYTICAL PRECISION

University of Wisconsin's (UW)  $\text{CO}_2$  laser-probe/mass-spectrometer designed for oxygen isotope analysis allowed us to obtain rapid and precise data from small samples in the range of 0.5-2 mg yielding 5-20  $\mu\text{mol}$ s of  $\text{CO}_2$ . In addition, we compared the accuracy of microanalysis of volcanic samples to conventional bulk analysis of the same or similar rocks (See Appendix III). Sample oxygen isotope ratios are reported as  $\delta^{18}\text{O}$  values in the standard per mil (‰) notation relative to Standard Mean Ocean Water (SMOW). Details of the UW laser-probe system and for preparation and analysis of plutonic rocks are described elsewhere (Elsenheimer and Valley, 1992, 1993; Kohn and Valley, 1993; Valley et al., 1995). We modified those procedures to be appropriate for the more altered and heterogeneous volcanic rocks of this study. Individual samples weighing 0.5-2 mg were loaded into 2 mm diameter wells drilled in a solid block of Ni. During standard sample pretreatment, successive aliquots of 300-1000  $\mu\text{mol}$  of  $\text{BrF}_5$  reagent were introduced into the sample chamber at 20°C and allowed to react for intervals of 1 minute, 10 minutes, and overnight. This process reduced extraneous oxygen by removing reactive contaminants, including  $\text{H}_2\text{O}$  remaining in the samples and in the sample chamber. Hydrous, secondary silicate minerals may persist in even the most carefully hand-picked and cleaned sample, and some oxygen isotope fractionation may occur at the surface of the sample during overnight

pretreatment with  $\text{BrF}_5$  prior to analysis. In order to decrease this effect, powdered samples of pumice clasts and of tuff matrix were gently fused *in vacuo* with a defocused, low-power laser beam. This process typically produced a sphere of glass, reducing surface area, and dehydrating the sample prior to the routine sample pretreatment described above. The sample chamber was then flushed with  $\sim 500 \mu\text{mol}$  of  $\text{BrF}_5$  reagent and the pretreatment procedure continued. Sanidine phenocrysts were prepared for overnight pretreatment by introducing several small fluxes of  $\text{BrF}_5$  into the sample chamber, followed by flushing the chamber. This generated a surface barrier of reacted material (Elsenheimer and Valley, 1992), hampering further deterioration of the feldspar without altering the isotope composition. The phenocrysts were then treated by the same routine as the powdered samples, except with  $200 \mu\text{mol}$  of  $\text{BrF}_5$ .

Before beginning sample analysis, the sample chamber was evacuated of gases produced by pretreatment and at least one blank background analysis run. Blanks were produced by flooding the sample chamber with  $1000 \mu\text{mol}$  of  $\text{BrF}_5$  (no sample is fused) which is then allowed to react for at least 20 minutes. Reactants were then treated as a sample and  $\mu\text{mol}$   $\text{CO}_2$  measured. Consecutive blanks were run until the  $\text{CO}_2$  concentration of the background is  $<1 \mu\text{mol}$ . For non-reactive samples such as garnet and zircon, these blanks typically yield on the order of  $\leq 0.1 \mu\text{mol}$   $\text{CO}_2$  (Valley et al., 1994a, 1995). For the more reactive glasses and minerals of this study, initial blanks were higher, 2 to  $7 \mu\text{mol}$ , but always diminished to  $\leq 1.2 \mu\text{mol}$ . In cases where blanks were high, such as for feldspar, analysis of the background  $\text{CO}_2$  yielded values of  $\delta^{18}\text{O}$  similar to the sample, suggesting that the effect on analytical accuracy would

be small (see also Elsenheimer and Valley, 1992). Samples were reacted in the presence of 1000  $\mu\text{mol}$  of  $\text{BrF}_5$ . Oxygen gas was cryogenically purified, converted to  $\text{CO}_2$  by reaction with heated graphite, and introduced directly into the mass-spectrometer.

UW intralaboratory Gore Mountain garnet standard, UWG-1 with a value of  $6.03 \pm 0.13\text{‰}$  ( $1\sigma$ ) (Kohn et al., 1993), was measured at the beginning and end of daily analysis. The overall average value of UWG-1 for this study was  $6.03 \pm 0.11\text{‰}$  ( $1\sigma$ ) ( $n=41$ ), and the daily reproducibility never varied beyond  $\pm 0.16\text{‰}$ . In addition, NBS-28 quartz standard samples were included in several daily runs, producing a monthly average of  $9.39 \pm 0.07\text{‰}$  ( $1\sigma$ ). This led to a  $\Delta_{\text{NBS28-UWG-1}} \approx 3.4\text{‰}$  for this study, a value identical to previous work conducted on this laser-probe/mass-spectrometer (Kohn et al., 1993).

Generally, repeats of samples were loaded to ensure the precision of analysis by the laser-probe system. Analyses of pumice clasts, quartz and sanidine phenocrysts, and metamorphic whole-rocks yielded precisions similar to the standard analyses of  $\pm 0.2\text{‰}$ . However, not all replicates were successfully measured. Infrequently, during fusing, powder samples sputtered out of the sample holder or deposited ejecta into other sample wells, contaminating both samples. In such cases, visual examination prevented analysis of contaminated samples. Analyses of Bishop Tuff matrix powders and Early Rhyolite intrusion powders or chips were less precise, ranging from  $\pm 0.1\text{‰}$  to  $0.5\text{‰}$ . Repeats of microscopically homogeneous samples selected from cuttings from single well depths showed a wide range of precision, from  $\pm 0.3$  to  $2.2\text{‰}$ . The very nature of cuttings samples makes it difficult to assess the reason for this poor precision of the measurements. In the case of the

altered Bishop Tuff matrix and Early Rhyolite intrusions, even the most carefully selected sample cannot totally eliminate the possibility of contamination by phenocrysts or lithics, or ubiquitous fine-grained alteration minerals.

### III.6 RESULTS

The complete data set of laser extracted oxygen isotope values is tabulated in Table III.1. Figure III.1 shows the well and sample locations and Figure III.2 the lithologic stratigraphy of the central caldera at the LVEW location. Figures III.3a-6 display  $\delta^{18}\text{O}$  vs. depth plots for the wells. A magmatic range of oxygen isotope composition of 7.0 to 8.3‰ set by the composition of sanidine and quartz phenocrysts from unaltered, outcrop samples of Bishop Tuff, and Early Rhyolite obsidian is marked. For clarity, average  $\delta^{18}\text{O}$  values discussed in the text are presented with  $1\sigma$  range of error.

#### *III.6.1 Long Valley Exploratory Well (LVEW)*

LVEW is the only well that has intersected the complete central intracaldera Quaternary stratigraphy, from the Early Rhyolite of the resurgent dome to the metamorphic basement rocks of the caldera floor. Figure 3a is a plot of the  $\delta^{18}\text{O}$  data vs. depth for LVEW samples and outcrop equivalents of the intracaldera lithic units.

It is evident that coexisting silicate components in the Bishop Tuff have extreme differences in their isotopic ratios and these differences increase with depth. Although the order of  $\delta^{18}\text{O}$  concentration of quartz>sanidine>pumice mimics magmatic trends, the relative differences between quartz and sanidine

are far beyond the generally accepted range for felsic igneous rocks of  $\Delta^{18}\text{O}_{(q-f)} \leq 2\text{‰}$  (O'Neil, 1986). Moreover, with the exception of quartz phenocrysts in the Bishop Tuff, all rocks or silicate minerals measured in the well are isotopically lighter than equivalent outcrop samples. In most instances, the  $\delta^{18}\text{O}$  for sanidine and pumice is not within the range reported for felsic igneous rocks and rock-forming minerals of +7 to +13‰ (Taylor, 1968, 1974; Taylor and Sheppard, 1986) indicating exchange.

It is necessary to carefully evaluate these results in view of the considerable variation in  $\delta^{18}\text{O}$  values reported for presumably unaltered outcrop samples. For example, Smith and Suemnicht (1991) record a range of values for Early Rhyolite pumice and tephra from +0.3 to +10.4‰. Fresh, vitreous obsidian samples most likely represent the magmatic  $\delta^{18}\text{O}$  composition of the Early Rhyolite. Values of  $8.3 \pm 0.1\text{‰}$  (McConnell et al., 1995; this study) and  $7.5 \pm 0.7\text{‰}$  (Smith and Suemnicht, 1991) are reported for Early Rhyolite obsidian. Outflow sheet Bishop Tuff pumice separates yielded  $\delta^{18}\text{O}$  values ranging from 5.1 to 10.3‰ (Halliday et al., 1984; Smith and Suemnicht, 1991; this study). Sanidine phenocrysts, thought to represent the best estimate of Bishop Tuff magmatic  $\delta^{18}\text{O}$  (Halliday et al., 1984), yield values of 6.1‰ from a single sanidine phenocryst (this study), and  $7.0 \pm 0.2\text{‰}$  for five sanidine separates (Halliday et al., 1984). Quartz phenocrysts in the Bishop Tuff have remained resistant to isotopic exchange over the time and temperature of hydrothermal flux with a mean value of  $7.7 \pm 0.5\text{‰}$  for all LVEW samples compared to  $8.0 \pm 0.3\text{‰}$  for outcrop samples (Taylor, 1968; this study). Thus a range of 7.0 to 8.3‰ is set as the unaltered and unweathered magmatic oxygen isotope composition for the felsic volcanic rocks.

Measurements were made on quartz displaying a variety of morphologies and taken from various locations in the tuff. For example, shards, anhedral, and euhedral phenocrysts were picked from locations both proximal and distal to hydrothermal veins in the matrix, and in pumices. Although the quartz values bracket the magmatic range on Figure III.3a, no one morphology or sample location dominates. The precision of these measurements might have benefited from more extensive sample preparation such as cleaning with HF to remove any clay or alteration contamination.

Pumice and sanidine appear to be the most sensitive monitors of isotopic exchange with low  $\delta^{18}\text{O}$  hydrothermal fluids at elevated temperatures. Partially to wholly devitrified and/or altered pumice, obsidian, and altered sanidine phenocrysts are the most depleted in  $\delta^{18}\text{O}$  relative to outflow sheet equivalents, showing subparallel trends of increasing depletion with depth in LVEW. Pumice or fiamme yielded a mean value of  $\delta^{18}\text{O} = -2.0 \pm 0.15\text{‰}$  at the deepest location where could be confidently identified (1183 m). Below 1200 m, the Bishop Tuff becomes too densely welded to identify pumice, and by 1700 m the entire Bishop Tuff matrix is hydrothermally leached to a uniform white.

Sanidine phenocrysts also visually display the effects of increasing hydrothermal alteration with depth, changing from clear to cloudy and containing patchy areas of calcite replacement. Sanidine has a mean  $\delta^{18}\text{O}$  value of  $-4.4 \pm 0.03\text{‰}$  for the deepest Bishop Tuff sample at 1794 m and an overall minimum mean value of  $-6.3 \pm 0.3\text{‰}$  at 1772 m depth. Sampling of the sanidine phenocrysts was intermittent due to some intervals with increased alteration and sparse phenocrysts.

Aphyric, cryptocrystalline Early Rhyolite intrusions into the Bishop Tuff (McConnell and Eichelberger, 1990; McConnell et al., 1995) were analyzed as whole rock samples. Samples at 784 m and 801 m from a 45 m thick intrusion yielded  $\delta^{18}\text{O}$  values of  $-1.2\pm 0.5\text{‰}$  and  $1.4\pm 0.2\text{‰}$ , respectively. McConnell et al. (1995) reported very different  $^{40}\text{Ar}/^{39}\text{Ar}$  ages from these two depths and suggest this may be the site of multiple intrusive activity over the time span of resurgence. Samples from deeper intrusions at 1222 m and 1530 m in LVEW have statistically identical values of  $\delta^{18}\text{O} = -0.5\pm 0.3\text{‰}$  and  $-0.5\pm 0.2\text{‰}$ , respectively. An intrusion at 927 m has a value of  $3.0\pm 0.5\text{‰}$ . All these values are depleted in  $\delta^{18}\text{O}$ , assuming their initial magmatic composition matched Early Rhyolite extrusive rocks. Furthermore, the deeper intrusions do not follow the trend of lowered  $\delta^{18}\text{O}$  with depth observed in the Bishop Tuff (Figure III.3a) but appear similar in composition regardless of depth.

It is worthwhile to note that Smith and Suemnicht (1991) report values of  $+0.3\text{‰}$  and  $+0.4\text{‰}$  for two isolated samples of vitreous, frothy Early Rhyolite pumice from tephra outcrops on the southwest edge of the resurgent dome. Smith et al. (1988) suggest the cause is short-lived diffusive oxygen isotope exchange with meteoric water at high temperatures immediately preceding or during eruption. Low  $\delta^{18}\text{O}$  granites have also been reported and their origin from low  $\delta^{18}\text{O}$  magma confirmed (Forester and Taylor, 1977; Taylor and Sheppard, 1986). The magma for the post-caldera collapse Early Rhyolites was not uniformly anomalously low in  $^{18}\text{O}$ , however. This is proven by the majority of whole-rock  $\delta^{18}\text{O}$  values that fall within normal isotopic ranges for silicic rocks. In addition, two Early Rhyolite pumice samples from LVEW were measured for their oxygen isotope compositions after extraction of oxygen by



conventional methods. The values are plotted on Figure III.3a. Although the  $\delta^{18}\text{O}$  values for hydrothermally altered whole rock and pumice samples may vary by as much as 2‰ (see Appendix III) between conventional and laser-extracted oxygen isotope values, the plotted values indicate the Early Rhyolite pumice from samples in LVEW brackets the normal magmatic range. Possibly one or more thin and isolated apophyses for individual vents or the relatively thin hypabyssal intrusions encountered meteoric water within the caldera fill, resulting in diffusive isotopic exchange during emplacement.

Two white lithic clasts with a microlithic texture and a vitreous quartz shard found in one of the clasts in the informally named Mystery Breccia that underlies the Bishop Tuff were also measured. The  $\delta^{18}\text{O}$  value of the lithic clasts falls along the depletion trend of the Bishop Tuff with values of -2.6 and -4.0‰, and the quartz sample has a composition of 8.6‰, similar to igneous quartz (Figure III.3a). The clasts are thought to be epiclastic pre-caldera debris from silicic rocks subjected to hydrothermal alteration (McConnell et al., 1995).

The metamorphic basement rocks of the well are isotopically lighter than similar outcrop sequences from the Mt. Ritter and Mt. Morrison Roof Pendants. Whole-rock metavolcanic samples containing chlorite and epidote from 1957 m and 2012 m depth yielded average  $\delta^{18}\text{O}$  values of  $-4.6 \pm 0.3$  and  $-6.3 \pm 0.8$ ‰, respectively. These values fall along the  $\delta^{18}\text{O}$  trend observed in the overlying Bishop Tuff in LVEW. A sample of silicic and graphitic, banded hornfels in the well yielded a average whole-rock value of  $-0.4 \pm 0.1$ ‰ showing considerable depletion from outcrop values of 14.2‰ and  $19.5 \pm 0.1$ ‰. When the basement rocks are plotted on Figure III.3a, the  $\delta^{18}\text{O}$  values display a shift

toward a heavier composition than the altered volcanic rocks. This is most likely related to the difference in the permeability of the rock types from porous and permeable volcanic rock to relatively non-porous, fine-grained hornfels and metaquartzites with apparent porosities of 3 to 13% and of near 0%, respectively (Nelson et al., 1994). Both contain abundant open and healed veins and fractures. Note, though, that the banded hornfels in the basement metasediments in LVEW show the greatest relative isotopic depletion from correlated outcrop samples of  $\Delta^{18}\text{O}_{(\text{outcrop-basement})} = -19.9\text{‰}$  (Mulhophadhyay et al., 1994; this study).

Two sequences of altered, fine grained metamorphic rocks with a volcanic fabric and intrusion-like borders were measured as whole-rock wafers. The measurements yielded in mean  $\delta^{18}\text{O}$  values of 2.8‰ for the sample at 2122 m and 3.9‰ for the sample at 2200 m.

### *III.6.2 LV13-26*

The LV13-26 geothermal exploratory well located on the lower southeast flank of the resurgent dome, 5 km from LVEW (Figure III.1), bottomed in densely welded Bishop Tuff after intersecting 914 m of the unit. Considering the welded nature of the tuff and its relative thickness in nearby wells, this well most likely was within 200 to 300 m of reaching underlying lithologies. Figure III.4a illustrates  $\delta^{18}\text{O}$  values vs. depth in the LV13-26 well. Not surprisingly, the same heterogeneity within single samples of tuff seen at the center of the resurgent dome also exists at this location. Furthermore, devitrified-to-glassy pumice, sanidine, and matrix samples all show subparallel trends of  $\delta^{18}\text{O}$  composition with depth. Contrary to the slope observed in

LVEW, however, this well has the lowest  $\delta^{18}\text{O}$  values near the top of the Bishop Tuff sequence and the heaviest, most magmatic values at the bottom of the tuff. The slope of the trend appears to reverse near the contact of the Bishop Tuff and the overlying Early Rhyolite, where pumice samples at depths of 248 and 287 m yield values of  $1.8 \pm 0.1\text{‰}$  and  $1.3\text{‰}$ , respectively.

Quartz phenocryst values are in the magmatic range of  $\delta^{18}\text{O}$  with a mean value of  $7.7 \pm 1.1\text{‰}$ . The large standard deviation may have resulted from the inclusion of a possible quartz xenocryst, sample RD365-Q3A&B, in the database. If the anomalous sample is deleted, the mean value becomes  $7.3 \pm 0.7\text{‰}$ . Pumice remains the most sensitive component in the tuff to isotopic exchange, with a  $\delta^{18}\text{O}$  value of  $-1.0 \pm 0.03\text{‰}$  at a depth of 479 m and the highest value of  $6.7 \pm 0.2\text{‰}$  at a depth of 1065 m. The matrix of the tuff closely parallels the pumice trend with a mean minimum value of  $1.6 \pm 0.3\text{‰}$  at the top of the tuff sequence and a mean value of  $7.9 \pm 0.8\text{‰}$  near the bottom of the well. Sanidine phenocrysts, where measured, have not exchanged as thoroughly as the pumice and matrix, and approach the magmatic range for  $\delta^{18}\text{O}$  with values of  $6.7 \pm 0.2$  and  $6.3 \pm 0.5\text{‰}$  near the bottom of the well.

### *III.6.3 Other wells*

Four other wells located on the resurgent dome were sampled to increase subsurface coverage. Well LV13-21 is located approximately 1 km to the east of LVEW, on the eastern horst of the resurgent dome medial graben (Figure III.1). Microcrystalline, aphyric rock cuttings in the Bishop Tuff sequence from this well petrographically match the Early Rhyolite intrusions found in LVEW (McConnell et al., 1995). To determine if these rocks have a

significantly different isotopic composition from the Bishop Tuff, sample cuttings of the aphyric rocks, matrix and phenocrysts from the tuff, and obsidian cuttings were selected from two depths, 732 and 793 m. Cuttings determined to be Bishop Tuff pumice on the basis of texture and the presence of quartz or sanidine phenocrysts were chosen from several other depths. Figure III.5a displays the  $\delta^{18}\text{O}$  values to depth in the well. Once again, heterogeneity of isotopic composition is seen in different components measured from a single depth interval. The white, aphyric cuttings have the lightest oxygen isotope values of  $1.2 \pm 0.1\text{‰}$  and  $0.0 \pm 0.19\text{‰}$ . Sanidine and fresh obsidian yielded values of 6.5 and 6.4‰, respectively. Quartz remains essentially unaltered with a  $\delta^{18}\text{O}$  of 7.5‰. The  $\delta^{18}\text{O}$  value of one cuttings chip identified as perlitic obsidian was anomalously high at 17.8‰, similar to heavy  $\delta^{18}\text{O}$  values collected from metaquartzite samples in LVEW basement rocks (Mulhophadyay et al., 1994) Bishop Tuff pumice values plot as decreasing in  $\delta^{18}\text{O}$  with depth from  $2.0 \pm 0.2\text{‰}$  at the top of the sequence to  $-0.8 \pm 0.04\text{‰}$  at the bottom of the well. Although the slope is positive, it is less steep than that of LVEW. When the  $\delta^{18}\text{O}$  compositions of the two possible Early Rhyolite intrusions are plotted in Figure III.5a, only the samples from 793 m fall off the trend line defined by the Bishop Tuff pumice samples.

Figure III.6 shows the oxygen isotope composition vs. depth of white, altered Bishop Tuff pumice and matrix samples from the upper, nonwelded section of the sequence in wells LV68-28, SF38-32 and LV48-29 (Figure III.1). In all cases, the samples are depleted in  $\delta^{18}\text{O}$  relative to surface outcrop samples, though the wells are too shallow to establish trends with depth.

### III.7 DISCUSSION

Several basic questions concerning the natural system can now be addressed:

#### *III.7.1 Did the intracaldera volcanic rocks reach equilibrium exchange with the hydrothermal water?*

There is a significant spread in the  $\delta^{18}\text{O}$  values for silicate components separated from samples of Bishop Tuff. In all wells and at all depths, quartz phenocrysts in both pumice and matrix in the Bishop Tuff have retained a primary  $\delta^{18}\text{O}$  composition. It has been shown that quartz exchanges oxygen isotopes slowly with water at hydrothermal temperatures (see Criss and Taylor, 1986). Thus, the hydrothermal flux that was active in the resurgent dome area was of insufficient duration to bring the entire system to a new isotopic equilibrium. Although pumice and sanidine separates, assumed to be compositionally equivalent for oxygen isotope geothermometric calculations, display the most depletion, there is a wide disparity in their comparative values. For example, a maximum  $\Delta_{\text{pum-san}}$  of  $-5.4\text{‰}$  for Bishop Tuff samples occurs between 622 and 982 m depth in LVEW. The differences approach  $0\text{‰}$  at the bottom of the Bishop Tuff sequence at 1800 m depth. Similar disequilibria can be observed in the other wells in Figures III.3a-6. In addition, one sanidine phenocryst selected for measurement in LV13-26 from a depth of 379 m showed zonation of the oxygen isotope composition. Two areas of the 3 mm diameter phenocryst were analyzed, one measurement from a milky, opaque area adjacent to calcite-filled microfractures, and one measurement

from a translucent area relatively free of fractures and alteration. The measurements yielded values of 2.6 and 5.6‰, respectively, indicating disequilibrium.

Oxygen isotope exchange of pumice and sanidine with thermal water, controlled by some combination of surface reactions and diffusion (Cole and Ohmoto, 1986) or crack healing (Valley and Graham, in press), could be considered a reliable indicator of degree and temperature of hydrothermal alteration. We tested the possibility that some silicate phases did reach equilibrium with paleothermal water. Three  $\delta^{18}\text{O}$  measurements from hydrothermal vein quartz were obtained from core samples in the intracaldera volcanic rocks, two from LVEW and one from LV13-26. In addition, fluid inclusions in quartz from the same veins were analyzed for their homogenization temperatures ( $T_h$ , Table III.2). A  $\delta^{18}\text{O}$  value for the fluid that existed in equilibrium with the quartz was calculated using the  $\Delta^{18}\text{O}_{(\text{quartz-water})}$  calibration of Clayton et al. (1972) and the mean homogenization temperature of the fluid inclusions. Table III.2 displays the results. It is assumed that the precipitation of vein quartz and the exchange of oxygen between intracaldera rocks and water occurred in a system controlled by a single fluid of constant  $\delta^{18}\text{O}$ . To calculate a  $\delta^{18}\text{O}$  value for the fluid in thermal equilibrium with the pumice and sanidine of the host volcanic rocks, it is assumed that their bulk composition broadly resembles alkali feldspar and therefore the calibration calculation for  $\Delta^{18}\text{O}_{(\text{Kfs-H}_2\text{O})}$  of O'Neil and Taylor (1967) was used. These results are also displayed in Table III.2.

In the intracaldera volcanic rocks in LVEW, the comparisons were conducted on an Early Rhyolite intrusion at 785 m and a Bishop Tuff sample

at 824 m. Analyses of fluid inclusions indicated a mean  $T_h$  of  $209^\circ\pm 39^\circ\text{C}$  for precipitation of quartz in veins in the Early Rhyolite intrusion and  $230^\circ\pm 30^\circ\text{C}$  for the vein hosted by the Bishop Tuff. The values for water in equilibrium with vein hydrothermal quartz at these depths and temperatures are  $-9.3$  and  $-11.1\text{‰}$ , respectively. The small difference ( $1.8\text{‰}$ ) is insignificant within one standard deviation of the fluid inclusion temperature measurements.

In the Early Rhyolite intrusion, water in equilibrium with a mean whole-rock  $\delta^{18}\text{O}$  value of  $-0.7\text{‰}$  has a composition of  $-10.1\text{‰}$ . Compared to the calculated value of  $-9.3\text{‰}$  for the fluid in the hydrothermal quartz vein, this is a difference of only  $0.8\text{‰}$ . Thus, exchange between the volcanic rock of original  $\delta^{18}\text{O}$  composition of  $\sim 7.0\text{‰}$  reached equilibrium with thermal water of  $\delta^{18}\text{O}$  composition of  $-9.3\pm 2\text{‰}$  at approximately  $204^\circ\pm 39^\circ\text{C}$ . Paleothermal water in equilibrium with pumice, matrix, and sanidine components from the Bishop Tuff yielded  $\delta^{18}\text{O}$  values of  $-8.1$ ,  $-6.0$ , and  $-2.2\text{‰}$ , respectively indicating disequilibrium. Assuming the temperature was constant at  $230^\circ\text{C}$ , the pumice has proceeded approximately  $73\%$  toward equilibrium with the hydrothermal water value of  $-11.1\pm 2\text{‰}$ . In LV13-26, pumice and sanidine samples from a depth of 479 m in the well show pumice is in equilibrium with the temperatures and thermal water  $\delta^{18}\text{O}$  listed above.

Values for the  $\delta^{18}\text{O}$  composition of hydrothermal quartz and host rock Paleozoic metaquartzite are listed in Table III.2. A mean  $T_h$  of  $245^\circ\pm 25^\circ\text{C}$  was determined for inclusions with similar chemistry to the fluid inclusions in the intracaldera rocks. Using the  $\Delta^{18}\text{O}_{(\text{quartz-water})}$  calibration, a value of  $7.9\text{‰}$  is calculated for the  $\delta^{18}\text{O}$  of the water in equilibrium with the hydrothermal quartz and a value of  $5.4\text{‰}$  for the metaquartzite host rock. These  $\delta^{18}\text{O}$  values sit far

from the meteoric water line as defined by Craig (1963) and are enriched enough to fall within either the magmatic or metamorphic water regime of Taylor (1979). Mukhopadhyay et al. (1994) suggest a complex hydrothermal system of channelized flow within the basement rocks. Thus, these samples represent evidence of fluids originating in the basement rocks from dewatering of the metamorphic rocks or from some component of juvenile water released from a magma chamber. Although the chemistry of the fluids, H<sub>2</sub>O -NaCl, is identical to the chemistry of the fluids from inclusions in the volcanic rocks, it is not possible to prove or disprove their relationship.

### *III.7.2 What was the temperature range of the hydrothermal fluid?*

Previous studies such as Eslinger and Savin (1973), Goff et al. (1985), Carothers et al. (1987), and Sturchio et al. (1990) have shown mineral-water isotopic exchange and mineral-mineral isotopic fractionations are useful geothermometers for describing the hydrothermal flux in existing and fossil systems. Equations are based on equilibrium exchange and knowledge of the isotopic composition of the starting materials. We have shown, where core sampling allowed separation of vein minerals, pumice in the Bishop Tuff and the Early Rhyolite intrusions are very nearly in isotopic equilibrium with water at reservoir temperatures inferred from fluid inclusions in hydrothermal quartz. Coevolution of a single hydrothermal fluid appears likely, and a reasonable value for the  $\delta^{18}\text{O}$  composition of the fluid can be assigned. Where hydrothermal quartz is hosted by intracaldera volcanic rocks, the average calculated value for the  $\delta^{18}\text{O}$  composition of hydrothermal water is  $-10.2 \pm 1.2\%$ . This is  $^{18}\text{O}$ -enriched relative to average present-day hydrothermal



waters in the caldera. The present-day hydrothermal water, with a mean  $\delta^{18}\text{O}$  value of  $-14.6 \pm 0.6\text{‰}$  (White and Peterson, 1991), reflects a shift of only 1‰ from the mean meteoric water flowing within the caldera,  $-15.8 \pm 0.8\text{‰}$ . It is assumed the present system is dominated by a single fluid of meteoric origin (Blackwell, 1985; Sorey et al., 1991). This implies the fluid in the fossil hydrothermal system could have either originated from meteoric water that was heavier than the present-day meteoric water, had prolonged contact with host rocks at elevated temperatures, or was subject to sudden decompressional boiling (Sturchio et al., 1990).

Oxygen isotope compositions of meteoric waters throughout the Pleistocene are believed to have been similar to or less than present-day values (Fontes, 1980). In the Long Valley paleohydrothermal system, the two primary sources of recharging meteoric water would have been from glacial melt off the Sierran front to the west and the Pleistocene Long Valley Lake (Bailey, 1989) that occupied the east and south moat from ~600 - 50 ka. Mixing of isotopically light water from glacial sources with heavier waters from an evaporative lake could produce a ground water similar to the  $\delta^{18}\text{O}$  composition of the present-day water. Sudden decompressional boiling in a hydrothermal system, in response to a gas-pressure release mechanism such as an earthquake or catastrophic draining of a lake, has been suggested as a method of enriching  $^{18}\text{O}$  in residual water and silica (Sturchio et al., 1990). There is no evidence of boiling from inspection of the fluid inclusions, nor does the hydrothermal quartz in the volcanic rocks display  $\delta^{18}\text{O}$  enrichment. Although these mechanisms of  $\delta^{18}\text{O}$  enrichment of the paleohydrothermal water cannot be completely ruled out as explanations, we have shown the

temperatures in the hydrothermal system were higher in the past; therefore, the water would have experienced more exchange with the rock, increasing  $\delta^{18}\text{O}$ . Thus, we invoke the assumption that the paleohydrothermal fluid was of a different  $\delta^{18}\text{O}$  composition from the present-day fluid.

Temperature profiles were calculated for the wells using an average  $\delta^{18}\text{O}$  water value of -10.2‰, as calculated above. Pumice analyses were used when available and sanidine analyses were used where pumice was absent or not identifiable due to alteration or welding. Calculations employed the isotope fractionation equation of O'Neil and Taylor (1967). The results from LVEW, LV13-21, LV13-26 are plotted vs. depth in wells on Figures III.3b-5b. Note the trends in temperature mirror the trends of  $\delta^{18}\text{O}$  (Figures III.3a-5a).

The temperature profiles show linear trends of either positive (LVEW, LV13-21) or negative (LV13-26) slope. Temperatures calculated using sanidine  $\delta^{18}\text{O}$  values from the base of the intracaldera Bishop Tuff in LVEW are the highest, ranging from 248 to 366°C. These are in excess of any present-day temperatures measured in wells in the caldera, where maximum temperatures of 202°C and 214°C have been reported in wells RDO-8 and 44-16 in the west moat, respectively (Sorey et al., 1991). The range of fluid inclusion homogenization temperatures, 163 to 370°C, is also far above the present-day temperatures measured in LVEW (Sass et al., 1991). Present-day maximum temperatures occur as spikes in temperature profiles from wells located in the intracaldera volcanics, implying shallow lateral flow of thermal water (Blackwell, 1985; Sorey, 1985).

The  $\delta^{18}\text{O}$  composition of Paleozoic basement rocks encountered at the bottom of LVEW appear to reflect a shift from  $\delta^{18}\text{O}$  values of equivalent Mt.

Morrison Roof Pendant rocks (Mukhopadhyay et al., 1994; this study). However, fluid flow in these deeper, metamorphic rocks has apparently been more restricted to complex, multigeneration fractures limiting  $\delta^{18}\text{O}$  exchange between the hydrothermal fluid and the rock matrix (Mukhopadhyay et al., 1994). Thus, it is not possible to calculate a valid geothermal gradient for these rocks based on mineral-rock fractionations. On the other hand, the overlying Early Rhyolite flows and tephras reflect relatively cool hydrothermal temperatures of  $<125^\circ\text{C}$  at LVEW. In addition, temperatures in LV13-26 also show a reversal at the upper contact of the Bishop Tuff with the extrusive Early Rhyolite sequence. This is corroborated in both wells by the absence of alteration mineralogy and pristine nature of the glass in this sequence (McConnell et al., 1995). This implies the Early Rhyolite extrusive rocks at these locations either was maintained at low temperatures by cold water flow during the alteration of the underlying Bishop Tuff or it had not yet been emplaced. K-Ar and whole-rock  $^{40}\text{Ar}/^{39}\text{Ar}$  dating of obsidian samples from outcrop and LVEW show the Early Rhyolite was emplaced approximately 675 ka (Mankinen et al., 1986; McConnell et al., 1995).

Estimated paleogeothermal gradients for LVEW vary from  $130^\circ\text{C}/\text{km}$  for the pumice samples and Mesozoic metavolcanic rocks to  $220^\circ\text{C}/\text{km}$  for the sanidine samples (Figure 6b). Temperatures calculated for samples from the Early Rhyolite intrusions measured do not follow the linear trend of increasing temperature with depth of the Bishop Tuff, but reflect a more restricted range of  $146\text{-}212^\circ\text{C}$ . Temperatures from shallow intrusions lie near the paleogeothermal gradient but those from deeper intrusions do not. Most likely,

these hypabyssal sills were intruded after the hydrothermal activity responsible for altering the tuff had waned.

The temperature profile calculated from the pumice samples from the Bishop Tuff sequence in LV13-26 has a steep negative slope of approximately  $-190^{\circ}\text{C}/\text{km}$ . This contrast in temperature profiles is best explained by the presence of a shallow, laterally flowing hydrothermal plume radiating from a deep conductive heat source beneath LVEW.

Whereas LVEW and LV13-26 have rather steep geothermal gradients, LV13-21 is nearly isothermal with depth (Figure III.5b). The difference in calculated temperature over the 650 m section of the well is  $<20^{\circ}\text{C}$ , and the calculated temperature for the projected bottom of the Bishop Tuff at 1700 m depth is  $<200^{\circ}\text{C}$ , far less than LVEW at that same depth only one kilometer to the west. The temperatures are less than the top of the Bishop Tuff sequence in the more distal LV13-26 well. The top of the Bishop Tuff in LV13-21 is 200 m higher than the top of the Bishop Tuff in LVEW indicating the presence of a major fault separating the two wells. The trace of this fault can be seen from offset in the flows and tephras of the Early Rhyolite at the surface. LV13-21 apparently sits in the shadow of channelized flow controlled by this fracture. If this is true, then the fault and the Early Rhyolite flows predate the hydrothermal activity. Two samples were chosen for analyses due to their petrographic similarity to the Early Rhyolite intrusions in LVEW. Temperature calculated from one of the two samples of cuttings from the well plots along the geothermal gradient for the Bishop Tuff, while the other shows a slightly higher temperature of  $187^{\circ}\text{C}$ . Both temperatures fall within the

range determined for the intrusions in LVEW but, in this case, are not distinct enough to distinguish them from Bishop Tuff.

### *III.7.3 What was the path of the hydrothermal flux?*

Depletion of  $\delta^{18}\text{O}$  in the volcanic rocks can best be accomplished by prolonged exchange with low  $\delta^{18}\text{O}$  water at elevated temperatures over time and space. Thus, the variation in the  $\delta^{18}\text{O}$  compositions of the intracaldera volcanic rocks in space beneath the resurgent dome reflects the path and duration of the hydrothermal flux in the fossil system in Long Valley Caldera.

The pattern of decreasing  $\delta^{18}\text{O}$  compositions of the Bishop Tuff with depth in LVEW, and less so in the nearby LV13-21, argues for a deep, centrally located hydrothermal system beneath the resurgent dome. When coupled with the contrasting geothermal gradients of LVEW and the distal LV13-26, a pattern of free convective flow operating in the central caldera some time in the past emerges (Valley et al., 1994; McConnell et al., 1994). Figure III.7 displays a west east cross-section showing the major structural features of the central caldera and contours of constant oxygen isotope composition for pumice and sanidine samples from intracaldera volcanic rocks. These isotopic isopleths can be considered analogous to the fluid streamlines of the hydrothermal flux. The structure that develops describes a model of closed system convective fluid circulation (Criss and Taylor, 1986) and outlines the shape of the fossil hydrothermal system.

It should be noted, however, that post-caldera-collapse volcanic activity and resurgence began within 100 ka of caldera formation (Bailey et al., 1976). The central caldera has hosted a complex sequence of volcanic and intrusive

events. In addition, the resurgent dome has been modified by tectonically controlled and repeatedly activated faults (Rinehart and Ross, 1964; Bailey et al., 1976), allowing maintenance of zones of weakness throughout the history of resurgence. Thus the resulting hydrothermal convection cannot be easily characterized as a single open or closed system through time. For example, the  $\delta^{18}\text{O}_{(\text{pumice})} \leq -2\text{‰}$  contour in Figure III.7 occurs only at the base of the intracaldera rocks in LVEW, a well located at the apex of the medial resurgent dome graben, overlain by the oldest of the Early Rhyolite flows ( $675 \pm 9$  ka) (Bailey et al., 1976; McConnell et al., 1995), and containing Early Rhyolite intrusions of  $590 \pm 17$  ka and  $454 \pm 17$  ka (Layer et al., 1992; McConnell, et al., 1995). All these factors indicate that the well intersects an area structurally weakened and repeatedly intruded. Similar eruptive chronologies for the post-caldera-collapse Inyo Domes vents have been described by Eichelberger et al. (1988). Note that the deeper Early Rhyolite intrusions do not fall into this contour.

Because there is fairly good control on the timing of the volcanic activity in the central caldera, it is possible to suggest a chronology of volcanic and hydrothermal events. Table III.3 lists the major volcanic events and their suggested correlation with the hydrothermal activity consistent with the oxygen isotope data. Contours of progressively higher  $\delta^{18}\text{O}$  compositions suggest a hydrothermal plume radiating laterally from the vicinity of LVEW and primarily restricted to the Bishop Tuff. Hydrothermal activity began to wane in the central caldera after 300 ka (Bailey et al., 1976; Sorey et al., 1991), possibly in response volcanic activity shifting to the west moat. Early Rhyolite sill-like intrusions that do not follow the trend of depletion with depth

indicate persistence of some intrusive activity after the hydrothermal system waned.

#### *III.7.4 Where was the source of the heat and when was it present?*

Table III.3 and Figure III.7 illustrate the fact that the central caldera region was the focus of intense volcanic activity and structural modification soon after the formation of the caldera and its filling by Bishop Tuff. We suggest that this focused intrusive activity over the period of early post-caldera-collapse rhyolitic volcanism provided the structural uplift to form the resurgent dome and the heat to drive a centrally located hydrothermal system.

One characteristic of the hydrothermal system that has not been addressed is the volume ratio of water/rock interaction. Studies have used the distribution of oxygen isotope compositions in hydrothermal systems to quantitatively estimate this parameter after the derivations of Taylor (1971) and Blattner (1985). These calculations are subject to many assumptions that are not easily verified in a fossil hydrothermal system and, indeed, are contraindicated by the findings of phase disequilibrium in this study.

#### III.8 SUMMARY

The oxygen isotope and fluid inclusion study has allowed us to determine the pathways of fluid circulation, set limits on the thermal regime, and link the source of the heat to prolonged volcanic activity. Additionally, the analyses of separate components of the intracaldera rocks demonstrates disequilibrium in hydrothermally driven mineral-fluid exchange of oxygen isotopes.

Not all post-caldera-collapse intrusions pierced through the Bishop Tuff to become extrusive units as witnessed by the multiple hypabyssal Early Rhyolite intrusions and Moat Rhyolite stock identified in well samples (R.A. Bailey, pers. commun., 1992 ; McConnell and Eichelberger, 1990; McConnell et al., 1995). Coeval with central caldera volcanic activity was a vigorous hydrothermal system that maintained a steep geothermal gradient over time.  $^{40}\text{Ar}/^{39}\text{Ar}$  ages determined for the Early Rhyolite intrusions reveal that intrusions with older ages ( $590\pm 17$  and  $450\pm 17$  ka, Layer et al., 1992) occur in the upper Bishop Tuff while an intrusion lower in the Bishop Tuff has an age of 366 ka (Chapter IV). Yet, the  $\delta^{18}\text{O}$  composition of all three intrusions are quite similar and all are lower than primary values measured for the Early Rhyolite extrusive rocks. If one assumes the ages represent the time of emplacement of the Early Rhyolite intrusions, a plausible assumption as these cryptocrystalline quartzo-feldspathic intrusions occur at depths that place them below the  $250^\circ\text{C}$  isotherm (the blocking temperature for Ar diffusion in feldspar) then onset of hydrothermal activity began no earlier than  $\sim 590$  ka, the age of older Early Rhyolite intrusions. The age of  $\sim 366$  ka determined for the lower Early Rhyolite intrusion with a  $\delta^{18}\text{O}$  composition of  $-0.5\text{‰}$  indicates hydrothermal activity continued past that age of emplacement. However, the lowered  $\delta^{18}\text{O}$  composition of this intrusion is not so low that it falls along the projection of the Bishop Tuff oxygen isotope exchange. If the hydrothermal system peaked approximately 300 ka, long after the peak of the bulk of Early Rhyolite volcanic activity in the central caldera (Bailey et al., 1976), then this lower and younger intrusion was emplaced shortly before waning of the



hydrothermal flux began, effectively exchanging with cooler water over less time.

It appears part of the hydrothermal circulation remained open as witnessed by hot springs deposits of comparable age outside the caldera (Bailey et al., 1976; Sorey et al., 1991). However, upward migration of the thermal water did not penetrate far into the lower layer of the overlying Early Rhyolite lava and tephra, which show only slight lowering of the  $\delta^{18}\text{O}$  values. In addition, there is ample evidence from the lateral pattern of low  $\delta^{18}\text{O}$  values in the Bishop Tuff that at least partly closed system convection dominated over much of the paleohydrothermal system. Reactivated faults that in part predate the hydrothermal events and have altered the form of the resurgent dome would have offered intermittent pathways for open system circulation. Although the Early Rhyolite flows and tephtras may have formed a partial near-surface barrier to hydrothermal alteration, they never altered enough to form a capping aquitard.

A convective plume of low  $\delta^{18}\text{O}$  thermal water circulated up and through the Bishop Tuff, exchanging with high  $\delta^{18}\text{O}$  silicic volcanic rocks. The source of the heat appears to have been centered beneath the apex of the resurgent dome graben as seen by the downward decreasing  $\delta^{18}\text{O}$  values in the Bishop Tuff in LVEW. Lowered  $\delta^{18}\text{O}$  values of metavolcanic and metasedimentary rocks of the caldera basement indicate some exchange with hydrothermal water.  $^{40}\text{Ar}/^{39}\text{Ar}$  age determinations of the altered Mesozoic metavolcanic rocks yield dates of 500 and 1000 ka (See Chapter IV). As these rocks are below the depth of the 250°C paleo-isotherm, it can be assumed these dates represent times of hydrothermal activity. The age of 500 ka in particular links

the basement rocks to the post-caldera-collapse hydrothermal system. Deeper metasedimentary rocks, with a rich texture of cross-cutting fractures (Mukhopadhyay et al., 1994; McConnell et al., 1995), could channelize flow of meteoric water through fractures, recharging the system as the repeated intrusion of near-surface stocks and intrusions contributed the heat source. As the intrusive volcanism waned in the central caldera and later reactivated in the western moat, so did the hydrothermal circulation. Today the hydrothermal activity stills manifests itself along the structurally weakened resurgent dome, but most likely the heat source can be attributed to Holocene dike intrusions and volcanic activity in the west moat (Sorey et al., 1991). Nevertheless, the substantial uplift and ongoing seismicity associated with the resurgent dome suggest that central caldera magmatism is not over, and that the resurgent dome may yet host a new cycle of hydrothermal activity. Long Valley Caldera continues to hold the potential for geothermal exploitation as well as serious volcanic hazard, and warrants the watchful eye of the scientific community.

### III.9 ACKNOWLEDGEMENTS

This work was funded in part by grants from U.S. Department of Energy's Office of Basic Energy Sciences, DE-FG02-93ER14389 (JWV), and by Sandia National Labs as part of a program under the Division of Geothermal Energy of the U.S. Department of Energy (VSM and JCE). Many thanks to Michael J. Spicuzza, Chris Niendorf, Nami Kitchen, Matthew Kohn for patience and support and gathering data in the Wisconsin Stable Isotope Lab, University of Wisconsin.. Thanks to Roy Bailey, USGS for helpful conversations in the office

and the field regarding the post-caldera-collapse rhyolite volcanic history of the Long Valley Caldera. Terry E.C. Keith, Mary J. Keskinen, and Paul W. Layer all provided helpful and timely support and reviews.

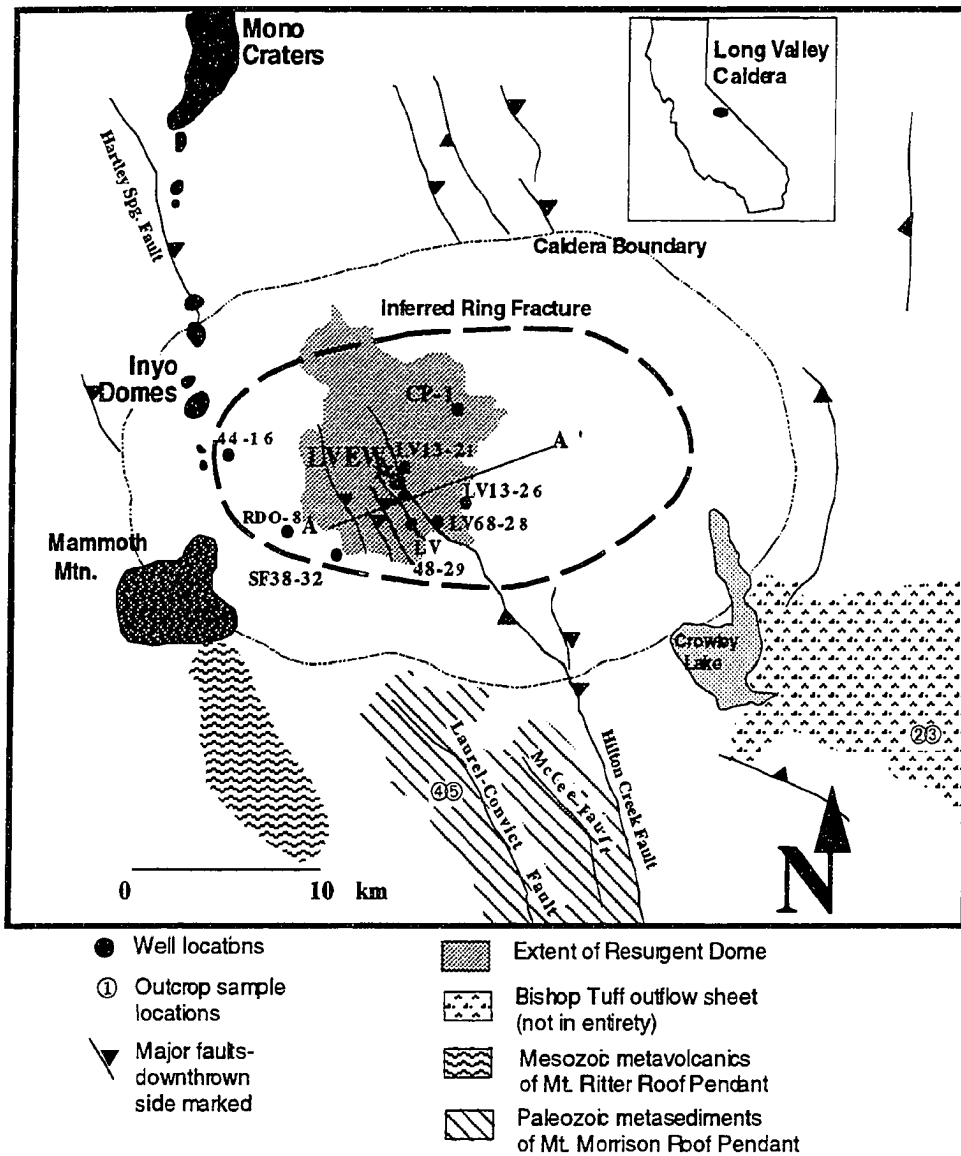


Figure III.1 Generalized geologic map of Long Valley Caldera. Major tectonic and volcanic features that are discussed in the text are identified. Wells from which samples were taken for analyses and stratigraphic logging are also identified. Line A-A' is plan view of cross-section in Figure III.7.

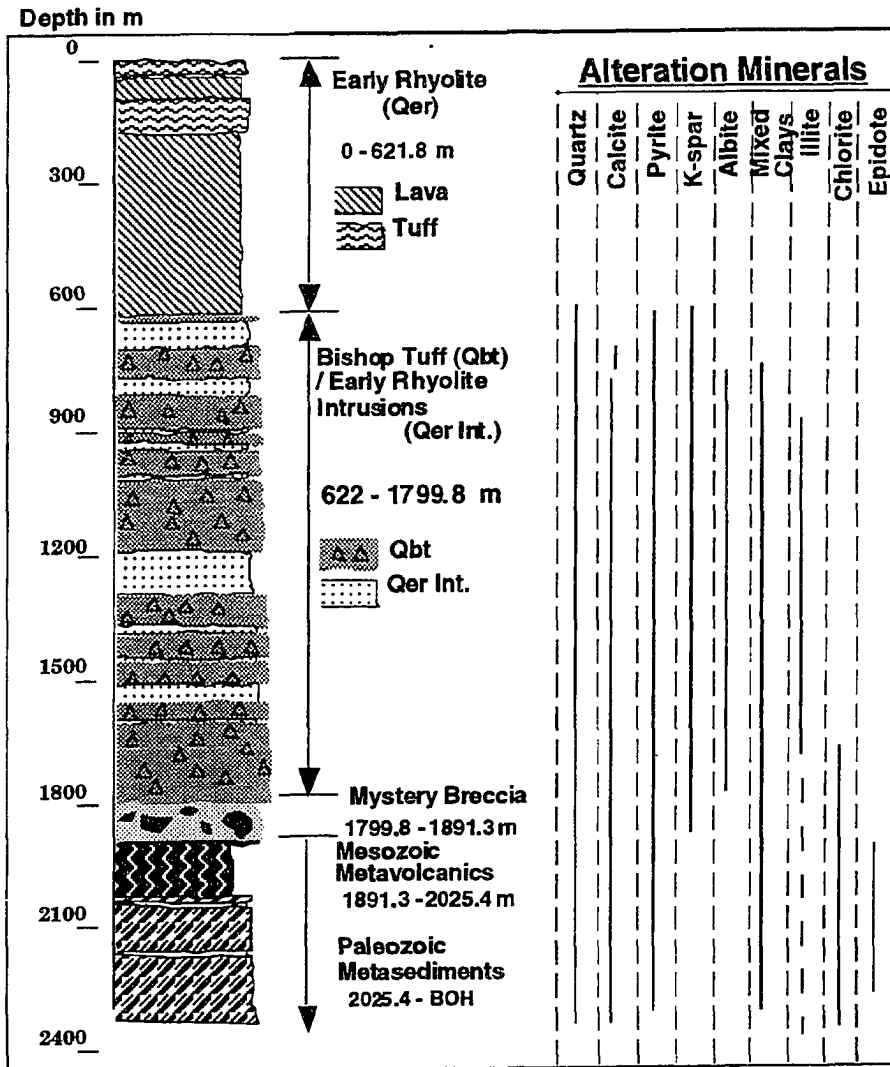


Figure III.2 Major stratigraphic units in LVEW with alteration mineralogy. The scale precludes displaying greater detail such as thin Qer intrusive units. See Appendix I for complete stratigraphy. Alteration mineralogy based on petrographic thin section observations and x-ray diffractometry.

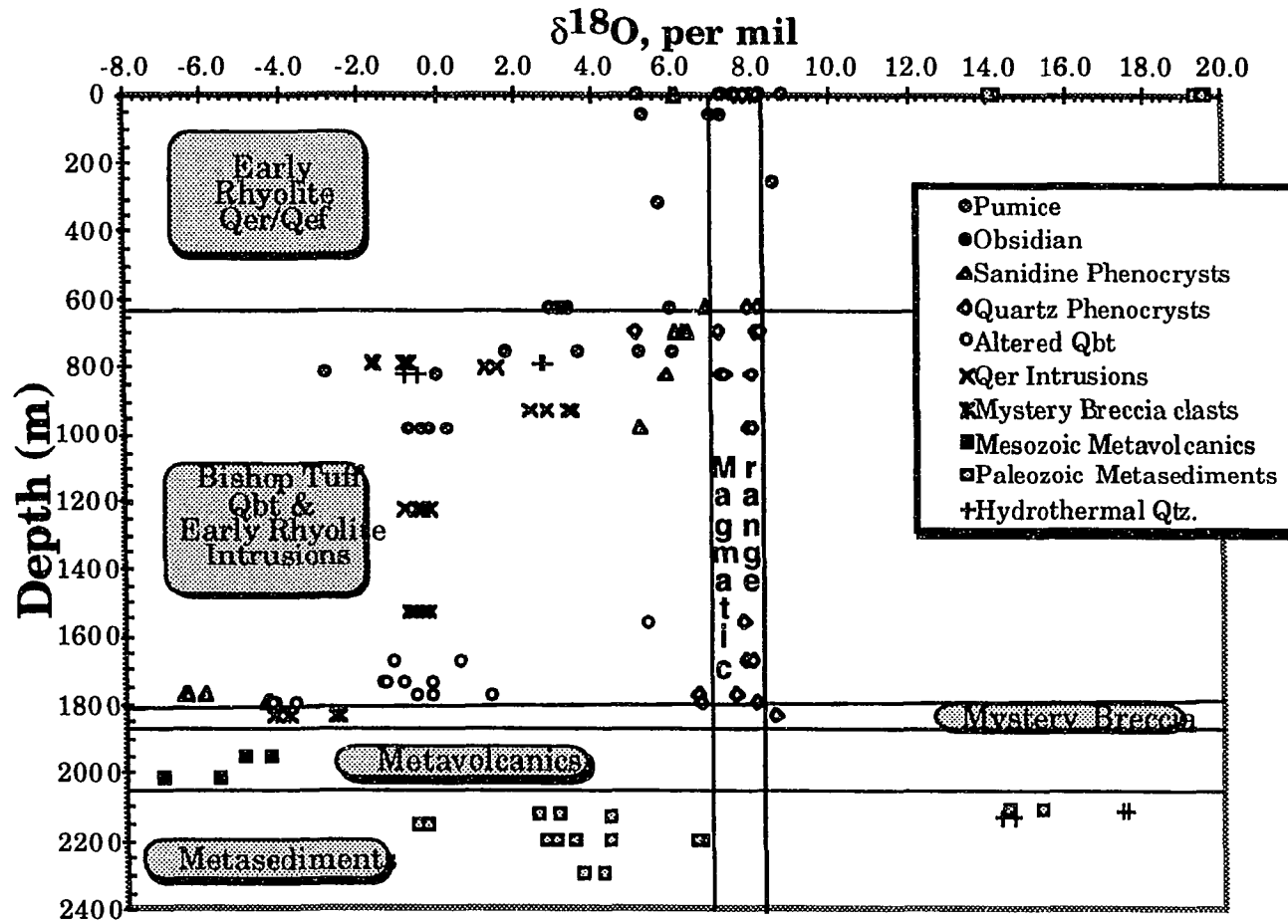


Figure III.3a Oxygen isotope compositions of silicate components in LVEW lithologies. Magmatic range outlined is based on measured and reported values for extrusive volcanic equivalent rocks. The sample symbols remain the same for all following plots. "Mystery Breccia" is an informal designation for the unit.

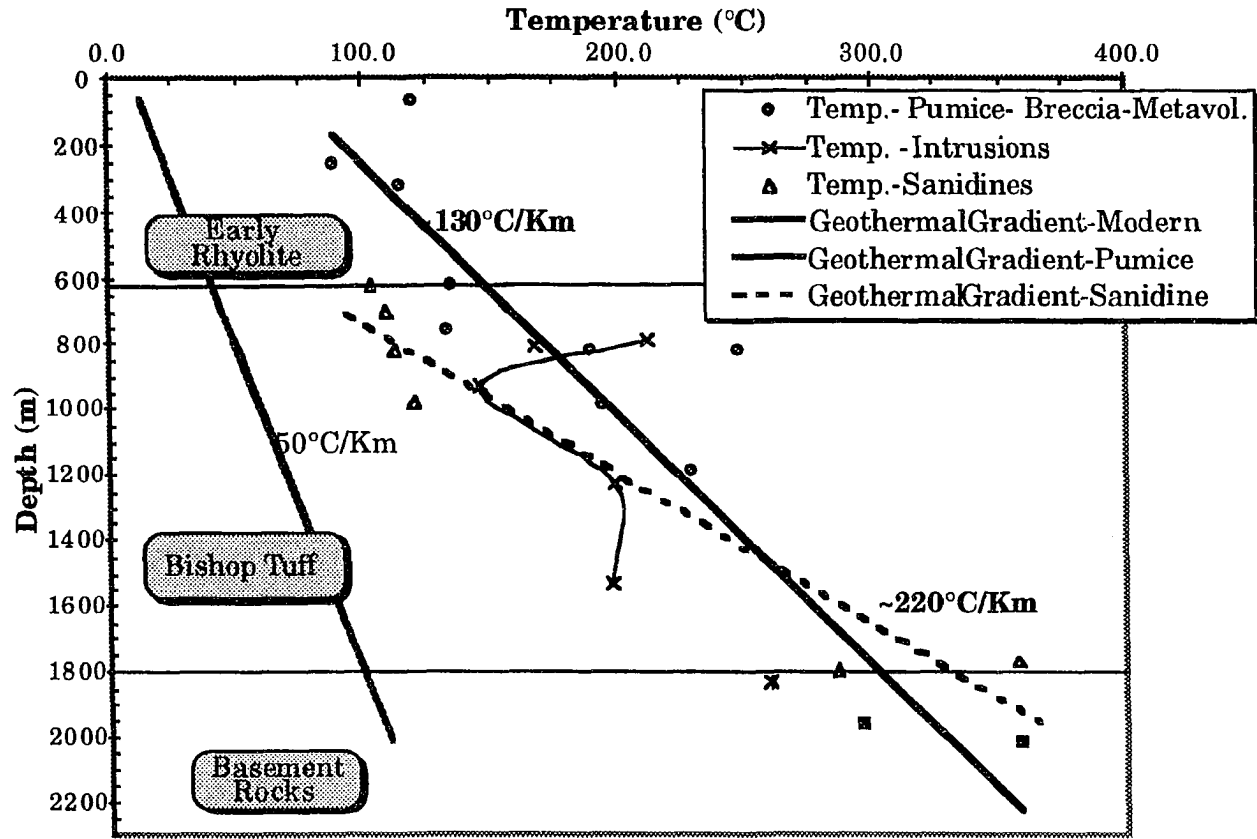


Figure III.3b Profiles of paleogeothermal gradients in LVEW. Note the temperature reversal in the temperature gradient of the Qer intrusives. Present-day gradient from Sass et al., 1991. Only the major lithologies in LVEW are identified for clarity.

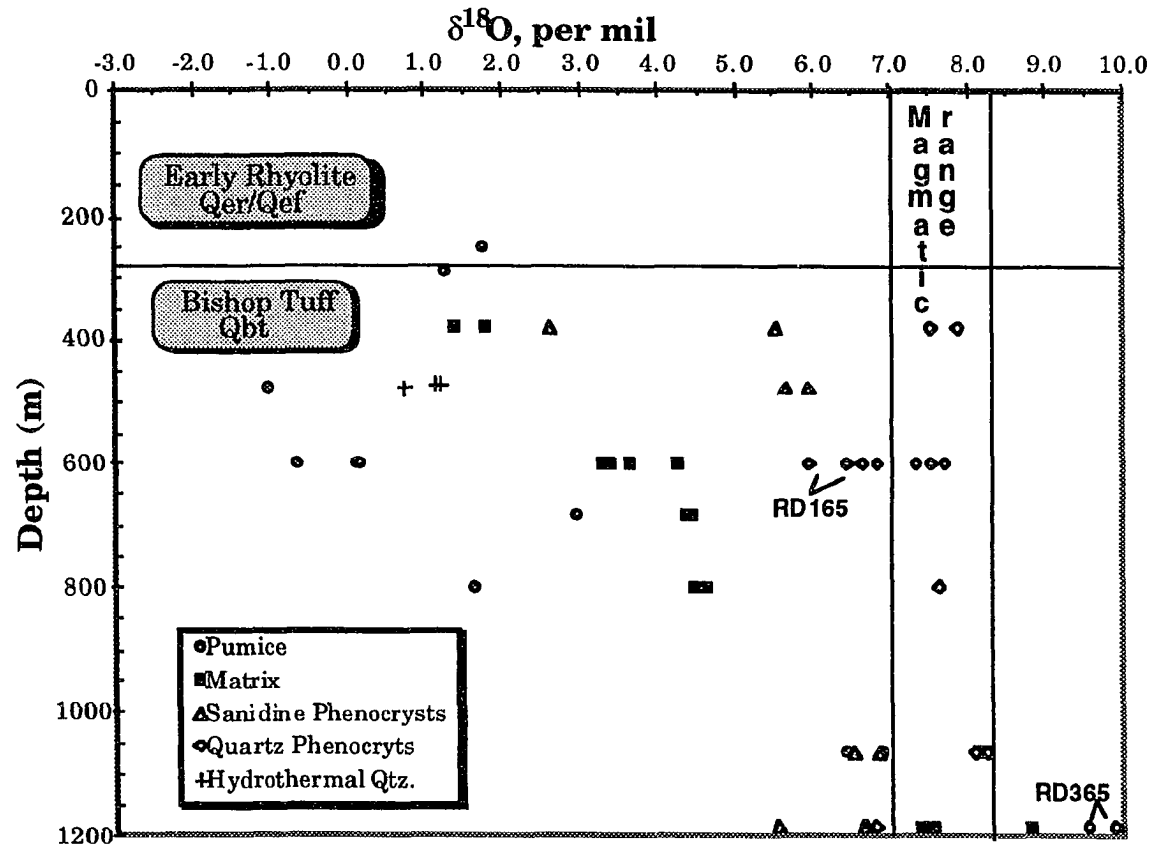


Figure III.4a Oxygen isotope compositions of silicate components in LV13-26. Magmatic ranges based on measured and reported values for oxygen isotope composition of extrusive outcrop equivalents to intracaldera volcanics.



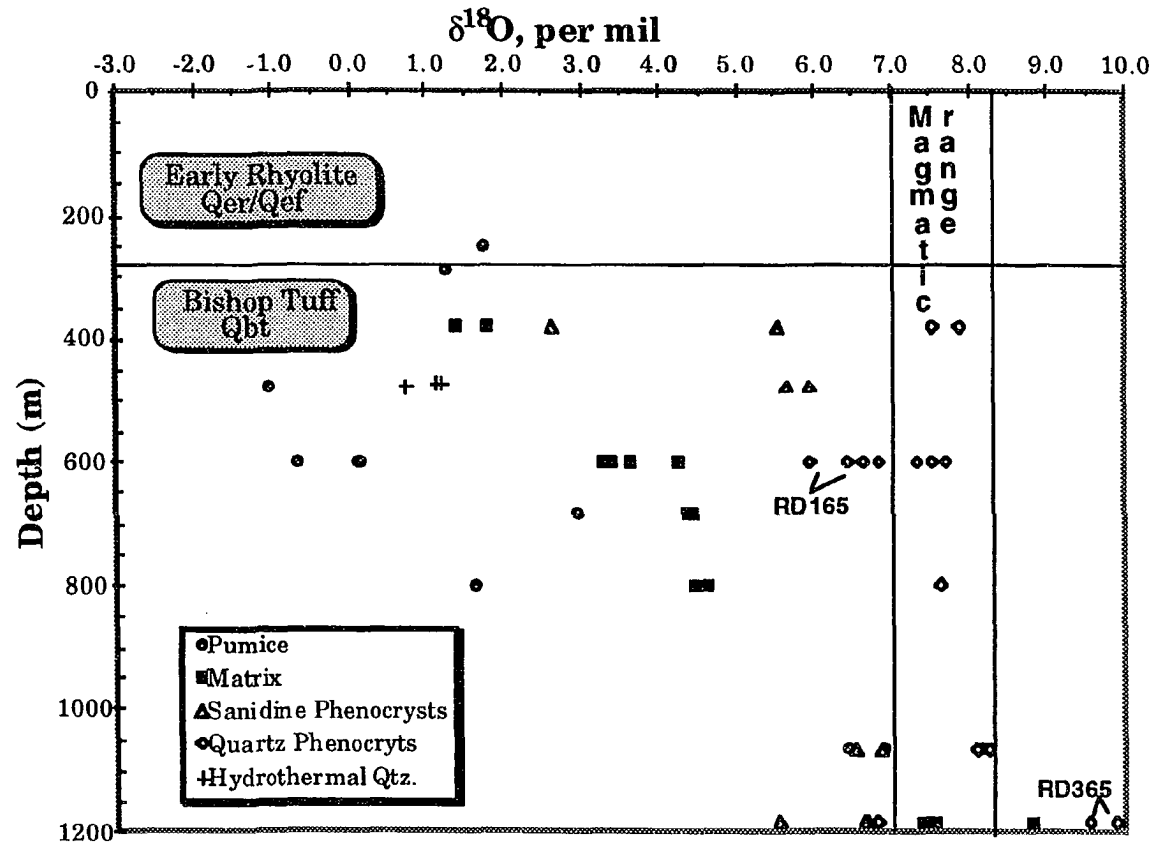


Figure III.4b Profile of paleogeothermal gradient in LV13-26. Gradient based on linear regression along temperature calculated for pumice samples. Major lithologies listed only.

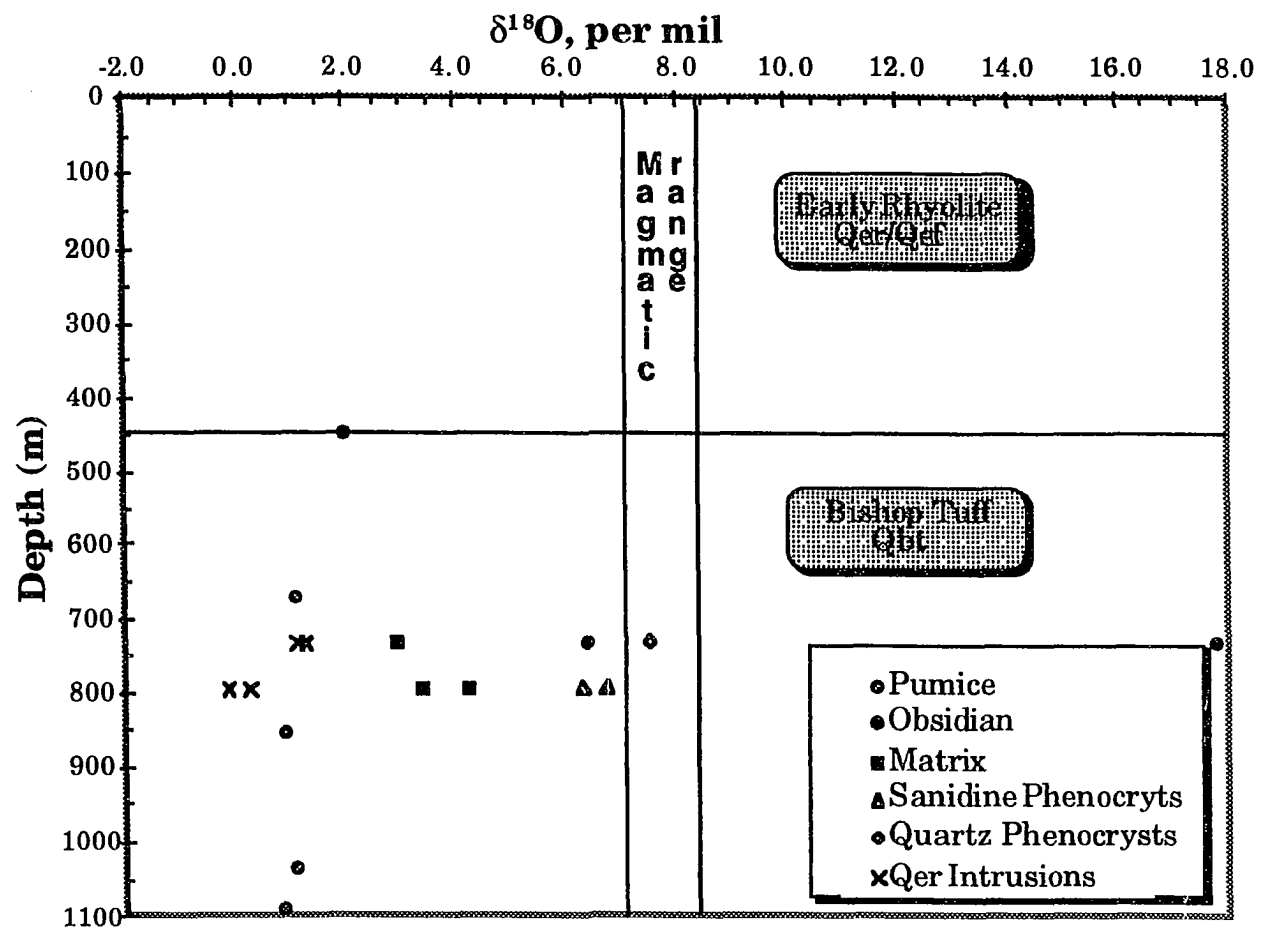


Figure III.5a Oxygen isotope compositions of silicate components in LV13-21 Magmatic range based on measured and reported oxygen isotope compositions from extrusive outcrop equivalents to intracaldera volcanic rocks.

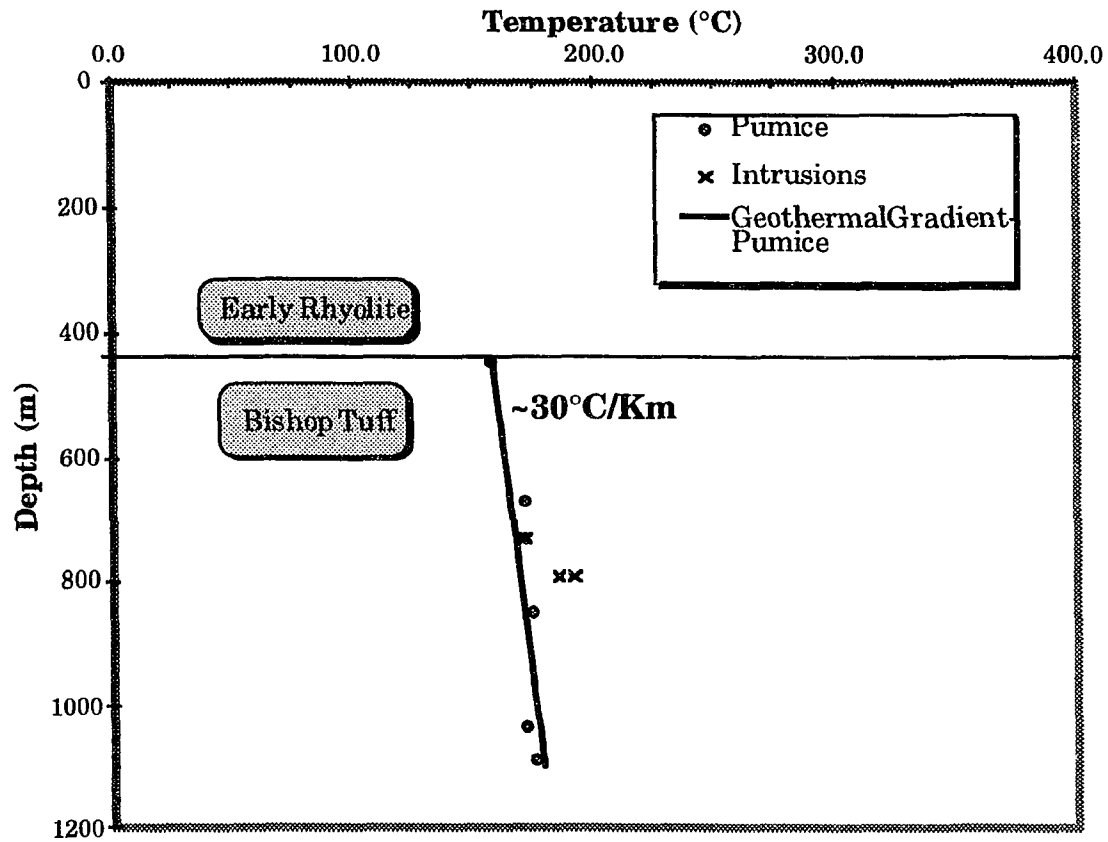


Figure III.5b Profile of paleogeothermal gradient in LV13-21 Gradient based on linear regression of temperatures calculated using pumice samples to depth in the well. Only major lithologies identified.

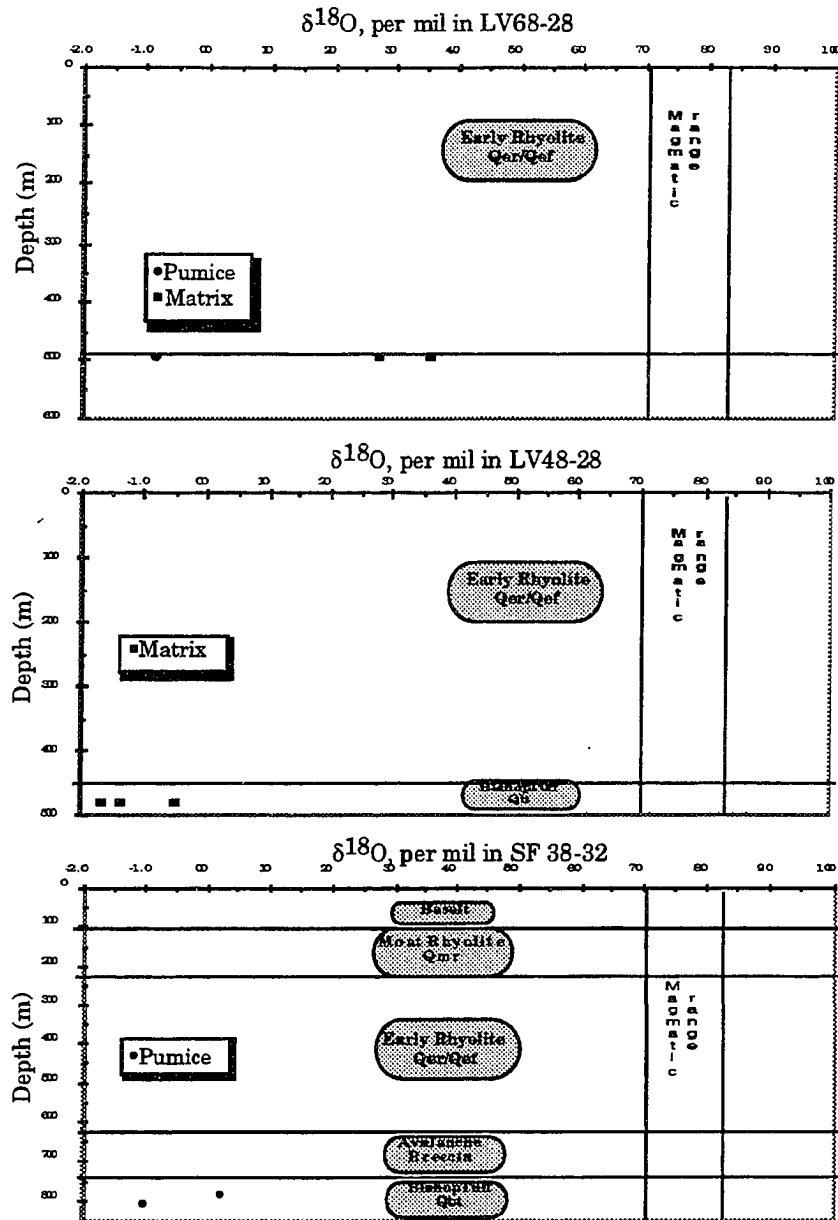


Figure III.6 Oxygen isotope compositions of silicate components in remaining wells. Wells are too shallow to be used for determining paleogeothermal gradients. Magmatic range based on measured and reported oxygen isotope values for extrusive outcrop equivalents to intracaldera volcanic. Major lithologies listed. See Figure III.1 for locations of wells.

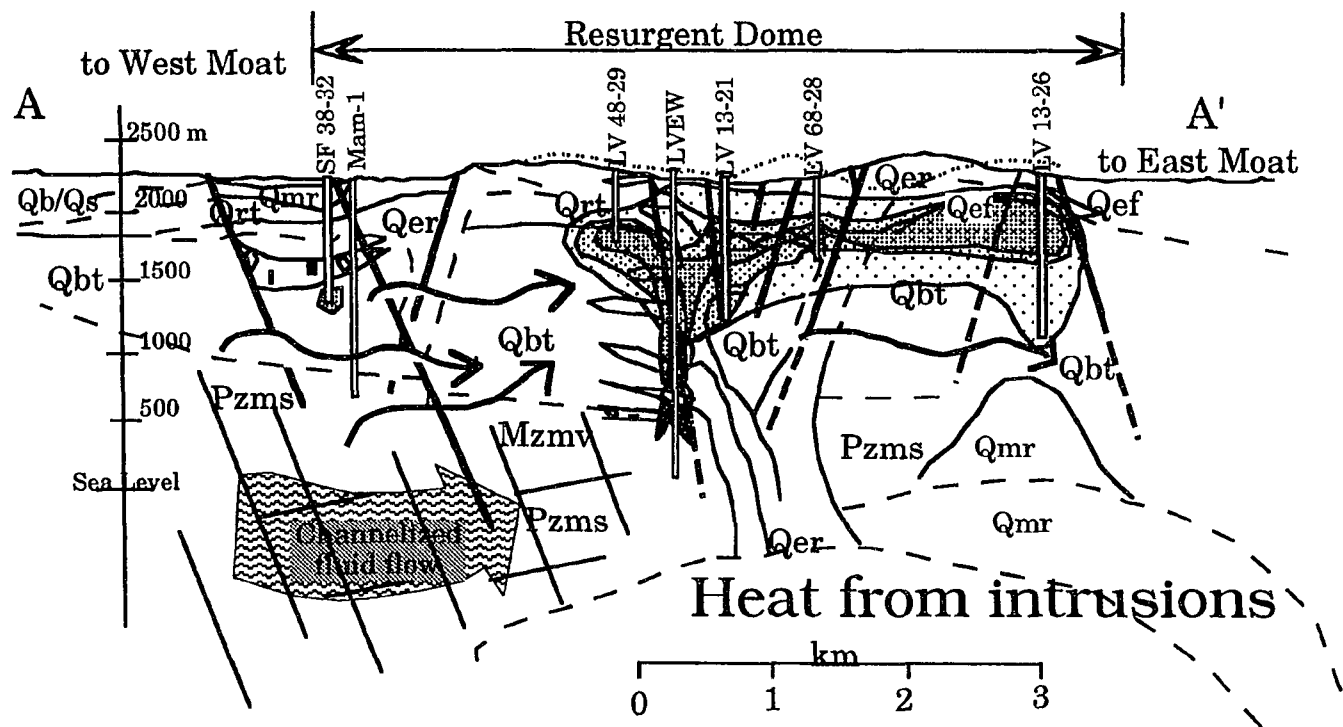


Figure III.7 Interpretative cross-section of Long Valley Caldera with oxygen isotope isopleths. Cross-section location (A-A') is shown in Figure II.1, dotted line in this figure indicates surface at well sites projected to cross-section line. See following page for legend.


### Legend

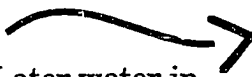
$\delta^{18}\text{O}$  contours


  $\leq -2\text{‰}$


  $\leq 0\text{‰}$

  $\leq 4\text{‰}$

  $\leq 7\text{‰}$


  
Later water in  
intracaldera volcanic rocks

  
Inferred contacts

  
Trace of faults

Pzms- Paleozoic metasediments

Mzmv- Mesozoic metavolcanics

 Mystery Breccia

Qbt- Bishop Tuff

Qer/Qef- Early Rhyolite flows and  
tephras

Qmr- Moat Rhyolite

Qb - Post-collapse basalt

Qs- Lake deposits

Base map from R.A. Bailey, 1974 and additional mapping V.S. McConnell, 1991

Legend for Figure III.7, preceding page.

Table III.1 Oxygen isotope values of silicate components in intracaldera lithologies

Sample ID	Depth (m)	Rock Type	Pm.	Mx.	Qtz.	San.	UW '93-'94
15B-pum1 ②	0	Qbt (pumice)	5.12				
15B-S1 ②	0	Qbt (sanidine)					
15B-Q1,2,3 ②	0	Qbt (quartz)			7.90 ± 0.19 [3]		
15B-Split6 ②	0	Qbt (pumice)					7.60
15B-Split5 ②	0	Qbt (pumice)					8.83
15D-Split2 ③	0	Qbt (pumice)					7.92 ± 0.03
15D-Split1 ③	0	Qbt (pumice)					7.32 ± 0.03
Qer-16 ①	0	Qer (obsidian)					8.38 ± 0.68
44A-out-1④	0	Pz hornfels (wr)		14.16 ± 0.06 [2]			
44B-out-1 ⑥	0	Pz hornfels (wr)		19.52 ± 0.08 [4]			
① indicates the outcrop location on Figure III.1.							
<b>LVEW</b>							
LVEW 200	61.0	Qer (tephra)	5.30 ± 0.01 [2]				
LVEW 200	61.0	Qer (obsidian)	7.09 ± 0.13 [2]				
2040-Q1,2	621.8	Qbt (quartz)			8.05 ± 0.12 [2]		
2040-S1,2	621.8	Qbt (sanidine)				6.89 ± 0.00 [2]	
2040-wht-2	621.8	Qbt (matrix)		5.97			
2040-wht-1	621.8	aphyric pumice	3.00 ± 0.11 [2]				
2040-obs-1	621.8	Qer (obsidian)	3.27 ± 0.06 [2]				
2290-S1,2,3,4	698.0	Qbt (sanidine)				6.27 ± 0.09 [4]	
2290-Q1,2,3,4	698.0	Qbt (quartz)			7.94 ± 0.39 [4]		
LVEW 2480	755.9	Qbt (white)	2.69 ± 0.91 [2]				
LVEW 2480-2	755.9	Qbt (gray, silicified)		1.09 ± 2.22 [2]			
LVEW 2480-3	755.9	Qbt (white)	5.60 ± 0.42 [2]				

Table III.1 Oxygen isotope values of silicate components in intracaldera lithologies

Sample ID	Depth (m)	Rock Type	Pm.	Mx.	Qtz.	San.	UW '93-'94
LVEW 2480-4	755.9	Qbt (gray, silicified)		3.50 ± 0.34 [2]			
2B1-wht-1	784.4	Qer intrusion		-1.24 ± 0.43 [4]			
2C1-H1	784.9	Qer int (hydroqtz)			2.68 ± 0.05 [2]		
8G	801.0	Qer intrusion					1.50 ± 0.22
80A	801.0	Qer int. (repeat)					1.21 ± 0.16
LVEW 14G-wht-1	819.9	Qbt (pumice)	-0.01				3.56 ± 0.27
LVEW 14G-mx	819.9	Qbt (matrix)		2.07			
LVEW 14G-S1	819.9	Qbt (sanidine)				5.89	
LVEW 14G-Q1,4,	819.9	Qbt (quartz)			7.53 ± 0.34 [3]		
16B-H-1	824.5	Qbt (hydrothermal)			-0.69 ± 0.20 [2]		
22B-wht-1	926.6	Qer intrusion		2.96 ± 0.41 [4]			
LVEW 3180	969.3	Qbt					4.65 ± 0.17
LVEW 22C-S2	981.5	Qbt (sanidine)				5.16	
LVEW 22C-Q1,2	981.5	Qbt (quartz)			7.97 ± 0.05 [2]		
LVEW 22C,2,3	981.5	Qbt (pumice)	-0.27 ± 0.25 [5]				
LVEW 22C-mx	981.5	Qbt (matrix)		3.47 ± 0.03 [2]			
LVEW 3600	1097.3	Qbt					4.62 ± 0.21
LVEW 22D-1,2	1182.7	Qbt (pumice)	-2.04 ± 0.10 [3]				
LVEW 22D-mx	1182.7	Qbt (matrix)		2.74			
LVEW 22E-wht-1	1222.2	Qer intrusion		-0.52 ± 0.18 [4]			
LVEW 4320	1316.7	Qbt					4.04 ± 0.09
LVEW 22K-wht1,	1530.1	Qer int. (SWC)		-0.51 ± 0.16 [4]			
LVEW 22K	1530.1	Qer int. (cuttings)					1.09 ± 0.16
22L-Q1	1557.2	Qbt(quartz)			7.81		
LVEW 22L-mx-1	1557.2	Qbt(matrix)		2.19 ± 0.57 [2]			
LVEW 22L-wht-1	1557.2	Qbt (silicified??)		5.34			



Table III.1 Oxygen isotope values of silicate components in intracaldera lithologies

Sample ID	Depth (m)	Rock Type	Pm.	Mx.	Qtz.	San.	UW '93-'94
LVEW 5380	1639.8	Qbt					2.24 ± 0.19
LVEW 22N-Q1,2	1673.4	Qbt (quartz)			7.95 ± 0.09 [2]		
LVEW 22-N	1673.4	Qbt (white, silicified)		0.56			
LVEW 22-N-2	1673.4	Qbt (gry/brn)		-1.13			
LVEW 5700-1,2	1737.4	Qbt (white)		-0.96 ± 0.41 [4]			0.58 ± 0.21
22O-wht-1	1772.4	Qbt (silicified)		0.60 ± 0.76 [2]			
22O-grn-1	1772.4	Qbt (chloritized)		-0.54			
22O-S12,3,4	1772.4	Qbt(sanidine)				-6.29 ± 0.22 [4]	
22O-Q1,2	1772.4	Qbt(quartz)			7.12 ± 0.48 [2]		
LVEW 22P-S1,2	1793.7	Qbt (sanidine)				-4.36 ± 0.03 [2]	
LVEW 22P-Q1,2	1793.7	Qbt (quartz)			7.18 ± 0.63 [3]		
LVEW 22-P2	1793.7	Qbt (white)		-3.65			
LVEW 22-P1	1793.7	Qbt (white)		-4.18 ± 0.03 [2]			
21F-A-wht1	1830.0	Mystery Breccia	-2.64 ± 0.03 [2]				
21F-A-wht2	1830.0	Mystery Breccia	-4.04 ± 0.18 [2]				
21F-A-Q1	1830.0	quartz from Breccia			8.60		
22W-1,2	1956.8	Mzmv (greenschist)		-4.64 ± 0.34 [2]			
22Y-1	2011.7	Mzmv (greenschist)		-6.32 ± 0.76 [2]			
30C-1,2	2111.0	metaquartzite		14.95 ± 0.43 [2]			
30C-H-1	2111.0	metaqtz. (hydroqtz)			17.5 ± 0.04 [2]		
33I-1	2122.0	meta-intrusion??		2.79 ± 0.22 [2]			
34G-1	2125.6	banded hornfels		4.39 ± 0.04 [2]			
34G-H1,2	2125.6	hydrovein quartz			14.5 ± 0.16 [2]		
42H-1	2149.8	banded hornfels		-0.43 ± 0.13 [2]			
I58C-3	2199.7	meta-intrusion??		3.93 ± 0.48 [2]			
II58C-2	2199.7	hornfels		6.69 ± 0.06 [2]			

Table III.1 Oxygen isotope values of silicate components in intracaldera lithologies

Sample ID	Depth (m)	Rock Type	Pm.	Mx.	Qtz.	San.	UW '93-'94
II58C-1	2199.7	meta-intrusion??		2.85 ± 0.11 [2]			
86P-1	2296.5	metapelite		3.95 ± 0.27 [2]			
<b>LV13-26</b>							
RD 43	248.4	Qer (pumice)					1.77 ± 0.06
134	287.4	Qbt (pumice)					1.25
165-S1A	379.4	Qbt (san. milky)				2.64	
165-S1B	379.4	Qbt (san. clear)				5.55	
165-Q1,2	379.4	Qbt (quartz)			7.72 ± 0.18 [2]		
165-mx-1,2	379.4	Qbt (matrix)		1.60 ± 0.20 [2]			
RD120-H1	470.8	Qbt(hydroqtz)			1.18 ± 0.05 [2]		
RD123A-wt-1	478.6	Qbt (pumice)	-1.04 ± 0.03 [2]				
RD123A-S1	478.6	Qbt(sanidine)				5.82 ± 0.15 [2]	
RD123A-H1	478.6	Hydrovein Qtz.			0.74		
RD165-Q1 to 6	599.5	Qbt (quartz)			6.93 ± 0.52 [7]		
1RD65-3	599.5	Qbt (pumice)	0.13				
RD165-mx-1,2	599.5	Qbt (matrix)		3.66 ± 0.31 [4]			
RD165-1,2	599.5	Qbt (pumice)	-0.24 ± 0.40 [2]				
RD 194	684.7	Qbt (pumice)					2.96
RD234-wht-1	801.6	Qbt (pumice)	1.62				
RD234-mtx-1	801.6	Qbt (matrix)		4.57 ± 0.07 [2]			
RD234-Q1	801.6	Qbt(quartz)			7.64		
RD323-S1,2	1064.7	Qbt (sanidine)				6.72 ± 0.17 [2]	
RD323-Q1,2	1064.7	Qbt (quartz)			8.17 ± 0.07 [2]		
RD323-mx-1	1064.7	Qbt (pumice)	6.69 ± 0.24 [2]				
RD323-pm-1	1064.7	Qbt (matrix)		8.19 ± 0.04 [2]			

Table III.1 Oxygen isotope values of silicate components in intracaldera lithologies

Sample ID	Depth (m)	Rock Type	Pm.	Mx.	Qtz.	San.	UW '93-'94
RD365-S1&2,3,4	1185.4	Qbt (sanidines)				6.31 ± 0.50 [3]	
RD365-Q1	1185.4	Qbt (qtz. clear)			6.82		
RD365-Q3A,B	1185.4	Qbt (qtz. xeno?)			9.73 ± 0.17 [2]		
RD365-mx-1,2	1185.4	Qbt (matrix)		7.92 ± 3.64 [3]			
<b>LV68-28</b>							
68-28-173-1	496.0	Qbt(white)		3.16 ± 0.42 [2]			
68-28-173-2	496.0	Qbt(white)	-0.85 ± 0.01 [2]				
<b>LV48-29</b>							
36A-wht-1	480.9	Qbt(white)		-0.50 ± 0.03 [2]			
36A-wht-2	480.9	Qbt(white)		-1.51 ± 0.14 [2]			
<b>LV13-21</b>							
1470a	448.1	Qbt (pumice)					1.99 ± 0.15
2200	670.6	Qbt (pumice)					1.07 ± 0.09
2400 wht-1	731.5	Int. or pum.	1.18 ± 0.07 [2]				
2400 mtx	731.5	metaqtz. xenolith?		17.81			
2400 mtx-4	731.5	Qbt matrix		2.95			
2400 obs	731.5	Qer obsidian?		6.40			
2400-Q1	731.5	Qbt (quartz)			7.54		
2600 wht-1,2	792.5	Int. or pum.	0.05 ± 0.19 [2]				
2600 mtx1,2	792.5	Qbt matrix		3.82 ± 0.42 [2]			
2600 S2	792.5	Qbt (sanidine)				6.54 ± 0.22 [2]	
2800	853.4	Qbt (pumice)					0.87 ± 0.02

Table III.1 Oxygen isotope values of silicate components in intracaldera lithologies

Sample ID	Depth (m)	Rock Type	Pm.	Mx.	Qtz.	San.	UW '93-'94
3400	1036.3	Qbt (pumice)					1.07 ± 0.06
3580	1091.2	Qbt (pumice)					0.84 ± 0.04
<b>SF 38-32</b>							
251	789.5	Qbt (pumice)					0.29
256	803.5	Qbt (pumice)					-1.16

Errors reported as average deviation (one-half the difference of 2 analyses) if 2 repeats and standard deviation if >2 repeats.

[ ] indicates the number repeats of sample for analysis.

Rock Type abbreviations: Qbt- Bishopt Tuff, Qer- Early Rhyolite, Pz- Paleozoic metasediments, Mzmv- Mesozoic metavolcanics, Qtz.- quartz, san.- sanidine, int.- intrusive rock. SWC indicates sample from sidewall core.

Pumice, Matrix, Quartz, Sanidine data collected by VSM, 11/92. UW'93-'94 data collected by MJ Spicuzza and C Niendorf.

Table III.2 Fluid inclusion temperatures and equilibrium  $\delta^{18}\text{O}(\text{H}_2\text{O})$  calculations

LVEW	Sample Type	$\delta^{18}\text{O}$ Sample	<i>Th</i> (°C)	$\delta^{18}\text{O}$ ( $\text{H}_2\text{O}$ )	Present $\delta^{18}\text{O}(\text{H}_2\text{O})$
2C1-H1	Vein Qtz.	2.68	204±39	<b>-9.3</b>	-14.6
2B1-wht-1	Rhyolite Int.	-1.24	204±39	-10.6	-14.6
2B1-wht-2	Rhyolite Int.	-0.24	204±39	-9.6	-14.6
2B1-wht-ave.	Rhyolite Int.	-0.74	204±39	<b>-10.1</b>	-14.6
16B-H-1	Vein Qtz.	-0.69	230±39	<b>-11.1</b>	-14.6
14G-wht-1	pumice	-0.01	230±39	<b>-8.1</b>	-14.6
14G-mx	matrix	2.07	230±39	-6.0	-14.6
14G-S1	sanidine	5.89	230±39	-2.2	-14.6
30C-H-1	Vein Qtz.	17.49	245±25	7.9	-14.6
30C-1,2	metaqtzite.	14.95	245±25	5.4	-14.6
<b>LV13-26</b>					
RD123A-H1	Hydro. Qtz.	0.74	230±39	<b>-9.7</b>	-14.6
RD123A-S1	sanidine	5.82	230±39	-2.3	-14.6
RD123A-wt-2	pumice	-1.04	230±39	<b>-9.1</b>	-14.6

Data for *Th* from McConnell (1996). *Th* values accurate to  $\pm 3^\circ\text{C}$ .  $\delta^{18}\text{O}(\text{H}_2\text{O})$  values calculated using  $\Delta(\text{qtz.}-\text{water})$  fractionation factor of Clayton et al. (1972) or the  $\Delta(\text{Ak feldspar}-\text{water})$  fractionation factor of O'Neil and Taylor (1967). Present  $\delta^{18}\text{O}(\text{H}_2\text{O})$  data determined by averaging thermal water  $\delta^{18}\text{O}$  values from across the caldera from White and Peterson (1991). **Bold**  $\delta^{18}\text{O}(\text{H}_2\text{O})$  values denote silica component nearest equilibrium exchange with thermal  $\text{H}_2\text{O}$ .

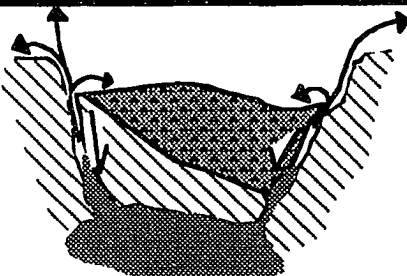
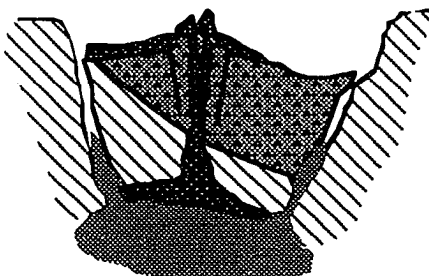
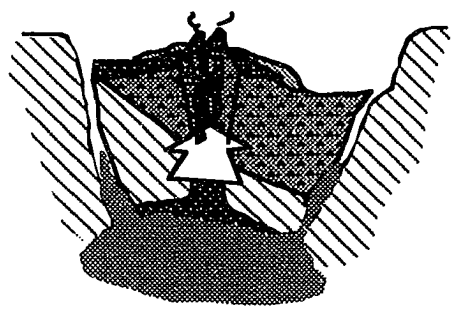
	Time	Event	Evidence
	~760 ka	Eruption of Qbt/Caldera collapse/Filling of caldera with Qbt	Outflow sheet Qbt/present-day caldera/age dates from Qbt <sup>1,2,3</sup> .
	~680-640 ka	Onset of Qer <sub>1</sub> eruptions in central moat/beginning of resurgent doming.	Thick Qer <sub>1</sub> flows and tephra with ages of 675-634 ka <sup>1</sup> including Qer <sub>1</sub> flow at LVEW <sup>2</sup> .
	~600 ka	Hydrothermal flux and beginning of oxygen isotope exchange between intracaldera rock at bottom of Qbt and water in central caldera.	Strong δ <sup>18</sup> O depletion (≤-2‰) of Qbt, Mystery Breccia, and metavolcanics in LVEW. Qer <sub>1</sub> intrusions into Bishop Tuff with ages of 590±17 ka <sup>2</sup> and δ <sup>18</sup> O depletion along Qbt trend beneath resurgent dome.
		Hypabyssal intrusions of Qer <sub>1</sub> into Qbt to ≤800 m from surface./continued resurgence.	Alteration age of metavolcanics indicate flux ~ 500 ka.

Table III.3 Chronology of central caldera volcanic and hydrothermal activity.

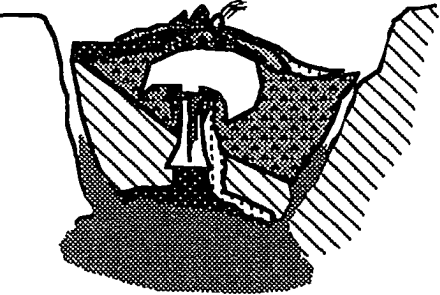
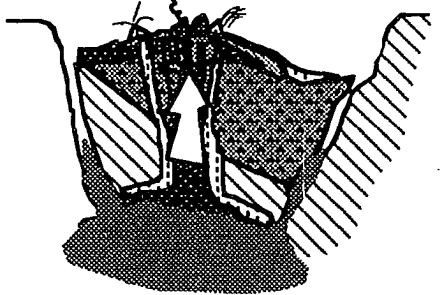
	Time	Event	Evidence
	~500-450 ka	Intrusions of Qer <sub>1</sub> into Qbt/Onset of Qmr intrusions and eruptions on flank of resurgent dome. Hydrothermal flux peaks with convective cell in central caldera.	Qer <sub>1</sub> intrusions into Qbt with ages of 454±17 ka <sup>2</sup> beneath resurgent dome at LVEW and δ <sup>18</sup> O depletion along trend of Qbt/Qmr flows with ages of 509±11 and 469±10 ka <sup>1</sup> and Qmr intrusion into Bishop Tuff at Clay Pit Well.
	~360 ka	Continuing Qer hypabyssal intrusions in Qbt at LVEW.	δ <sup>18</sup> O depletion of ~360 ka Qer intrusions less than depletion trend of Qbt; insufficient time to exchange.
	~300 ka	Qmr volcanic activity migrates away from central resurgent dome to south and east.	Hydrothermal alteration of lacustrine deposits interbedded with 300±10 ka Qmr <sup>1</sup> and U/Th age dates from travertine deposits outside caldera and blue chert deposits inside caldera <sup>4</sup> .
	~200-100 ka	Hydrothermal flux wanes in central caldera as volcanic activity migrates to west moat.	No hydrothermal deposits with ages between 200 and 40 ka <sup>4</sup> /Qmr flows and domes, basalt flows (Qb) and rhyodacite flows in west moat.
	~40 ka	Hydrothermal and volcanic activity resumes.	Mono Craters volcanic activity and Th/U ages of siliceous sinter of 31±9 ka <sup>4</sup> .

Table III.3 Chronology of central caldera volcanic and hydrothermal activity. Qbt-Bishop Tuff, Qer<sub>1</sub> - oldest Early Rhyolite flows, Qmr - Moat Rhyolite. References: <sup>1</sup>Bailey et al., 1976; <sup>2</sup>McConnell et al., 1995; <sup>3</sup>Izett and Obradovich, 1991; <sup>4</sup>Sorey et al., 1991.

## III.10 REFERENCES

- Bailey, R.A., 1974. Preliminary geologic map and cross sections of the Casa Diablo geothermal area, Long Valley Caldera, Mono County, California. USGS Open File Report, Reston, VA, 1-2.
- Bailey, R.A., Dalrymple, G.B., and Lanphere, M.A., 1976. Volcanism, structure, and geochronology of the Long Valley Caldera, Mono County, California. *J. Geophys. Res.*, 81(5):725-744.
- Bailey, R.A., 1989. Geologic map of Long Valley Caldera, Mono- Inyo volcanic chain, and vicinity, Eastern California. USGS Miscellaneous Investigations Series Map I-1933.
- Blackwell, D.D., 1985. A transient model of the geothermal system of the Long Valley Caldera, California. *J. Geophys. Res.*, 90:11,229-11,241.
- Blattner, P., 1985. Isotopic shift data and natural evolution of geothermal systems, *Chem. Geol.*, 45:187-203.
- Carothers, W.W., Mariner, R.H., and Keith, T.E.C., 1987. Isotope geochemistry of minerals and fluids from Newberry Volcano, Oregon. *J. Volcanol. Geotherm. Res.* 31:47-63.
- Chaudet, R.C., 1986. The petrology and geochemistry of precaldera magmas, Long Valley caldera, eastern California, M.Sc. thesis, Virginia Polytechnical Institute, 151 pp.
- Clayton, R.N. and Mayeda, T.K., 1963. The use of bromine pentafluoride in the extraction of oxygen from oxides and silicates for isotopic analysis. *Geochim. Cosmochim. Acta.*, 27:43-52.
- Clayton, R.N., O'Neil, J.R., and Mayeda, T.K., 1972. Oxygen isotope exchange between quartz and water, *Jour. Geophys. Research*, 77:3057-3067.
- Cole, D.R. and Ohmoto, H., 1986. Kinetics of isotope exchange at elevated temperatures and pressures, in J.W. Valley, H.P. Taylor, Jr., and J.R. O'Neil (Eds.), *Stable Isotopes in High Temperature Geologic Processes*, *Rev. in Mineral.*, 16:63-84.
- Craig, H., 1963. The isotopic geochemistry of water and carbon in geothermal areas, In: *Nuclear Geology on Geothermal Areas*, Ed.: Tongiorgi, E., Spoleto: Pisa, Consiglia Nazionale della Richerche, Laboratorio de Geologia Nucleare, 17-53.



- Criss, R.E. and Taylor, H.P., Jr., 1986. Meteoric-hydrothermal systems, in J.W. Valley, H.P. Taylor, Jr., and J.R. O'Neil (Eds.), *Stable Isotopes in High Temperature Geologic Processes*, Rev. in Mineral., 16:373-424.
- Deer, W.A., Howie, R.A., and Zussman, J., 1992. *Sheet Silicates in An Introduction to the Rock-Forming Minerals* (2nd ed.), J. Wiley and Sons, NY, p. 357-381.
- Eiler, J.M., Valley, J.W., Graham, C.M., and Baumgartner, L.P., 1995. Ion microprobe evidence for the mechanisms of stable isotope retrogression in high-grade metamorphic rocks, *Contrib. Mineral Petrol.*, 118:365-378.
- Elsenhaimer, D. and Valley, J.W., 1992. In-situ oxygen isotope analysis of feldspars and quartz by Nd:YAG laser microprobe. *Chem. Geology (Isotope Geosc. Sec.)*, 101:21-42.
- Elsenhaimer, D. and Valley, J.W., 1993. Sub-millimeter scale zonation of  $\delta^{18}\text{O}$  in quartz and feldspar, Isle of Skye, Scotland. *Geochim. Cosmochim. Acta*, 57:3669-3676.
- Eichelberger, J.C., Vogel, T.A., Younker, L.W., Miller, C.D., Heiken, G.H., and Wohletz, K.H., 1988. Structure and stratigraphy beneath a young phreatic vent: South Inyo Crater, Long Valley Caldera, California. *J. Geophys. Res.*, 93:13208-13220.
- Eichelberger, J.C. and McConnell, V.S., 1990. Initial stratigraphic results from the Magma Energy Exploratory Well, Long Valley Caldera, California. *Eos, Trans. Am. Geophys. Union*, 71:6, 260.
- Epstein, S. and Taylor, H.P., Jr., 1967. Variation of  $^{18}\text{O}/^{16}\text{O}$  in minerals and rocks, in P.H. Abelson ed., *Researches in Geochemistry*, John Wiley, New York, 2:29-62.
- Eslinger, E.V. and Savin, S.M., 1973. Mineralogy and oxygen isotope geochemistry of the hydrothermally altered rocks of the Ohaki-Broadlands, New Zealand Geothermal Area. *Am. J. Science*, 273:240-267.
- Fontes, J.Ch., 1980. Environmental isotopes in groundwater hydrology, in: P. Fritz and J.Ch. Fontes (Editors), *Handbook of Environmental Isotope Geochemistry*, Elsevier, Amsterdam, 1:75-140.
- Forester, R.W. and Taylor, H.P., 1977.  $^{18}\text{O}/^{16}\text{O}$ , D/H, and  $^{13}\text{C}/^{12}\text{C}$  studies of the Tertiary igneous complex of Skye, Scotland. *Am. J. Sci.*, 277:136-177.

- Gardner, J.N., Goff, F., Garcia, S., and Hagan, R.C., 1986. Stratigraphic relations and lithologic variations in the Jemez volcanic field, New Mexico. *J. Geophys. Res.*, 91:1763-1778.
- Gilbert, C.M., Christensen, M.N., Al Rawi, Y., and Lajoie, K.R., 1968. Structural and volcanic history of Mono Basin, California-Nevada, *Geol. Soc. Amer. Mem.*, 116:275-329.
- Goff, F., Gardner, J.N., Vidale, R., and Charles, R., 1985. Geochemistry and isotopes of fluids from Sulphur Springs, Valles caldera, New Mexico. *J. Volcanol. Geotherm. Res.*, 23:2734-2797.
- Goff, F., Wollenberg, H.A., Brookins, D.C., Kistler, R.W., 1991. A Sr-isotopic comparison between thermal waters, rocks, and hydrothermal calcites, Long Valley caldera, California. *J. Volcanol. Geotherm. Res.*, 48:265-282.
- Halliday, A.N., Fallick, A.E., Hutchinson, J. and Hildreth, W., 1984. A Nd, Sr and O isotopic investigation into the causes of chemical and isotopic zonation in the Bishop Tuff, California. *Earth Planet. Sci. Lett.*, 68: 379-374.
- Hamza, M.S. and Epstein, S, 1980. Oxygen isotopic fractionation between oxygen of different sites in hydroxyl-bearing silicate minerals. *Geochim. Cosmochim. Acta*, 44:173-182.
- Hildreth, E.W., 1977. The magma chamber of the Bishop Tuff: gradients in temperature, pressure, and composition, Ph.D. thesis, University of California, Berkeley, 328 pp.
- Hildreth, W., 1979. The Bishop Tuff: evidence for the origin of compositional zoning in silicic magma chambers. In: C.E. Chapin and W.E. Elston (Editors), *Ash Flow Tuffs*. *Geol. Soc. Am. Special Paper* 180:43-75.
- Hildreth, W., 1981. Gradients in silicic magma chambers: implications for lithospheric magmatism. *J. Geophys. Res.*, 86:10,153-10,192.
- Huber, N.K., 1981. Amount and timing of Late Cenozoic uplift and tilt of the central Sierra, California-evidence from the upper San Joaquin River Basin, U.S. Geological Survey, Professional Paper 1197:28pp.
- Izett, G.A., and Obradovich, J.D., 1991. Dating of the Matuyama-Brunhes Boundary based on  $^{40}\text{Ar}/^{39}\text{Ar}$  ages of the Bishop Tuff and Cerro San Luis Rhyolite. *Geol. Soc. Am. Abstract*, 23(5):A106.
- Kohn, M.J., Valley, J.W., Elsenheimer, D., and Spicuzza, M.J., 1993. O isotope zoning in garnet and staurolite: Evidence for closed-system mineral growth during regional metamorphism. *Amer. Mineral.*, 78:988-1001.

- Layer, P.W., McConnell, V.S., and Eichelberger, J.C., 1992. New age constraints on magmatic and hydrothermal activity in central Long Valley Caldera, California. *Eos, Trans. Am. Geophys. Union*, 73(14):345.
- Lipman, P.W., 1984. The roots of ash flow calderas in Western North America: windows into the tops of granitic batholiths. *J. Geophys. Res.*, 89:B10:8801-8841.
- Long Valley Science Panel, 1991. Investigation of active volcanic processes in Long Valley Caldera via deep continental drilling. U.S. DOE, UCRL-PROP-108826, 1-31.
- Mankinen, E.A., Gromme, C.S., Dalrymple, G.B., Lanphere, M.A., and Bailey, R.A., 1986. Paleomagnetism and K-Ar ages of volcanic rocks from Long Valley caldera, California. *J. Geophys. Res.*, 91:633-652.
- Metz, J.M. and Mahood, G.A., 1985. Precursors to the Bishop Tuff eruption: Glass Mountain, Long Valley, California. *J. Geophys. Res.*, 90:11121-11126.
- McConnell, V.S. and Eichelberger, J.C., 1990. Initial results from the Magma Energy Exploratory Well, Long Valley Caldera, EOS *Trans. Geophys. U.*, 71:1676-1677.
- McConnell, V.S., Eichelberger, J.C., and Keskinen, M.J., 1991. Phase II of the Long Valley Exploratory Well, Long Valley Caldera, California: early geologic results. *Eos, Trans. Am. Geophys. Union*, 72(44):550.
- McConnell, V.S., Eichelberger, J.C., Keskinen, M.J., Shearer, C.K., and Papike, J.J., 1992. Investigation of rhyolitic intrusions into intracaldera Bishop Tuff: the Long Valley exploratory Well, Long Valley, California, EOS *Trans. Geophys. U.*, 73:
- McConnell, V.S., 1993. Post-emplacement alteration beneath the resurgent dome of the Long Valley Caldera, California, . EOS *Trans. Am. Geophys. Union*, 74:354.
- McConnell, V.S., Valley, J.W., Spicuzza, M.J., and Eichelberger, J.C., 1994. Oxygen isotope microanalyses of silicic rocks in Long Valley Caldera: uncovering trends in the paleohydrothermal systems, U.S. Geol. Surv. Circular 1107:209.
- McConnell, V.S., Shearer, C.K., Eichelberger, J.C., Keskinen, M.J., Layer, P.W., and Papike, J.J., 1995. Rhyolitic Intrusions in the Intracaldera Bishop Tuff, Long Valley Caldera, California, *J. Volcanol. Geotherm. Res.*, 67:41-60.

- Miller, C.D., 1985. Holocene eruptions at the Inyo volcanic chain, California: implications for possible eruptions in Long Valley. *Geology*, 13:14-17.
- Mukhopadhyay, B., Valley, J.W., Spicuzza, M.J., Niendorf, C.R., 1994. Millimeter scale oxygen isotope zonation in drill core from Long Valley Exploratory Well: implications for fluid flow, *GSA Abstracts*, 26(7):A-280.
- Nelson, P.H., Kibler, J.E., Mikeseil, J., 1994. Geophysical Logs in the Long Valley Exploratory Well, VIIth Intern. Symposium Obsev. Continental Crust through Drilling.
- O'Neil, J.R. and Taylor, H.P., Jr., 1967. The oxygen isotope and cation exchange chemistry of feldspars. *Am. Mineral.*, 52: 1414-1437.
- O'Neil, J.R., 1986. Theoretical and experimental aspects of isotopic fractionation, in J.W. Valley, H.P. Taylor, Jr., and J.R. O'Neil (Eds.), *Stable Isotopes in High Temperature Geologic Processes*, *Rev. in Mineral.*, 16:1-37.
- Rinehart, C.D. and Ross, D.C., 1964. Geology and mineral deposits of the Mount Morrison Quadrangle Sierra Nevada, California. *U.S. Geol. Surv. Prof. Paper* 385:7-30.
- Rundle, J.B., and Hill, D.P., 1988. The geophysics of a restless caldera-Long Valley, California. *Ann. Rev. Earth Planet, Science*, 16:251-271.
- Sass, J.H., Jacobson, R., and Sorey, M.L., 1991. Implications of thermal observations in the Long Valley Exploratory Well. *Eos, Trans. Am. Geophys. Union*, 72(44):504.
- Savin, S.M. and Lee, M., 1988. Isotope studies of phyllosilicates, in S.W. Bailey (Ed.), *Hydrous Phyllosilicates (exclusive of micas)*, *Rev. Mineral.* 19:189-219.
- Smith, R.L. and Bailey, R.A., 1968. Resurgent cauldrons, *Geol. Soc. Amer. Mem.*, 116:613-662.
- Smith, R.L. and Shaw, H.R., 1975. Igneous-related geothermal systems, *Assessment of Geothermal Resources of the United States*, edited by D.E. White and D.L. Williams. *U.S. Geol. Surv. Circ.* 726: 58-83.
- Smith, B.M. and Suemnicht, G.A., 1991. Oxygen isotope evidence for past and present hydrothermal regimes of Long Valley caldera, California. *J. Volcanol. Geotherm. Res.*, 48:319-339.

- Smith, B.M., Gunderson, R.P., and Suemnicht, G.A., 1988. Oxygen isotope evidence for magma-groundwater interactions in early, post-collapse rhyolites from the Long Valley Caldera. *Geol. Soc. Am., Abstr. Programs*, A114.
- Snow, E. and Yund, R.A., 1988. Origin of cryptoperthites in the Bishop Tuff and their bearing on its thermal history, *J. Geophys. Res.*, 93(B8):8975-8984.
- Sorey, M.L., 1985. Evolution and present state of the hydrothermal system in Long Valley caldera, *J. Geophys. Res.*, 90:11,219-11,228.
- Sorey, M.L., Suemnicht, G.A., Sturchio, N.C., and Nordquist, G.A., 1991. New evidence on the hydrothermal system in Long Valley Caldera, California, from wells, fluid sampling, electrical geophysics, and age determinations of hot-spring deposits. *J. Volcanol. Geotherm. Res.*, 48:229-263.
- Sturchio, N.C., Keith, T.E.C., and Muehlenbachs, K., 1990. Oxygen and carbon isotope ratios of hydrothermal minerals from Yellowstone drill cores. *J. Volcanol. Geotherm. Res.*, 40:23-37.
- Suemnicht, G., 1987. Results of deep drilling in the western moat of Long Valley, California. *Eos, Trans. Am. Geophys. Union*, 68 (40): 785.
- Suemnicht, G.A. and Varga, R.J., 1988. Basement structure and implications for hydrothermal circulation patterns in the western moat of Long Valley caldera, California. *J. Geophys. Res.*, 93 (B11): 191-207.
- Taylor, H.P., 1968. The oxygen isotope geochemistry of igneous rocks. *Contr. Mineral. and Petrol.*, 19: 1-71.
- Taylor, H.P., Jr., 1971. Oxygen isotope evidence for large-scale interaction between meteoric groundwaters and Tertiary granodiorite intrusions, Western Cascade Range, Oregon, *J. Geophys. Res.*, 76:7855-7874.
- Taylor, H.P., Jr., 1974. The application of oxygen and hydrogen isotope studies to problems of hydrothermal alteration and ore deposition, *Econ. Geol.*, 69:843-883.
- Taylor, H.P., Jr., 1979. Oxygen and hydrogen isotope relationships in hydrothermal mineral deposits, In: *Geochemistry of Hydrothermal Ore Deposits*, Ed.: Barnes, H.L., J. Wiley and Sons, 236-277.
- Taylor, H.P., Jr. and Sheppard, S.M.F., 1986. Igneous rocks: I. processes of isotopic fractionation and isotope systematics in Stable Isotopes in High Temperature Processes, *Reviews in Mineralogy*, 16:273-316.

- Valley, J.W., and Graham, C.M., 1991. Ion microprobe analysis of oxygen isotope ratios in granulite facies magnetites: diffusive exchange as a guide to cooling history, *Contr. Mineral. and Petrol.*, 109:38-52.
- Valley, J.W., and Graham, C.M., 1993. Cryptic grain-scale heterogeneity of oxygen isotope ratios in metamorphic magnetite, *Science*, 259:1729-1733.
- Valley, J.W., Chiarenzelli, J.R., and McLelland J.M., 1994a. Oxygen isotope geochemistry of zircon, *Earth and Planet. Sci. Letters*, 126:187-206.
- Valley, J.W., McConnell, V.S., and Eichelberger, J.C., 1994b. Microanalysis of oxygen isotope ratios: Long Valley Caldera, VIIth Intern. Symposium Obsev. Continental Crust through Drilling, 74-77.
- Valley, J.W., and Graham, C.M.,. Ion microprobe analysis of oxygen isotope ratios in quartz phenocrysts: healed micro-cracks, fluid flow, and hydrothermal exchange, in review *Contrib. Mineral. Petrol.*
- Valley, J.W., Kitchen, N., Kohn, M.J., Niendorff, C.R., and Spicuzza, M.J., 1995, UWG-2, A garnet standard for oxygen isotope ratio: strategies for high precision and accuracy with laser heating, submitted to *Geochim. Cosmochim. Acta*.
- Vogel, T.A., Woodburne, T.B., Eichelberger, J.C., and Layer, P.W., 1994. Chemical evolution and periodic eruption of mafic lava flows in the west moat of Long Valley Caldera, California, *J. Geophys. Res.*, 99:19829-19842.
- White, A.F. and Peterson, M.L., 1991. Chemical equilibrium and mass balance relationships associated with the Long Valley hydrothermal system, California, U.S.A. . *J. Volcanol. Geotherm. Res.*, 48:283-300.

#### **IV.1 Age correlations in intracaldera rocks from Long Valley Caldera, California: implications of intrusion, resurgence, and hydrothermal pulses<sup>3</sup>**

##### IV.2 ABSTRACT

Laser probe  $^{40}\text{Ar}/^{39}\text{Ar}$  age determinations of hydrothermally altered intracaldera rocks from the Long Valley Caldera reveal heterogeneity of Ar isotopic signatures not visible by bulk step heating techniques. These variations in ages within individual samples when viewed as a composite along a vertical cross-section beneath the resurgent dome, indicate a rich history of post-caldera-collapse rhyolitic intrusive and hydrothermal activity.  $^{87}\text{Sr}/^{86}\text{Sr}$  and  $\delta^{18}\text{O}$  isotope compositions of the same rocks and minerals provide crucial corroboration of age data interpretations.

Post-caldera-collapse Early Rhyolite extrusive activity in the central resurgent dome area ended  $649\pm 5$  ka and show no isotopic evidence of alteration. Age determinations of Early Rhyolite intrusions, however, show evidence of later hydrothermal effects as well as primary emplacement ages. Sanidine phenocrysts within the Bishop Tuff show ages of emplacement of  $749\pm 12$  and  $750\pm 5$  ka where the sample location is below the blocking temperature of potassium feldspar ( $250^\circ\text{C}$ ) on the projected paleogeothermal gradient. Phenocrysts selected from deeper in the caldera fill, and where

---

<sup>3</sup> Age correlations of intracaldera rocks in Long Valley Caldera, California: implications of intrusion, resurgence, and hydrothermal pulses by V. S McConnell for submittal to Geology.

temperatures reached upward to 350°C, no longer record the volcanic history. Instead, they yield dates both much younger than the emplacement age of the Bishop Tuff, interpreted as indicating resetting by hydrothermal activity, and much older, indicating the presence of excess Ar. Ages of altered metavolcanic rocks from the basement of the caldera indicate hydrothermal activity was extensive enough to reset the emplacement ages of these older, deeper rocks. Taken together, the ages reveal continued emplacement of the Early Rhyolite into the central caldera that, in turn, drove upwelling hydrothermal pulses into the intracaldera Bishop Tuff and originating within the basement rocks.

Fluid inclusions analyzed from vein quartz and calcite hosted by intracaldera rocks are uniformly moderate to high salinity (0 to 16 wt.% NaCl) water in the intracaldera volcanic rocks. A change in the affect hydrothermal fluids on intracaldera rocks occurs within the fine-grained and competent Paleozoic metasediments. Here, the complexly fractured Paleozoic metasediments that comprise the basement of the central caldera have more variation in their fluid compositions, from moderate-to-high salinity water to inclusions that are exclusively CH<sub>4</sub> and CO<sub>2</sub>. Radiogenic Sr compositions of alteration calcite in the Bishop Tuff in excess of either the volcanic rock or the present-day thermal water indicates some volume of the paleohydrothermal fluid originated during dewatering of the metasediments.



### IV.3 INTRODUCTION

Caldera-sized eruptions are in many cases followed by post-caldera-collapse volcanic activity and/or hydrothermal pulses (Lipman, 1984) especially in continental crustal locations. This post-collapse activity has the potential of mobilizing and concentrating ore deposits and fueling hydrothermal systems. While the relationship between post-caldera-collapse magmatic activity and cyclic hydrothermal pulses appears fundamental, understanding the processes is limited by our ability to provide evidence of isolated individual events. However, in many cases the complex eruptive history of caldera-forming events masks the petrographic or chemical relationships between magmatic and hydrothermal activity.

The Long Valley Caldera, located in east-central California, formed by a single catastrophic Plinian and ash-flow eruption (Bailey et al., 1976; Hildreth, 1977) approximately 760 ka (Izett and Obradovich, 1992; van den Bogaard and Schirnick, 1995). Intracaldera volcanic activity and resurgence began vigorously in the central caldera area within 100 ka after collapse (Bailey et al., 1976) and there is isotopic and petrographic evidence of hydrothermal activity centered about the resurgent dome (Goff et al., 1991; McConnell et al., 1995).

In this study, I use laser probe  $^{40}\text{Ar}/^{39}\text{Ar}$  ages determined from intracaldera rocks and minerals to constrain paleohydrothermal events and establish a link between magmatic and hydrothermal activity. Ages were determined from whole rock samples of aphyric and cryptocrystalline post-caldera-collapse Early Rhyolite lavas and intrusions, sanidine

phenocrysts from the Bishop Tuff, and whole rock samples of fine-grained metamorphic basement rocks. The complex, multiple ages that are revealed by microanalysis are used to construct a timeline of volcanic and hydrothermal events.

Oxygen isotope compositions of the samples indicate exchange with high temperature fluids, valuable evidence of hydrothermal activity. Although it is generally accepted that argon isotopes do not exchange with water but are mobilized by solid state diffusion in response to partial pressure differentials (Faure, 1986), evidence of hydrothermal activity is crucial to the interpretation of the multiple ages determined in this study. In addition,  $^{87}\text{Sr}/^{86}\text{Sr}$  compositions of rocks can provide important correlation of intracaldera rocks to outcrop equivalents and act as a tracer for fluid flow. Because the rate of strontium diffusion in feldspars increases by an order of magnitude in a hydrous environment (Davies et al., 1994), deviation in the samples of this study from the primary range also indicates post-emplacement hydrothermal events.

Analysis of fluid inclusions in fractures in intracaldera volcanic and metamorphic rocks was undertaken with the aim of determining paleohydrothermal fluid compositions and pathways.

#### IV.4 SAMPLING AND ANALYSES

Most of the samples of the intracaldera lithologies were taken from core and cuttings from the Long Valley Exploratory Well (LVEW). This well penetrated 2.3 km into the central resurgent dome, bottoming in the

pre-caldera Paleozoic metasedimentary basement of the central caldera (McConnell et al., 1995). Sample Qer-16 was collected from an Early Rhyolite obsidian flow at the wellhead. The vent for this flow is approximately 1 km to the east. Early Rhyolite obsidian and intrusive rocks, and fine-grained metamorphic rocks were prepared as whole rock samples for all analyses.

The oxygen isotope study is reported in detail in Chapter III.

#### *IV.4.1 For $^{40}\text{Ar}/^{39}\text{Ar}$*

In preparation for  $^{40}\text{Ar}/^{39}\text{Ar}$  analyses, hand-picked chips from core samples or drill cuttings were cleaned in deionized water and acetone with an ultrasonic disintegrator. Care was taken when hand-picking samples to avoid veinlets of alteration minerals. Ubiquitous, disseminated quartz, calcite, and pyrite were not eliminated from the samples. Sanidine phenocrysts from the Bishop Tuff were concentrated by heavy liquid separation and subsequently hand-picked to eliminate plagioclase and quartz phenocrysts, and matrix material. Sanidine phenocrysts were cleaned in the same manner as whole rock samples after etching in 1.5 N acetic acid to remove calcite alteration contamination. All samples were irradiated for 2 MW hours at the McMaster University Nuclear Reactor, Ontario, Canada. Lateral and vertical irradiation flux quantities were monitored by Bern 4B biotite standard with an age of 17.25 Ma. Samples were fused with a coherent 6W Ar-ion laser and argon isotopic ratios measured on a VG3600 mass spectrometer at the University of Alaska Geochronology Laboratory equipped with both a Faraday collector and a Daly multiplier with a gain of ~100 over the Faraday. Gas clean-up was

accomplished by use of a liquid N<sub>2</sub> cold finger and a SAES ST-101 getter at 400°C. Ages are reported with 1  $\sigma$  error.

#### *IV.4.2 For <sup>87</sup>Sr/<sup>86</sup>Sr*

Samples were prepared and analyzed at the Berkeley Center for Isotope Geochemistry, University of California Berkeley. Crushed whole rock samples to be measured for <sup>87</sup>Sr/<sup>86</sup>Sr were cleaned in deionized water and acetone prior to being prepared by standard silicate acid digestion except where matrix calcite was to be measured. In these cases, a preliminary step of slow, overnight dissolution of calcite in 1 N acetic acid solution was added to the procedure. This aliquot was then prepared as a sample. Hand-picked calcite from hydrothermal veins was also digested in 1 N acetic acid overnight. Sanidine phenocrysts were processed in heavy liquid and then hand-picked to assure purity. They were etched in 7% HF to remove matrix material before dissolution by the same method as the whole rock samples. Strontium was isolated by high pressure liquid chromatography using a Dionex HPLC unit with a Sr specific ion resin column, loaded on tantalum filaments, and measured for isotopic ratios using a multi-collector VG 54 mass spectrometer. <sup>87</sup>Sr/<sup>86</sup>Sr ratios are reported with 1  $\sigma$  error within last significant figure. Laboratory accuracy is monitored by comparison to NBS 98 standard for strontium with a reported value of 0.71024310±15 for Jan.-June of 1995.

#### *IV.4.3 For Fluid Inclusion Analysis*

Analysis of fluid inclusions was conducted at the Geology and Geophysics Department at the University of Wisconsin-Madison under the guidance of Dr. Philip Brown. Thick sections were prepared from selected veins filled with quartz, calcite, and pyrite from Early Rhyolite intrusions, Bishop Tuff, and metasedimentary basement rocks from cored sections in LVEW. Measurements on the fluid inclusions were carried out using a Linkam THMSG 600 heating-freezing stage mounted on a Zeiss Universal microscope. Observations were made with a 40X objective. Freezing runs generally have precisions of  $\pm 0.1^\circ\text{C}$ , high temperature measurements were repeatable to  $\pm 0.5^\circ\text{C}$ .

#### IV.5 DISCUSSION OF RESULTS

##### *IV.5.1 Laser probe vs. bulk step heating techniques for $^{40}\text{Ar}/^{39}\text{Ar}$ dating of altered rocks*

Altered rocks from beneath the resurgent dome of the Long Valley Caldera contain isotopic information pertaining to the post-caldera-collapse history. It is possible to reconstruct this history through examination of complementary isotopic systems, for example,  $\delta^{18}\text{O}$  compositions of silicate components of intracaldera rocks,  $^{87}\text{Sr}/^{86}\text{Sr}$  compositions of intracaldera rocks and minerals, and  $^{40}\text{Ar}/^{39}\text{Ar}$  dating of intracaldera rocks. Yet the interpretations may become obscured if the analyses are conducted at a

resolution that masks the heterogeneity of the samples (McConnell et al., in press). Perhaps the most definitive example from this study comes from comparing the differences observed in the  $^{40}\text{Ar}/^{39}\text{Ar}$  ages determined by bulk step heating to those obtained by laser probe vaporization of the same sample. For bulk step heating analysis, approximately 1 g. of crushed sample is required, thus assuming, for whole rock, that the sample is homogeneous. In contrast, for laser probe analysis, chips of whole rock sample or single crystals as small as  $3\text{ mm}^3$  can be analyzed and homogeneity of the sample no longer need be assumed.

Figure IV.1 depicts this point by comparing the ages determined from one sample by both techniques. Figure IV.1a is the age plot from sample 2-B1 obtained by bulk step heating fractions. The sample has a plateau age of  $454\pm 17$  ka. Figure IV.1b shows the same data as Figure IV.1a in a different format. In this figure and following age plots, ages for individual fractions (for bulk) or grains (for laser) are represented as gaussian curves of unit area with the analytical mean and the standard deviation used to construct the curve. The cumulative gaussian distributions for the individual data form an age probability plot. The gaussian distribution of the age plateau determined from the age spectra in Figure IV.1a is a unimodal peak in Figure IV.1b. Interpretation of the geologic significance of either Figure IV.1a or b would be limited to inferring one primary event set the argon isotope ratio. In this case where the sample consists of altered intrusive rocks, the age could represent either the timing of emplacement or later diffusion of argon in response to hydrothermal fluids. On the other hand, the results of the laser probe analysis

of 11 separate grains from the same sample (Figure IV.1c) show a range of peaks from approximately 300 to 740 ka. Whereas the bulk step heating analysis would have to be interpreted as a single geologic event that locked in a homogeneous argon composition, the laser probe analysis indicates a series of events that affected the isotopic ratio of argon in the sample. If, on the other hand, the laser probe data are averaged their arithmetic mean is  $465 \pm 15$  ka. This is identical to the plateau age derived from the bulk step heating technique and again “homogenizes” the detail in the sample. The interpretation of this complexity of ages is discussed below in the context of stratigraphy beneath the resurgent dome.

#### *IV.5.2 $^{40}\text{Ar}/^{39}\text{Ar}$ age determinations of samples and Sr and O isotopes*

Figure IV.2 displays selected laser probe  $^{40}\text{Ar}/^{39}\text{Ar}$  ages along a timeline from 0 to 900 ka. Table IV.1 lists all the samples discussed in this study along with their depths in the well and their measured isotopic values. For  $^{40}\text{Ar}/^{39}\text{Ar}$  dates, interpreted ages are listed if the sample yielded multiple age modes; average and standard deviation are reported when unimodal. In addition, the table lists a range of isotopic compositions for outcrop rocks equivalent to these intracaldera rocks. Stratigraphic diagrams of LVEW are compiled in Appendix I. Appendix IV contains individual ages and errors for  $^{40}\text{Ar}/^{39}\text{Ar}$  age determinations, and Appendix V contains  $^{87}\text{Sr}/^{86}\text{Sr}$  data.

Sanidine phenocrysts from five locations within the Bishop Tuff were analyzed (Table IV.1). Dates of  $749 \pm 12$  (10 analyses) and  $750 \pm 5$  (1 analysis), determined for two samples, LV3880 and LV5100, respectively, correlate to

the eruption age for the Bishop Tuff outflow sheet of approximately 760 ka (Izett and Obradovich, 1991; van den Bogaard and Schirnack, 1995). Sample 14-G (10 analyses) yielded an age of  $635 \pm 13$  ka, a date that is related to emplacement of Early Rhyolite intrusions. It is not clear why the phenocrysts measured from this shallower location in the Bishop Tuff appear to be completely reset. The oxygen isotope composition of this sample,  $5.9 \pm 0.1\text{‰}$ , is not greatly lowered from the magmatic range of 7.0 to 8.4‰. On the other hand, the  $^{87}\text{Sr}/^{86}\text{Sr}$  ratio is anomalously high, outside the range of any reported Bishop Tuff sanidine measurements or, for that case, any unaltered post-caldera-collapse volcanic rocks (Table IV.1). Two sanidine samples, from locations in the well above the 250°C isotherm calculated for the paleogeothermal gradient from  $\delta^{18}\text{O}$  geothermometry, yield bimodal dates bracketing the eruption age of the Bishop Tuff. Peaks appear at ~390 and ~530 ka for LV5810 (10 analyses) and ~310 ka for LV5880 (7 analyses) indicating later geologic events reset the  $^{40}\text{Ar}/^{39}\text{Ar}$  ratio in these samples. In addition, these sanidines yield much older apparent ages, 1500 to 3000 ka. Their oxygen isotope compositions are lowered in  $\delta^{18}\text{O}$  from eruptive values by nearly -15‰ indicating exchange with hydrothermal fluids at temperatures as high as 350°C (Figure IV.3). Isochron ages for LV5880 show a  $^{40}\text{Ar}/^{39}\text{Ar}$  ratio of  $310 \pm 4$  indicating excess radiogenic argon in the system. Paleozoic basement rocks that underlie the Bishop Tuff are the most likely source for argon contamination.



After the collapse of the Long Valley caldera and its filling with intracaldera Bishop Tuff at 760 ka, volcanic activity resumed possibly as early as 751 ka (Mankinen et al., 1986). Data from this study suggest the Early Rhyolite flows and tephra which comprise much of the centrally located resurgent dome ended emplacement at  $649 \pm 5$  ka, the age determined for the obsidian sample (Qer-16) from the topmost flow at the LVEW wellhead. These aphyric to sparsely plagioclase-phyric obsidians and tephra show no petrographic evidence of alteration by hydrothermal fluids (McConnell et al., 1995), and the  $\delta^{18}\text{O}$  composition of Qer-16 is within the primary magmatic range for the Early Rhyolite (Table IV.1). Intrusions of Early Rhyolite into the Bishop Tuff, however, display a more complex history. Samples 2-B1 and 8-G are from within a 45 m-thick intrusion at a depth of 766 to 811 m. Both display multiple age modes (Figure IV.2). Sample 2-B1 has an isolated peak (S1A, Figure IV.2) that overlaps the 649 ka emplacement age of the overlying obsidian. A broad triplet peak between 600 and 400 ka and a strong peak at  $\sim 300$  ka (S3, Figure IV.2) indicate partial resetting of the argon clock in this intrusion. The oxygen isotope composition of this sample is lowered in  $\delta^{18}\text{O}$  relative to the magmatic range by as much as  $-10\text{‰}$ , while the  $^{87}\text{Sr}/^{86}\text{Sr}$  value has increased. Both changes can be attributed to circulation of hydrothermal fluids that are low in  $\delta^{18}\text{O}$  and high in basement-derived radiogenic strontium, conditions assumed to represent the paleohydrothermal fluids in the caldera. Sample 8-G has a strong peak at  $\sim 610$  ka, termed S1B. In addition, a doublet occurs between 400 and 500 ka (S2) with both peaks coincident with peaks

observed in 2B-1. Sample 8-G is lowered in  $\delta^{18}\text{O}$  composition from the magmatic value, but not as significantly as 2-B1. Nor does it contain any evidence of the later ~300 ka peak seen in 2-B1.. Here it becomes necessary to examine the anatomy of the shallow intrusion. Appendix Ic diagrams the stratigraphy of the intrusion, describing the petrographic variations. Most significant to this study is the occurrence of a brecciated, fractured zone within the intrusion and at the location of 2-B1. The disruption of the cryptocrystalline intrusion by brecciated material could imply a second, more isolated intrusive event or a vigorous hydrothermal pulse. Eichelberger et al. (1988) noted the occurrence of multiple-age dike intrusions beneath the South Inyo Domes crater located in the West Moat of the Long Valley Caldera.

In this case, multiple age spectra along with the evidence of shifting of magmatic isotopic compositions and petrographic evidence of disturbance within the intrusion are interpreted as reflecting times of post-emplacment events such as a hydrothermal pulse or the emplacement of a second, younger intrusion. Note that 2-B1 has a peak at ~740 ka. This is interpreted as contamination by entrainment of Bishop Tuff material that hosts the intrusions but could possibly represent very early post-caldera-collapse intrusive activity similar in age to that reported in Mankinen et al. (1986).

A deeper intrusion in the intracaldera Bishop Tuff, LV4000, shows a small peak at ~650 ka and a strong doublet coincident with S2 and S3 at ~420 and ~350 ka. These multiple age modes could be interpreted as indicating initial intrusive activity beginning ~630 ka, coincident with peaks S1A and S1B

observed in the shallower intrusion. Examination of the  $\delta^{18}\text{O}$  composition of LV4000 shows this deeper intrusion is no more depleted in  $\delta^{18}\text{O}$  than the shallower intrusion (Table IV.1). If LV4000 had been emplaced at the same time as 2B-1 and 8-G but at this deeper location in the intracaldera Bishop Tuff, then it should have an oxygen isotope composition of  $<-2\text{‰}$ , reflecting more exchange with hotter fluids over the same period of time. Thus I invoke an alternate explanation, that the peak observed at  $\sim 650$  ka represents contamination of material from older intrusions either incorporated during emplacement of this intrusion at  $\geq 420$  ka or reflecting contamination of the well cuttings samples. Later intrusive/hydrothermal fluxes at  $\sim 350$  ka, coincident with ages observed in the overlying 2-B1 modified the emplacement  $^{40}\text{Ar}/^{39}\text{Ar}$  ratio. All age modes from samples at the LVEW location are devoid of any activity after  $\sim 250$  ka.

A sample of the chlorite and epidote-rich metavolcanic rocks that underlie the Bishop Tuff yielded incremental laser spectra of  $\sim 500$  and  $\sim 1000$  ka (Figure IV.3). The  $\sim 500$  ka date coincides with S2 from the modal ages of the intrusion. This indicates these basement rocks were involved in at least one of the post-caldera-collapse events. An age of 1000 ka could represent a pre-caldera-collapse hydrothermal event. Assuming these rocks are Mesozoic in age (see Chapter II) then this sample has effectively diffused more than 99% of the original radiogenic argon as the age spectra does not reflect a plateau age of Mesozoic time. A  $\delta^{18}\text{O}$  composition of  $-4.6 \pm 0.5\text{‰}$  is well

below any primary volcanic value, and is as much as -13‰ below the range for caldera volcanic rocks. An alternate explanation for the origin of these volcanic rocks would be that the 1000 ka age represents the timing of emplacement of the 134 m-thick sequence. An age of 1000 ka correlates to the time of emplacement of the Glass Mountain rhyolitic complex that predates the caldera-forming event (Davies et al., 1994) and sits adjacent to the north-east rim of the caldera. The  $^{87}\text{Sr}/^{86}\text{Sr}$  composition of the whole rock sample is  $0.70715 \pm 1$ , a value within the range of compositions of Mesozoic metavolcanic rocks (see Table IV.1), not within a range of measured values of glass separates of Glass Mountain lavas, 0.7173-1.0012, reported by Davies et al. (1994). These are most likely metavolcanic rocks that have been hydrothermally altered both before caldera formation and during emplacement of post-caldera-collapse rhyolite intrusions.

Laser probe step heating of samples from a pelitic hornfels from the Paleozoic metasedimentary basement rocks converged at approximately 100 Ma (Figure IV.4). Oxygen isotope compositions of the various rock units that comprise the metasediments are variable and dependent upon the rock type. Table IV.1 lists the values for  $\delta^{18}\text{O}$  from a quartzite and a hornfels. The quartzite still maintains a value in the range of outcrop equivalents while the hornfels composition could indicate exchange with hydrothermal water. Strontium isotope compositions of all rocks remain in the reported range for outcrop equivalents (see Table IV.1). An age of 100 Ma correlates to the timing of intrusion of Cretaceous granitic plutons adjacent to the caldera

(Rinehart and Ross, 1964; Kistler and Swanson, 1981) and defines the last regional-scale resetting of the argon clocks in the metasediments. Later hydrothermal flow in these rocks appears to be restricted to multiple fracture systems (Mukhopadhyay et al., 1994) and is discussed in the following fluid inclusion study.

#### *IV.5.3 Fluid inclusion study and Sr isotopes in calcite*

Both metamorphic basement rocks and intracaldera volcanic rocks host fractures filled with hydrothermal minerals. Additionally, the more porous volcanic rocks have calcite- and quartz-filled vugs and matrix alteration mineralogy (McConnell et al., 1995). Determination of reservoir temperatures for mineral deposition and the composition of the paleohydrothermal fluid(s) was the primary aim of the analyses. Table IV.2 lists the temperatures of homogenization ( $Th$ ), the composition of the fluid inclusions, and the  $^{87}\text{Sr}/^{86}\text{Sr}$  composition of the host mineral and rocks where measured. Figure IV.6 plots salinity versus temperature and Figure IV.7 plots  $Th$  against depth in LVEW. Inclusions were identified as primary when they occurred as isolated individuals or clusters or, at least, were not obviously part of trails which crosscut grain boundaries. The fine-grained nature of the minerals hosting the inclusions in several of the samples made the unambiguous determination of primary versus secondary quite difficult but these were avoided during analyses. There were definitely secondary inclusions and this is significant as it implies the introduction of fluids at a later time (Roedder, 1986).

The composition of the  $<10\mu\text{m}$  fluid inclusions in the volcanic rocks is low-to-moderate salinity (0.2-3.3 wt.% equivalent NaCl)  $\text{H}_2\text{O}-\text{NaCl}\pm\text{KCl}$ , with one sample having a value of 16 wt.%. The presence of potassium chloride is indicated by the depression of the temperature of the eutectic for the system  $\text{H}_2\text{O}-\text{NaCl}$ .  $\text{CO}_2$  is most likely present in amounts  $<10$  vol.%, but the small size of the inclusions hampers determination of the concentration (P. Brown, pers. comm., 1995). Inclusion morphology is irregular, varying from positive to semi-negative. Most primary inclusions occur as clusters although inclusions with cross-cutting trails were observed but not analyzed. Compositions of the fluid inclusions analyzed in the more complexly fractured basement rocks fall into four categories,  $\text{H}_2\text{O}-\text{CO}_2-\text{CH}_4-\text{NaCl}$ ,  $\text{H}_2\text{O}-\text{CO}_2-\text{NaCl}$ ,  $\text{H}_2\text{O}-\text{NaCl}-\text{KCl}\pm\text{CO}_2$ , and  $\text{CO}_2-\text{CH}_4$  with the first listed compositions being predominant. Sample 35-J contained only two-phase  $\text{H}_2\text{O}-\text{NaCl}$  composition in irregular to rounded inclusions occurring predominately as internal trails. Equivalent NaCl concentration ranges from 0.0 to 16.8 wt.%. Only one sample, 30-C, contained the  $\text{CO}_2-\text{CH}_4$  inclusions. In all cases, the  $\text{CH}_4$  concentration is  $<2$  mol%, which is in the usual range for geothermal systems (Roedder, 1986). It is not surprising to find methane within fluid inclusions hosted by a pile of metamorphosed sedimentary rocks and its presence in the fluid inclusion suggests some dewatering of the sediments and transportation by hydrothermal fluids (Roedder, 1986). Although the composition of the fluid inclusions in the shallower intracaldera volcanic rocks is similar to compositions in fluid inclusions in some of the basement rocks (e.g., 35-J), it is

not conclusive they coevolved. However, in Figure IV.6, the relationship of temperature to equivalent NaCl concentration of the samples is plotted as a function of composition for the samples with available data. It is possible to infer a slight mixing trend of cooler, less saline fluids in the volcanic rocks with higher temperature, higher salinity fluids from the basement rocks assuming a common origin. This could be accomplished by some lateral flow of meteoric water deep within the volcanic rocks diluting the more saline fluids of the basement, a condition reported for the present-day hydrothermal system (Goff et al., 1991). Within the volcanic rocks, there appears to be a trend toward increased salinity with decreasing temperature, a process usually associated with boiling (Shepherd et al., 1985). There is no evidence of boiling or necking down in the inclusions, although it is rare to find boiling pairs in studies, even where boiling is occurring (P. Brown, pers. comm., 1995). In Figure IV.7, the samples are plotted as their depth in LVEW versus  $T_h$ . The reference boiling-point curve for water with 5 wt.% equivalent NaCl is also plotted (solid line) as is the present day geothermal gradient (dashed line). Temperatures for the samples are far above the present-day geothermal gradient but most samples are below the reference boiling point curve assuming the present day ground surface and hydrostatic conditions. The reference boiling point curve would shift to the left if part of the overburden were removed from the LVEW location, a condition possible if not all of the overlying Early Rhyolite had been emplaced at the time of trapping of the fluid inclusions. This would place many of the fluid inclusions above the boiling point curve and would result in increasing the salinity of the fluid phase with decreasing temperature

(Shepherd et al., 1985; Roedder, 1986). In addition, a certain amount of simple cooling is indicated and would be accomplished by trapping of fluid in inclusions at locations more distant from the heat source, a condition inferred in LVEW from  $\delta^{18}\text{O}$  compositions (McConnell et al., in press).

Strontium isotopes of the calcite in fractures hosted by the metamorphic basement rocks are in equilibrium with the matrix rocks (Tables IV.1 and IV.2). This is not the case for the intracaldera volcanic rocks where the alteration calcite from fractures and leached from the matrix is more radiogenic (Table IV.2) than either the volcanic rocks (Table IV.1) or present day hydrothermal waters (0.70770 - 0.70811, Goff et al., 1991). This can be explained by mixing of meteoric water with more radiogenic cognate water in the metasedimentary rocks to form the post-caldera-collapse paleohydrothermal fluids. Mixing of paleometeoric fluids with fluids originating in the more radiogenic basement rocks is the best evidence for deep circulation of the hydrothermal waters.

#### IV.6 CONCLUSIONS

Laser probe  $^{40}\text{Ar}/^{39}\text{Ar}$  microanalysis of hydrothermally altered rocks within the enclosed volcanic basin of the Long Valley Caldera reveals a complex series of ages related to post-caldera-collapse intrusive and hydrothermal events. Bulk step heating techniques conducted on the same altered rocks yield an homogenized, weighted mean average age, essentially burying the more subtle events (Figure IV.1).



When  $^{40}\text{Ar}/^{39}\text{Ar}$  age determinations of Early Rhyolite obsidians and intrusions are compared along a timeline, several discrete events appear (Figure IV.2). From the modal analysis alone, it is not possible to determine what geologic event has disturbed the  $^{40}\text{Ar}/^{39}\text{Ar}$  isotopic ratio. It is necessary to consider anatomy of the intrusions in concert with their oxygen and strontium isotope compositions to construct the history of the area. I suggest the central caldera witnessed a series of intermittent post-caldera-collapse intrusions which initiated resurgence and associated hydrothermal pulses.

Early Rhyolite eruptions formed obsidian flows and tephra layers in the central resurgent dome area, building the edifice of the resurgent dome. By approximately 649 ka (Qer-16) evidence for surface eruptions of the Early Rhyolite cease. Coincident with the extrusive activity was the emplacement of sill-like intrusions into the Bishop Tuff to relatively shallow depths (sequences S1A & B, 2-B1 and 8-G). Multiple-age modal analysis of the intrusions suggest at least two later intrusive/hydrothermal cycles, S2 at ~500-400 ka and S3 at ~350-300. It is not possible to definitively identify these later events as intrusive or hydrothermal. However, the dates determined for older intracaldera rocks with better constrained ages suggest that two periods of hydrothermal activity moved through the central caldera. Sanidines from the older, syn-eruptive Bishop Tuff and the whole rock sample of the metavolcanic basement rock no longer record their emplacement ages but rather indicate times of resetting of their argon clocks at 635 ka, ~500 ka, and at ~350 ka. The deeper intrusion, LV4000, varies in its  $\delta^{18}\text{O}$  composition from that

predicted if it had been exposed to the predominant paleogeothermal gradient calculated for LVEW, apparently because this lower intrusion is younger than ~630 ka. I suggest intermittent hydrothermal pulses lag behind the intrusive activity when viewed on a modal age timeline. Emplacement of extrusive Early Rhyolite and intrusions took place ~640 ka to be followed by convective fluid circulation in the intracaldera volcanic rocks ~500 ka. A final hydrothermal pulse occurs at approximately 300 ka possibly driven by intrusive activity that emplaced LV4000 ~450 ka or by later intrusions not sampled in this study. In addition, eruption of biotite- and hornblende-rich Moat Rhyolite began ~500 ka along the northeast flank of the resurgent dome and peaked again at 300 ka during emplacement of the Hot Creek flow along the southeast flank (Bailey et al., 1976). Hydrothermal events begin to wane in the central caldera area as eruptive activity of the Moat Rhyolites shifted toward the West Moat (Bailey et al., 1976) and intrusive activity of the Early Rhyolites ceased.

Hydrothermal fluids appear to be primarily the result of meteoric water circulating within the volcanic rocks and mixing with cognate and deeper meteoric water from basement rocks. Heated by the post-caldera-collapse intrusions, the fluids traveled upwards by fracture flow throughout the metasedimentary basement rocks which left the host rocks relatively unaffected by alteration or isotopic exchange (Mukhopadhyay et al., 1994). Volumetrically pervasive water/rock exchange was restricted to the more porous and permeable intracaldera volcanics. Radiogenic-enriched strontium scavenged from the Paleozoic basement rocks was deposited in calcite in veins

and matrix in the younger intracaldera rocks. Oxygen isotope exchange at elevated temperatures lowered the  $\delta^{18}\text{O}$  composition of the host rocks and enriched the fluids (Chapter III).

Speculation as to the future activity in Long Valley Caldera is linked to understanding the history of the caldera. This continental silicic volcanic complex holds the promise of further geothermal potential while continuing to threaten the economy and well-being of the surrounding populations. For example, present-day intrusive activity in the West Moat and hydrothermal activity along the south and west flanks of the resurgent dome appear to be connected via shallow lateral fluid flow in the intracaldera volcanics (Sorey et al., 1991). Yet the central caldera has also been the focus of increased deformation and seismicity over the last 10 years (Rundle and Hill, 1988) and geophysical studies are interpreted as indicating an intrusion at 6-10 km beneath the resurgent dome. Quite possibly the resurgent dome is in for another series of intrusions which will, in turn, modify the edifice of the resurgent dome and drive one or more hydrothermal pulses.

#### IV.7 ACKNOWLEDGEMENTS

The strontium isotope study was conducted by V.S. McConnell at the Berkeley Center for Isotope Geochemistry during the first half of 1994 and was funded by an American Western University Thesis Parts Fellowship. Many thanks to T. Owens, J. Lassiter, T. Johnson, and all the crew of the Geology and Geophysics Dept. at UC-B for help and camaraderie. Thanks also to

H. Wollenberg and S. Flexer of Lawrence Berkeley Labs (LBL) for such interest in my work at Long Valley Caldera and to E. Franconi and K. Janda of LBL for sticking by me.

The  $^{40}\text{Ar}/^{39}\text{Ar}$  age determinations conducted at the Geochronology Lab of University of Alaska Fairbanks. I am indebted to P. Layer and J. Drake for assistance with sampling and interpretations. The fluid inclusion study was conducted at the Dept. of Geology and Geophysics, University of Wisconsin, Madison. Both the argon and the fluid inclusion studies were funded by Sandia National Labs as part of a program under the Division of Geothermal Energy of the U.S. Department of Energy.

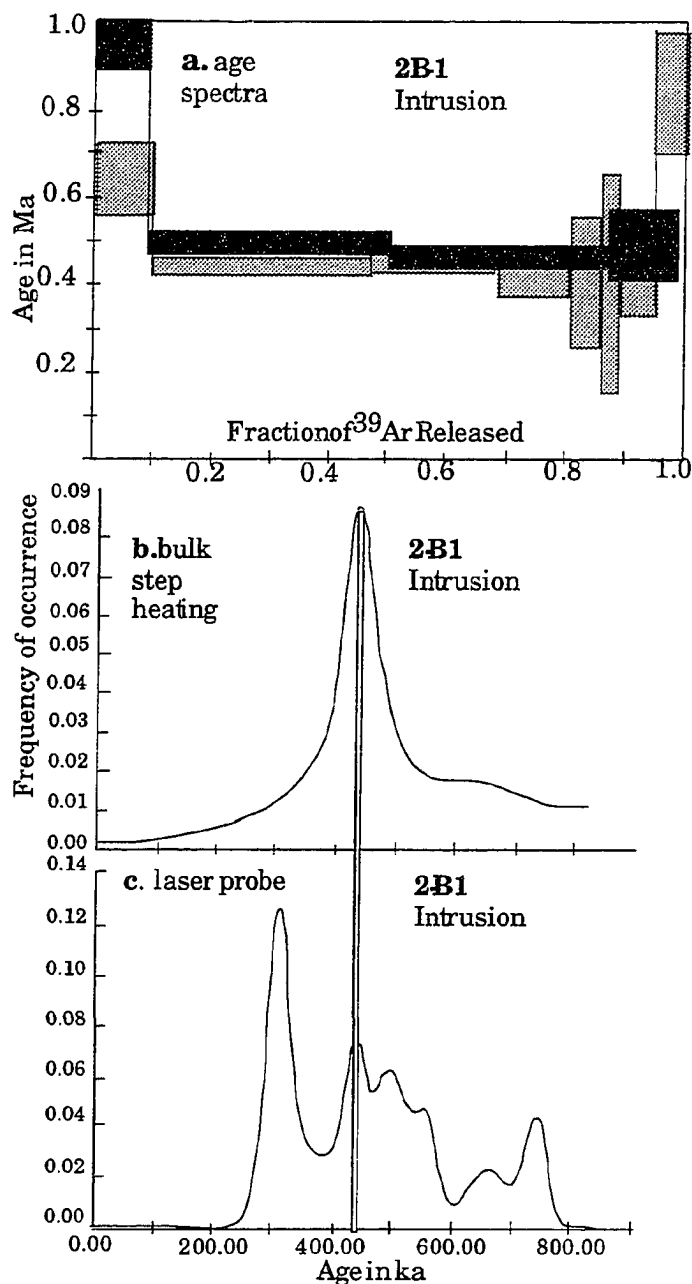


Figure IV.1 Ages determined by bulk step heating and laser probe. a) Age spectra for sample 2B-1 (2 analyses), plateau age is indicated by line. b) Analyses (a) plotted as a gaussian distribution about the analytical mean and standard deviation and c) gaussian distribution of laser probe analyses of 11 grains of the same sample.

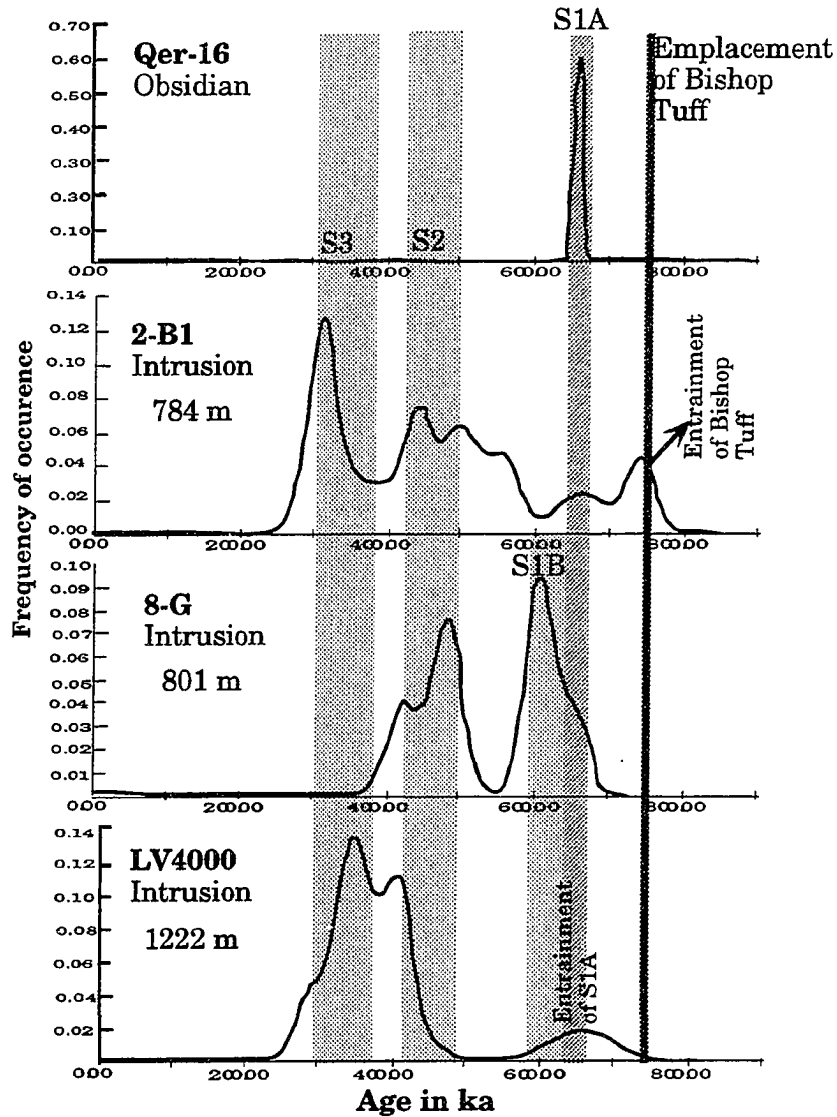


Figure IV.2 Comparison of multiple age series of Early Rhyolite samples. Modal-age determinations of Early Rhyolite extrusive and intrusive samples stacked in decreasing depth in LVEW. Dark shaded areas indicate times of known emplacement (e.g. Bishop Tuff, S1A), light shaded areas indicate peaks that correlate across the samples.

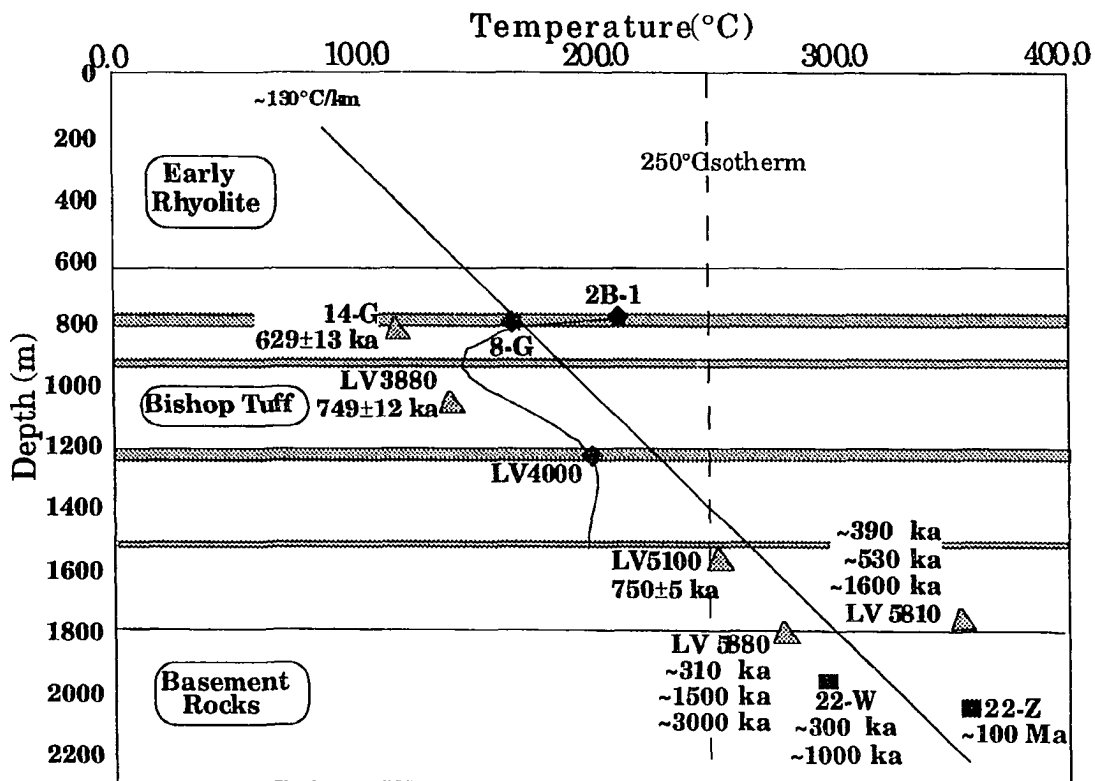


Figure IV.3 Location of dated samples in LVEW. Samples are plotted relative to depth in LVEW and the calculated paleogeothermal gradient (see Chapter II). The placement of sanidine samples LV3880 and LV5100 is inferred from regression of a paleogeothermal gradient calculated from sanidine  $\delta^{18}\text{O}$  values. Gray shaded areas are Early Rhyolite intrusions in Bishop Tuff. See Table IV.1 for data compilation.

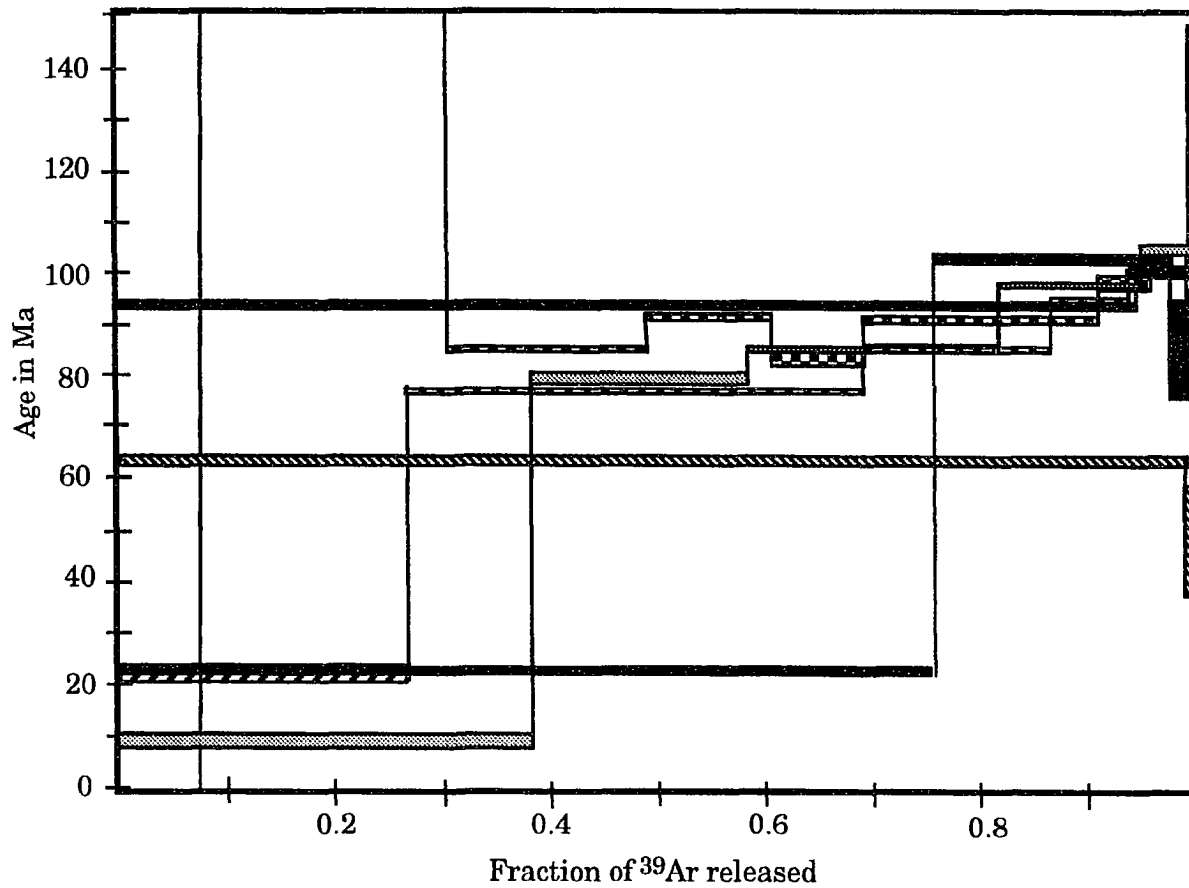


Figure IV.4 Age spectra for laser probe analysis of Paleozoic metasediments. Multiple step laser fusions of samples converge at ~100 Ma. This correlates to the age of emplacement of the nearby Round Valley batholith and represents the last age of regional alteration of these rocks.



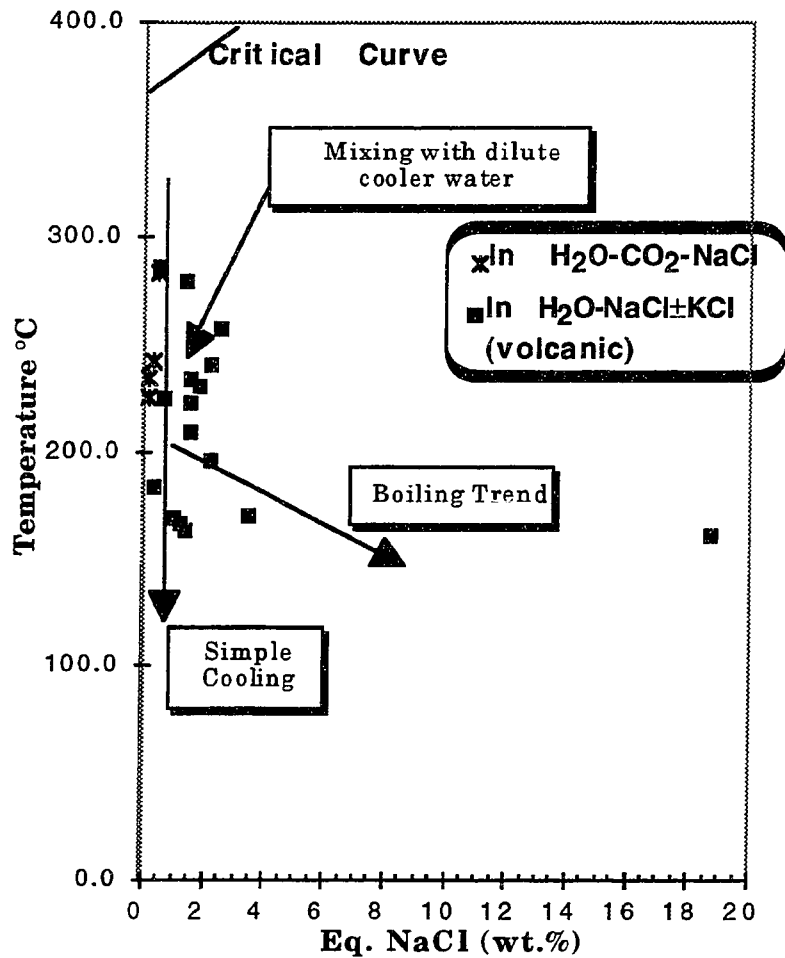


Figure IV.5 Salinity vs. Temperature of Homogenization (Th). The trends suggest some cooling and dilution has taken place in the volcanic rocks as well as the possibility of increase in salinity due to boiling.

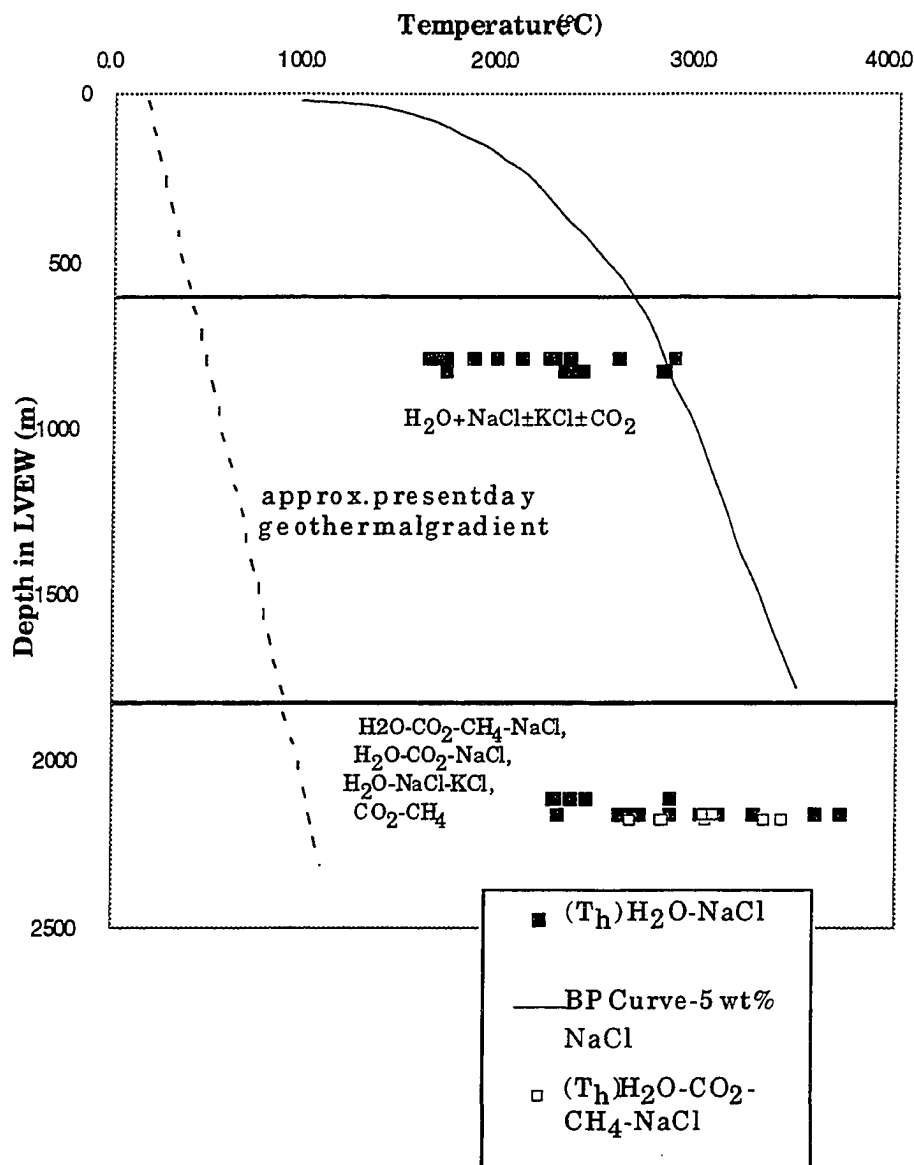


Figure IV.6 Temperature of homogenization of fluid inclusion plotted to depth in LVEW. Plot shows the location of the fluid inclusion samples relative to their depth in LVEW. Major lithologies are indicated. The present-day geothermal gradient is marked with a dashed line and the reference boiling point curve for 5 wt.% equivalent NaCl is marked by the solid line. Reference boiling point curve would shift to the left if overburden were removed, placing fluid inclusions in boiling regime.

Table IV.1 Isotopic values of selected samples.

Sample	Depth (m)	$\delta^{18}\text{O}$ , ‰	$^{87}\text{Sr}/^{86}\text{Sr}_m$	$^{40}\text{Ar}/^{39}\text{Ar}$ age (ka)
<b>Qer Samples</b>		<b>7.0-8.4<sup>e</sup></b>	<b>0.70662- 0.70668<sup>d,f</sup></b>	<b>751-652<sup>b</sup></b>
Qer-16	0	8.4±0.4		649±5
LV200	200	7.1±0.1	0.70649±2	
2B-1	784	-1.2±0.4	0.70683±1	~300 ~460 ~660 ~760
8-G	801	1.4±0.2		~460 ~610
9-L	805		0.70697±2	
LV4000	1222	-0.52±0.2		~350 ~420 ~650
<b>Qbt Sanidine Samples</b>		<b>6.7-7.9<sup>d,f</sup></b>	<b>0.70596- 0.70699<sup>d,g</sup></b>	<b>771-748<sup>h</sup></b>
LV2290	698	6.3±0.1	0.70616±2	
14-G	819	5.9±0.1	0.70739±1	629±14
17-M	830		0.70621±2	
LV3880	1183			749±12
LV5100	1554			750±5
LV5810	1772	-6.3±0.2		~390 ~530 ~1600 ~11000
LV5880	1792	-4.4±0.03		~360 ~1500 ~30000
<b>Mzmv</b>		<b>6.5-8.4</b>	<b>0.7061- 0.7246<sup>c</sup></b>	<b>237- 100<sup>c</sup> Ma</b>
22-W	1957	-4.6±0.3	0.70715±2	~500 ~1000
<b>Pzms</b>		<b>14.2-19.5<sup>*</sup></b>	<b>0.70904- 0.74685<sup>e,i</sup></b>	<b>450- 279<sup>a</sup> Ma</b>
22-Z hornfels	2045			~100 Ma
30-C Qtzite.	2111	15.0±0.4	0.72359±1	
44-H hornfels	2150	-0.4±0.1	0.72561±1	

Table IV.1 Isotopic values of selected samples

Qer- Early Rhyolite; Qbt- Bishop Tuff

Mzmv- Mesozoic metavolcanics; Pzms- Paleozoic metasediments

*Italic* ages for samples indicate age of highest probability.

<sup>87</sup>Sr/<sup>86</sup>Sr<sub>m</sub>- measured values.

\*- limited number of values reported.

**Bold** values indicate ranges for isotopic systems in outcrop rocks or minerals. Ranges for outcrop samples compiled from:

<sup>a</sup>Rinehart and Ross, 1964; <sup>b</sup>Mankinen et al., 1986; listed range of ages are from K-Ar determinations <sup>c</sup>Kistler and Swanson, 1981; <sup>d</sup>Halliday et al., 1984; <sup>e</sup>Goff et al., 1991; <sup>f</sup>Smith and Suemnicht, 1991; <sup>g</sup>Christensen and DePaolo, 1993; <sup>h</sup>van den Bogaard and Schirnack, 1995; <sup>i</sup>McConnell, 1995.

$\delta^{18}\text{O}$  values for samples reported in McConnell et al., in press. Note the 751 ka age for Early Rhyolite was reported in Mankinen et al., 1986 as a single K-Ar age determination of a pyroxene rhyolite obsidian sample. Although the sampling and laboratory are beyond reproach, we suggest the size of these samples would smear the age spectra eliminating peaks indicating contamination by xenoliths and/or alteration. Barring that sample, the age range for Early Rhyolite extrusive samples becomes 694-652 ka.

Sample	Depth (m)	<i>Th</i> °C	FI Composition	<sup>87</sup> Sr/ <sup>86</sup> Sr <sub>m</sub> (in calcite)
<b>Volcanic Rocks</b>				
LVEW 2290	698			0.70858±1*
LVEW 2C	784	204±39	H <sub>2</sub> O-NaCl±KCl	
LVEW 16C	824	230±39	H <sub>2</sub> O-NaCl±KCl	
LVEW 4320	1317			0.70740±1*
LVEW 5700	1737			0.70883±1*
<b>Basement Rocks</b>				
LVEW 6420	1957			0.70718±1*
30-C	2111	246±25	H <sub>2</sub> O-NaCl±KCl	0.72354±1*
30-C	2111		H <sub>2</sub> O-CO <sub>2</sub> -CH <sub>4</sub> -NaCl	
30-C	2111		CO <sub>2</sub> -CH <sub>4</sub>	
35-J	2128		H <sub>2</sub> O-NaCl±KCl	0.72146±1 0.72151±1
44-B	2152	274±89	H <sub>2</sub> O-NaCl±KCl	
44-B	2152	303±3	H <sub>2</sub> O-CO <sub>2</sub> -CH <sub>4</sub> -NaCl	
51-D	2173	303±33	H <sub>2</sub> O-CO <sub>2</sub> -CH <sub>4</sub> -NaCl	0.72022±1

Table IV.2 Fluid inclusion values and <sup>87</sup>Sr/<sup>86</sup>Sr compositions.

*Th*- Temperature of homogenization. Pressure adjustments not applied as hydrostatic pressure is minimal (<250 bars) at the maximum depth of 2.1 km. Assuming a similar elevation (~2400 m) and depth of burial in the caldera pile at onset of the hydrothermal activity approximately 630 ka and a maximum equivalent NaCl concentration of 5 wt.%, the pressure correction on the saline fluids would be ~25°C, within the scatter of the *Th* measurements. The more complex inclusions are unlikely to have steeper isochores than the saline-water fluids at depths <2.1 km. Thus the pressure correction would not be significantly different from the one detailed above.

\*- indicates Sr leached from calcite in matrix of rock.

## IV.8 REFERENCES

- Bailey, R.A., Dalrymple, G.B., and Lanphere, M.A., 1976, Volcanism, structure, and geochronology of Long Valley Caldera, Mono County, California: *Journal of Geophysical Research*, v. 81, p. 725-744.
- Christensen, J.N., and DePaolo, D.J., 1993, Time scales of large volume silicic magma systems: Sr isotopic systematics of phenocrysts and glass from the Bishop Tuff, Long Valley, California: *Contributions to Mineralogy and Petrology*, v. 113, p.100-114.
- Davies, G.R., Halliday, A.N., Mahood, G.A., and Hall, C.M., 1994, Isotopic constraints on the production rates, crystallization histories and residence times of pre-caldera silicic magmas, Long Valley, California: *Earth and Planetary Science Letters*, v. 125, p. 17-37.
- Eichelberger, J.C., Younker, L.W., Vogel, T.A., and Miller, C.D., 1988, Structure and stratigraphy beneath a young phreatic crater: South Inyo Crater, Long Valley caldera, California: *Journal Geophysical Research*, v. 93, p. 13,208-13,220.
- Faure, G., 1986, *Principles of Isotope Geology*: J.P. Wiley & Sons, Inc., New York, NY, pp. 589.
- Goff, F., Wollenberg, H.A., Brookins, D.C., and Kistler, R.W., 1991, A Sr-isotopic comparison between thermal waters, rocks, and hydrothermal calcites, Long Valley caldera, California: *Journal of Volcanology and Geothermal Research*, v. 48, p. 265-281.

- Halliday, A.N., Fallick, A.E., Hutchinson, J. and Hildreth, W., 1984, A Nd, Sr, and O isotopic investigation into the causes of chemical and isotopic zonation in the Bishop tuff, California: *Earth and Planetary Science Letters*, v. 68, p. 379-391.
- Hildreth, E.W., 1977, The magma chamber of the Bishop Tuff: gradients in temperature, pressure, and composition: Ph.D. dissertation, University of California, Berkeley, p. 1-328.
- Izett, G.A and Obradovich, J.D., 1991, Dating of the Matuyama-Brunhes boundary based on  $^{40}\text{Ar}/^{39}\text{Ar}$  ages of the Bishop Tuff and Cerro San Luis rhyolite: *Geological Society of America Abstracts with Programs*, v. 23, no. 5, p. A106.
- Kistler, R.W. and Swanson, S.E., 1981, Petrology and geochemistry of metamorphosed volcanic rocks and a Middle Cretaceous volcanic neck in the east-central Sierra Nevada, California: *Journal of Geophysical Research*, v. 86, p. 10489-10501.
- Lipman, P.W., 1984, The roots of ash flow calderas in western North America: windows into the tops of granitic batholiths: *Journal of Geophysical Research*, v. 89, p. 8801-8841.
- Mankinen, E.A., Gromme, C.S., Dalrymple, G.B., Lanphere, M.A., and Bailey, R.A., 1986, Paleomagnetism and K-Ar ages of volcanic rocks from Long Valley Caldera, California: *Journal of Geophysical Research*, v. 91, no. B1, p.633-652.

- McConnell, V.S., Shearer, C.K., Eichelberger, J.C., Keskinen, M.J, Layer, P.W., and Papike, J.J., 1995, Rhyolite intrusions in the intracaldera Bishop Tuff, Long Valley Caldera, California: *Journal of Volcanology and Geothermal Research*, v. 67, p. 41-60.
- Mukhopadhyay, B., Valley, J.W., Spicuzza, M.J., and Niendorf, C.R., 1994, Millimeter scale oxygen isotope zonation in drill core from Long Valley Exploratory Well: implication for fluid flow: *Geological Society of America, Abstracts with Programs*, v. ,p. A-280.
- Rinehart, C.D. and Ross, D.C., 1964, *Geology and mineral deposits of the Mount Morrison quadrangle, Sierra Nevada, California*: U.S. Geological Survey Professional Paper 385. p 7-30.
- Roedder, E., 1986, *Fluid inclusions: Reviews in Mineralogy*, Mineralogical Society of America, v. 12, pp. 646.
- Rundle, J.B., and Hill, D.P., 1988, The geophysics of a restless caldera--Long Valley, California: *Ann. Rev. Earth Planet, Science*, 16:251-271.
- Shepherd, T.J., Rankin, A.H., and Alderton, D.H.M., 1985, *A practical guide to fluid inclusion studies*: Blackie and Sons, Ltd., Chapman and Hall, New York, pp. 239.
- Smith, B.M. and Suemnicht, G.A., 1991, Oxygen isotope evidence for past and present hydrothermal regimes of Long Valley caldera, California: *Journal of Volcanology and Geothermal Research*, v. 48, p. 319-339.



van den Bogaard, P. and Schirnick, C., 1995,  $^{40}\text{Ar}/^{39}\text{Ar}$  laser probe ages of Bishop Tuff phenocrysts substantiate long-lived silicic magma chamber at Long Valley, United States: *Geology*, v. 23, p. 759-762.

## V.1 CONCLUSIONS

Calderas are considered economically important sites of ore deposition and geothermal systems and, of fundamental importance, they have their roots in the volcano-plutonic transition zone (Lipman, 1984). It is not sufficient, nor necessary given the available technology of scientific drilling and in analytical geochemistry, to restrict study to older, more eroded caldera systems when these younger, more pristine systems are available for investigation. Instead, study of young intracaldera volcanic rocks sampled *in situ*, while still relatively pristine, allows direct interpretations of the thermal life and emplacement characteristics of large, upper crustal magma bodies. This study addressed the relationship between volcanic activity and hydrothermal pulses in a Quaternary caldera with the aim of constraining timing and intensity of the post-caldera-collapse thermal history. In the process, our attention is directed to fundamental issues regarding the internal structures within calderas such as the timing of collapse and fill of the caldera and later resurgence. It must first be noted that the success of this or any other work to be conducted on relatively young and uneroded volcanic centers requires drilling into the system to establish stratigraphic control and supply samples for geologic and geochemical characterization (Long Valley Science Panel, 1991). Only through continued efforts to sample and explain the volcanic regime will we increase the understanding of the volcanic-plutonic relationships and their potential impact on and by human activity.

There are two significant aspects of this work. First, the work presents a detailed site characterization of the post-caldera-collapse hydrothermal history of the Long Valley Caldera and its relationship to repeated rhyolitic intrusive activity and resurgence. The importance of this physical model lies in our need to understand the dynamics of these silicic volcanic centers if we are to tap their thermal and economic potential. But, in order to interpret the history at a macro level, it is necessary to delve into the volcanic system at a micro level through the implementation of new technology. Thus, the second important result of this study was the successful integration of state-of-the-art microanalytical isotope geochemical techniques to address problems of interpreting the history of complexly altered volcanic rocks.

Interestingly enough, this study reveals a long and varied history of post-caldera-collapse rhyolitic activity with the aphyric Early Rhyolite being emplaced during times of eruption of the obviously hydrous, biotite-rich Moat Rhyolite (Bailey et al., 1976). In addition, it is noted in Chapter II that the chemical composition of the *shallow* Early Rhyolite intrusion is closer to the composition of the Early Rhyolite in the West Moat than that of the resurgent dome. Both statements lead to the speculation that the parent magma system is not a single batholithic-sized body being periodically tapped at varying depths. Instead, it may consist of more isolated pods of magma, assimilating and differentiating, then erupting in response to their location relative to the prevailing tectonic fabric of the area. A more detailed age correlation study of the intracaldera volcanic rocks, in particular the

post-caldera-collapse rhyolite sequences, would help constrain the timing of magma emplacement beneath the caldera. This, in turn, provides significant information toward refining the models of continental silicic igneous activity.

Recent work has been focused on determining both the residence time of the Bishop Tuff magma chamber (e.g., Halliday et al., 1984; Christensen and DePaolo, 1994; van den Bogaard and Schirnick, 1995) and the influence of pre- and post-caldera rhyolitic activity on the caldera complex (e.g., Davies et al., 1995 and Bailey, pers. comm., 1992). The present study provides crucial proof of the cyclic nature of activity in a mature caldera and reveals the hydrothermal potential and hazards related to the intrusive and resurgent activity.

In the past 20 years, the Long Valley Caldera has displayed evidence of two of the three related post-caldera-collapse activities: intrusions and resurgence (Rundle and Hill, 1988; Hill et al, 1990). In reviewing the history of the past activity presented in this study, we can expect a change in the intensity and location of hydrothermal activity within the caldera in response to the intrusions. What becomes of practical importance to economic and volcanic hazards concerns is understanding and forecasting the timing of this change. This points to the direction of further work: Does the cyclic igneous activity possess a periodicity that can be predicted? Is it possible to determine the time lapse between intrusion and hydrothermal pulse? And on a more fundamental level, what keeps these volcanic centers alive over such a long period of time?

## V.1.2 REFERENCES

- Bailey, R.A., Dalrymple, G.B., and Lanphere, M.A., 1976, Volcanism, structure, and geochronology of Long Valley Caldera, Mono County, California: *Journal of Geophysical Research*, v. 81, p. 725-744.
- Christensen, J.N., and DePaolo, D.J., 1993, Time scales of large volume silicic magma systems: Sr isotopic systematics of phenocrysts and glass from the Bishop Tuff, Long Valley, California: *Contributions to Mineralogy and Petrology*, v. 113, p.100-114.
- Davies, G.R., Halliday, A.N., Mahood, G.A., and Hall, C.M., 1994, Isotopic constraints on the production rates, crystallization histories and residence times of pre-caldera silicic magmas, Long Valley, California: *Earth and Planetary Science Letters*, v. 125, p. 17-37.
- Halliday, A.N., Fallick, A.E., Hutchinson, J. and Hildreth, W., 1984, A Nd, Sr, and O isotopic investigation into the causes of chemical and isotopic zonation in the Bishop tuff, California: *Earth and Planetary Science Letters*, v. 68, p. 379-391.
- Hill, D.P., Ellsworth, W.L., Johnston, M.J.S., Langbein, J.O., Oppenheimer, D.H., Pitt, A.M., Reasenber, P.A., Sorey, M.L., and McNutt, S.R., 1990, The 1989 earthquake swarm beneath Mammoth Mountain, California: An initial look at the 4 May through 30 September activity, *Bull Seismol. Soc. Am*, 80:325-339.
- Lipman, P.W., 1984, The roots of ash flow calderas in western North America: windows into the tops of granitic batholiths: *Journal of Geophysical Research*, v. 89, p. 8801-8841.

Long Valley Science Panel, 1991. Investigation of active volcanic processes in Long Valley Caldera via deep continental drilling. U.S. DOE, UCRL-PROP-108826, 1-31.


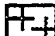







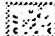


Rundle, J.B., and Hill, D.P., 1988. The geophysics of a restless caldera--Long Valley, California. *Ann. Rev. Earth Planet, Science*, 16:251-271.

van den Bogaard, P. and Schirnick, C., 1995,  $^{40}\text{Ar}/^{39}\text{Ar}$  laser probe ages of Bishop Tuff phenocrysts substantiate long-lived silicic magma chamber at Long Valley, United States: *Geology*, v. 23, p. 759-762.

## APPENDIX I. STRATIGRAPHY DIAGRAMS FOR LVEW

Legend

Post- and syn-caldera collapse related

<b>EARLY RHYOLITE (Qer)</b>	<b>Qer INTRUSION</b>
 microlite glass	 rhyolite intrusion
 vesicular glass	
 flow banded rhyolite	
 obsidian	
<b>BISHOP TUFF (Qbt)</b>	<b>MYSTERY BRECCIA</b>
 welded tuff	 epiclastic breccia
 fiamme tuff	
 chlorite alteration	
<b>Pre-caldera</b>	
<b>MESOZOIC METAVOLCANICS (Mzmv)</b>	<b>PALEOZOIC METASEDIMENTS (Pzms)</b>
 chlorite-rich metavolcanics	 banded hornfels
	 metaquartzite

MINERALS

Qtz- Quartz	Py- Pyrite
Pl- Plagioclase	Chl- Chlorite
San- Sanidine	Bt- Biotite
Cpx- clinopyroxene	
Rt- Rutile	Cal- Calcite
Mt/Il- Magnetite/Ilmenite	

Figure AI.1 Detailed stratigraphy of LVEW. Page above presents the legend for the strat section. Contact locations listed in the Comments Column and primary and secondary mineralogy listed in Mineralogy Column. Stratigraphic interpretations based on study of standard e-log, mudlog, and core logs.

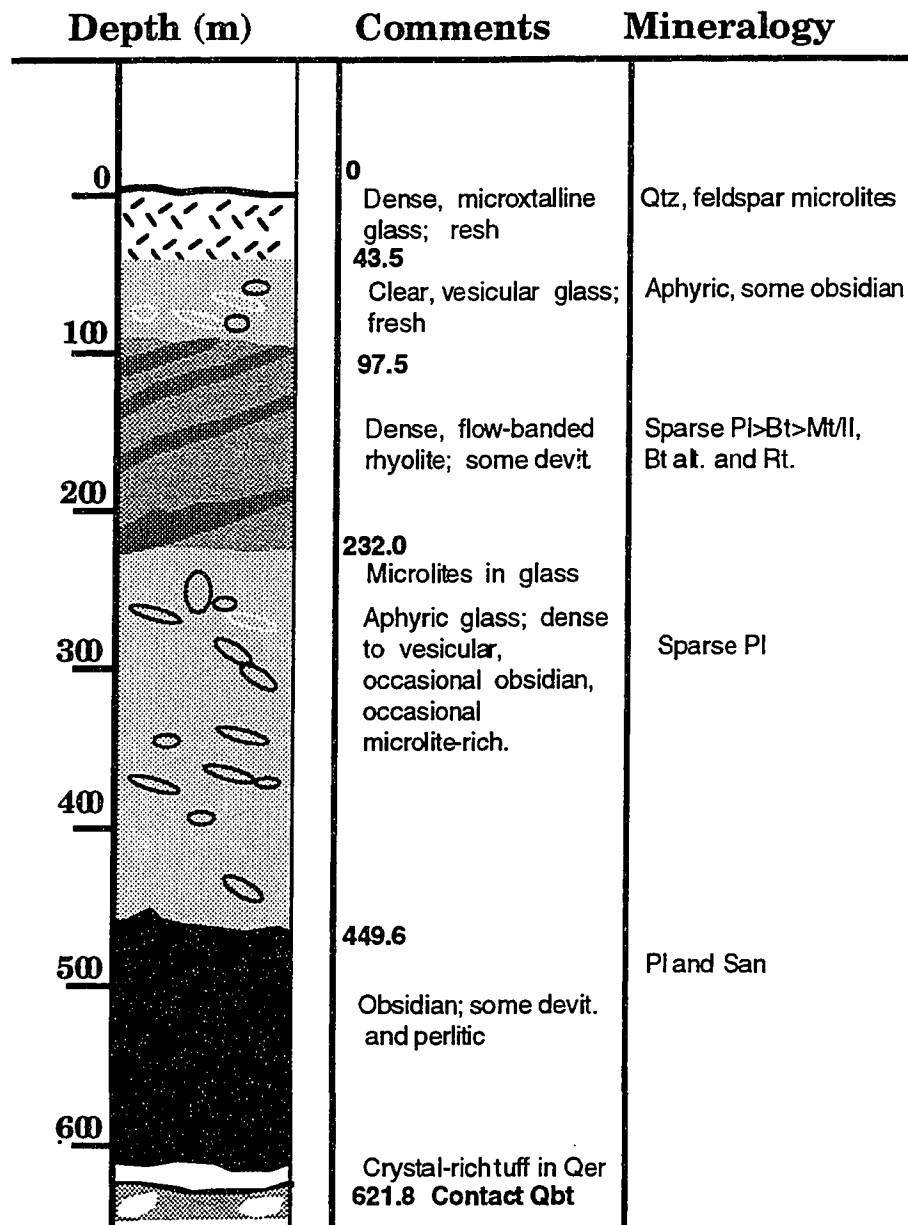


Figure AI.1 con't. First 600 m of the well consists of the Early Rhyolite flows and tephra that overlie the intracaldera Bishop Tuff and form the top of the resurgent dome. The vent for the obsidian is located approximately 1 km to the east, vent location of the tephra eruptions has not been identified.



Depth (m)	Comments	Mineralogy
700	621.8 Qer/Qbt contact	Qbt: Qtz>Pl and San>>Bt>Zr, clay alt. of devit. matrix, Bt alt. to Cht.; Ba in San; no Cal
	624.8 aphyric, microcrystalline Qer intrusion w/ obsidian	Qtz>>Pl>San>>Bt, rare Py, no Cal
800	696.5  Qbt; white due to clay alt. of matrix	Qtz>>San>Pl>Bt, Ba in San, Py-rich, Bt alt. to mica
	768.1 810.6 Pl microlaths @ 784	Illite/smectite, Qtz, Pl, K-spar
900	811.2-812.5, 821.9-822.2, 828.5, 829.3; small intrusions	Illite/smectite, Qtz, micro slickensides (XRD, SEM)
	Qbt @ 820 Cal alt. phenos Qbt @ 835 Cly alt. phenos	Qtz=San>Pl>>Bt, allanite Qtz, Cly, Py, Cal-2ndry
1000	891.5-905.3; intrusion	Granophytic Cly
	Qbt @ 914 fiamme welding	Qtz>alt. feldspars>>Bt
1100	925.1-928.8; intrusion	Qtz, Pl, K-spar, Illite
	Qbt; Cly/Cal in matrix, Pl to Cal., San to Cly, devit, wld.	Qtz>San>Pl>>Bt
1200	1005.0-1016.5; intrusion	Qtz, Cly, no phenos
	Qbt; fiamme welded, coarse devit., Pl to Albite/Cal, San to Albite enriched, Cly in matrix and fractures	Qtz>San>Pl>>Bt  2ndry Cal, Cly, Py, Qtz  Qtz>San>Pl>>Bt

Figure A1.1 con't. Top of the 1200 m section of the intracaldera Bishop Tuff at LVEW. Three Qer intrusions marked with dashed lines are discussed in Chapter II, the first marked intrusion is *Shallow* intrusion discussed in Chapters II, III, and IV.

Depth (m)	Comments	Mineralogy
1200	1188.7 fg mosaic xtallization, Cly alt., Pl to Cal., vesicles filled w/ Qtz, Cly, Cal	Illite/smectite, Qtz, Cly, Cal, fg Py, k-spar, Pl: (XRD)
1300	1295.4 Qbt; Cly in matrix, Pl to Cly, fiamme, no Cal	Qtz>San>Pl>Bt, rare Cpx
1400	1365.5 filled vesicles	Qtz, feldspars, Cly, Cal
1500	1390.0 Qbt; wht to gray, dense weld, chlorite staining @1417 1448.1463.0; intrusion	Qtz>San,Pl>Py, alteration Qtz, feldspar, Py, Cal/Cly filled vesicles
1600	1508.8 no phenos, filled vesicles 1548.4 1597.2-1603.2; intrusion	Illite/smectite, Pl, K-spar, Qtz, Py (XRD) Qtz, Pl, K-spar, Cly, Py (XRD)
1700	Qbt; densely welded, devit, very Cly rich in matrix, rare shard remnants  Chlorite staining	Qtz>Pl, San>>Py 2ndry Cly, Cal, Py, Chl

Figure AI.1 con't. Bottom of the 1200 m section of the intracaldera Bishop Tuff. Note the onset of chlorite. Epidote is also present in minute amounts below 1700 m.

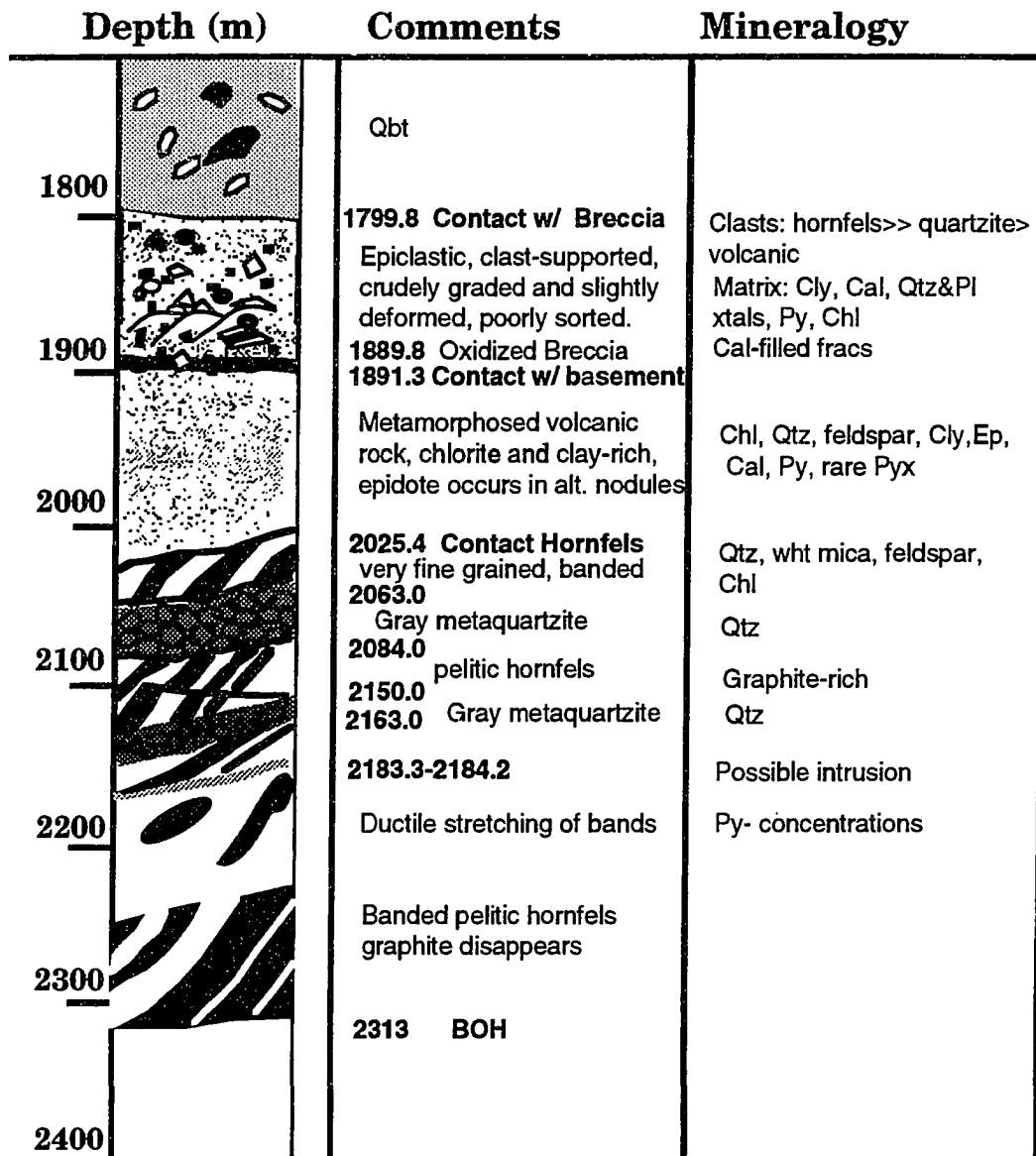


Figure AI.1 con't. Stratigraphy of the Mystery Breccia and the metamorphic basement rocks.  
Note: very thin units (<1 m) are not indicated on the diagram unless the unit is considered of lithologic importance (i.e., possible intrusion @ 2183.3-2184.2).

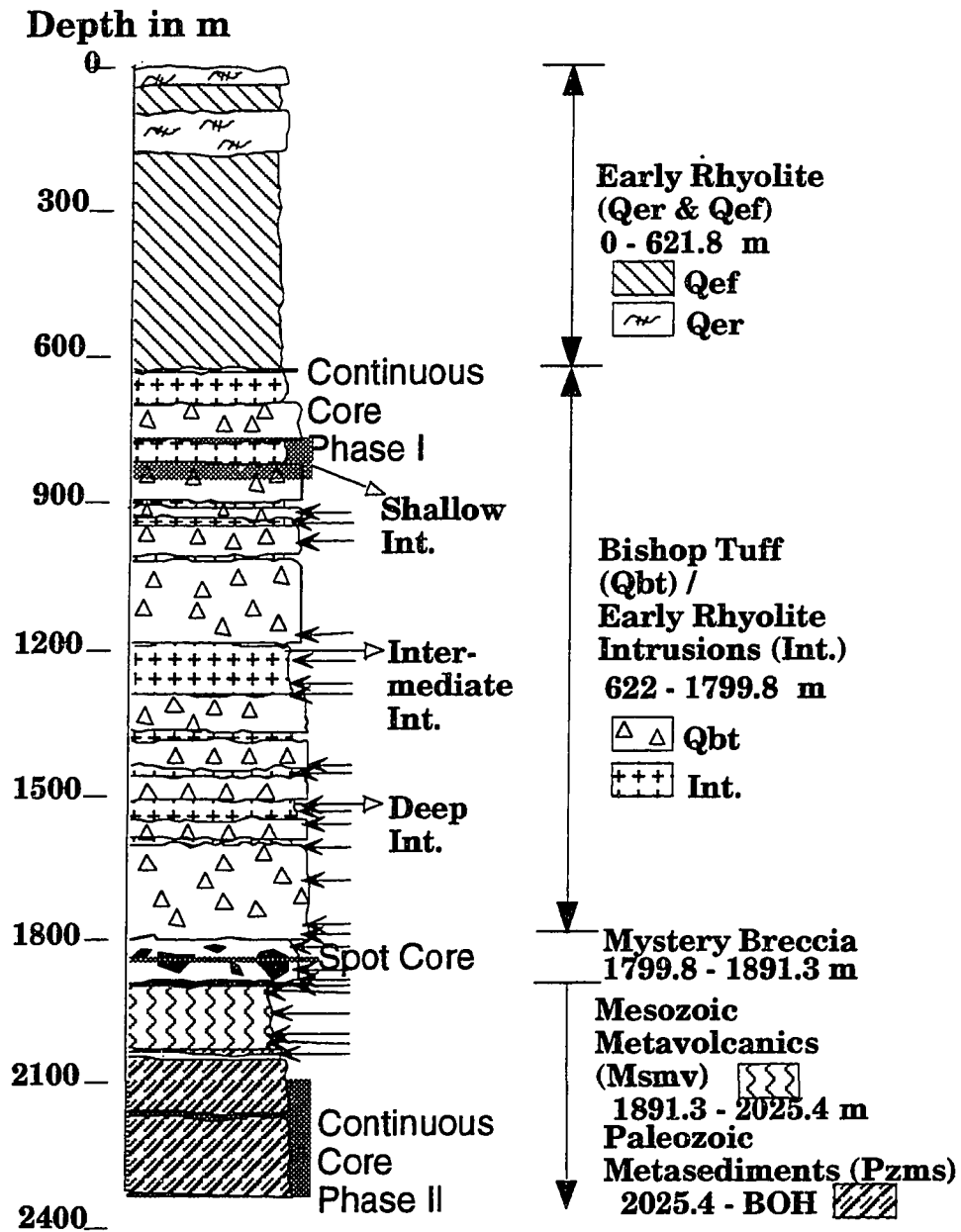


Figure A1.2 Core sampling locations in LVEW. Sidewall core indicated by left arrows. Total depth in well is 2313 m.

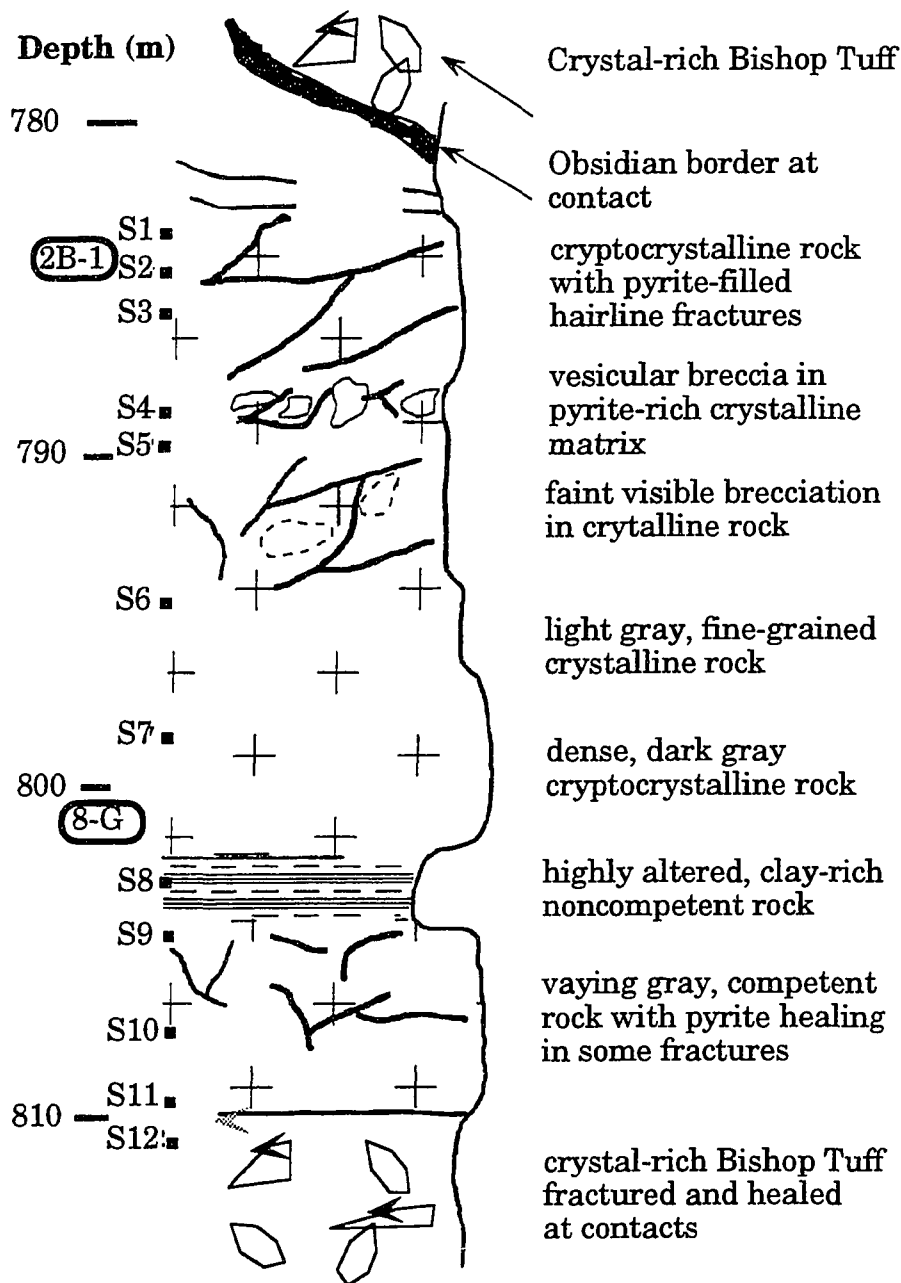


Figure A1.3 Cored section of Shallow Early Rhyolite intrusion. S# locations indicate whole-rock composition analyses (Table II.1, Chapter II). Samples 2B-1 and 8-G are discussed in Chapter IV. Total thickness of intrusion is 43 m.

APPENDIX II. Feldspar Phenocryst Compositions in Intracaldera Bishop Tuff  
 Table AII.1 Feldspar compositions: electron microprobe analyses

All microprobe analyses done by V.S. McConnell at the Geology and Geophysics Microprobe facility, UAF.  
 Note the following designations: (R)-crystal rim, (C)-crystal core, Ab-Albite, Or-Orthoclase, An-Anorthosite.  
 Oxide compositions reported as wt.%, feldspar normative values in percent.

**Sample Type:** Bishop Tuff ash flow - Gorges: lower cooling unit

Plagioclase		SiO <sub>2</sub>	Al <sub>2</sub> O <sub>3</sub>	Na <sub>2</sub> O	K <sub>2</sub> O	CaO	Fe <sub>2</sub> O <sub>3</sub>	BaO	total	Ab	Or	An
Sample	Depth (m)											
15-A_PLAG1	surface	64.74	22.14	9.06	1.33	2.73	0.01	0.00	100.00	79.18	7.65	13.16
15-A_PLAG1(R)	surface	64.65	22.10	8.94	1.03	2.96	0.20	0.05	99.93	79.44	6.02	14.54
15-A_PLAG3	surface	63.78	21.91	8.73	1.10	3.04	0.30	0.00	98.86	78.42	6.54	15.04
15-A_PLAG3(R)	surface	64.44	22.06	9.12	1.02	3.06	0.03	0.03	99.76	79.41	5.88	14.71
15-A_PLAG5	surface	55.41	28.62	5.71	0.10	9.95	0.17	0.00	99.97	50.61	0.61	48.78
15-A_PLAG5	surface	58.61	26.04	7.25	0.15	7.42	0.16	0.00	99.63	63.38	0.80	35.81
15-A_PLAG6(R)	surface	65.01	22.30	8.96	1.30	2.85	0.32	0.02	100.76	78.64	7.53	13.83
15-A_PLAG6	surface	64.50	22.18	8.75	1.15	2.93	0.33	0.00	99.84	78.62	6.81	14.57
15-A_PLAG6	surface	65.14	21.79	9.00	1.29	2.74	0.01	0.02	99.99	79.14	7.50	13.36
15-A_PLAG7(R)	surface	64.09	22.38	8.87	1.10	2.95	0.15	0.04	99.59	79.07	6.42	14.51
15-A_PLAG7	surface	63.90	22.46	8.89	1.21	3.08	0.16	0.00	99.70	78.12	6.95	14.93
15-A_PLAG7	surface	64.25	22.02	9.10	1.36	2.82	0.06	0.02	99.61	78.79	7.74	13.47
15-A_PLAG7	surface	63.73	22.38	9.01	1.08	3.59	0.19	0.03	100.01	77.01	6.07	16.92
15-A_PLAG8	surface	64.36	21.89	8.78	1.01	3.01	0.18	0.02	99.23	79.10	5.96	14.94
15-A_PLAG8	surface	65.34	21.78	9.09	1.25	2.76	0.13	0.00	100.35	79.49	7.18	13.33

Table All.1 con't.

**Sample Type:**

Bishop Tuff ash flow - Gorges: lower cooling unit

Sanidine		SiO <sub>2</sub>	Al <sub>2</sub> O <sub>3</sub>	Na <sub>2</sub> O	K <sub>2</sub> O	CaO	Fe <sub>2</sub> O <sub>3</sub>	BaO	total	Ab	Or	An
Sample	Depth (m)											
15-A_SAN1(R)	surface	65.42	19.22	4.04	10.85	0.17	0.27	0.00	99.97	35.79	63.41	0.81
15-A_SAN1	surface	65.75	19.04	4.08	10.63	0.19	0.17	0.02	99.87	36.52	62.56	0.92
15-A_SAN1	surface	65.78	19.46	4.11	10.63	0.20	0.25	0.00	100.42	36.63	62.45	0.92
15-A_SAN2(R)	surface	65.86	19.14	4.11	10.56	0.16	0.17	0.08	100.08	36.87	62.31	0.82
15-A_SAN2	surface	65.60	19.39	4.16	10.76	0.18	0.12	0.05	100.26	36.68	62.41	0.90
15-A_SAN2	surface	65.88	19.17	4.01	10.84	0.19	0.19	0.03	100.32	35.70	63.39	0.91
15-A_SAN3	surface	65.30	19.01	3.82	10.98	0.15	0.16	0.02	99.44	34.35	64.94	0.71
15-A_SAN3	surface	65.82	19.14	3.88	11.21	0.14	0.11	0.06	100.36	34.17	65.13	0.70
15-A_SAN4(R)	surface	66.00	18.79	4.17	10.49	0.18	0.01	0.00	99.63	37.30	61.79	0.91
15-A_SAN4	surface	66.47	19.14	3.94	11.19	0.12	0.11	0.02	101.00	34.61	64.78	0.61
15-A_SAN4	surface	66.00	19.17	3.88	10.63	0.17	0.10	0.00	99.94	35.41	63.76	0.83
15-A_SAN5	surface	66.19	19.17	3.89	10.55	0.19	0.00	0.01	99.99	35.59	63.47	0.94
15-A_SAN5	surface	65.15	19.00	3.92	10.85	0.17	0.07	0.03	99.18	35.19	64.00	0.81
15-A_SAN6	surface	65.55	19.05	3.84	10.74	0.21	0.11	0.04	99.55	34.84	64.13	1.03
15-A_SAN6	surface	65.24	19.12	4.12	10.73	0.11	0.14	0.00	99.47	36.68	62.71	0.60
15-A_SAN7	surface	65.75	18.87	3.91	10.54	0.12	0.04	0.00	99.23	35.79	63.59	0.62
15-A_SAN7	surface	65.55	18.99	3.80	10.74	0.16	0.00	0.01	99.25	34.67	64.50	0.83
15-A_SAN8(R)	surface	66.38	19.05	3.92	10.96	0.16	0.02	0.01	100.50	34.96	64.22	0.82
15-A_SAN8	surface	65.69	19.13	3.90	11.15	0.12	0.00	0.00	100.00	34.47	64.92	0.60
15-A_SAN9	surface	65.42	19.33	3.87	11.05	0.16	0.11	0.05	99.98	34.41	64.78	0.81
15-A_SAN9	surface	65.20	19.20	3.95	11.21	0.19	0.15	0.00	99.90	34.59	64.52	0.89
15-A_SAN10	surface	65.16	19.13	4.05	10.88	0.16	0.15	0.01	99.52	35.84	63.36	0.80
15-A_SAN10	surface	66.06	18.94	4.21	10.42	0.17	0.13	0.04	99.97	37.69	61.49	0.82

Table AII.1 con't.

**Sample Type:**

Bishop Tuff ash flow - Gorges: lower cooling unit

Plagioclase		SiO <sub>2</sub>	Al <sub>2</sub> O <sub>3</sub>	Na <sub>2</sub> O	K <sub>2</sub> O	CaO	Fe <sub>2</sub> O <sub>3</sub>	BaO	total	Ab	Or	An
Sample	Depth (m)											
15-B_PLAG1A	surface	64.90	22.38	9.03	0.98	3.27	0.19	0.01	100.75	78.67	5.64	15.69
15-B_PLAG1B	surface	64.49	22.52	8.85	1.04	3.30	0.21	0.00	100.42	77.84	6.08	16.08
15-B_PLAG1C	surface	65.13	22.47	9.13	1.20	3.01	0.19	0.00	101.14	78.82	6.82	14.36
15-B_PLAG2	surface	64.08	22.38	9.01	1.18	2.96	0.18	0.02	99.81	78.82	6.82	14.36
15-B_PLAG2	surface	64.81	22.47	9.02	1.15	3.12	0.16	0.00	100.73	78.51	6.55	14.94
15-B_PLAG2(R)	surface	64.74	22.17	8.87	1.22	2.78	0.26	0.03	100.06	79.23	7.10	13.67
15-B_PLAG3	surface	65.21	21.83	9.30	1.41	2.68	0.15	0.03	100.60	79.46	7.92	12.63
15-B_PLAG3	surface	65.31	22.03	9.40	1.29	2.78	0.02	0.01	100.84	79.74	7.19	13.07
15-B_PLAG4(R)	surface	64.73	22.13	9.08	0.97	2.93	0.10	0.01	99.95	80.10	5.67	14.23
15-B_PLAG4	surface	64.49	22.48	8.86	1.02	3.03	0.16	0.03	100.06	79.12	5.95	14.93
15-B_PLAG5(R)	surface	64.65	22.45	9.12	1.14	2.95	0.17	0.00	100.47	79.31	6.52	14.17
15-B_PLAB5	surface	64.93	22.25	9.17	1.16	2.93	0.19	0.00	100.62	79.35	6.61	14.04
15-B_PLAG6	surface	64.64	22.84	8.96	1.18	3.24	0.21	0.00	101.07	77.71	6.75	15.54
15-B_PLAG6	surface	64.68	22.24	9.09	1.14	3.10	0.19	0.01	100.44	78.68	6.50	14.82
15-B_PLAG7(R)	surface	64.65	21.82	8.87	0.94	2.73	0.08	0.01	99.09	80.68	5.60	13.73
15-B_PLAG7	surface	64.61	21.85	9.11	1.38	2.78	0.09	0.01	99.82	78.83	7.86	13.31
15-B_PLAG8(R)	surface	56.63	28.23	5.93	0.22	9.28	0.19	0.00	100.47	52.89	1.34	45.77
15-B_PLAG8	surface	56.97	27.42	6.41	0.15	8.86	0.03	0.00	99.83	56.25	0.81	42.94
15-B_PLAG9(R)	surface	64.02	22.53	9.15	1.02	3.19	0.04	0.05	100.01	78.97	5.84	15.19
15-B_PLAG9	surface	64.32	22.42	8.70	1.27	2.99	0.00	0.02	99.72	77.73	7.49	14.78
15-B_PLAG10	surface	65.03	22.14	9.04	1.06	2.92	0.07	0.08	100.33	79.57	6.19	14.24



Table AII.1 con't.

**Sample Type:**

Bishop Tuff ash flow - Gorges: lower cooling unit

Sanidine		SiO <sub>2</sub>	Al <sub>2</sub> O <sub>3</sub>	Na <sub>2</sub> O	K <sub>2</sub> O	CaO	Fe <sub>2</sub> O <sub>3</sub>	BaO	total	Ab	Or	An
Sample	Depth (m)											
15-B_SAN1	surface	66.50	19.44	3.48	12.04	0.11	0.00	0.17	101.75	30.42	69.08	0.50
15-B_SAN1	surface	66.21	19.36	2.40	13.61	0.06	0.05	0.18	101.86	21.05	78.65	0.30
15-B_SAN3	surface	65.96	19.00	4.10	10.64	0.15	0.25	0.02	100.11	36.66	62.63	0.71
15-B_SAN3	surface	64.82	18.94	4.05	10.66	0.13	0.03	0.04	98.67	36.35	62.94	0.70
15-B_SAN4(E)	surface	65.42	18.80	4.24	10.48	0.21	0.00	0.03	99.17	37.65	61.35	1.00
15-B_SAN4	surface	65.64	19.32	4.15	10.88	0.10	0.15	0.00	100.24	36.51	62.99	0.50
15-B_SAN5	surface	65.54	19.42	4.20	10.82	0.16	0.10	0.01	100.25	36.83	62.38	0.80
15-B_SAN5(R)	surface	65.41	18.98	4.30	10.09	0.15	0.16	0.05	99.14	39.01	60.27	0.72
15-B_SAN7	surface	65.09	18.64	4.30	10.53	0.20	0.13	0.04	98.92	37.96	61.05	0.99
15-B_SAN7	surface	65.68	19.06	4.16	10.78	0.12	0.06	0.00	99.87	36.77	62.63	0.60
15-B_SAN8	surface	66.52	19.32	4.39	10.97	0.21	0.00	0.05	101.47	37.43	61.59	0.98
15-B_SAN8(C)	surface	64.99	19.13	4.12	10.56	0.18	0.32	0.00	99.28	36.91	62.18	0.91
15-B_SAN9(R)	surface	65.33	19.20	4.43	10.79	0.20	0.21	0.00	100.15	38.09	61.04	0.88
15-B_SAN9	surface	65.53	19.05	4.11	10.79	0.17	0.23	0.02	99.90	36.35	62.85	0.80
15-B_SAN10	surface	65.30	18.51	4.12	11.11	0.10	0.19	0.01	99.34	35.88	63.63	0.49

Table AII.1 con't.

**Sample Type:** Bishop Tuff - LVEW

Plagioclase		SiO <sub>2</sub>	Al <sub>2</sub> O <sub>3</sub>	Na <sub>2</sub> O	K <sub>2</sub> O	CaO	Fe <sub>2</sub> O <sub>3</sub>	BaO	total	Ab	Or	An
Sample	Depth (m)											
2040_PLAG1	621.8	62.90	23.45	8.33	1.31	4.35	0.16	0.00	100.50	71.83	7.44	20.72
2040_PLAG1	621.8	62.72	22.37	8.27	1.55	3.92	0.23	0.04	99.09	72.23	8.85	18.91
2040_PLAG1	621.8	62.17	22.59	8.12	1.42	4.09	0.13	0.03	98.56	71.76	8.30	19.94
2040_PLAG2	621.8	61.85	22.87	8.10	1.29	4.29	0.19	0.00	98.59	71.59	7.48	20.93
2040_PLAG2	621.8	62.33	23.56	8.13	1.26	4.53	0.25	0.05	100.11	70.92	7.19	21.88
2040_PLAG3	621.8	61.35	23.47	7.36	1.70	4.84	0.23	0.09	99.03	66.05	9.98	23.97
2040_PLAG3	621.8	52.77	28.66	4.76	0.27	11.61	0.70	0.06	98.84	41.94	1.58	56.48
2040_PLAG3	621.8	57.02	26.49	6.41	0.51	8.17	0.34	0.08	99.02	56.93	2.93	40.14
2040_PLAG3	621.8	60.73	24.54	7.52	0.83	6.02	0.37	0.19	100.18	66.02	4.78	29.20
2040_PLAG4	621.8	60.80	23.86	7.78	1.23	4.75	0.21	0.04	98.67	69.32	7.24	23.45
2040_PLAG6	621.8	57.56	26.04	6.52	0.61	8.08	0.40	0.08	99.29	57.27	3.51	39.22
2040_PLAG7	621.8	61.82	22.92	8.16	1.17	4.70	0.33	0.05	99.14	70.79	6.68	22.53
2040_PLAG7	621.8	61.84	23.11	8.09	1.21	4.45	0.14	0.00	98.84	71.36	6.98	21.66
2040_PLAG9	621.8	59.72	25.09	7.02	0.82	6.70	0.29	0.07	99.70	62.33	4.81	32.86
2040_PLAG12	621.8	62.66	23.60	7.91	1.40	4.26	0.08	0.02	99.92	70.69	8.21	21.10

**Sample Type:** Bishop Tuff - LVEW

Sanidine		SiO <sub>2</sub>	Al <sub>2</sub> O <sub>3</sub>	Na <sub>2</sub> O	K <sub>2</sub> O	CaO	Fe <sub>2</sub> O <sub>3</sub>	BaO	total	Ab	Or	An
Sample	Depth (m)											
2040_SAN3	621.8	63.94	19.15	4.00	10.32	0.33	0.18	0.86	98.77	36.42	61.95	1.63
2040_SAN3	621.8	64.55	18.69	3.56	10.97	0.24	0.10	0.73	98.85	32.65	66.12	1.23
2040_SAN3B	621.8	65.94	18.74	3.77	11.29	0.21	0.06	0.00	100.00	33.33	65.66	1.00
2040_SAN3C	621.8	65.13	18.83	3.79	11.35	0.19	0.16	0.00	99.45	33.33	65.77	0.89
2040_SAN4	621.8	64.09	19.03	3.47	10.86	0.26	0.13	0.74	98.58	32.23	66.42	1.35
2040_SAN4	621.8	64.54	19.28	3.66	11.16	0.25	0.16	0.61	99.65	32.83	65.96	1.21
2040_SAN5	621.8	65.16	18.98	3.92	11.00	0.19	0.32	0.04	99.60	34.80	64.29	0.90
2040_SAN5	621.8	63.86	21.72	9.05	1.28	2.87	0.32	0.01	99.10	78.85	7.35	13.80
2040_SAN6	621.8	65.36	18.38	3.59	11.45	0.20	0.22	0.01	99.21	31.93	67.07	1.00
2040_SAN6	621.8	65.18	18.41	3.62	11.17	0.19	0.03	0.00	98.61	32.66	66.33	1.01
2040_SAN7	621.8	65.58	19.58	3.67	10.82	0.34	0.22	0.33	100.53	33.47	64.86	1.66
2040_SAN7	621.8	65.21	19.38	5.22	8.44	0.44	0.12	0.52	99.33	47.42	50.41	2.16
2040_SAN9	621.8	65.46	18.38	3.90	11.11	0.17	0.15	0.00	99.17	34.50	64.71	0.80
2040_SAN9	621.8	65.26	18.51	3.75	10.89	0.17	0.19	0.04	98.82	34.08	65.10	0.82
2040_SAN10	621.8	65.78	18.87	5.51	8.98	0.23	0.06	0.03	99.45	47.74	51.18	1.08
2040_SAN10	621.8	64.75	18.63	3.54	11.75	0.24	0.00	0.01	98.92	31.01	67.81	1.18

**Sample Type:** Bishop Tuff: LVEW

Plagioclase		SiO <sub>2</sub>	Al <sub>2</sub> O <sub>3</sub>	Na <sub>2</sub> O	K <sub>2</sub> O	CaO	Fe <sub>2</sub> O <sub>3</sub>	BaO	total	Ab	Or	An
Sample	Depth (m)											
14-GPL1	820.0	68.13	20.78	11.20	0.06	0.83	0.00		100.99	95.82	0.31	3.87
14-GPL1	820.0	68.67	20.52	11.10	0.09	0.84	0.14		101.36	95.47	0.51	4.01
14-GPL1	820.0	69.32	19.98	11.30	0.08	0.21	0.00		100.88	98.64	0.42	0.94
14-GPL2	820.0	67.23	21.19	11.08	0.10	1.37	0.00		100.97	93.02	0.60	6.38
14-GPL2	820.0	69.00	20.12	11.93	0.03	0.05	0.00		101.13	99.60	0.20	0.20
14-GPL2	820.0	68.37	20.20	11.95	0.08	0.38	0.00		100.98	97.76	0.49	1.75
14-GPL2	820.0	68.68	20.28	11.71	0.03	0.19	0.00		100.88	98.99	0.10	0.91
14-GPL2	820.0	69.13	20.30	11.38	0.10	0.21	0.07		101.19	98.55	0.52	0.93
14-GPL2	820.0	66.48	20.97	11.13	0.05	1.17	0.04		99.84	94.23	0.30	5.47
14-GPL2	820.0	67.95	21.06	11.28	0.08	1.08	0.09		101.53	94.59	0.40	5.01
14-GPL2	820.0	67.74	20.86	11.34	0.06	1.20	0.00		101.21	94.17	0.30	5.53
14-GPL2	820.0	67.99	20.18	11.63	0.08	0.18	0.00		100.07	98.70	0.50	0.80
14-GPL2	820.0	67.35	20.10	11.57	0.08	0.56	0.00		99.66	97.04	0.39	2.56
14-GPL2	820.0	67.87	20.74	11.39	0.09	0.88	0.01		100.99	95.42	0.50	4.08
14-GPL2	820.0	67.61	21.32	11.11	0.10	1.45	0.04		101.62	92.81	0.50	6.69
14-GPL3	820.0	67.54	21.34	11.22	0.12	1.21	0.00		101.43	93.73	0.70	5.58
14-GPL3	820.0	70.65	20.22	11.46	0.04	0.19	0.04		102.60	98.85	0.21	0.94
14-GPL3	820.0	68.90	20.68	11.53	0.09	0.51	0.02		101.73	97.17	0.51	2.33
14-GPL3	820.0	67.37	21.00	11.24	0.05	1.01	0.00		100.67	94.99	0.30	4.71
14-GPL4	820.0	68.71	20.47	11.38	0.15	0.29	0.04		101.04	97.85	0.82	1.33
14-GPL4	820.0	68.76	20.56	11.46	0.16	0.27	0.11		101.33	97.76	0.92	1.33
14-GPL4	820.0	68.23	20.63	11.05	0.14	0.79	0.04		100.87	95.47	0.72	3.81
14-GPL4	820.0	67.71	20.52	11.27	0.03	0.82	0.00		100.36	95.97	0.20	3.83
14-GPL4	820.0	68.32	20.33	11.62	0.06	0.42	0.07		100.82	97.80	0.30	1.90
14-GPL4	820.0	68.88	21.08	11.35	0.32	0.29	0.08		102.01	96.82	1.85	1.33

Table AII.1 con't.

Sample	Depth (m)	SiO <sub>2</sub>	Al <sub>2</sub> O <sub>3</sub>	Na <sub>2</sub> O	K <sub>2</sub> O	CaO	Fe <sub>2</sub> O <sub>3</sub>	BaO	total	Ab	Or	An
<b>Plagioclase</b>												
14-GPL4	820.0	68.86	20.58	11.21	0.12	0.63	0.03		101.43	96.40	0.62	2.99
14-GPL4	820.0	68.69	20.67	10.80	0.09	1.04	0.03		101.31	94.46	0.52	5.02
14-GPL4	820.0	68.56	20.92	10.91	0.13	0.59	0.00		101.10	96.41	0.74	2.85
14-GPL4	820.0	64.28	23.38	9.42	1.81	0.34	0.15		99.38	87.26	11.02	1.73
14-GPL4	820.0	67.29	20.19	11.38	0.12	0.39	0.00		99.37	97.49	0.70	1.81
14-GPL4	820.0	68.63	20.33	11.14	0.10	0.18	0.17		100.54	98.63	0.53	0.84
14-GPL4	820.0	68.30	20.48	11.17	0.23	0.41	0.16		100.76	96.71	1.34	1.95
14-GPL4	820.0	67.71	20.85	11.36	0.09	0.79	0.10		100.90	95.79	0.50	3.71
14-GPL4	820.0	69.13	20.44	11.25	0.09	0.34	0.09		101.35	97.81	0.52	1.67
14-GPL5	820.0	66.93	20.84	10.37	0.12	0.87	0.12		99.26	94.85	0.75	4.40
14-GPL5	820.0	68.07	20.57	11.76	0.09	0.34	0.00		100.82	97.92	0.49	1.58
14-GPL5	820.0	67.07	21.53	10.54	0.12	1.40	0.02		100.67	92.60	0.63	6.77
14-GPL5	820.0	68.66	20.35	11.59	0.05	0.45	0.02		101.12	97.59	0.30	2.11
14-GPL5	820.0	66.51	20.78	11.01	0.05	1.00	0.00		99.35	94.95	0.30	4.74
14-GPL5	820.0	67.37	21.00	11.29	0.05	0.85	0.00		100.56	95.68	0.30	4.02
14-GPL5	820.0	68.50	20.93	11.17	0.09	0.65	0.00		101.34	96.39	0.52	3.10
14-GPL5	820.0	68.34	20.97	11.40	0.14	0.62	0.00		101.48	96.26	0.81	2.93
14-GPL5	820.0	66.68	21.16	10.80	0.08	1.63	0.00		100.34	91.96	0.40	7.64
14-GPL6	820.0	68.63	21.04	10.97	0.14	0.70	0.04		101.51	95.81	0.84	3.35
14-GPL6	820.0	65.44	19.44	4.12	10.91	0.20	0.03		100.14	36.09	62.91	1.00
14-GPL6	820.0	67.51	20.16	11.29	0.12	0.83	0.12		100.02	95.42	0.70	3.88
14-GPL6	820.0	68.20	21.10	11.10	0.09	0.89	0.06		101.43	95.28	0.51	4.21
14-GPL6	820.0	65.94	19.26	3.87	11.39	0.20	0.02		100.68	33.76	65.34	0.90
14-GPL6	820.0	66.31	19.45	3.76	11.34	0.15	0.15		101.15	33.27	66.02	0.71

Table AII.1 con't.

**Sample Type:**

Bishop Tuff: LVEW

Sanidine		SiO <sub>2</sub>	Al <sub>2</sub> O <sub>3</sub>	Na <sub>2</sub> O	K <sub>2</sub> O	CaO	Fe <sub>2</sub> O <sub>3</sub>	BaO	total	Ab	Or	An
Sample	Depth (m)											
14-GSA6	820.0	66.26	19.31	4.15	10.97	0.24	0.11		101.03	36.06	62.84	1.10
14-GSA6	820.0	65.33	19.54	3.88	11.39	0.11	0.23		100.48	33.96	65.54	0.50
14-GSA6	820.0	65.14	19.40	3.99	11.32	0.18	0.07		100.11	34.58	64.54	0.88
14-GSA6	820.0	65.47	18.91	4.09	10.83	0.17	0.17		99.63	36.17	63.03	0.80
14-GSA6	820.0	65.53	19.20	3.99	11.14	0.18	0.00		100.04	34.93	64.18	0.90
14-GSA6	820.0	65.48	19.16	3.79	11.40	0.12	0.07		100.02	33.37	66.03	0.60
14-GSA6	820.0	65.28	18.91	4.04	11.22	0.16	0.22		99.82	35.07	64.15	0.79
14-GSA6	820.0	65.97	19.38	3.85	10.96	0.16	0.00		100.33	34.49	64.69	0.82
14-GSA6	820.0	65.99	19.60	3.95	11.08	0.17	0.11		100.90	34.88	64.31	0.81
14-GSA6	820.0	66.43	19.36	3.83	11.16	0.15	0.11		101.05	34.08	65.20	0.71
14-GSA6	820.0	65.25	19.41	3.97	11.20	0.19	0.26		100.28	34.69	64.41	0.89
14-GSA6	820.0	65.87	19.50	3.78	11.20	0.19	0.10		100.64	33.54	65.55	0.91
14-GSA6	820.0	66.38	18.91	1.30	12.08	0.46	1.09		100.23	13.69	83.67	2.64
14-GSA6	820.0	66.75	18.04	1.12	13.94	0.07	0.08		100.00	10.86	88.82	0.33
14-GSA7	820.0	65.83	19.19	4.05	11.02	0.23	0.09		100.41	35.43	63.47	1.10
14-GSA7	820.0	65.66	19.18	3.96	11.03	0.17	0.15		100.16	35.01	64.19	0.80
14-GSA7	820.0	67.08	19.41	4.04	10.99	0.20	0.01		101.74	35.47	63.52	1.02
14-GSA7	820.0	66.14	19.85	4.13	11.12	0.25	0.14		101.62	35.66	63.15	1.20
14-GSA7	820.0	65.20	19.19	3.64	11.04	0.19	0.12		99.38	33.06	66.02	0.92
14-GSA7	820.0	65.92	19.13	3.99	11.47	0.22	0.00		100.72	34.18	64.74	1.08
14-GSA7	820.0	65.91	19.86	3.98	11.35	0.15	0.14		101.40	34.53	64.77	0.70
14-GSA7	820.0	65.70	19.10	3.89	11.03	0.13	0.22		100.08	34.69	64.71	0.61
14-GSA8	820.0	66.36	19.13	3.95	11.37	0.24	0.15		101.21	34.13	64.68	1.19
14-GSA8	820.0	66.01	19.56	3.91	11.23	0.23	0.17		101.11	34.24	64.66	1.10
14-GSA8	820.0	66.63	19.50	3.92	11.11	0.18	0.14		101.49	34.62	64.46	0.92

Table AII.1 con't.

Sample	Depth (m)	SiO <sub>2</sub>	Al <sub>2</sub> O <sub>3</sub>	Na <sub>2</sub> O	K <sub>2</sub> O	CaO	Fe <sub>2</sub> O <sub>3</sub>	BaO	total	Ab	Or	An
<b>Sanidine</b>												
14-GSA8	820.0	66.49	19.03	3.91	11.31	0.20	0.22		101.16	34.13	64.86	1.00
14-GSA8	820.0	65.96	19.51	3.72	11.57	0.17	0.21		101.15	32.60	66.60	0.80
14-GSA8	820.0	66.11	19.89	4.00	11.20	0.21	0.10		101.51	34.84	64.16	1.00
14-GSA8	820.0	65.78	19.77	4.22	10.90	0.22	0.23		101.11	36.59	62.31	1.10
14-GSA8	820.0	66.58	19.22	4.06	10.97	0.19	0.20		101.21	35.69	63.40	0.91
14-GSA8	820.0	66.47	19.61	4.07	10.94	0.23	0.08		101.40	35.73	63.16	1.11
14-GSA8	820.0	66.71	19.55	4.22	10.64	0.21	0.04		101.36	37.21	61.77	1.02
14-GSA8	820.0	65.78	19.38	4.21	11.04	0.19	0.16		100.76	36.36	62.75	0.89
14-GSA8	820.0	66.48	19.34	3.99	11.03	0.19	0.05		101.07	35.16	63.93	0.91
14-GSA8	820.0	66.42	19.32	4.10	10.92	0.17	0.03		100.95	36.06	63.13	0.81
14-GSA8	820.0	65.64	19.43	4.11	11.14	0.22	0.06		100.60	35.54	63.38	1.09
14-GSA8	820.0	65.38	19.26	3.95	11.33	0.13	0.04		100.09	34.42	64.99	0.59
14-GSA8	820.0	65.48	19.09	3.86	11.33	0.17	0.03		99.96	33.90	65.31	0.80
14-GSA8	820.0	65.97	19.44	4.06	10.96	0.19	0.10		100.72	35.65	63.44	0.91
14-GSA8	820.0	65.24	19.44	3.84	11.16	0.23	0.16		100.07	33.94	64.96	1.10
14-GSA8	820.0	66.55	19.42	4.09	11.17	0.18	0.12		101.53	35.36	63.74	0.90
14-GSA8	820.0	65.98	19.94	4.22	11.02	0.16	0.10		101.41	36.49	62.81	0.70
14-GSA8	820.0	65.83	19.05	3.87	11.12	0.16	0.03		100.08	34.31	64.88	0.81
14-GSA8	820.0	64.95	19.06	4.17	11.19	0.20	0.13		99.71	35.85	63.18	0.97
14-GSA8	820.0	65.57	19.18	4.00	11.16	0.15	0.00		100.05	35.02	64.28	0.70
14-GSA8	820.0	65.91	19.34	4.07	11.20	0.17	0.02		100.70	35.28	63.92	0.79
14-GSA8	820.0	65.39	19.37	4.08	10.93	0.21	0.17		100.13	35.80	63.20	1.00
14-GSA8	820.0	66.34	19.12	3.96	11.15	0.20	0.05		100.81	34.67	64.32	1.01
14-GSA8	820.0	66.26	19.50	3.89	11.33	0.20	0.07		101.23	33.94	65.06	1.00
14-GSA8	820.0	66.53	19.40	3.90	11.42	0.14	0.08		101.45	33.94	65.46	0.60

Table AII.1 con't.

Sample	Depth (m)	SiO <sub>2</sub>	Al <sub>2</sub> O <sub>3</sub>	Na <sub>2</sub> O	K <sub>2</sub> O	CaO	Fe <sub>2</sub> O <sub>3</sub>	BaO	total	Ab	Or	An
<b>Sanidine</b>												
14-GSA8	820.0	65.27	19.21	3.86	11.31	0.16	0.17		99.99	33.90	65.31	0.80
14-GSA8	820.0	66.18	19.08	3.80	11.67	0.16	0.16		101.05	32.87	66.34	0.79
14-GSA8	820.0	66.08	19.29	3.99	11.39	0.14	0.20		101.08	34.49	64.82	0.69
14-GSA8	820.0	66.03	19.60	3.91	11.60	0.18	0.08		101.41	33.63	65.48	0.89
14-GSA8	820.0	65.54	19.42	3.92	11.00	0.16	0.14		100.18	34.92	64.27	0.81
14-GSA8	820.0	65.45	19.44	4.09	11.30	0.14	0.00		100.42	35.23	64.08	0.69
14-GSA8	820.0	66.15	18.67	1.14	14.18	0.12	0.32		100.57	10.78	88.58	0.65
14-GSA9	820.0	65.44	19.52	3.84	11.12	0.21	0.10		100.23	34.04	64.95	1.01
14-GSA9	820.0	64.94	19.32	3.91	11.08	0.26	0.07		99.58	34.46	64.24	1.29
14-GSA9	820.0	65.88	19.21	4.03	10.91	0.27	0.00		100.30	35.48	63.22	1.31
14-GSA9	820.0	65.43	19.21	3.77	11.00	0.24	0.04		99.68	33.77	65.01	1.22
14-GSA9	820.0	65.68	19.29	3.96	11.31	0.23	0.13		100.60	34.32	64.59	1.09
14-GSA9	820.0	65.14	19.61	3.90	10.74	0.18	0.05		99.62	35.25	63.83	0.92
14-GSA9	820.0	65.46	19.25	3.80	11.08	0.23	0.07		99.89	33.81	65.08	1.11
14-GSA9	820.0	65.32	19.22	4.12	10.98	0.19	0.18		100.00	36.01	63.10	0.89
14-GSA9	820.0	66.33	19.41	3.81	11.08	0.19	0.25		101.08	34.02	65.06	0.92
14-GSA9	820.0	65.40	19.37	3.75	11.35	0.23	0.09		100.19	33.07	65.83	1.10
14-GSA9	820.0	65.05	19.39	0.79	15.47	0.05	0.08		100.83	7.19	92.60	0.21
14-GSA9	820.0	66.34	17.82	0.95	14.15	0.05	0.07		99.38	9.18	90.49	0.33



**Sample Type:** Bishop Tuff: LVEW

Plagioclase		SiO <sub>2</sub>	Al <sub>2</sub> O <sub>3</sub>	Na <sub>2</sub> O	K <sub>2</sub> O	CaO	Fe <sub>2</sub> O <sub>3</sub>	BaO	total	Ab	Or	An
Sample	Depth (m)											
PLAGSCRAP 2	981.5	66.75	20.00	11.51	0.10	0.35	0.20		98.91	97.82	0.50	1.68
PLAGSCRAP 2	981.5	66.12	20.27	11.88	0.23	0.38	0.00		98.88	97.06	1.23	1.71
22-C_PLAG3	981.5	65.86	21.80	11.20	0.11	0.34	0.05		99.37	97.75	0.61	1.63
22-C_PLAG3	981.5	66.25	20.19	11.90	0.10	0.24	0.00		98.68	98.37	0.58	1.06

**Sample Type:** Bishop Tuff: LVEW

Sanidine		SiO <sub>2</sub>	Al <sub>2</sub> O <sub>3</sub>	Na <sub>2</sub> O	K <sub>2</sub> O	CaO	Fe <sub>2</sub> O <sub>3</sub>	BaO	total	Ab	Or	An
Sample	Depth (m)											
22-C_SAN1	981.5	64.63	19.51	4.57	10.37	0.24	0.16	0.00	99.48	39.61	59.22	1.18
22-C_SAN1	981.5	64.81	19.31	4.23	10.03	0.23	0.13	0.00	98.74	38.64	60.23	1.13
22-C_SAN1	981.5	65.14	19.65	4.41	10.13	0.29	0.00	0.00	99.62	39.29	59.29	1.41
22-C_SAN1	981.5	64.36	19.75	4.49	10.03	0.27	0.10	0.00	99.00	39.98	58.72	1.30
22-C_SAN1	981.5	63.53	19.98	4.40	10.18	0.36	0.06	0.00	98.51	38.91	59.31	1.78
22-C_SAN1	981.5	65.24	19.54	4.58	10.18	0.26	0.11	0.00	99.92	40.10	58.61	1.29
22-C_SAN1	981.5	65.42	20.11	4.56	10.13	0.35	0.00	0.00	100.57	39.92	58.38	1.71
22-C_SAN1	981.5	65.72	19.80	4.49	10.34	0.34	0.20	0.00	100.89	39.16	59.24	1.60
22-C_SAN1	981.5	64.07	19.80	4.32	10.27	0.31	0.04	0.00	98.81	38.40	60.10	1.50
22-C_SAN1	981.5	65.89	20.45	4.49	9.94	0.49	0.23	0.00	101.49	39.75	57.89	2.36
22-C_SAN1A	981.5	64.41	19.52	4.24	10.29	0.28	0.20	0.00	98.93	37.97	60.62	1.41
22-C_SAN1A	981.5	63.53	19.75	4.42	10.03	0.30	0.17	0.00	98.19	39.52	58.98	1.50
22-C_SAN1A	981.5	64.18	19.26	4.52	10.08	0.31	0.03	0.00	98.39	39.92	58.60	1.48
22-C_SAN1A	981.5	65.03	19.85	4.56	9.84	0.33	0.15	0.00	99.76	40.67	57.71	1.62
22-C_SAN1A	981.5	65.15	19.75	4.48	9.75	0.35	0.20	0.00	99.67	40.41	57.85	1.74

Table AII.1 con't.

Sample	Depth (m)	SiO <sub>2</sub>	Al <sub>2</sub> O <sub>3</sub>	Na <sub>2</sub> O	K <sub>2</sub> O	CaO	Fe <sub>2</sub> O <sub>3</sub>	Ba $\oplus$	total	Ab	Or	An
<b>Sanidine</b>												
22-C_SAN1A	981.5	61.94	19.16	4.36	9.94	0.34	0.23	0.00	95.97	39.33	59.00	1.67
22-C_SAN1A	981.5	62.92	18.92	0.32	16.23	0.05	0.18	0.00	98.63	2.89	96.91	0.20
22-C_SAN2	981.5	65.30	19.66	4.46	10.59	0.20	0.11	0.00	100.33	38.64	60.38	0.99
22-C_SAN2	981.5	64.48	19.71	4.36	10.90	0.26	0.09	0.00	99.81	37.37	61.37	1.26
22-C_SAN2	981.5	64.27	19.52	4.59	10.46	0.24	0.22	0.01	99.32	39.51	59.32	1.17
22-C_SAN3	981.5	64.29	19.57	4.42	10.69	0.26	0.00	0.00	99.24	38.12	60.62	1.26
22-C_SAN3	981.5	64.85	19.74	4.35	10.52	0.22	0.07	0.00	99.75	38.21	60.80	1.00
22-C_SAN3	981.5	64.92	19.35	4.04	10.45	0.20	0.00	0.00	98.96	36.67	62.31	1.02
22-C_SAN3	981.5	66.35	19.98	4.12	10.95	0.15	0.14	0.00	101.69	36.17	63.12	0.71
22-C_SAN3	981.5	64.45	19.72	4.38	10.68	0.20	0.12	0.00	99.54	38.04	60.98	0.98
22-C_SAN3	981.5	64.68	19.48	4.30	10.51	0.16	0.12	0.00	99.26	38.02	61.18	0.80
22-C_SAN3	981.5	64.80	19.57	4.34	10.86	0.22	0.14	0.00	99.94	37.37	61.56	1.07
22-C_SAN3	981.5	64.94	19.68	4.46	10.81	0.18	0.13	0.00	100.20	38.17	60.95	0.88
22-C_SAN3	981.5	64.90	19.62	4.44	10.73	0.19	0.12	0.00	99.99	38.32	60.80	0.88
22-C_SAN3	981.5	64.22	19.67	4.50	10.56	0.27	0.16	0.00	99.39	38.83	59.90	1.26
22-C_SAN3	981.5	63.07	19.38	0.33	16.46	0.02	0.00	0.00	99.26	2.96	96.94	0.10
22-C_SAN3	981.5	66.66	19.64	4.74	9.84	0.35	0.00	0.00	101.22	41.54	56.74	1.72
22-C_SAN4	981.5	64.71	19.46	4.37	10.14	0.19	0.14	0.01	99.03	39.23	59.86	0.91
22-C_SAN4	981.5	63.85	19.82	4.27	10.57	0.30	0.24	0.00	99.06	37.54	60.99	1.48
22-C_SAN4	981.5	66.49	19.72	4.50	10.11	0.31	0.15	0.00	101.28	39.76	58.72	1.53
22-C_SAN4	981.5	64.69	19.25	4.37	10.57	0.25	0.15	0.00	99.26	38.15	60.67	1.18
22-C_SAN4	981.5	64.70	19.36	4.45	10.24	0.26	0.05	0.00	99.06	39.26	59.44	1.29
22-C_SAN4	981.5	64.04	19.77	4.64	10.00	0.38	0.20	0.00	99.02	40.55	57.58	1.87
22-C_SAN4	981.5	66.35	19.50	4.53	9.96	0.30	0.07	0.00	100.72	40.25	58.22	1.53
22-C_SAN4	981.5	64.23	19.76	4.67	10.07	0.35	0.00	0.00	99.08	40.63	57.70	1.67
22-C_SAN4	981.5	63.63	20.33	4.47	9.88	0.35	0.10	0.00	98.76	40.08	58.21	1.71

Table AII.1 con't.

Sample	Depth (m)	SiO <sub>2</sub>	Al <sub>2</sub> O <sub>3</sub>	Na <sub>2</sub> O	K <sub>2</sub> O	CaO	Fe <sub>2</sub> O <sub>3</sub>	BaO	total	Ab	Or	An
<b>Sanidine</b>												
22-C_SAN4	981.5	63.63	20.33	4.47	9.88	0.35	0.10	0.00	98.76	40.08	58.21	1.71
22-C_SAN5	981.5	66.76	19.57	4.42	10.31	0.31	0.08	0.00	101.45	38.86	59.61	1.53
22-C_SAN5	981.5	66.12	20.40	11.60	0.60	0.26	0.06	0.00	99.03	95.59	3.26	1.15
22-C_SAN5	981.5	65.63	19.22	4.02	11.27	0.23	0.13	0.00	100.49	34.71	64.20	1.08
22-C_SAN5	981.5	66.58	19.45	4.46	10.58	0.27	0.06	0.00	101.41	38.58	60.12	1.30
22-C_SAN5	981.5	64.27	19.42	4.49	10.51	0.26	0.01	0.00	98.97	38.87	59.86	1.26
22-C_SAN5	981.5	63.76	19.52	4.31	10.66	0.29	0.05	0.00	98.60	37.51	61.03	1.46
22-C_SAN5	981.5	66.09	19.37	4.37	10.35	0.22	0.02	0.00	100.40	38.66	60.22	1.11
22-C_SAN5	981.5	64.09	19.53	4.29	10.56	0.25	0.03	0.00	98.75	37.67	61.14	1.18
22-C_SAN5	981.5	66.01	19.16	4.24	10.58	0.30	0.01	0.01	100.31	37.29	61.21	1.51
22-C_SAN5	981.5	64.35	19.07	1.87	14.20	0.05	0.00	0.00	99.53	16.62	83.18	0.20
22-C_SAN5	981.5	64.53	19.79	4.56	9.94	0.30	0.07	0.00	99.19	40.42	58.07	1.50
22-C_SAN6	981.5	64.31	19.40	4.46	10.27	0.30	0.12	0.00	98.86	39.15	59.37	1.48
22-C_SAN6	981.5	66.26	19.61	4.37	10.19	0.27	0.17	0.00	100.86	38.93	59.73	1.33
22-C_SAN6	981.5	66.11	19.54	4.66	10.19	0.21	0.09	0.00	100.80	40.60	58.40	1.00
22-C_SAN6	981.5	62.96	19.99	2.81	12.61	0.15	0.00	0.00	98.52	25.12	74.18	0.70
22-C_SAN6	981.5	64.84	19.45	4.30	10.52	0.25	0.00	0.00	99.35	37.81	61.00	1.19
22-C_SAN6	981.5	65.61	19.40	4.56	10.54	0.22	0.15	0.00	100.47	39.23	59.78	0.98
22-C_SAN6	981.5	64.38	19.86	4.69	10.10	0.27	0.15	0.00	99.45	40.85	57.87	1.28
22-C_SAN6	981.5	66.80	19.50	4.28	10.27	0.29	0.15	0.00	101.28	38.22	60.33	1.45
22-C_SAN6	981.5	64.56	19.47	4.56	10.29	0.31	0.00	0.01	99.21	39.67	58.86	1.47
22-C_SAN6	981.5	64.97	19.18	4.33	10.31	0.28	0.10	0.00	99.17	38.44	60.16	1.40
22-C_SAN6	981.5	65.63	19.28	4.46	10.22	0.23	0.15	0.00	99.98	39.44	59.46	1.11
22-C_SAN6A	981.5	64.62	19.66	4.42	10.60	0.27	0.18	0.00	99.73	38.27	60.45	1.28
22-C_SAN6A	981.5	64.35	20.10	4.85	10.21	0.23	0.25	0.00	99.99	41.46	57.48	1.07
22-C_SAN6A	981.5	65.14	19.97	4.28	10.26	0.30	0.06	0.00	100.00	38.19	60.39	1.43

Table AII.1 con't.

Sample	Depth (m)	SiO <sub>2</sub>	Al <sub>2</sub> O <sub>3</sub>	Na <sub>2</sub> O	K <sub>2</sub> O	CaO	Fe <sub>2</sub> O <sub>3</sub>	BaO	total	Ab	Or	An
<b>Sanidine</b>												
22-C_SAN6A	981.5	63.26	19.64	2.18	13.81	0.12	0.03	0.00	99.03	19.22	80.20	0.59
22-C_SAN6A	981.5	64.49	20.06	4.56	10.65	0.23	0.05	0.00	100.04	38.99	59.94	1.07
22-C_SAN6A	981.5	64.55	20.10	4.51	10.37	0.28	0.01	0.00	99.82	39.23	59.39	1.38
22-C_SAN7	981.5	66.16	19.61	4.18	10.40	0.25	0.08	0.00	100.69	37.45	61.32	1.23
22-C_SAN7	981.5	64.08	19.28	4.59	10.33	0.27	0.00	0.00	98.54	39.81	58.93	1.26
22-C_SAN7	981.5	65.89	19.77	4.69	10.07	0.30	0.08	0.00	100.80	40.86	57.64	1.50
22-C_SAN7	981.5	64.43	19.81	4.59	10.04	0.32	0.23	0.00	99.43	40.36	58.05	1.59
22-C_SAN7	981.5	64.97	19.76	4.66	10.34	0.30	0.16	0.00	100.19	40.06	58.57	1.37
22-C_SAN7	981.5	63.46	18.88	4.54	10.03	0.39	0.00	0.00	97.29	39.96	58.19	1.85
22-C_SAN8	981.5	64.18	19.36	4.35	10.46	0.23	0.29	0.00	98.87	38.28	60.63	1.09
22-C_SAN8	981.5	65.39	19.53	4.64	10.27	0.33	0.11	0.00	100.27	40.06	58.37	1.57
22-C_SAN8	981.5	65.87	19.57	4.50	10.41	0.25	0.21	0.00	100.81	39.22	59.58	1.20
22-C_SAN8	981.5	66.48	19.25	4.36	10.35	0.24	0.22	0.00	100.91	38.66	60.22	1.12
22-C_SAN8	981.5	65.37	19.61	4.49	10.37	0.28	0.00	0.00	100.12	39.13	59.48	1.39
22-C_SAN8	981.5	64.65	18.90	4.44	10.59	0.22	0.06	0.00	98.86	38.46	60.47	1.07
22-C_SAN8	981.5	64.70	19.08	3.94	11.26	0.23	0.01	0.00	99.22	34.31	64.61	1.08
22-C_SAN8	981.5	64.06	19.11	4.36	10.60	0.25	0.17	0.00	98.56	38.01	60.82	1.17
22-C_SAN8	981.5	64.17	19.65	4.33	10.13	0.23	0.13	0.00	98.64	38.99	59.90	1.11
22-C_SAN8	981.5	64.33	19.01	4.44	10.23	0.29	0.15	0.00	98.45	39.23	59.39	1.38
22-C_SAN8	981.5	64.90	18.75	4.62	10.16	0.24	0.00	0.00	98.67	40.37	58.45	1.18
22-C_SAN8	981.5	65.18	19.81	4.74	10.16	0.29	0.13	0.00	100.30	40.94	57.68	1.38
22-C_SAN8	981.5	64.58	19.15	4.41	10.49	0.26	0.04	0.00	98.93	38.47	60.26	1.28
22-C_SAN8	981.5	65.24	19.62	4.35	10.19	0.25	0.11	0.00	99.77	38.82	59.96	1.22
22-C_SAN8	981.5	64.20	19.97	4.28	10.31	0.26	0.06	0.00	99.08	38.19	60.50	1.31
22-C_SAN8	981.5	65.96	19.50	4.04	11.49	0.19	0.16	0.00	101.33	34.51	64.61	0.88
22-C_SAN8	981.5	69.57	17.14	1.81	11.84	0.09	0.00	0.00	100.45	18.76	80.76	0.48

Table AII.1 con't.

Sample	Depth (m)	SiO <sub>2</sub>	Al <sub>2</sub> O <sub>3</sub>	Na <sub>2</sub> O	K <sub>2</sub> O	CaO	Fe <sub>2</sub> O <sub>3</sub>	BaO	total	Ab	Or	An
<b>Sanidine</b>												
22-C_SAN9	981.5	65.15	19.20	4.58	9.95	0.38	0.19	0.00	99.44	40.36	57.74	1.90
22-C_SAN9	981.5	66.13	19.54	4.51	10.43	0.31	0.12	0.00	101.05	39.04	59.46	1.49
22-C_SAN9	981.5	64.40	19.45	4.12	10.58	0.25	0.13	0.00	98.93	36.77	62.02	1.20
22-C_SAN9	981.5	65.14	19.62	4.46	10.49	0.29	0.17	0.00	100.17	38.70	59.92	1.38
22-C_SAN9	981.5	66.01	19.41	4.35	10.28	0.34	0.11	0.01	100.51	38.44	59.94	1.62
22-C_SAN9	981.5	66.05	19.76	4.58	10.41	0.38	0.05	0.00	101.23	39.37	58.85	1.78
22-C_SAN9	981.5	64.29	19.49	4.44	10.18	0.26	0.10	0.00	98.77	39.34	59.36	1.29
22-C_SAN9	981.5	65.39	19.36	4.25	10.50	0.22	0.15	0.00	99.87	37.66	61.23	1.11
22-C_SAN10	981.5	64.57	19.75	3.68	10.81	0.34	0.06	0.00	99.20	33.54	64.81	1.65
22-C_SAN10	981.5	65.58	19.28	2.98	12.69	0.22	0.00	0.01	100.77	26.02	72.89	1.09
22-C_SAN10	981.5	66.31	19.54	4.58	10.32	0.23	0.10	0.00	101.08	39.78	59.12	1.10
22-C_SAN10	981.5	65.08	19.03	4.52	10.21	0.31	0.16	0.00	99.30	39.60	58.91	1.49
22-C_SAN10	981.5	64.78	19.46	4.57	10.08	0.34	0.25	0.00	99.47	40.12	58.19	1.69
22-C_SAN10	981.5	65.92	19.27	4.49	10.30	0.30	0.00	0.00	100.27	39.26	59.24	1.50
22-C_SAN10	981.5	66.35	19.60	4.64	10.05	0.34	0.19	0.00	101.17	40.63	57.76	1.61
22-C_PLAG4	981.5	63.73	19.45	4.49	10.35	0.32	0.14	0.00	98.49	39.11	59.34	1.56
22-C_PLAG4	981.5	63.76	18.70	0.39	16.27	0.01	0.08	0.00	99.20	3.49	96.51	0.00
22-C_PLAG4	981.5	65.40	19.54	4.81	9.66	0.36	0.25	0.00	100.02	42.33	55.87	1.81
22-C_PLAG4	981.5	64.68	19.11	2.81	13.11	0.17	0.11	0.00	100.00	24.39	74.83	0.78
22-C_PLAG4	981.5	64.96	18.74	4.95	9.34	0.36	0.11	0.00	98.45	43.78	54.43	1.79
22-C_PLAG4	981.5	63.01	18.67	0.45	16.59	0.00	0.00	0.00	98.71	3.95	96.05	0.00
22-C_PLAG5	981.5	89.06	5.50	0.58	3.03	0.10	0.40	0.01	98.67	22.07	76.06	1.88
22-C_PLAG5	981.5	65.91	19.38	4.03	10.87	0.26	0.09	0.00	100.54	35.56	63.13	1.31
22-C_PLAG5	981.5	64.94	19.18	4.65	10.53	0.21	0.05	0.00	99.57	39.81	59.23	0.97
22-C_PLAG5	981.5	66.00	19.28	4.16	10.76	0.21	0.17	0.00	100.58	36.66	62.34	1.01
22-C_PLAG5	981.5	65.87	19.20	4.41	10.77	0.23	0.00	0.00	100.48	37.95	60.96	1.08

Table AII.1 con't.

Sample	Depth (m)	SiO <sub>2</sub>	Al <sub>2</sub> O <sub>3</sub>	Na <sub>2</sub> O	K <sub>2</sub> O	CaO	Fe <sub>2</sub> O <sub>3</sub>	BaO	total	Ab	Or	An
<b>Sanidine</b>												
22-C_PLAG5	981.5	65.87	19.10	4.48	10.48	0.22	0.10	0.00	100.25	38.89	60.02	1.09
22-C_PLAG5	981.5	65.45	19.79	4.47	10.88	0.18	0.00	0.00	100.77	38.11	61.01	0.88
22-C_PLAG5	981.5	64.03	19.27	4.41	10.83	0.21	0.11	0.00	98.85	37.88	61.15	0.96
22-C_PLAG5	981.5	64.59	19.19	4.54	10.61	0.26	0.04	0.00	99.23	38.90	59.85	1.25
22-C_PLAG5	981.5	64.08	19.12	4.52	10.19	0.27	0.00	0.00	98.18	39.74	58.98	1.28
22-C_PLAG5	981.5	64.09	19.51	4.41	10.59	0.27	0.02	0.00	98.89	38.27	60.47	1.27
22-C_PLAG5	981.5	66.08	19.36	4.42	10.51	0.20	0.10	0.00	100.67	38.64	60.36	1.00
22-C_PLAG5	981.5	64.35	19.49	4.30	10.62	0.21	0.05	0.00	99.02	37.71	61.30	0.99
22-C_PLAG5	981.5	64.80	19.75	4.40	10.24	0.22	0.05	0.00	99.46	39.10	59.80	1.11
22-C_PLAG5	981.5	43.94	13.95	2.80	6.09	0.23	0.20	0.00	67.20	40.42	57.80	1.78
22-C_PLAG5	981.5	64.37	19.52	4.68	10.43	0.27	0.08	0.00	99.34	40.02	58.73	1.25
22-C_PLAG5	981.5	43.36	13.79	3.38	6.33	0.19	0.06	0.00	67.10	44.20	54.40	1.40
22-C_PLAG5A	981.5	74.50	16.75	1.01	3.67	0.16	0.69	0.01	96.79	28.62	69.02	2.36
22-C_PLAG5A	981.5	64.36	19.24	4.52	10.20	0.31	0.21	0.00	98.84	39.67	58.86	1.48
22-C_PLAG5A	981.5	64.60	20.18	4.61	10.45	0.24	0.05	0.00	100.13	39.69	59.14	1.17
22-C_PLAG5A	981.5	63.99	20.21	4.21	10.34	0.27	0.08	0.00	99.10	37.68	61.01	1.31
22-C_PLAG5A	981.5	64.37	19.52	4.44	10.44	0.24	0.00	0.00	99.01	38.74	60.08	1.18
22-C_PLAG5A	981.5	64.77	19.37	4.32	10.39	0.25	0.00	0.00	99.09	38.32	60.48	1.20
22-C_PLAG5A	981.5	65.20	19.82	4.65	10.20	0.27	0.08	0.00	100.21	40.34	58.37	1.29
22-C_PLAG5A	981.5	57.78	26.18	3.57	9.90	0.36	0.00	0.00	97.79	34.74	63.32	1.94
22-C_PLAG5A	981.5	64.10	18.75	4.28	10.44	0.25	0.14	0.00	97.95	37.91	60.91	1.18
22-C_PLAG5A	981.5	65.19	19.46	4.39	10.50	0.19	0.07	0.00	99.80	38.51	60.60	0.90
22-C_PLAG5A	981.5	64.57	19.34	4.40	10.44	0.20	0.00	0.00	98.97	38.64	60.38	0.99
22-C_PLAG5A	981.5	47.60	35.02	0.18	8.75	0.28	1.39	0.00	93.22	2.96	94.43	2.61
22-C_PLAG5A	981.5	60.88	18.33	1.53	14.14	0.13	0.03	0.00	95.04	13.94	85.38	0.68
22-C_PLAG5A	981.5	63.91	19.68	4.41	10.35	0.25	0.00	0.00	98.59	38.86	59.96	1.18

Table AII.1 con't.

Sample	Depth (m)	SiO <sub>2</sub>	Al <sub>2</sub> O <sub>3</sub>	Na <sub>2</sub> O	K <sub>2</sub> O	CaO	Fe <sub>2</sub> O <sub>3</sub>	BaO	total	Ab	Or	An
<b>Sanidine</b>												
22-C_PLAG5A	981.5	64.15	18.18	3.53	11.25	0.17	0.18	0.00	97.47	31.96	67.13	0.90
22-C_PLAG6	981.5	64.31	19.88	4.39	10.37	0.31	0.04	0.00	99.30	38.55	59.96	1.49
22-C_PLAG6	981.5	64.45	19.26	4.53	10.37	0.33	0.06	0.00	99.01	39.28	59.16	1.56
22-C_PLAG6	981.5	67.14	19.56	4.75	10.33	0.33	0.11	0.00	102.23	40.48	57.94	1.59
22-C_PLAG6	981.5	63.96	19.69	4.67	10.18	0.28	0.00	0.00	98.77	40.51	58.13	1.36
22-C_PLAG6	981.5	65.19	19.40	4.46	10.16	0.26	0.07	0.00	99.54	39.50	59.30	1.21
22-C_PLAG6	981.5	63.90	19.26	4.66	10.26	0.28	0.14	0.00	98.49	40.29	58.36	1.35
22-C_PLAG6	981.5	64.60	19.53	4.54	10.18	0.25	0.01	0.00	99.10	39.94	58.87	1.19
22-C_PLAG6	981.5	65.15	19.56	4.64	10.37	0.30	0.19	0.00	100.20	39.90	58.73	1.37
22-C_PLAG6	981.5	64.15	19.51	4.53	10.46	0.31	0.13	0.00	99.09	39.13	59.42	1.46
22-C_PLAG6	981.5	65.95	19.54	4.53	10.24	0.30	0.09	0.00	100.65	39.58	58.92	1.50
22-C_PLAG6A	981.5	64.40	19.07	4.52	10.18	0.30	0.09	0.01	98.57	39.72	58.80	1.47
22-C_PLAG6A	981.5	66.14	19.81	4.57	10.36	0.25	0.05	0.00	101.19	39.66	59.14	1.20
22-C_PLAG6A	981.5	64.00	19.32	4.58	10.42	0.24	0.03	0.00	98.57	39.56	59.28	1.16
22-C_PLAG6A	981.5	64.09	19.89	4.39	10.31	0.30	0.07	0.00	99.05	38.69	59.82	1.49
22-C_PLAG6A	981.5	63.93	19.50	4.40	10.00	0.30	0.07	0.00	98.21	39.46	59.04	1.51
22-C_PLAG6A	981.5	64.09	19.30	4.55	10.18	0.38	0.12	0.00	98.61	39.69	58.46	1.86
22-C_PLAG6A	981.5	59.84	19.63	4.86	9.88	0.58	0.08	0.00	94.87	41.61	55.64	2.75
22-C_PLAG6A	981.5	66.54	19.44	4.56	10.36	0.28	0.03	0.00	101.20	39.54	59.16	1.30
22-C_PLAG6A	981.5	64.56	19.50	4.56	10.10	0.28	0.25	0.00	99.24	40.12	58.49	1.39
22-C_PLAG6A	981.5	63.95	19.01	4.51	10.38	0.32	0.06	0.00	98.23	39.11	59.34	1.55

Table AII.1 con't.

**Sample Type:** Bishop Tuff: LVEW

<b>Plagioclase</b>		SiO <sub>2</sub>	Al <sub>2</sub> O <sub>3</sub>	Na <sub>2</sub> O	K <sub>2</sub> O	CaO	Fe <sub>2</sub> O <sub>3</sub>	BaO	total	Ab	Or	An
Sample	Depth (m)											
PLAG3_3600	1097.3	68.11	20.56	11.54	0.10	0.33	0.10	0.04	100.77	97.88	0.60	1.51
PLAG3_3600	1097.3	69.27	20.53	11.60	0.13	0.28	0.12	0.00	101.92	97.97	0.71	1.32
PLAG3_3600	1097.3	69.14	20.03	11.26	0.11	0.16	0.00	0.03	100.74	98.64	0.63	0.73
PLAG3_3600	1097.3	69.80	19.76	11.35	0.11	0.12	0.18	0.01	101.32	98.85	0.63	0.52

**Sample Type:** Bishop Tuff: LVEW

<b>Sanidine</b>		SiO <sub>2</sub>	Al <sub>2</sub> O <sub>3</sub>	Na <sub>2</sub> O	K <sub>2</sub> O	CaO	Fe <sub>2</sub> O <sub>3</sub>	BaO	total	Ab	Or	An
Sample	Depth (m)											
3600_PLAG2	1097.3	65.13	18.76	4.44	10.45	0.30	0.00	0.00	99.08	38.63	59.90	1.47
3600_PLAG2	1097.3	66.03	19.21	4.15	10.17	0.28	0.06	0.00	99.90	37.76	60.79	1.45
PLAG2_3600	1097.3	66.04	19.00	4.43	10.47	0.31	0.08	0.00	100.33	38.57	59.94	1.49
PLAG2_3600	1097.3	65.91	19.35	4.27	10.33	0.29	0.00	0.00	100.14	38.05	60.53	1.42
PLAG5_3600	1097.3	66.22	18.93	4.02	10.89	0.22	0.17	0.03	100.48	35.56	63.33	1.11
PLAG5_3600	1097.3	66.27	19.20	4.12	10.60	0.24	0.20	0.01	100.63	36.71	62.17	1.12
PLAG5_3600	1097.3	65.97	18.88	4.00	10.94	0.22	0.13	0.04	100.18	35.31	63.58	1.11
PLAG5_3600	1097.3	65.15	18.83	4.18	10.41	0.24	0.33	0.06	99.20	37.47	61.31	1.21
PLAG5	1097.3	65.12	19.37	3.93	10.53	0.27	0.07	0.10	99.39	35.73	62.94	1.33



**Sample Type:** Bishop Tuff: LVEW

<b>Plagioclase</b>												
Sample	Depth (m)	SiO <sub>2</sub>	Al <sub>2</sub> O <sub>3</sub>	Na <sub>2</sub> O	K <sub>2</sub> O	CaO	Fe <sub>2</sub> O <sub>3</sub>	BaO	total	Ab	Or	An
PLAG2_22-D	1158.2	69.28	19.97	11.76	0.09	0.19	0.00	0.03	101.31	98.60	0.50	0.90
PLAG2_22-D	1158.2	68.26	21.20	10.89	0.63	0.31	0.18	0.00	101.46	94.99	3.55	1.46
PLAG2_22-D	1158.2	69.24	19.95	11.79	0.07	0.29	0.11	0.04	101.49	98.30	0.40	1.30
PLAG2_22-D	1158.2	69.31	20.02	11.60	0.08	0.22	0.01	0.02	101.26	98.58	0.41	1.02
PLAG2_22-D	1158.2	68.15	20.78	11.34	0.10	0.38	0.00	0.00	100.75	97.65	0.51	1.84
FELD1_22-D	1158.2	68.89	20.67	11.52	0.08	0.17	0.01	0.00	101.34	98.77	0.41	0.82
FELD1_22-D	1158.2	68.36	19.99	11.49	0.07	0.25	0.00	0.00	100.14	98.48	0.41	1.12
FELD1_22-D	1158.2	69.09	19.76	11.76	0.08	0.08	0.07	0.00	100.85	99.20	0.40	0.40
SAN5 22-D	1158.2	68.84	20.10	11.61	0.12	0.18	0.06	0.00	100.91	98.48	0.71	0.81

**Sample Type:** Bishop Tuff: LVEW

<b>Sanidine</b>												
Sample	Depth (m)	SiO <sub>2</sub>	Al <sub>2</sub> O <sub>3</sub>	Na <sub>2</sub> O	K <sub>2</sub> O	CaO	Fe <sub>2</sub> O <sub>3</sub>	BaO	total	Ab	Or	An
PLAG3 22-D	1158.2	64.83	19.54	4.11	10.82	0.32	0.09	0.43	100.14	36.05	62.36	1.59

**Sample Type:** Bishop Tuff: LVEW

Plagioclase		SiO <sub>2</sub>	Al <sub>2</sub> O <sub>3</sub>	Na <sub>2</sub> O	K <sub>2</sub> O	CaO	Fe <sub>2</sub> O <sub>3</sub>	BaO	total	Ab	Or	An
Sample	Depth (m)											
22-H_PLAG1	1441.7	66.51	21.20	11.68	0.18	0.13	0.00		99.69	98.42	0.99	0.59
22-H_PLAG1	1441.7	66.84	20.19	11.72	0.07	0.23	0.00		99.05	98.53	0.39	1.08
22-H_PLAG1	1441.7	67.30	20.55	11.85	0.06	0.09	0.06		99.92	99.21	0.39	0.39
22-H_PLAG1	1441.7	67.12	20.33	11.78	0.10	0.01	0.13		99.46	99.41	0.59	0.00
22-H_PLAG1	1441.7	66.76	20.26	11.69	0.09	0.17	0.07		99.04	98.72	0.49	0.79
22-H_PLAG1	1441.7	67.58	20.33	11.92	0.09	0.11	0.07		100.09	99.02	0.49	0.49
22-H_PLAG2	1441.7	67.10	20.24	11.53	0.12	0.01	0.15		99.14	99.19	0.70	0.10
22-H_PLAG2	1441.7	65.79	20.69	11.53	0.10	0.57	0.13		98.81	96.78	0.58	2.63
22-H_PLAG2	1441.7	67.39	20.63	11.83	0.07	0.16	0.02		100.09	98.92	0.39	0.69
22-H_PLAG2	1441.7	67.02	20.41	11.91	0.05	0.03	0.15		99.58	99.51	0.29	0.20
22-H_PLAG2	1441.7	65.90	22.27	10.68	0.87	0.43	0.05		100.19	92.93	5.02	2.05
22-H_PLAG2	1441.7	67.83	20.67	11.83	0.16	0.07	0.35		100.90	98.81	0.89	0.30
22-H_PLAG2	1441.7	67.87	21.06	11.56	0.24	0.16	0.00		100.89	97.98	1.31	0.71
22-H_PLAG2	1441.7	68.45	20.45	11.72	0.15	0.24	0.12		101.12	98.10	0.80	1.10
22-H_PLAG2	1441.7	68.04	20.68	11.63	0.10	0.29	0.00		100.74	98.10	0.50	1.40
22-H_PLAG2	1441.7	67.95	20.35	11.78	0.08	0.16	0.00		100.32	98.81	0.40	0.79
22-H_PLAG2	1441.7	66.48	21.03	11.85	0.25	0.38	0.01		100.00	96.93	1.34	1.73
22-H_PLAG3	1441.7	66.85	19.85	11.94	0.11	0.12	0.10		98.97	98.84	0.58	0.58
22-H_PLAG3	1441.7	66.92	20.06	11.55	0.05	0.09	0.07		98.75	99.30	0.30	0.40
22-H_PLAG3	1441.7	66.59	20.49	11.17	0.14	0.47	0.00		98.86	96.96	0.81	2.23
22-H_PLAG3	1441.7	67.88	20.12	11.44	0.07	0.02	0.09		99.62	99.49	0.41	0.10
22-H_PLAG3	1441.7	68.12	20.41	11.70	0.07	0.05	0.00		100.35	99.40	0.40	0.20
22-H_PLAG3	1441.7	67.13	19.90	11.74	0.05	0.22	0.10		99.15	98.63	0.29	1.08
22-H_PLAG3	1441.7	67.78	20.47	11.76	0.03	0.15	0.00		100.19	99.10	0.20	0.70
22-H_PLAG3A	1441.7	67.06	20.77	11.89	0.21	0.20	0.08		100.20	98.06	1.07	0.87

Table AII.1 con't.

Sample	Depth (m)	SiO <sub>2</sub>	Al <sub>2</sub> O <sub>3</sub>	Na <sub>2</sub> O	K <sub>2</sub> O	CaO	Fe <sub>2</sub> O <sub>3</sub>	BaO	total	Ab	Or	An
<b>Plagioclase</b>												
22-H_PLAG3A	1441.7	66.37	20.22	11.81	0.07	0.20	0.11		98.78	98.64	0.39	0.97
22-H_PLAG3A	1441.7	66.41	20.05	12.12	0.09	0.38	0.07		99.12	97.84	0.47	1.69
22-H_PLAG3A	1441.7	67.25	19.85	11.93	0.05	0.07	0.00		99.14	99.42	0.29	0.29
22-H_PLAG3A	1441.7	67.50	20.54	11.54	0.08	0.26	0.00		99.92	98.29	0.50	1.20
22-H_PLAG3A	1441.7	67.11	20.38	11.79	0.11	0.24	0.00		99.63	98.34	0.59	1.08
22-H_PLAG4	1441.7	67.61	20.18	12.00	0.11	0.22	0.12		100.23	98.45	0.58	0.97
22-H_PLAG4	1441.7	68.34	20.40	11.77	0.07	0.14	0.05		100.78	98.90	0.40	0.70
22-H_PLAG4	1441.7	71.92	17.97	9.35	0.58	0.40	0.12		100.34	93.87	3.85	2.28
22-H_PLAG4	1441.7	68.18	20.25	12.05	0.08	0.10	0.01		100.67	99.12	0.39	0.49
22-H_PLAG4	1441.7	66.93	20.53	11.49	0.08	0.23	0.00		99.26	98.50	0.40	1.10
22-H_PLAG4	1441.7	67.10	19.72	12.05	0.12	0.15	0.03		99.17	98.66	0.67	0.67
22-H_PLAG4	1441.7	66.72	20.45	11.68	0.09	0.15	0.03		99.12	98.81	0.49	0.69
22-H_PLAG4	1441.7	66.91	20.53	11.95	0.07	0.17	0.12		99.75	98.83	0.39	0.78
22-H_PLAG5	1441.7	69.22	20.10	11.43	0.38	0.11	0.16		101.40	97.35	2.14	0.51
22-H_PLAG5	1441.7	66.85	20.16	11.68	0.12	0.04	0.00		98.85	99.11	0.69	0.20
22-H_PLAG5	1441.7	70.34	19.51	6.81	2.50	0.15	0.72		100.02	79.81	19.22	0.97
22-H_PLAG5	1441.7	66.66	19.89	12.05	0.11	0.18	0.00		98.89	98.57	0.57	0.86
22-H_PLAG5	1441.7	67.92	20.52	11.47	0.21	0.50	0.08		100.69	96.51	1.20	2.30
22-H_PLAG5	1441.7	67.70	21.03	12.24	0.16	0.39	0.00		101.51	97.44	0.85	1.71
22-H_PLAG5	1441.7	66.38	20.56	11.47	0.29	0.14	0.14		98.97	97.72	1.59	0.69
22-H_PLAG5	1441.7	67.13	19.95	11.44	0.11	0.07	0.16		98.87	99.09	0.61	0.30
22-H_PLAG5	1441.7	66.23	21.13	11.40	0.48	0.21	0.16		99.61	96.34	2.67	0.99
22-H_PLAG6	1441.7	67.72	20.01	10.82	0.33	0.14	0.05		99.06	97.26	2.00	0.74
22-H_PLAG6	1441.7	65.16	21.96	11.01	0.92	0.47	0.23		99.75	92.72	5.12	2.17
22-H_PLAG6	1441.7	65.38	20.46	10.84	0.18	0.31	1.42		98.58	97.40	1.04	1.56
22-H_PLAG6	1441.7	66.71	20.02	11.84	0.14	0.15	0.02		98.88	98.55	0.78	0.68
22-H_PLAG6	1441.7	65.35	21.03	10.96	0.70	0.38	0.36		98.77	94.22	3.98	1.79

Table AII.1 con't.

Sample Plagioclase	Depth (m)	SiO <sub>2</sub>	Al <sub>2</sub> O <sub>3</sub>	Na <sub>2</sub> O	K <sub>2</sub> O	CaO	Fe <sub>2</sub> O <sub>3</sub>	BaO	total	Ab	Or	An
22-H_PLAG7A	1441.7	67.23	20.79	11.37	0.11	0.59	1.07		101.15	96.57	0.60	2.82
22-H_PLAG7A	1441.7	68.26	20.44	11.86	0.04	0.10	0.00		100.70	99.30	0.20	0.50
22-H_PLAG7A	1441.7	70.07	18.41	10.10	0.98	0.12	0.07		99.76	93.34	6.00	0.66
22-H_PLAG8	1441.7	67.03	20.25	11.90	0.08	0.07	0.04		99.37	99.32	0.39	0.29
22-H_PLAG8	1441.7	66.18	20.56	11.44	0.27	1.34	0.00		99.79	92.61	1.42	5.97
22-H_PLAG8	1441.7	67.00	20.80	11.75	0.05	0.03	0.09		99.72	99.60	0.30	0.10
22-H_PLAG8	1441.7	67.21	20.45	11.58	0.14	0.24	0.00		99.61	98.11	0.80	1.09
22-H_PLAG8	1441.7	66.66	20.86	11.94	0.20	0.35	0.02		100.02	97.41	1.05	1.53
22-H_PLAG8	1441.7	67.38	20.40	11.91	0.09	0.08	0.03		99.90	99.12	0.49	0.39
22-H_PLAG8	1441.7	66.94	20.30	11.49	0.22	0.18	0.06		99.18	97.91	1.29	0.80
22-H_PLAG8	1441.7	66.43	20.70	11.45	0.33	0.38	0.12		99.42	96.36	1.87	1.77

Table AII.1 con't.

**Sample Type:**

Bishop Tuff: LVEW

Plagioclase		SiO <sub>2</sub>	Al <sub>2</sub> O <sub>3</sub>	Na <sub>2</sub> O	K <sub>2</sub> O	CaO	Fe <sub>2</sub> O <sub>3</sub>	BaO	total	Ab	Or	An
Sample	Depth (m)											
22-LPL1	1557.2	69.34	20.08	11.29	0.11	0.03	0.13		100.99	99.16	0.63	0.21
22-LPL2	1557.2	68.45	20.43	11.14	0.08	0.64	0.10		100.84	96.40	0.51	3.09
22-LPL2	1557.2	69.81	20.06	11.48	0.08	0.17	0.18		101.78	98.76	0.41	0.83
22-LPL2	1557.2	64.79	18.88	0.36	16.28	0.00	0.00		100.31	3.24	96.76	0.00
22-LPL2	1557.2	69.45	20.32	11.48	0.13	0.14	0.00		101.53	98.66	0.72	0.62
22-LPL2A	1557.2	64.15	18.76	0.35	16.43	0.02	0.13		99.85	3.18	96.72	0.10
22-LPL2A	1557.2	64.92	18.98	1.02	15.52	0.01	0.12		100.56	9.02	90.98	0.00
22-LPL2A	1557.2	68.66	20.95	11.23	0.11	0.49	0.04		101.47	97.00	0.62	2.38
22-LPL2A	1557.2	64.65	19.15	0.90	14.64	0.04	0.11		99.50	8.48	91.30	0.21
22-LPL2A	1557.2	64.79	19.30	0.56	15.84	0.00	0.13		100.62	5.03	94.97	0.00
22-LPL2A	1557.2	68.81	20.22	8.83	2.76	0.35	0.00		100.97	81.49	16.76	1.75
22-LPL2A	1557.2	64.62	19.55	0.48	15.59	0.00	0.00		100.24	4.50	95.50	0.00
22-LPL3	1557.2	88.54	6.20	0.42	3.27	0.05	0.49		98.99	16.11	82.94	0.95
22-LPL3	1557.2	71.37	16.42	0.52	10.10	0.07	0.72		99.20	7.23	92.28	0.48
22-LPL3A	1557.2	67.99	20.72	11.44	0.09	0.24	0.00		100.47	98.37	0.51	1.12
22-LPL3A	1557.2	65.10	18.93	0.35	16.29	0.01	0.08		100.76	3.15	96.85	0.00
22-LPL3A	1557.2	64.69	19.04	0.40	16.59	0.01	0.03		100.75	3.57	96.43	0.00
22-LPL4	1557.2	64.95	19.05	0.29	16.55	0.02	0.04		100.91	2.61	97.29	0.10
22-LPL4	1557.2	68.32	20.92	11.03	0.05	1.18	0.00		101.50	94.17	0.31	5.52
22-LPL4	1557.2	65.68	18.88	9.25	0.08	0.30	0.08		94.27	97.63	0.59	1.78
22-LPL4	1557.2	65.41	18.91	3.56	12.11	0.29	0.00		100.29	30.46	68.19	1.36
22-LPL5	1557.2	64.43	19.08	0.59	16.62	0.00	0.04		100.75	5.06	94.94	0.00
22-LPL5	1557.2	65.34	18.97	0.31	16.55	0.00	0.12		101.30	2.82	97.18	0.00
22-LPL9	1557.2	64.68	19.06	0.34	16.54	0.00	0.05		100.67	3.10	96.90	0.00
22-LPL9	1557.2	51.59	36.19	0.21	9.15	0.21	1.54		98.90	3.21	95.01	1.78
22-LPL9	1557.2	65.25	19.43	0.33	16.19	0.02	0.04		101.26	2.99	96.91	0.10
22-LPL9	1557.2	64.90	19.13	0.43	16.10	0.00	0.05		100.60	3.87	96.13	0.00

**Table AII.1 con't.**  
**Plagioclase**

Sample	Depth (m)	SiO <sub>2</sub>	Al <sub>2</sub> O <sub>3</sub>	Na <sub>2</sub> O	K <sub>2</sub> O	CaO	Fe <sub>2</sub> O <sub>3</sub>	BaO	total	Ab	Or	An
22-LPL9	1557.2	68.79	20.99	11.31	0.08	0.33	0.00		101.49	97.92	0.52	1.56
22-LPL9	1557.2	64.69	19.26	0.75	15.32	0.01	0.12		100.15	6.85	93.15	0.00
22-LPL9	1557.2	68.79	20.99	11.31	0.08	0.33	0.00		101.49	97.92	0.52	1.56
22-LPL9	1557.2	64.69	19.26	0.75	15.32	0.01	0.12		100.15	6.85	93.15	0.00
22-LPL10	1557.2	69.56	20.30	10.71	0.08	0.07	0.10		100.82	99.11	0.55	0.33
22-LPL10	1557.2	69.31	20.24	11.48	0.04	0.13	0.32		101.52	99.17	0.21	0.62

Table AII.1 con't.

**Sample Type:**

Bishop Tuff: LVEW

Sanidine		SiO <sub>2</sub>	Al <sub>2</sub> O <sub>3</sub>	Na <sub>2</sub> O	K <sub>2</sub> O	CaO	Fe <sub>2</sub> O <sub>3</sub>	BaO	total	Ab	Or	An
Sample	Depth (m)											
22-LSA1	1557.2	65.23	18.96	0.31	16.63	0.02	0.06		101.21	2.71	97.19	0.10
22-LSA1	1557.2	63.81	18.67	0.38	16.49	0.07	0.00		99.42	3.34	96.36	0.29
22-LSA1	1557.2	65.28	18.85	0.43	16.66	0.01	0.00		101.23	3.76	96.24	0.00
22-LSA1	1557.2	65.35	18.58	0.69	16.81	0.07	0.05		101.56	5.84	93.87	0.29
22-LSA1	1557.2	64.87	19.05	0.34	16.42	0.00	0.14		100.82	3.03	96.97	0.00
22-LSA1	1557.2	65.13	18.75	0.34	16.35	0.00	0.00		100.56	3.04	96.96	0.00
22-LSA1	1557.2	65.13	19.34	0.32	16.42	0.00	0.00		101.21	2.85	97.15	0.00
22-LSA1	1557.2	65.23	18.95	0.56	16.12	0.03	0.00		100.88	5.04	94.86	0.10
22-LSA2	1557.2	60.82	21.09	10.10	0.09	0.21	6.96		99.26	98.34	0.55	1.11
22-LSA3	1557.2	65.10	18.98	0.53	16.20	0.03	0.00		100.84	4.72	95.18	0.10
22-LSA3	1557.2	64.93	18.72	0.80	15.65	0.02	0.11		100.22	7.16	92.73	0.10
22-LSA3	1557.2	66.04	19.14	3.84	11.47	0.14	0.14		100.77	33.50	65.80	0.70
22-LSA3	1557.2	66.56	19.18	2.97	12.55	0.08	0.08		101.43	26.37	73.22	0.41
22-LSA3	1557.2	66.78	19.36	3.87	11.07	0.13	0.20		101.41	34.47	64.92	0.62
22-LSA3	1557.2	65.87	19.01	3.72	11.21	0.13	0.14		100.08	33.30	66.09	0.61
22-LSA3	1557.2	66.59	19.33	3.74	11.53	0.14	0.05		101.39	32.80	66.50	0.71
22-LSA3	1557.2	66.33	19.15	3.96	10.87	0.17	0.13		100.62	35.34	63.84	0.82
22-LSA3	1557.2	64.83	19.18	0.59	16.09	0.00	0.00		100.69	5.24	94.76	0.00
22-LSA3	1557.2	65.03	19.01	0.57	16.15	0.00	0.05		100.81	5.13	94.87	0.00
22-LSA3	1557.2	65.42	18.94	0.58	16.21	0.01	0.00		101.15	5.13	94.87	0.00
22-LSA3	1557.2	64.99	19.15	4.10	10.47	0.12	0.07		98.90	37.07	62.32	0.61

Table AII.1 con't.

**Sample Type:**

Bishop Tuff: LVEW

Plagioclase		SiO <sub>2</sub>	Al <sub>2</sub> O <sub>3</sub>	Na <sub>2</sub> O	K <sub>2</sub> O	CaO	Fe <sub>2</sub> O <sub>3</sub>	BaO	total	Ab	Or	An
Sample	Depth (m)											
22-N_PLAG1	1673.4	70.01	18.66	10.98	0.24	0.23	0.00		100.12	97.47	1.37	1.16
22-N_PLAG1	1673.4	66.37	21.27	10.71	0.88	1.09	0.05		100.36	90.10	4.85	5.05
22-N_PLAG1	1673.4	64.22	19.27	0.43	16.55	0.00	0.00		100.47	3.76	96.24	0.00
22-N_PLAG1	1673.4	64.00	19.34	2.55	13.51	0.10	0.00		99.50	22.18	77.33	0.49
22-NPLAG1A	1673.4	68.11	20.62	11.78	0.13	0.10	0.00		100.75	98.80	0.70	0.50
22-NPLAG1A	1673.4	66.44	21.16	10.95	0.13	1.22	0.00		99.92	93.57	0.70	5.72
22-NPLAG1A	1673.4	64.07	20.03	2.33	12.29	0.54	0.00		99.27	21.70	75.47	2.83
22-NPLAG1A	1673.4	67.63	20.35	11.54	0.21	0.23	0.00		99.97	97.70	1.20	1.10
22-N_PLAG2	1673.4	68.01	20.38	11.79	0.08	0.28	0.11		100.64	98.32	0.40	1.29
22-N_PLAG2	1673.4	66.12	21.97	11.16	0.84	0.39	0.09		100.57	93.57	4.65	1.78
22-N_PLAG2	1673.4	67.52	20.79	11.75	0.10	0.05	0.07		100.29	99.20	0.60	0.20
22-N_PLAG2	1673.4	66.44	21.85	11.02	0.47	1.05	0.06		100.89	92.54	2.59	4.88
22-N_PLAG2	1673.4	68.05	20.44	11.74	0.10	0.39	0.07		100.77	97.73	0.49	1.78
22-N_PLAG2	1673.4	67.59	20.66	11.49	0.08	0.62	0.00		100.43	96.71	0.40	2.89
22-N_PLAG2	1673.4	67.02	20.21	11.88	0.08	0.29	0.08		99.56	98.26	0.39	1.36
22-N_PLAG?3	1673.4	66.46	18.85	5.44	8.21	0.12	0.10		99.18	49.90	49.48	0.63
22-N_PLAG?3	1673.4	66.72	21.17	11.56	0.19	0.85	0.00		100.48	95.14	0.97	3.89
22-N_PLAG?3	1673.4	64.02	19.35	0.79	16.07	0.00	0.12		100.36	6.98	93.02	0.00
22-N_PLAG?3	1673.4	65.68	20.40	11.67	0.15	0.96	0.00		98.85	94.82	0.85	4.34
22-N_PLAG?3	1673.4	66.34	20.24	11.62	0.14	0.67	0.12		99.13	96.15	0.77	3.08
22-N_PLAG4	1673.4	67.29	20.15	12.06	0.11	0.07	0.13		99.80	99.13	0.58	0.29
22-N_PLAG4	1673.4	66.17	21.38	10.85	0.58	0.64	0.08		99.71	93.63	3.34	3.03
22-N_PLAG4	1673.4	64.76	19.05	0.24	16.58	0.16	0.00		100.79	2.10	97.10	0.80
22-N_PLAG4	1673.4	64.45	19.31	1.90	14.55	0.04	0.12		100.36	16.52	83.28	0.20
22-N_PLAG4	1673.4	64.89	18.93	3.08	11.94	0.12	0.20		99.15	27.96	71.43	0.61



Plagioclase		SiO <sub>2</sub>	Al <sub>2</sub> O <sub>3</sub>	Na <sub>2</sub> O	K <sub>2</sub> O	CaO	Fe <sub>2</sub> O <sub>3</sub>	BaO	total	Ab	Or	An
Sample	Depth (m)											
22-N_PLAG5	1673.4	67.55	20.10	10.77	1.51	0.06	0.18		100.17	91.24	8.47	0.30
22-N_PLAG5	1673.4	63.24	19.20	0.50	16.08	0.02	0.23		99.27	4.49	95.41	0.10
22-N_PLAG5	1673.4	65.56	19.49	4.62	9.99	0.13	0.28		100.07	41.03	58.36	0.61
22-N_PLAG6	1673.4	69.13	20.41	11.54	0.17	0.05	0.09		101.39	98.87	0.92	0.21
22-N_PLAG6	1673.4	66.60	20.14	9.52	2.49	1.70	0.04		100.49	78.70	13.55	7.74
22-N_PLAG6	1673.4	65.04	19.06	0.56	16.08	0.08	0.02		100.84	4.94	94.66	0.40
22-N_PLAG7	1673.4	65.95	21.56	10.79	0.52	1.27	0.25		100.35	91.15	2.88	5.96
22-N_PLAG7	1673.4	67.16	20.69	11.71	0.18	0.20	0.09		100.03	98.12	0.99	0.89
22-N_PLAG7	1673.4	66.67	20.40	11.50	0.10	0.23	0.21		99.11	98.30	0.60	1.10
22-N_PLAG7	1673.4	64.53	21.97	10.75	1.06	0.23	0.21		98.74	92.90	6.00	1.10
22-N_PLAG8	1673.4	66.66	20.42	11.74	0.19	0.31	0.30		99.62	97.47	1.07	1.46
22-N_PLAG8	1673.4	65.91	21.46	11.27	0.69	0.43	0.05		99.84	94.23	3.82	1.96
22-N_PLAG8	1673.4	68.37	20.63	11.82	0.11	0.17	0.14		101.25	98.61	0.60	0.80
22-N_PLAG8	1673.4	66.89	20.72	11.57	0.07	0.52	0.08		99.85	97.24	0.39	2.37
22-N_PLAG8	1673.4	66.74	20.41	11.59	0.08	0.46	0.16		99.45	97.44	0.39	2.16
22-N_PLAG8	1673.4	68.14	20.77	11.64	0.10	0.14	0.07		100.86	98.79	0.51	0.71
22-N_PLAG8	1673.4	65.25	21.86	10.73	0.16	1.88	0.03		99.90	90.42	0.89	8.69

Table AII.1 con't.

**Sample Type:**

Bishop Tuff: LVEW

Sanidine		SiO <sub>2</sub>	Al <sub>2</sub> O <sub>3</sub>	Na <sub>2</sub> O	K <sub>2</sub> O	CaO	Fe <sub>2</sub> O <sub>3</sub>	BaO	total	Ab	Or	An
Sample	Depth (m)											
22-N_SAN1	1673.4	68.90	18.53	10.20	0.79	0.38	0.02		98.83	93.36	4.71	1.93
22-N_SAN1	1673.4	66.04	20.70	11.26	0.74	0.44	0.11		99.28	93.88	4.08	2.04
22-N_SAN1	1673.4	63.91	19.48	1.96	14.22	0.00	0.22		99.78	17.31	82.69	0.00
22-N_SAN1	1673.4	64.11	19.59	2.41	13.53	0.02	0.14		99.81	21.29	78.61	0.10
22-N_SAN1	1673.4	63.52	19.28	2.56	13.19	0.02	0.08		98.66	22.78	77.12	0.10
22-N_SAN1	1673.4	64.56	19.53	2.49	13.38	0.05	0.03		100.04	21.99	77.81	0.20
22-N_SAN1	1673.4	64.95	19.39	2.35	13.30	0.02	0.05		100.06	21.14	78.76	0.10
22-N_SAN2	1673.4	66.84	19.64	11.36	0.31	0.20	0.30		98.66	97.22	1.79	0.99
22-N_SAN2	1673.4	64.84	19.32	2.84	12.85	0.05	0.15		100.05	25.05	74.75	0.20
22-N_SAN2	1673.4	65.01	19.54	2.25	13.68	0.00	0.09		100.57	20.02	79.98	0.00
22-N_SAN2	1673.4	65.29	21.37	10.42	1.03	0.81	0.00		98.92	90.16	5.92	3.92
22-N_SAN2	1673.4	64.19	19.68	2.76	13.01	0.05	0.02		99.71	24.36	75.45	0.20
22-N_SAN2	1673.4	64.27	19.49	2.29	13.57	0.04	0.14		99.80	20.36	79.44	0.20
22-N_SAN2	1673.4	63.80	19.33	3.46	11.74	0.06	0.13		98.54	30.88	68.82	0.30
22-N_SAN2	1673.4	67.98	20.60	11.54	0.16	0.31	0.00		100.60	97.69	0.90	1.41

Table AII.1 con't.

**Sample Type:**

Bishop Tuff: LVEW

Plagioclase		SiO <sub>2</sub>	Al <sub>2</sub> O <sub>3</sub>	Na <sub>2</sub> O	K <sub>2</sub> O	CaO	Fe <sub>2</sub> O <sub>3</sub>	BaO	total	Ab	Or	An
Sample	Depth (m)											
5700-NA1	1737.4	65.79	21.09	10.73	0.09	1.03	1.29		100.02	94.43	0.52	5.06
5700-NA1	1737.4	68.64	20.15	11.71	0.02	0.16	0.00		100.67	99.19	0.10	0.70
5700-NA1	1737.4	68.42	20.24	11.46	0.06	0.42	0.00		100.60	97.77	0.30	1.93
5700-NA1	1737.4	69.19	20.12	11.64	0.10	0.06	0.03		101.14	99.19	0.51	0.31
5700-NA1	1737.4	69.12	20.37	11.66	0.09	0.12	0.00		101.37	98.88	0.51	0.61
5700-NA1	1737.4	68.87	20.18	11.81	0.05	0.09	0.00		101.01	99.30	0.30	0.40
5700-PL1	1737.4	68.45	20.07	11.42	0.07	0.13	0.00		100.16	98.97	0.41	0.62
5700-PL1	1737.4	69.15	20.27	11.39	0.06	0.06	0.00		100.92	99.37	0.31	0.31
5700-PL1	1737.4	69.38	19.98	11.48	0.10	0.10	0.05		101.09	99.07	0.52	0.41
5700-PL1	1737.4	68.91	20.29	11.60	0.07	0.11	0.00		100.97	99.08	0.41	0.51
5700-PL1A	1737.4	69.03	20.61	11.47	0.04	0.33	0.00		101.48	98.25	0.21	1.54
5700-PL1A	1737.4	69.48	19.97	11.66	0.09	0.15	0.08		101.43	98.78	0.51	0.71
5700-PL1A	1737.4	68.93	20.32	11.69	0.13	0.12	0.11		101.30	98.69	0.71	0.61
5700-PL1A	1737.4	65.92	20.93	5.16	8.28	0.08	0.00		100.37	48.43	51.14	0.43
5700-PL1A	1737.4	69.70	20.11	11.19	0.13	0.17	0.05		101.35	98.42	0.74	0.84
5700-PL1A	1737.4	67.26	19.77	11.35	0.05	0.18	0.11		98.72	98.78	0.30	0.91
5700-PL1A	1737.4	68.46	21.51	10.38	0.73	0.28	0.13		101.49	94.23	4.35	1.41

Table AII.1 con't.

**Sample Type:**

Bishop Tuff: LVEW

Sanidine		SiO <sub>2</sub>	Al <sub>2</sub> O <sub>3</sub>	Na <sub>2</sub> O	K <sub>2</sub> O	CaO	Fe <sub>2</sub> O <sub>3</sub>	BaO	total	Ab	Or	An
Sample	Depth (m)											
5700-SA2	1737.4	64.42	18.87	0.37	15.76	0.03	0.00		99.45	3.42	96.48	0.10
5700-SA2	1737.4	65.57	19.08	0.76	15.73	0.02	0.06		101.21	6.82	93.08	0.10
5700-SA2	1737.4	65.27	19.02	0.50	16.00	0.00	0.11		100.90	4.50	95.50	0.00
5700-SA2	1737.4	64.65	18.70	0.33	16.51	0.02	0.00		100.21	2.99	96.91	0.10
5700-SA2	1737.4	66.51	18.79	2.46	12.26	0.02	0.12		100.16	23.33	76.57	0.11
5700-SA3	1737.4	64.84	19.09	0.36	16.23	0.02	0.00		100.55	3.25	96.65	0.10
5700-SA3	1737.4	64.94	18.66	0.64	15.34	0.08	0.10		99.76	5.92	93.67	0.42
5700-SA3	1737.4	65.18	19.42	0.47	15.83	0.03	0.04		100.97	4.36	95.54	0.10
5700-SA3	1737.4	65.36	18.98	0.55	16.37	0.03	0.09		101.39	4.89	95.01	0.10
5700-SA3A	1737.4	65.33	18.96	0.47	15.99	0.17	0.08		101.01	4.28	94.91	0.81
5700-SA3A	1737.4	62.75	18.56	0.32	16.37	0.00	0.09		98.08	2.85	97.15	0.00

Table AII.1 con't.

**Sample Type:**

Bishop Tuff: LVEW

Sanidine		SiO <sub>2</sub>	Al <sub>2</sub> O <sub>3</sub>	Na <sub>2</sub> O	K <sub>2</sub> O	CaO	Fe <sub>2</sub> O <sub>3</sub>	BaO	total	Ab	Or	An
Sample	Depth (m)											
5700-SA2	1737.4	64.42	18.87	0.37	15.76	0.03	0.00		99.45	3.42	96.48	0.10
5700-SA2	1737.4	65.57	19.08	0.76	15.73	0.02	0.06		101.21	6.82	93.08	0.10
5700-SA2	1737.4	65.27	19.02	0.50	16.00	0.00	0.11		100.90	4.50	95.50	0.00
5700-SA2	1737.4	64.65	18.70	0.33	16.51	0.02	0.00		100.21	2.99	96.91	0.10
5700-SA2	1737.4	66.51	18.79	2.46	12.26	0.02	0.12		100.16	23.33	76.57	0.11
5700-SA3	1737.4	64.84	19.09	0.36	16.23	0.02	0.00		100.55	3.25	96.65	0.10
5700-SA3	1737.4	64.94	18.66	0.64	15.34	0.08	0.10		99.76	5.92	93.67	0.42
5700-SA3	1737.4	65.18	19.42	0.47	15.83	0.03	0.04		100.97	4.36	95.54	0.10
5700-SA3	1737.4	65.36	18.98	0.55	16.37	0.03	0.09		101.39	4.89	95.01	0.10
5700-SA3A	1737.4	65.33	18.96	0.47	15.99	0.17	0.08		101.01	4.28	94.91	0.81
5700-SA3A	1737.4	62.75	18.56	0.32	16.37	0.00	0.09		98.08	2.85	97.15	0.00

### **Appendix III. Comparison of Techniques for Whole-rock $\delta^{18}\text{O}$ Analysis**

The analysis of whole-rock powders of hydrothermally altered samples presents special problems. Elsenheimer and Valley (1993)<sup>4</sup> showed that altered feldspar powder or chips can react completely during overnight pretreatment with  $\text{BrF}_5$ . While our fusion technique greatly reduces or eliminates reaction during pretreatment and analysis, systematic changes may occur during fusion. Potential problems with hydrous samples are not restricted to laser analysis. Altered samples may contain waters of diverse and exotic oxygen isotope composition. In some cases, such as expandable clays, an analysis may be improved by removal of water during pre-analysis fusion.

Values for powdered whole-rock samples measured by conventional Ni reaction vessel oxygen isotope extraction were compared to values obtained from the same samples using the UW laser-probe extraction system. The resulting  $\delta^{18}\text{O}$  values do not agree within one standard deviation, with the exception of an obsidian sample, Qer-16 (Figure AIII.1). This was true for samples measured by conventional methods at the University of Wisconsin as well as Krueger Enterprises, Inc., Geochron Laboratories Division (GLD). Laser extraction values were always heavier than the conventionally extracted values from the same whole-rock samples by as much as 1.5‰ (Figure AIII.1, Table AIII.4). There are several possible sources for this systematic disagreement: 1] inconsistencies within the laser extraction procedure (for example, oxygen isotope memory within the extraction lines or non-standardized operator methods), 2] poor control on samples measured at

---

<sup>4</sup> See Reference list for Chapter III for all references in this appendix.

different labs by different techniques (for example, sample mishandling or contamination such as incompletely dried samples in Ni rod bomb), 3] sample preparation required for laser extraction (for example, increased effect of alteration minerals contamination on small samples), or 4] synthetic oxygen isotope fractionation during pretreatment fusing of powdered samples.

Inconsistencies within the laser extraction system (possibility 1) have been addressed in earlier work (Elsenheimer and Valley, 1992; Kohn et al., 1993; Valley et al., 1995). We incorporated their methods into the laser-probe procedures for this study. A detailed description of the procedures is reported in Chapter III.4: Data collection, standardization, and analytical precision. Although operators may vary slightly the timing of extraction steps, the sequence of steps is followed rigorously. The good agreement of standard data prove that this is not the problem. Furthermore, not all the data show the systematic variations in  $\delta^{18}\text{O}$  values (i.e., the unaltered volcanic outcrop sample, Qer-16).

The remaining possibilities were addressed by continuing the comparative study. First, samples from the original suite of whole-rock powders prepared for measurement at Geochron Labs (see Chapter III.3.3: *Previous oxygen isotope studies*) were measured by both conventional Ni reaction vessel and laser extraction methods at UW.  $\text{CO}_2$  extracted by both methods was measured for isotopic ratios on Finnigan/MAT 251 mass-spectrometers at UW standardized against the same  $\text{CO}_2$  gas. We first compared the values obtained at different labs using the same conventional extraction technique. The results show the conventional data agree well. A lack of analytical agreement between the two values could indicate if the shift

in oxygen isotope values may have resulted from sample contamination or mishandling (possibility 2). Internal precision was determined by measuring replicates of samples and one blind repeat sample (8-G and 80-A). The results are compiled in Table AIII.1, and illustrated in Figures AIII.1 and AIII.2a. Standard deviations are listed in the table and plotted as error bars on Figure AIII.1. Figure AIII.2.a displays the values from the two labs as a difference where a value of zero would indicate exact agreement. The difference in the values obtained from the two labs using Ni reaction vessel extraction methods are in agreement within a standard deviation of  $\pm 0.33\%$ . As a result of these tests, we have eliminated the possibility of uncertainty of sample measurements from different labs and thus the cause of the inconsistencies lies with sample preparation or extraction of oxygen when using the laser extraction method.

The most striking observation in Figure AIII.1 is the change from good agreement between techniques in the  $\delta^{18}\text{O}$  value ( $8.3 \pm 0.09\%$ ) for the unaltered sample of obsidian from an outcrop (Qer-16) to increased scatter in the data for hydrothermally altered samples from LVEW. In all cases where the bulk measurements were repeated by the laser extraction method on the samples containing secondary hydrous minerals, the values are systematically heavier by an average of  $0.21\%$ . The alteration suite of minerals found in the intracaldera rocks at LVEW site include varying amounts of smectite, mixed layer illite/smectite, illite clays, quartz, calcite, pyrite, chlorite, potassium feldspar, epidote, and sericitic mica. A detailed discussion of the alteration minerals can be found in McConnell et al. (1995). Due to their easily exchanged interlayer water and structural hydroxyls, the



hydroxylated clays have the highest potential for influencing the oxygen isotope composition of the primary silicate phases.

The main variation between the two methods for isolating oxygen lies in the sample pretreatment employed in the laser extraction method. Powdered samples to be lased were fused to a glass bead to reduce surface area and eliminate adsorbed water before pretreating in  $\text{BrF}_5$ , thus briefly introducing high temperatures above  $1000^\circ\text{C}$ . This drives off oxygen bonded in  $(\text{OH})^-$ ,  $\text{H}_2\text{O}$ ,  $\text{CO}_2$ , and Si/Al tetrahedra. Loosely bonded and abundant  $(\text{OH})^-$  and  $\text{H}_2\text{O}$  ions contained in alteration clays such as illite and smectite begin to be rapidly expelled at temperatures as low as  $300^\circ\text{C}$  (Deer et al., 1992). If equilibration is maintained, dehydroxylation of the clays and dehydration of the expandable smectite and I/S mixed clays during bead formation favors freeing of oxygen lower in  $\delta^{18}\text{O}$  (Hamza and Epstein, 1980) increasing the relative mole percent of heavier oxygen contained in Si-O-Si and Al-O-Si bonds (Savin and Lee, 1988). Assuming little or no exchange between expelled  $\text{H}_2\text{O}$  and residual glass, this would result in higher  $\delta^{18}\text{O}$  values when isotopic ratios are determined for the bulk of the sample remaining in the fused bead. However, these samples have experienced multiple hydrothermal events at varying temperatures and in the presence of fluids of exotic oxygen isotope ratio. If expandable clays contain meteoric water ( $\delta^{18}\text{O} \cong -12\text{‰}$ ), then dehydration would drive  $\delta^{18}\text{O}$  (bulk sample) to higher values, but if waters were magmatic,  $\delta^{18}\text{O}$  would be decreased.

### AIII.1 CONVENTIONAL VS. LASER ANALYSIS OF WHOLE ROCK AND PUMICE SAMPLES

In order to determine if analytical discrepancies appear in the bulk of the samples for this study, the separated silicate components of the volcanic rocks, pumice separate samples were also investigated. Oxygen from pumice separate samples from the extrusive Bishop Tuff and Early Rhyolite tephras and from well samples was extracted by conventional and laser methods at UW. Pumices were carefully hand-picked and prepared to eliminate phenocrysts and lithic clasts. Note, however, that all the pumices have some degree of devitrification, and some samples are densely welded. In addition, core and cuttings samples from the wells display varying stages of hydrothermal alteration. No attempt was made to separate alteration minerals. Mineral phases were determined by XRD of unoriented bulk sample powders. Results are listed in Table AIII.1 and plotted in Figure AIII.2b as the difference between laser and conventional ( $\Delta^{18}\text{O}_{(\text{UWlaser-UWconventional})}$ ) vs. conventional values.

Unaltered extrusive volcanic rock samples, Qbt 15-B, Qbt 15-D, and Qer-16 show the best agreement of  $\delta^{18}\text{O}$  values between the two methods; the average  $\Delta^{18}\text{O}_{(\text{UWlaser-UWconventional})}$  is 0.01‰. Mineral phases identified in the Bishop Tuff pumice include  $\alpha$ -cristobalite, tridymite, sanidine and potassium feldspar, quartz, and biotite as well as glass. The occurrence of biotite and sanidine indicates very fine grained phenocrysts were not completely separated from the pumice but do not appear to affect the precision or accuracy of the measurements. One sample, Qer-16, is petrographically

isotropic, consisting of amorphous volcanic glass showing no devitrification or perlitization.

From the altered pumices from the drill well samples,  $\Delta^{18}\text{O}_{(\text{UWlaser-UWconventional})}$  values vary between 0.08‰ to 2.1‰; the average  $\Delta^{18}\text{O}_{(\text{UWlaser-UWconventional})}$  is 0.73‰. Although most laser-extracted samples tend to be heavier, 19 of the 23 altered samples and 23 of 27 total samples, this is not always the case. Instead, the  $\Delta^{18}\text{O}_{(\text{UWlaser-UWconventional})}$  for pumice values obtained from laser extraction are both positive and negative relative to the Ni reaction vessel extraction values (Figure AIII.2b). The mineralogy of the well samples includes illite, smectite, and illite/smectite (I/S) mixed layer clay; calcite, pyrite, potassium feldspar, and rarely zeolite in addition to the primary igneous minerals identified in the outflow sheet Bishop Tuff (See Table AIII.1). There does not appear to be a relationship between the type of alteration mineral found in a sample and the difference in that sample's oxygen isotope composition between extraction methods. For example, four of the pumice samples have laser extraction values that are significantly lower than the Ni reaction vessel extraction values,  $\Delta^{18}\text{O}_{(\text{UWlaser-UWconventional})} < 0$ . Two of those samples (LVEW 14-A<sub>2</sub> and SF38-32 256) contain I/S mixed layer clays and two samples are relatively low in alteration mineralogy. Other samples with the same alteration mineralogy as LVEW 14-A<sub>2</sub>, such as LVEW 8-G and LV 13-26 RD43, have significantly higher  $\Delta^{18}\text{O}_{(\text{UWlaser-UWconventional})}$ .

### AIII.2 WATER MEASUREMENTS OF SAMPLES

Representative splits from fourteen of the samples were measured for their water content to determine if a correlation exists between hydrous mineral content and analytical discrepancy. Measurements were made using a Cosa coulometric Karl-Fischer titrator coupled to a Pt furnace. The <100 mesh-size fraction splits of whole-rock samples, or the remainder of pumice samples not used up during oxygen isotope analysis, were sequentially heated to 150, 400, and 1000°C and the water content determined at each temperature step. These temperatures were chosen to assess the amount of oxygen contained in water adsorbed on the surface of the samples plus released as interlayer water in clays (below 150°C), in water associated with structural water from (OH)<sup>-</sup> ions in expandable clays (below 400°C), and in water associated with disruption of silicate bonds (below 1000°C). The results are plotted against  $\Delta^{18}\text{O}_{(\text{UW}_{\text{laser}}-\text{UW}_{\text{conventional}})}$  values in Figure AIII.3. The most noticeable contrast in the water content is between the unaltered extrusive volcanic rocks (Qer-16, Qbt 15-B, and Qbt 15-D) and their altered volcanic equivalents from LVEW. The extrusive volcanic rocks are dry, with total water contents of 0.18, 0.09, 0.44 wt.% H<sub>2</sub>O, respectively. Intracaldera volcanic rock samples range from 1.08 to 3.30 wt.% total H<sub>2</sub>O. As there are no major differences in the primary composition of the volcanic rocks between the extrusive outflow sheet Bishop Tuff and the intracaldera Bishop Tuff, the difference in water content must be attributed to alteration mineralogy. Water contents of the altered Bishop Tuff samples are independent of the difference in oxygen isotope composition. Only the two Early Rhyolite intrusions and the Early Rhyolite obsidian samples show a linear relationship

between  $\Delta^{18}\text{O}_{(\text{UWlaser-UWconventional})}$  and water content. The linear regression trendline for these samples only is plotted for the total water content in Figure AIII.3. Thus it does not appear there is a strong linear relationship between the water content and  $\Delta^{18}\text{O}_{(\text{UWlaser-UWconventional})}$  for all the intracaldera rocks.

What does emerge from this study is the strong correlation of increased values of  $|\Delta^{18}\text{O}_{(\text{UWlaser-UWconventional})}|$  and the presence of alteration minerals and/or increased water content in the sample. Unfortunately, no predictive correlation could be determined between the increase in water content in the pumice samples, inferring the increase in clay minerals, and the deviation between extraction methods for oxygen isotope composition of the altered, heterogeneous Bishop Tuff. Note that the two pumice samples from intracaldera wells with no identifiable secondary mineralogy, RD-194 and 2200 (See Figure AIII.2b), display good agreement between measurements. Additionally, the more homogeneous Early Rhyolite obsidian and cryptocrystalline intrusions do display a linear correlation between  $\Delta^{18}\text{O}_{(\text{UWlaser-UWconventional})}$  and water content, as shown by the trendline on Figure AIII.3. The complexity and timing of alteration mineralization may mask any straightforward relationship between water content and oxygen isotope composition. Nevertheless, pretreatment effect on water-bearing alteration minerals still remains a likely explanation for the deviation between laser-probe and conventional vessel bomb techniques.

In conclusion, when measuring the oxygen isotope ratios of altered and heterogeneous rocks, uncertainties of absolute value of the measurement can be expected. These problems are not significant when measuring silicate

phases in volcanic rocks which have not been subjected to alteration or secondary mineralization. In the case of this study, the shifts in isotopic values observed between the two methods of extraction do little to affect the overall trends of the alteration associated with hydrothermal activity. Indeed, it is possible that dehydroxylation and dehydration of the pumice samples during bead formation allows more realistic modeling of the thermal regime when using the potassium feldspar isotope geothermometer. Although the discrepancy of analytical techniques should be borne in mind, the deviation in values does not significantly change the range of temperatures calculated for the paleohydrothermal system or the conclusions of this study.

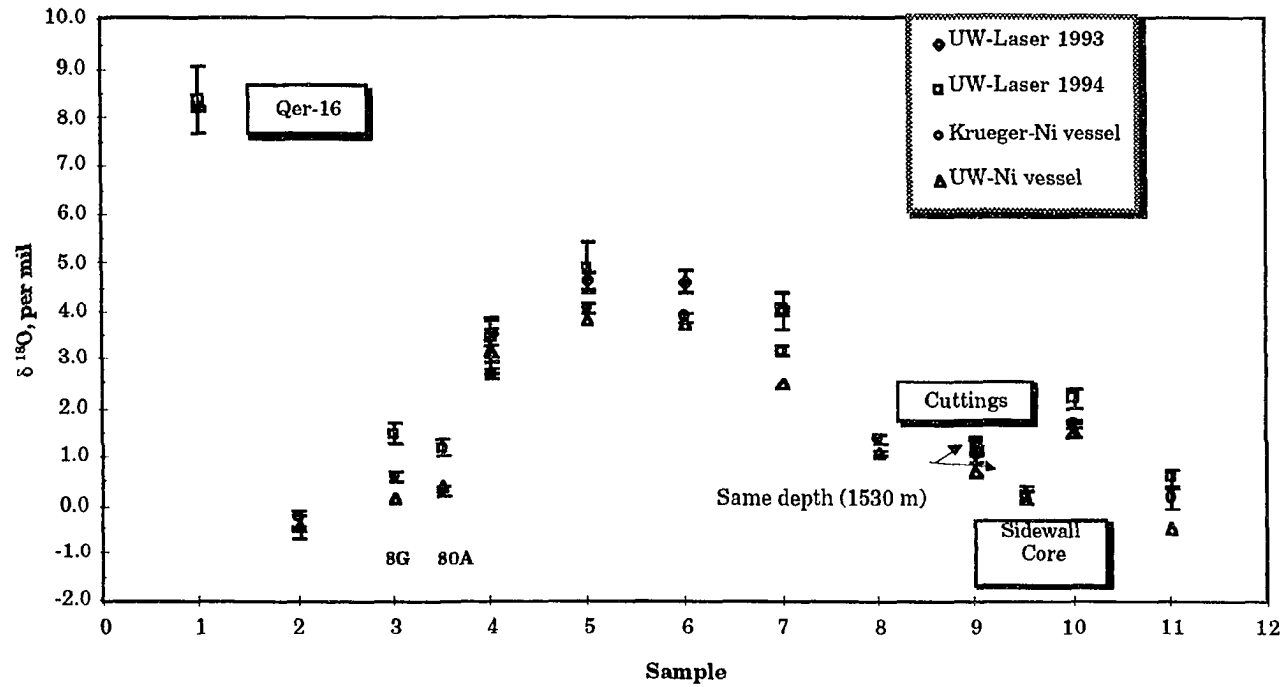


Figure AIII.1 Comparison of analytical techniques using whole-rock samples. Data are compiled in Table AIII.1. Samples are plotted with increasing depth in LVEW. Samples 2, 3, 8, and 9 are Early Rhyolite intrusions. Samples 8G and 80A are blind repeats. Error bars represent one standard deviation about the mean.

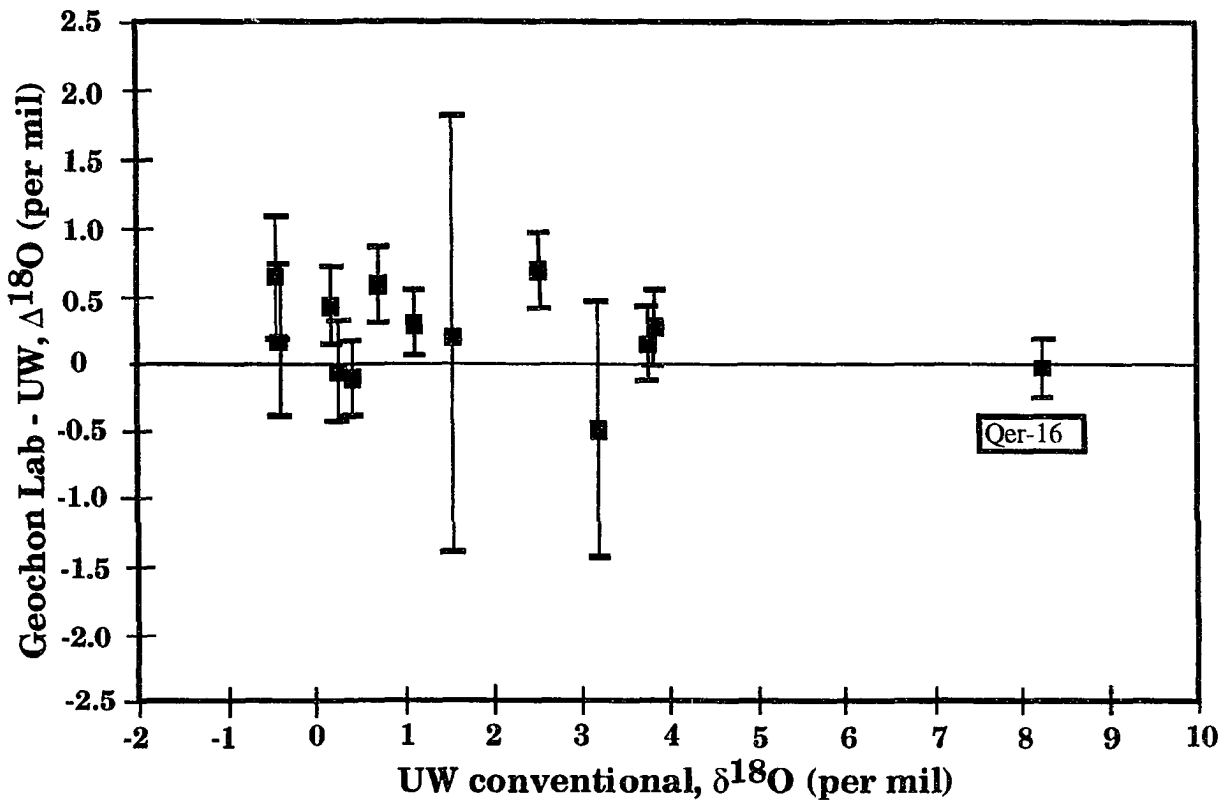


Figure AIII.2a Comparison of conventional extraction analysis. Difference between oxygen isotope values determined for same samples by reaction vessel extraction technique at Geochron Laboratories Div. of Krueger Enterprises, Inc. and Geology and Geophysics Dept. of University of Wisconsin. Zero value on y-axis represents an exact repeat of  $\delta^{18}\text{O}$  value. Sigma equals the square root of the sum of the individual sigmas squared. Data compiled in Table AIII.1.



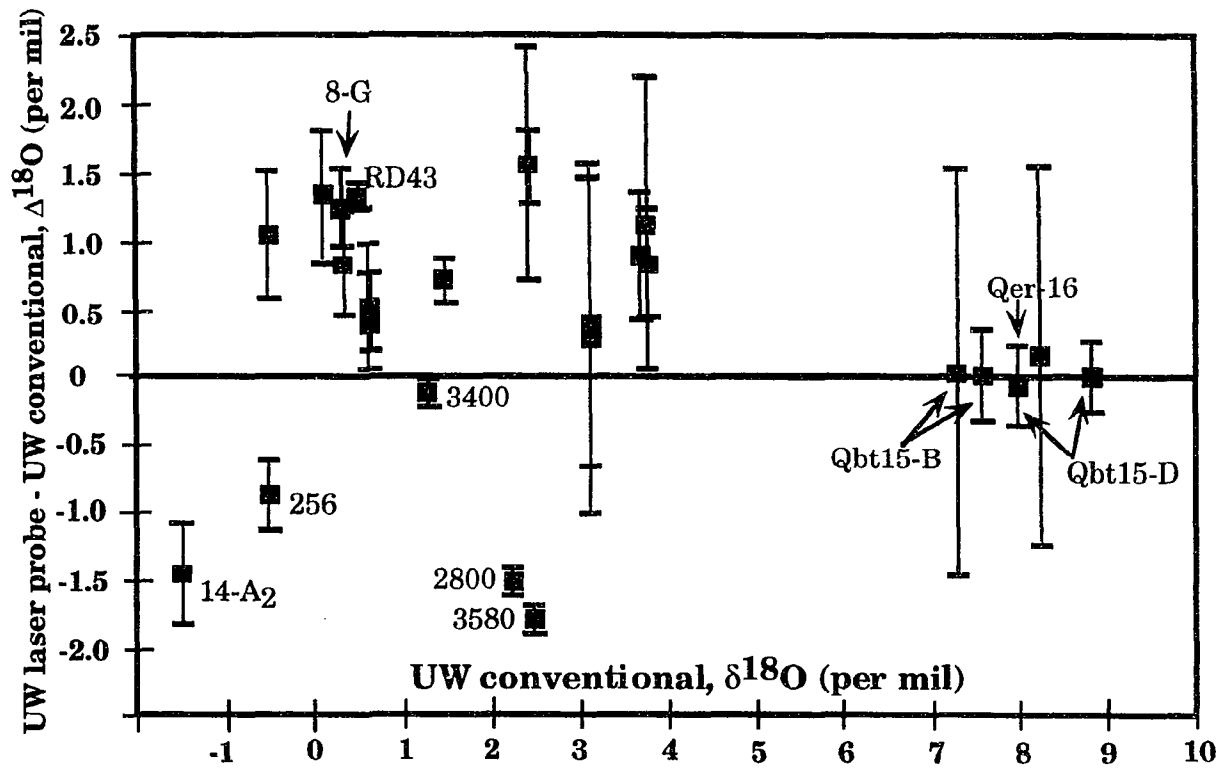


Figure AIII.2b Comparison of laser-probe and reaction vessel extraction analysis. Difference between oxygen isotope values determined for the same samples by laser-probe extraction and reaction vessel extraction. All analyses done at the Geology and Geophysics Dept., University of Wisconsin. Zero value on y-axis represents an exact repeat of  $\delta^{18}\text{O}$  values. Sigma equals the square root of the sum of the individual sigmas squared.

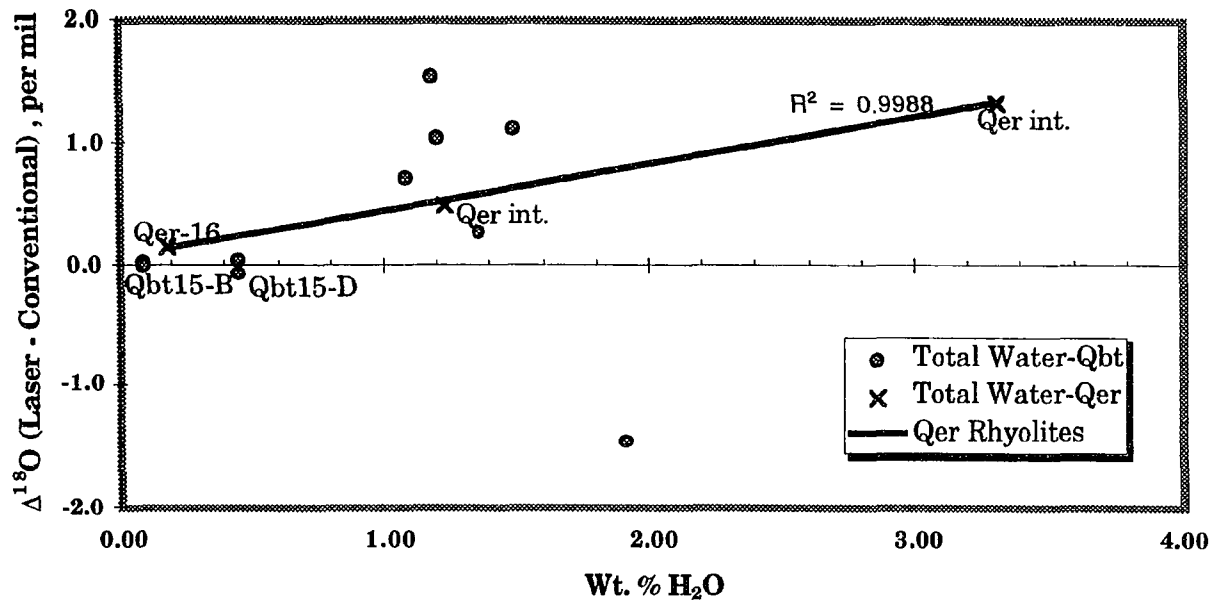


Figure AIII.3 Total water content of volcanic rocks versus oxygen isotope differences. Data compiled in Table AIII.1. Water concentration determined coulometrically. Bishop Tuff (Qbt) does not display any strong correlation of water content to deviation in oxygen isotope compositions between extraction techniques. Early Rhyolite (Qer) does.

Sample ID	Depth (m)	Sample Type	$\delta^{18}\text{O}$ Geo-chron lab		$\delta^{18}\text{O}$ UW laser 1993		$\delta^{18}\text{O}$ UW laser 1994		$\delta^{18}\text{O}$ UW Ni bomb		$\Delta^{18}\text{O}$ Geo-chron - UW	$\Delta^{18}\text{O}$ UW laser-conv. (1994)	$\Delta^{18}\text{O}$ UW laser-conv. (1993)	wt. % H <sub>2</sub> O 150°C	wt. % H <sub>2</sub> O 400°C	wt. % H <sub>2</sub> O 1000°C	wt. % H <sub>2</sub> O total	[XRD Results]
			a	b	a	b	a	b										
15B-Split6	0	Qbt (pumice)					7.6	7.60	0.13		0.00			0.05	0.03	0.01	0.09	[a-crist., san., qtz., bt]
15B-Split5	0	Qbt (pumice)					8.83	8.83	0.08		0.00			0.05	0.03	0.01	0.09	[a-crist., san., qtz., bt]
15D-Split1	0	Qbt (pumice)					7.92	8.01	0.14		-0.09			0.32	0.10	0.03	0.44	[a-crist., try., san., plag., qtz., bt]
15D-Split2	0	Qbt (pumice)					7.32	7.30	0.31		0.02			0.32	0.10	0.03	0.44	[a-crist., try., san., plag., qtz., bt]
Qer-16	0	Qer obsidian	8.2	0.05										0.05	0.06	0.07	0.18	fresh, aphyric glass
Qer-16'94	0	Qer obsidian	8.2				8.38	8.24			-0.04	0.14		0.05	0.06	0.07	0.18	fresh, aphyric glass
LVEW 2B1-wr	784.4	Qer intrusion	-0.25	0.15				-0.42	0.24		0.17			0.45	0.23	0.59	1.27	[qtz., k-spar., >plag., >>I/S]
8C	801.0	Qer intrusion	0.6	0.10			1.5	0.22			0.43	1.33		1.17	0.35	1.78	3.30	[qtz., k-spar., poorly xtl ill., tr. smec.] cly. -2-3%
80A	801.0	Qer intrusion	0.3	0.10			1.22	0.16			-0.10	0.82						[qtz., k-spar., poorly xtl ill., tr. smec.] cly. -2-3%
LVEW 14-A2	818.1	Qbt (pumice)					-2.87	-1.41	0.16		-1.46			0.60	0.22	1.09	1.90	[qtz., san., try., poorly xtl ill., tr. smec.] cly. -2-3%
LVEW 14-G-wr	819.9	Qbt	2.7	0.10	3.56	0.27	3.44	0.45			-0.48	0.26	0.38	0.50	0.17	0.68	1.35	
LVEW 20-7	837.2	Qbt-wr(pwdr)					2.87	0.86										
LVEW 20-7	837.2	Qbt-wr(fused)					3.47	0.46										
LVEW 3180	969.3	Qbt	4.1	0.10	4.65	0.17	4.93	0.53	3.83	0.27	1.10	0.82		0.50	0.16	0.83	1.49	
LVEW 3600	1097.3	Qbt	3.9	0.10	4.62	0.21		3.75			0.15	0.87						
LVEW 4320	1316.7	Qbt	3.2	0.10	4.04	0.09	4.05	0.41	2.51	0.69	1.54	1.53		0.28	0.12	0.78	1.18	
LVEW 22J-wr	1514.9	Qer intrusion	1.4	0.10				1.1	0.07		0.30							[qtz., k-spar., plag., I/S, py.]
LVEW 5020	1530.1	Qer intrusion	1.3	0.10	1.09	0.16	1.21	0.20	0.71	0.59	0.50	0.38		0.30	0.11	0.81	1.22	[qtz., plag., >k-spar., >I/S, py.]
LVEW 22K-wr	1530.1	Qer intrusion	0.2	0.10				0.25	0.16		-0.05							[qtz., plag., >k-spar., >I/S, py.]
LVEW 5380	1639.8	Qbt	1.75	0.05			2.24	0.20	1.54	0.08	0.21	0.70		0.29	0.14	0.65	1.08	
LVEW 5700	1737.4	Qbt (white)	0.2	0.20			0.58	0.21	-0.45	0.65	1.03			0.26	0.13	0.81	1.20	[qtz., san.]
LV13-28																		
RD 43	248.4	Qer (pumice)					1.77	0.06	0.38	0.24		1.39						[qtz., ill., tr smect., tr cal.] cly. 3-5%
134	287.4	Qbt (pumice)					1.25	-0.17				1.42						[qtz., ill., tr smect.] cly. > 10%
RD 194	684.7	Qbt (pumice)					2.96	2.88				0.08						[qtz. & sanidine]
LV13-21																		
1470a	448.1	Qbt (pumice)					1.99	0.15	-0.07		2.06							[qtz., k-spar]
2200	670.6	Qbt (pumice)					1.07	0.09	0.77		0.30							[qtz., san., k-spar]
2800	853.4	Qbt (pumice)					0.87	0.02	2.23		-1.36							[qtz., san., >cal., >>zeo.] zeo. - 1%
3400	1036.3	Qbt (pumice)					1.07	0.06	1.28		-0.21							[qtz., san., >illite & try.]
3580	1091.2	Qbt (pumice)					0.84	0.04	2.44		-1.60							[qtz., san., try., >cal., >>zeo.] zeo. - 1%
SF 38-32																		
251	789.5	Qbt (pumice)					0.29	-1.36	0.28		1.65							
256	803.5	Qbt (pumice)					-1.16	-0.26	0.40		-0.90							[I/S, qtz.]

Table AIII.1 Comparative data from conventional and laser-probe extraction methods.

Samples are listed by drill well identity and depth in well, locations ( ) are indicated in Figure 1.

a - Average deviation (one-half the difference of two values) where two samples, analytical error of 0.10 per mil otherwise.

b - Average deviation where two samples, standard deviation where more than two samples.

Wt.% H<sub>2</sub>O determined by Karl-Fischer coulometric titration, analytical error 0.1 wt. %.

[XRD Results] report mineral phases in semi-quantitative relative abundance based on peak height and resolution. Mineral designated by: qtz. - quartz,

san. - sanidine, k-spar. - potassium feldspar, try. - tridymite, plag. - plagioclase, bt. - biotite, cal. - calcite, py. - pyrite, I/S - Illite/smectite mixed layer clay, gl-glass, ill-illite, zeo-zeolite, smec-smectite.

**APPENDIX IV.  $^{40}\text{Ar}/^{39}\text{Ar}$  data from laser probe analysis.**Table AIV.1  $^{40}\text{Ar}/^{39}\text{Ar}$  age data.

Grain number refers to grain location in sample holder for daily runs and is used to identify individual samples. Step number refers to individual laser fusion steps during multi-step fusions on whole rock samples. Integrated ages for samples are reported in the table but are considered meaningless for those samples with multiple age peaks. See Table IV.1, Chapter IV for depth and sample type information.

**UAF051-33 #21 QER-16 7-31-95**

**Weighted average of J from standards = 0.000243 +/- 0.000002**

<b>Grain No.</b>	<b>Cumulative 39Ar</b>	<b>40Ar/39Ar measured</b>	<b>37Ar/39Ar measured</b>	<b>36Ar/39Ar measured</b>	<b>% Atmospheric 40Ar</b>	<b>37Ca/39K</b>	<b>+/-</b>	<b>40*/39K</b>	<b>+/-</b>	<b>Age (Ma)</b>	<b>+/- (Ma)</b>
19	0.1996	2.349	0.060	0.003	35.948	0.060	0.000	1.486	0.010	0.651	0.004
20	0.3439	2.149	0.060	0.002	30.491	0.060	0.000	1.474	0.011	0.646	0.005
22	0.5421	1.892	0.061	0.001	19.750	0.061	0.000	1.495	0.009	0.655	0.004
23	0.7774	1.957	0.070	0.002	22.964	0.070	0.000	1.486	0.009	0.651	0.004
24	1.0000	2.232	0.063	0.003	33.507	0.063	0.000	1.465	0.009	0.642	0.004
Integrated		2.111	0.063	0.002	28.870	0.063	0.000	1.481	0.004	0.649	0.005

UAF049-21 LV3880 5/2/95

Weighted average of J from standards = 0.000233 +/- 0.000000

Grain No.	Cumulative 39Ar	40Ar/39Ar measured	37Ar/39Ar measured	36Ar/39Ar measured	% Atmospheric 40Ar	37Ca/39K	+/-	40*/39K	+/-	Age (Ma)	+/- (Ma)
1	0.0438	3.714	0.007	0.006	45.104	0.007	0.001	2.023	0.197	0.851	0.083
3	0.1183	3.160	0.010	0.005	44.337	0.010	0.001	1.743	0.116	0.734	0.049
2	0.1788	6.170	0.007	0.014	68.908	0.007	0.001	1.909	0.144	0.804	0.061
8	0.2504	3.498	0.011	0.006	48.839	0.011	0.001	1.775	0.121	0.747	0.051
6	0.3809	4.111	0.012	0.008	57.067	0.012	0.000	1.752	0.068	0.737	0.029
1	0.5742	4.244	0.024	0.009	60.054	0.024	0.000	1.684	0.048	0.709	0.020
2	0.6757	5.334	0.009	0.012	66.118	0.009	0.000	1.797	0.088	0.756	0.037
3	0.8232	7.960	0.009	0.021	79.046	0.009	0.000	1.662	0.068	0.699	0.029
4	0.9169	4.440	0.008	0.008	56.092	0.008	0.001	1.937	0.094	0.815	0.040
5	1.0000	8.615	0.010	0.023	78.120	0.010	0.001	1.879	0.110	0.791	0.046
Integrated		5.226	0.012	0.012	65.743	0.012	0.000	1.780	0.028	0.749	0.012

UAF049-26 14-G

Weighted average of J from standards = 0.000233 +/- 0.000000

Grain No.	Cumulative 39Ar	40Ar/39Ar measured	37Ar/39Ar measured	36Ar/39Ar measured	% Atmospheric 40Ar	37Ca/39K	+/-	40*/39K	+/-	Age (Ma)	+/- (Ma)
32	0.0548	24.649	0.008	0.079	95.140	0.008	0.001	1.196	0.169	0.504	0.071
39	0.1679	25.484	0.008	0.082	94.858	0.008	0.000	1.309	0.135	0.551	0.057
40	0.2963	4.435	0.008	0.009	62.398	0.008	0.000	1.657	0.056	0.697	0.023
35	0.3452	7.630	0.011	0.020	77.381	0.011	0.001	1.719	0.141	0.724	0.059
33	0.4413	25.457	0.007	0.081	93.662	0.007	0.000	1.612	0.140	0.678	0.059
33	0.5325	8.943	0.007	0.025	83.528	0.007	0.000	1.468	0.084	0.618	0.036
27	0.6129	2.993	0.007	0.005	51.196	0.007	0.000	1.447	0.084	0.609	0.035
21	0.7170	14.958	0.007	0.046	90.639	0.007	0.000	1.398	0.095	0.588	0.040
22	0.8637	15.550	0.008	0.047	89.905	0.008	0.000	1.567	0.086	0.659	0.036
15	1.0000	9.499	0.009	0.027	84.236	0.009	0.000	1.493	0.066	0.628	0.028
Integrated		13.812	0.008	0.042	89.159	0.008	0.000	1.494	0.032	0.629	0.014

**UAF049-22 LV4000 QER-INT**

**Weighted average of J from standards = 0.000233 +/- 0.000000**

Grain No.	Cumulative 39Ar	40Ar/39Ar measured	37Ar/39Ar measured	36Ar/39Ar measured	% Atmospheric 40Ar	37Ca/39K	+/-	40*/39K	+/-	Age (Ma)	+/- (Ma)
4	0.0758	7.997	0.007	0.024	89.749	0.007	0.000	0.817	0.051	0.344	0.022
5	0.1508	7.029	0.006	0.021	90.102	0.006	0.000	0.693	0.049	0.292	0.021
9	0.2638	6.796	0.006	0.020	85.429	0.006	0.000	0.986	0.039	0.415	0.017
10	0.3427	5.118	0.006	0.015	84.209	0.006	0.000	0.804	0.042	0.338	0.018
11	0.4043	6.981	0.006	0.020	86.420	0.006	0.000	0.944	0.054	0.397	0.023
12	0.4882	6.665	0.004	0.020	87.112	0.004	0.000	0.855	0.045	0.360	0.019
6	0.6643	19.470	0.006	0.063	95.403	0.006	0.000	0.894	0.095	0.376	0.040
7	0.7997	20.214	0.007	0.063	92.233	0.007	0.000	1.568	0.099	0.660	0.042
19	1.0000	18.575	0.006	0.059	94.716	0.006	0.000	0.980	0.090	0.412	0.038
Integrated		13.180	0.006	0.041	92.514	0.006	0.000	0.985	0.029	0.414	0.012



UAF049 23 LV5100 5/2/95

Weighted average of J from standards = 0.000233 +/- 0.000000

Grain No.	Cumulative 39Ar	40Ar/39Ar measured	37Ar/39Ar measured	36Ar/39Ar measured	% Atmospheric 40Ar	37Ca/39K	+/-	40*/39K	+/-	Age (Ma)	+/- (Ma)
21	1.0000	2.859	0.012	0.003	36.480	0.012	0.001	1.798	0.141	0.756	0.060
Integrated		2.859	0.012	0.003	36.480	0.012	0.001	1.798	0.141	0.756	0.060

UAF049 LV5810

Weighted average of J from standards = 0.000233 +/- 0.000000

Grain No.	Cumulative 39Ar	40Ar/39Ar measured	37Ar/39Ar measured	36Ar/39Ar measured	% Atmospheric 40Ar	37Ca/39K	+/-	40*/39K	+/-	Age (Ma)	+/- (Ma)
22	0.1978	59.739	0.005	0.112	55.428	0.005	0.000	26.614	0.274	11.167	0.115
15	0.2049	37.918	-0.003	0.108	84.369	-0.003	0.011	5.922	2.117	2.491	0.890
16	0.2459	100.299	0.120	0.327	96.439	0.120	0.002	3.570	0.605	1.502	0.255
8	0.4466	9.482	0.005	0.028	86.515	0.005	0.000	1.275	0.088	0.537	0.037
14	0.6586	25.432	0.008	0.082	95.796	0.008	0.000	1.068	0.142	0.449	0.060
20	0.7127	59.112	0.016	0.187	93.562	0.016	0.002	3.804	0.401	1.600	0.169
26	0.9468	8.052	0.003	0.024	88.539	0.003	0.000	0.920	0.075	0.387	0.032
32	1.0000	43.086	0.033	0.141	96.685	0.033	0.002	1.427	0.355	0.601	0.149
Integrated		30.864	0.012	0.083	79.143	0.012	0.000	6.431	0.077	2.705	0.033

UAF049 LV5880 5-03-95

Weighted average of J from standards = 0.000233 +/- 0.000000

Grain No.	Cumulative 39Ar	40Ar/39Ar measured	37Ar/39Ar measured	36Ar/39Ar measured	% Atmospheric 40Ar	37Ca/39K +/-	40*/39K +/-	Age (Ma)	+/-		
18	0.1692	30.410	0.014	0.094	91.768	0.014	0.000	2.501	0.173	1.052	0.073
24	0.4051	68.246	0.001	0.017	7.206	0.001	0.000	63.302	0.340	26.448	0.141
16	0.5216	48.787	0.010	0.151	91.299	0.010	0.001	4.242	0.270	1.785	0.114
9	0.8654	87.787	0.003	0.025	8.290	0.003	0.000	80.483	0.429	33.560	0.177
10	1.0000	16.191	0.005	0.052	94.660	0.005	0.001	0.863	0.142	0.363	0.060
Integrated		59.286	0.005	0.053	26.366	0.005	0.000	43.634	0.154	18.272	0.071

**UAF051-32 LV2B1**

**Weighted average of J from standards = 0.000243 +/- 0.000002**

**UAF051-32 LV2B1-9**

Step No.	Cumulative 39Ar	40Ar/39Ar measured	37Ar/39Ar measured	36Ar/39Ar measured	% Atmospheric 40Ar	37Ca/39K	+/-	40*/39K	+/-	Age (Ma)	+/- (Ma)
1	1.0000	17.634	0.022	0.057	95.333	0.022	0.000	0.822	0.077	0.360	0.034
Integrated		17.634	0.022	0.057	95.333	0.022	0.000	0.822	0.077	0.360	0.034

**UAF051-32 LV2B1-8**

Step No.	Cumulative 39Ar	40Ar/39Ar measured	37Ar/39Ar measured	36Ar/39Ar measured	% Atmospheric 40Ar	37Ca/39K	+/-	40*/39K	+/-	Age (Ma)	+/- (Ma)
1	1.0000	17.291	0.022	0.055	94.299	0.022	0.000	0.984	0.081	0.431	0.036
Integrated		17.291	0.022	0.055	94.299	0.022	0.000	0.984	0.081	0.431	0.036

**UAF051-32 LV2B1 -18**

Step No.	Cumulative 39Ar	40Ar/39Ar measured	37Ar/39Ar measured	36Ar/39Ar measured	% Atmospheric 40Ar	37Ca/39K	+/-	40*/39K	+/-	Age (Ma)	+/- (Ma)
1	1.0000	9.412	0.012	0.026	82.009	0.012	0.000	1.688	0.040	0.740	0.018
Integrated		9.412	0.012	0.026	82.009	0.012	0.000	1.688	0.040	0.740	0.019

**UAF051-32 LV2B1**

**UAF051-32 LV2B1-17**

Step No.	Cumulative 39Ar	40Ar/39Ar measured	37Ar/39Ar measured	36Ar/39Ar measured	% Atmospheric 40Ar	37Ca/39K	+/-	40*/39K	+/-	Age (Ma)	+/- (Ma)
1	0.9343	17.811	0.013	0.055	91.217	0.013	0.000	1.562	0.081	0.685	0.035
2	1.0000	37.056	0.114	0.123	98.047	0.114	0.006	0.723	0.419	0.317	0.184
Integrated		19.074	0.020	0.059	92.089	0.020	0.001	1.507	0.080	0.661	0.036

**UAF051-32 LV2B1-16**

Step No.	Cumulative 39Ar	40Ar/39Ar measured	37Ar/39Ar measured	36Ar/39Ar measured	% Atmospheric 40Ar	37Ca/39K	+/-	40*/39K	+/-	Age (Ma)	+/- (Ma)
1	0.8633	10.588	0.011	0.031	86.728	0.011	0.000	1.401	0.046	0.614	0.020
2	1.0000	20.258	0.048	0.067	97.686	0.048	0.001	0.468	0.121	0.205	0.053
Integrated		11.909	0.016	0.036	89.278	0.016	0.000	1.274	0.043	0.559	0.019

**UAF051-32 LV2B1 -15**

Step No.	Cumulative 39Ar	40Ar/39Ar measured	37Ar/39Ar measured	36Ar/39Ar measured	% Atmospheric 40Ar	37Ca/39K	+/-	40*/39K	+/-	Age (Ma)	+/- (Ma)
1	0.8245	14.224	0.011	0.046	94.949	0.011	0.000	0.717	0.062	0.314	0.027
2	1.0000	10.194	0.031	0.032	92.864	0.031	0.001	0.725	0.061	0.318	0.027
Integrated		13.516	0.014	0.043	94.673	0.014	0.000	0.719	0.052	0.315	0.023

**UAF051-32 LV2B1**

**UAF051-32 LV2B1-14**

Step No.	Cumulative 39Ar	40Ar/39Ar measured	37Ar/39Ar measured	36Ar/39Ar measured	% Atmospheric 40Ar	37Ca/39K	+/-	40*/39K	+/-	Age (Ma)	+/- (Ma)
1	0.6346	12.692	0.011	0.039	91.681	0.011	0.000	1.053	0.055	0.462	0.024
2	1.0000	9.039	0.020	0.027	89.848	0.020	0.000	0.915	0.042	0.401	0.018
Integrated		11.357	0.015	0.035	91.148	0.015	0.000	1.003	0.038	0.440	0.017

**UAF051-32 LV2B1-13**

Step No.	Cumulative 39Ar	40Ar/39Ar measured	37Ar/39Ar measured	36Ar/39Ar measured	% Atmospheric 40Ar	37Ca/39K	+/-	40*/39K	+/-	Age (Ma)	+/- (Ma)
1	1.0000	10.863	0.012	0.034	93.664	0.012	0.000	0.686	0.047	0.301	0.021
Integrated		10.863	0.012	0.034	93.664	0.012	0.000	0.686	0.047	0.301	0.021

**UAF051-32 LV2B1-12**

Step No.	Cumulative 39Ar	40Ar/39Ar measured	37Ar/39Ar measured	36Ar/39Ar measured	% Atmospheric 40Ar	37Ca/39K	+/-	40*/39K	+/-	Age (Ma)	+/- (Ma)
1	0.5258	4.582	0.009	0.012	80.651	0.009	0.000	0.881	0.033	0.386	0.014
2	0.7642	8.584	0.021	0.026	91.053	0.021	0.001	0.765	0.070	0.336	0.031
3	0.8707	11.400	0.035	0.038	98.188	0.035	0.002	0.206	0.142	0.090	0.062
4	1.0000	27.872	0.062	0.093	98.987	0.062	0.002	0.282	0.165	0.124	0.072
Integrated		9.273	0.021	0.029	92.383	0.021	0.000	0.704	0.035	0.309	0.016

**UAF051-32 LV2B1**

**UAF051-32 LV2B1-11**

Step No.	Cumulative 39Ar	40Ar/39Ar measured	37Ar/39Ar measured	36Ar/39Ar measured	% Atmospheric 40Ar	37Ca/39K	+/-	40*/39K	+/-	Age (Ma)	+/- (Ma)
1	1.0000	13.776	0.016	0.043	91.830	0.016	0.000	1.123	0.059	0.492	0.026
Integrated		13.776	0.016	0.043	91.830	0.016	0.000	1.123	0.059	0.492	0.026

**UAF051-32 LV2B1-10**

Step No.	Cumulative 39Ar	40Ar/39Ar measured	37Ar/39Ar measured	36Ar/39Ar measured	% Atmospheric 40Ar	37Ca/39K	+/-	40*/39K	+/-	Age (Ma)	+/- (Ma)
1	1.0000	13.009	0.019	0.040	91.077	0.019	0.000	1.158	0.056	0.508	0.025
Integrated		13.009	0.019	0.040	91.077	0.019	0.000	1.158	0.056	0.508	0.025

051-31 LVF2628

Weighted average of J from standards = 0.000243 +/- 0.000002

LVF2628 HOLE #1

Step No.	Cumulative 39Ar	40Ar/39Ar measured	37Ar/39Ar measured	36Ar/39Ar measured	% Atmospheric 40Ar	37Ca/39K	+/-	40*/39K	+/-	Age (Ma)	+/- (Ma)
1	1.0000	12.660	0.009	0.039	91.387	0.009	0.000	1.088	0.050	0.477	0.022
Integrated		12.660	0.009	0.039	91.387	0.009	0.000	1.088	0.050	0.477	0.022

051-31 LVF2628 #3

Step No.	Cumulative 39Ar	40Ar/39Ar measured	37Ar/39Ar measured	36Ar/39Ar measured	% Atmospheric 40Ar	37Ca/39K	+/-	40*/39K	+/-	Age (Ma)	+/- (Ma)
1	1.0000	10.539	0.018	0.032	89.370	0.018	0.000	1.117	0.046	0.490	0.020
Integrated		10.539	0.018	0.032	89.370	0.018	0.000	1.117	0.046	0.490	0.021

051-31 LVf2628 #4

Step No.	Cumulative 39Ar	40Ar/39Ar measured	37Ar/39Ar measured	36Ar/39Ar measured	% Atmospheric 40Ar	37Ca/39K	+/-	40*/39K	+/-	Age (Ma)	+/- (Ma)
1	1.0000	11.407	0.009	0.035	91.526	0.009	0.000	0.964	0.050	0.423	0.022
Integrated		11.407	0.009	0.035	91.526	0.009	0.000	0.964	0.050	0.423	0.022



UAF051-31 LVF2628

UAF051-31 LVF2628 #5

Step No.	Cumulative 39Ar	40Ar/39Ar measured	37Ar/39Ar measured	36Ar/39Ar measured	% Atmospheric 40Ar	37Ca/39K	+/-	40*/39K	+/-	Age (Ma)	+/- (Ma)
1	1.0000	8.837	0.006	0.025	84.335	0.006	0.000	1.380	0.041	0.605	0.018
Integrated		8.837	0.006	0.025	84.335	0.006	0.000	1.380	0.041	0.605	0.018

UAF051-31 LVF2628 #6

Step No.	Cumulative 39Ar	40Ar/39Ar measured	37Ar/39Ar measured	36Ar/39Ar measured	% Atmospheric 40Ar	37Ca/39K	+/-	40*/39K	+/-	Age (Ma)	+/- (Ma)
1	1.0000	7.958	-0.496	-0.019	-71.161	-0.496	0.296	13.567	16.168	5.939	7.066
Integrated		7.958	-0.496	-0.019	-71.161	-0.496	0.296	13.567	16.168	5.939	7.066

UAF051-31 LVF2628 #7

Step No.	Cumulative 39Ar	40Ar/39Ar measured	37Ar/39Ar measured	36Ar/39Ar measured	% Atmospheric 40Ar	37Ca/39K	+/-	40*/39K	+/-	Age (Ma)	+/- (Ma)
1	1.0000	10.639	0.004	0.031	86.080	0.004	0.000	1.477	0.048	0.647	0.021
Integrated		10.639	0.004	0.031	86.080	0.004	0.000	1.477	0.048	0.647	0.022

**UAF049 LV22-W DIFFUSE BEAM STEP HEATING**

**Weighted average of J from standards = 0.000233 +/- 0.000000**

**UAF049 LV22-W-40**

Step No.	Cumulative 39Ar	40Ar/39Ar measured	37Ar/39Ar measured	36Ar/39Ar measured	% Atmospheric 40Ar	37Ca/39K	+/-	40*/39K	+/-	Age (Ma)	+/- (Ma)
1	1.0000	28.173	0.122	0.091	95.870	0.122	0.001	1.162	0.137	0.489	0.058
Integrated		28.173	0.122	0.091	95.870	0.122	0.001	1.162	0.137	0.489	0.058

**UAF049 LV22-W-11**

Step No.	Cumulative 39Ar	40Ar/39Ar measured	37Ar/39Ar measured	36Ar/39Ar measured	% Atmospheric 40Ar	37Ca/39K	+/-	40*/39K	+/-	Age (Ma)	+/- (Ma)
1	0.7346	22.364	0.059	0.071	94.385	0.059	0.000	1.254	0.108	0.528	0.046
2	1.0000	30.930	0.215	0.096	91.675	0.215	0.001	2.573	0.152	1.083	0.064
Integrated		24.638	0.100	0.078	93.482	0.100	0.000	1.604	0.089	0.675	0.038

**UAF049 LV22-W-17**

Step No.	Cumulative 39Ar	40Ar/39Ar measured	37Ar/39Ar measured	36Ar/39Ar measured	% Atmospheric 40Ar	37Ca/39K	+/-	40*/39K	+/-	Age (Ma)	+/- (Ma)
1	0.5488	28.074	0.059	0.091	95.597	0.059	0.000	1.235	0.137	0.520	0.058
2	1.0000	29.728	0.156	0.094	93.011	0.156	0.001	2.076	0.143	0.874	0.060
Integrated		28.821	0.103	0.092	94.393	0.103	0.000	1.614	0.099	0.679	0.042

**UAF049 LV22-W DIFFUSE BEAM STEP HEATING**

**UAF049 LV22-W-23**

Step No.	Cumulative 39Ar	40Ar/39Ar measured	37Ar/39Ar measured	36Ar/39Ar measured	% Atmospheric 40Ar	37Ca/39K	+/-	40*/39K	+/-	Age (Ma)	+/- (Ma)
1	0.8570	24.130	0.052	0.078	96.174	0.052	0.000	0.922	0.118	0.388	0.050
2	1.0000	44.740	0.434	0.136	89.842	0.434	0.002	4.543	0.223	1.911	0.094
Integrated		27.078	0.107	0.087	94.677	0.107	0.000	1.440	0.106	0.606	0.045

**UAF049 LV22-W-29**

Step No.	Cumulative 39Ar	40Ar/39Ar measured	37Ar/39Ar measured	36Ar/39Ar measured	% Atmospheric 40Ar	37Ca/39K	+/-	40*/39K	+/-	Age (Ma)	+/- (Ma)
1	0.6207	28.200	0.060	0.090	94.864	0.060	0.000	1.447	0.137	0.609	0.058
2	1.0000	21.252	0.110	0.065	90.628	0.110	0.001	1.989	0.105	0.837	0.044
Integrated		25.564	0.079	0.081	93.528	0.079	0.000	1.653	0.094	0.695	0.040

**UAF049 LV22-W-35**

Step No.	Cumulative 39Ar	40Ar/39Ar measured	37Ar/39Ar measured	36Ar/39Ar measured	% Atmospheric 40Ar	37Ca/39K	+/-	40*/39K	+/-	Age (Ma)	+/- (Ma)
1	0.9668	25.572	0.083	0.082	94.287	0.083	0.000	1.459	0.123	0.614	0.052
2	1.0000	72.931	0.696	0.241	97.674	0.696	0.004	1.696	0.470	0.714	0.198
Integrated		27.146	0.104	0.087	94.590	0.104	0.000	1.467	0.120	0.617	0.051

UAF049 LV22-Z

Weighted average of J from standards = 0.000233 +/- 0.000000

UAF049 LV22-Z-18 STEP HEAT

Step No.	Cumulative 39Ar	40Ar/39Ar measured	37Ar/39Ar measured	36Ar/39Ar measured	% Atmospheric 40Ar	37Ca/39K	+/-	40*/39K	+/-	Age (Ma)	+/- (Ma)
1	0.9933	391.156	0.006	0.804	60.740	0.006	0.001	153.558	1.734	63.500	0.705
2	1.0000	386.003	-0.139	0.900	68.944	-0.139	0.140	119.856	26.215	49.753	10.734
Integrated		391.121	0.005	0.805	60.794	0.005	0.001	153.333	1.732	63.4	0.7

UAF049 LV22-Z-24 STEP HEAT

Step No.	Cumulative 39Ar	40Ar/39Ar measured	37Ar/39Ar measured	36Ar/39Ar measured	% Atmospheric 40Ar	37Ca/39K	+/-	40*/39K	+/-	Age (Ma)	+/- (Ma)
1	0.9447	353.424	0.010	0.414	34.623	0.010	0.001	231.039	1.592	94.711	0.636
2	0.9758	310.854	0.101	0.220	20.936	0.101	0.029	245.766	6.860	100.583	2.731
3	1.0000	377.467	0.185	0.516	40.400	0.185	0.038	224.980	8.483	92.290	3.393
Integrated		352.681	0.017	0.411	34.398	0.017	0.002	231.351	1.533	94.8	0.6

UAF049 LV22-Z (cont.)

UAF049 LV22-Z-30 STEP HEAT

Step No.	Cumulative 39Ar	40Ar/39Ar measured	37Ar/39Ar measured	36Ar/39Ar measured	% Atmospheric 40Ar	37Ca/39K	+/-	40*/39K	+/-	Age (Ma)	+/- (Ma)
1	0.3833	441.362	0.006	1.419	95.044	0.006	0.002	21.874	2.156	9.183	0.903
2	0.5835	226.861	0.005	0.108	14.105	0.005	0.003	194.838	1.292	80.196	0.520
3	0.8167	234.303	0.003	0.087	10.914	0.003	0.003	208.706	1.293	85.770	0.519
4	0.9366	267.975	0.012	0.095	10.522	0.012	0.005	239.756	1.818	98.189	0.725
5	1.0000	315.933	0.057	0.236	22.070	0.057	0.010	246.194	2.818	100.753	1.122
Integrated		321.397	0.009	0.612	56.307	0.009	0.001	140.417	0.951	58.2	0.4

UAF049 LV22-Z-36 STEP HEAT

Step No.	Cumulative 39Ar	40Ar/39Ar measured	37Ar/39Ar measured	36Ar/39Ar measured	% Atmospheric 40Ar	37Ca/39K	+/-	40*/39K	+/-	Age (Ma)	+/- (Ma)
1	0.2670	639.309	0.009	1.982	91.628	0.009	0.003	53.519	3.092	22.386	1.286
2	0.6889	220.971	0.008	0.109	14.645	0.008	0.002	188.587	1.123	77.678	0.453
3	0.8651	240.613	0.005	0.105	12.850	0.005	0.004	209.671	1.487	86.157	0.597
4	0.9392	263.078	0.037	0.103	11.516	0.037	0.010	232.762	2.644	95.399	1.056
5	1.0000	329.165	0.028	0.219	19.650	0.028	0.013	264.466	3.340	108.012	1.324
Integrated		345.833	0.011	0.615	52.539	0.011	0.002	164.124	1.015	67.8	0.4

**UAF049 LV22-Z (cont.)**

**UAF049 LV22-Z-41 STEP HEAT**

Step No.	Cumulative 39Ar	40Ar/39Ar measured	37Ar/39Ar measured	36Ar/39Ar measured	% Atmospheric 40Ar	37Ca/39K	+/-	40*/39K	+/-	Age (Ma)	+/- (Ma)
1	0.0076	4896.279	-0.026	17.094	103.166	-0.026	0.115	-155.001	33.294	-66.447	14.539
2	0.0782	1759.038	0.038	7.133	119.822	0.038	0.012	-348.680	10.202	-153.069	4.674
3	0.3039	4756.545	0.008	0.681	4.233	0.008	0.004	4555.188	26.168	1306.194	5.340
4	0.4883	242.192	0.014	0.112	13.644	0.014	0.005	209.126	1.527	85.939	0.613
5	0.6060	287.099	0.019	0.211	21.701	0.019	0.007	224.777	2.093	92.209	0.837
6	0.6910	252.585	0.029	0.164	19.136	0.029	0.010	204.232	2.463	83.974	0.990
7	0.9110	256.792	0.014	0.111	12.795	0.014	0.004	223.912	1.509	91.863	0.604
8	0.9793	291.778	0.023	0.164	16.653	0.023	0.013	243.168	3.179	99.549	1.266
9	0.9955	369.348	0.168	0.403	32.222	0.168	0.053	250.346	12.159	102.405	4.835
10	1.0000	845.428	0.726	2.279	79.647	0.726	0.212	172.144	38.681	71.036	15.652
Integrated		1420.707	0.022	0.899	18.693	0.022	0.003	1155.124	4.780	430.5	1.7

**UAF049 LV22-Z-43 STEP HEAT**

Step No.	Cumulative 39Ar	40Ar/39Ar measured	37Ar/39Ar measured	36Ar/39Ar measured	% Atmospheric 40Ar	37Ca/39K	+/-	40*/39K	+/-	Age (Ma)	+/- (Ma)
1	0.7550	239.314	0.014	0.625	77.155	0.014	0.002	54.666	1.158	22.863	0.481
2	0.9757	273.826	0.034	0.068	7.387	0.034	0.008	253.578	2.199	103.690	0.874
3	0.9933	370.103	0.137	0.553	44.124	0.137	0.094	206.803	19.796	85.006	7.949
4	1.0000	1343.934	1.360	3.515	77.282	1.361	0.320	305.585	62.255	124.239	24.459
Integrated		256.643	0.030	0.520	59.891	0.030	0.003	102.927	1.074	42.8	0.4

APPENDIX V. Sr isotope measurements and related trace element concentrations

Sample ID	Depth (m)	Sample Type	Sr (ppm)	Rb (ppm)	Rb/Sr	<sup>87</sup> Sr/ <sup>86</sup> Sr(m)	% std error	2 σ
42A-OUT	0.0	Calc Hfls.	88	204	2.32	0.746851	0.0008	0.000012
42B-OUT,2	0.0	Banded Hfls.	207	66	0.32	0.717863	0.0008	0.000011
42B-OUT,1	0.0	Banded Hfls.	207	66	0.32	0.717849	0.0009	0.000011
44A-OUT	0.0	Banded Hfls.	135	91	0.67	0.719184	0.0007	0.000010
44B-OUT	0.0	Banded Hfls.	282	157	0.56	0.716430	0.0009	0.000013
44F-OUT	0.0	Banded Hfls.	102	105	1.03	0.729131	0.0008	0.000012
46A-OUTA	0.0	Meta tuff	248	142	0.57	0.711073	0.0007	0.000010
46C-OUT	0.0	Meta tuff	156	295	1.89	0.721143	0.0008	0.000012
LVEW 200	61.0	Qer volcanics	91	144	1.58	0.706487	0.0011	0.000016
LVEW 2290S	698.0	Qbt sanidine	97	107	1.10	0.706158	0.0011	0.000016
LVEW 2290ML	698.0	Qbt matrix	87	161	1.85	0.706830	0.0007	0.000010
LVEW 2290M2	698.0	Qbt matrix	85	155	1.82	0.706888	0.0009	0.000013
LVEW 2-B1	784.4	Qer intrusion	81	124	1.53	0.706832	0.0007	0.000010
LVEW 9-L	804.7	Qer intrusion	37	125	3.38	0.706968	0.0012	0.000017
LVEW 14-G-S	819.9	Qbt sanidine	90	131	1.46	0.707388	0.0009	0.000013
LVEW 14-G-M	819.9	Qbt matrix	52	177	3.40	0.707228	0.0010	0.000014
LVEW 17-H	829.0	Qer intrusion	23	222	9.65	0.707020	0.0008	0.000011
LVEW 17-M-S	830.3	Qbt sanidine	55	112	2.04	0.706210	0.0011	0.000016
LVEW 17-MM	830.3	Qbt matrix	19	181	9.53	0.707210	0.0008	0.000011
LVEW 6420	1956.8	Mzmv	62	6	0.10	0.707154	0.0011	0.000016
LVEW 30-C	2111.0	Quartzite	64	3	0.05	0.723591	0.0007	0.000010
LVEW 31-K	2116.4	Banded Hfls.	45	87	1.93	0.738937	0.0007	0.000010
LVEW 42-H	2149.8	Banded Hfls.	192	148	0.77	0.725610	0.0008	0.000012
LVEW 50-G	2168.4	Meta??	284	156	0.55	0.717098	0.0010	0.000014
LVEW 50-O3	2170.5	Banded Hfls.	94	93	0.99	0.726463	0.0008	0.000012
LVEW 53-C2a	2183.6		270	148	0.55	0.723825	0.0009	0.000013
LVEW 58-C	2199.6	Metaintrusion	294	132.5	0.45	0.717362	0.0007	0.000010
LVEW 67-K	2226.0	Banded Hfls.	120	111	0.93	0.736954	0.0007	0.000010
LVEW 70-L	2236.3	Banded Hfls.	177	87	0.49	0.729520	0.0009	0.000013
LVEW 76-A3	2259.1	Black Hfls.	108	95	0.88	0.730560	0.0008	0.000012
LVEW 88-B3	2306.3	meta argillite	184	130	0.71	0.729561	0.0011	0.000016

Figure AV.1 Sr isotope values for intracaldera rocks and extrusive equivalents. Samples designated "OUT" collected in Mt.

Morrison Roof Pendant in High Sierras. See sample sites 4 and 5, Figure III.1.

Sample ID	Depth (m)	Sample Info	Sr (ppm) ± ppm	Rb (ppm) ± ppm	K (ppm) ± ppm	Nd (ppm) ± ppm				
LVEW2290-L	698.0	in Qbt matrix	76	0	54.2700	0.18000	1.44 wt%	30.00	70.71	0.26
LVEW 4320	1316.7	in Qbt matrix	503	2	8.1840	0.00700	0.8658 wt%	4.70	11.42	0.04
LVEW 5700	1737.4	in Qbt matrix	4729	37	112.0284	0.09790	10.01 wt%	113.00	193.71	0.39
LVEW 21-Beta	1846.8	Vein in breccia	5333	13	0.0934	0.00260	96.4	0.17	65.67	0.34
LVEW 21-Beta1	1846.8	Vein in breccia	3430	48	nd		>10000		42.47	0.14
LVEW 6420	1956.8	in Mxmv matrix	256	1	0.4699	0.00040	495.0	0.63	4.21	0.10
LVEW 27-F	2102.8	Vein in Hfls.	2900	144	nd		66.2	0.42	3.22	0.08
LVEW 27-F1	2102.8	Vein in Hfls.	2368	4	0.2407	0.00950	8.6	0.08	3.05	0.02
LVEW 30-C	2111.0	in Qtzite. matrix	917	4	2.7600	0.00550	1318.2	1.10	12.51	0.08
LVEW 35-J	2128.3	Vein in Qtzite.	968	2	0.9075	0.04037	51.4	0.14	11.17	0.18
LVEW 35-J1	2128.3	Vein in Qtzite.	1285	3	0.2621	0.00440	34.3	0.1	9.66	0.08
LVEW 37-E	2133.9	Vein in Hfls.	888	8	0.0025	0.00004	38.2	0.21	nd	
LVEW 37-E1	2133.9	Vein in Hfls.	1081	5	0.1478	0.00330	37.0	0.15	3.8	0.07
LVEW 51-D	2173.8	Vein in Hfls.	1928	3	0.4771	0.00067	193.2	0.93	7.77	0.05
LVEW 58-C	2199.6	in Int.? matrix	1747	4	14.2550	0.01200	0.9858	12.4	23.02	0.14
LVEW 67-K	2226.0	in Hfls. matrix	1430	4	103.5500	0.16000	7.62 wt%	100	22.01	0.06
LVEW70-L	2236.3	Vein in Hfls.	2862	8	1.7910	0.00360	376	0.4	5.05	0.04
LVEW 88-B3	2306.3	in Hfls. matrix	1362	5	55.0724	0.08889	2.89 wt%	78.1	12.68	0.04

Table AV.2 Sr isotope concentration in alteration calcite in LVEW. Sr, Rb, K, Nd, and Sm concentrations determined by isotope dilution measured on VG 54 single collector mass spectrometer at UC-B.  $^{87}\text{Sr}/^{86}\text{Sr}$  concentration reported as the measured value.



Table AV.2 con't.

Sm (ppm)	± ppm	147Sm/144Nd	<sup>87</sup> Sr/ <sup>86</sup> Sr (m)	% sd error	2 σ	<sup>87</sup> Rb/ <sup>86</sup> Sr	Sample ID
11.455	0.03	0.09799	0.708577	0.0009	0.000013	2.05326000	LVEW2290-L
2.811	0.01	0.14887	0.707395	0.001	1.415E-05	0.04703500	LVEW 4320
66.52	0.28	0.20772	0.708828	0.0008	1.134E-05	0.06817630	LVEW 5700
18.64	# 0.07	0.17168	0.708972	0.0008	1.452E-05	0.00005070	LVEW 21-Beta
11.64	0.1	0.16480	0.708939	0.0008	1.134E-05		LVEW 21- Beta1
0.798	0	0.11459	0.707178	0.0009	1.273E-05	0.00531700	LVEW 6420
nd			0.717652	0.0009	1.148E-05		LVEW 27-F
0.635	0.01	0.12589	0.717429	0.0008	1.148E-05	0.00029430	LVEW 27-F1
2.889	0.01	0.13967	0.723541	0.0008	1.158E-05	0.00872100	LVEW 30-C
2.446	0.15	0.13251	0.721456	0.0008	1.154E-05	0.00271000	LVEW 35-J
nd			0.721505	0.0015		0.00059040	LVEW 35-J1
nd			0.726045	0.0008	1.162E-05	0.00000828	LVEW 37-E
nd			0.726217	0.001	1.452E-05	0.00039590	LVEW 37-E1
2.17	0.08	0.168553	0.720222	0.001	1.44E-05	0.00071019	LVEW 51-D
6.841	0.03	0.17975	0.715562	0.0008	1.145E-05	0.023615	LVEW 58-C
6.2	0.03	0.170431	0.730563	0.0008	1.169E-05	0.209578	LVEW 67-K
nd			0.725048	0.0007	1.015E-05	0.00180066	LVEW70-L
3.574	0.02	0.17052	0.725834	0.0011	1.597E-05	0.117061	LVEW 88-B3